1 OF 2
AD A106402

LEVEL

chool of

OCEANOGRAPHY

O S S U

CONTENTS:

A LARGE, OPENING-CLOSING MIDWATER TRAWL FOR SAMPLING OCEANIC
NEKTON, AND COMPARISON OF CATCHES WITH AN ISAACS-KIDD
MIDWATER TRAWL

   William G. Pearcy.   Reprinted from Fishery Bulletin
   78(2): 529-534.   1980.

OCEANIC RADIATION INSTRUMENTS

   C. A. Paulson.   Reprinted from Air-Sea Interaction
   F. Dobson, L. Hasse and R. Davis (eds.).   1980.
   pgs. 509-521.

INTERMEDIATE NEPHELOID LAYERS OBSERVED OFF OREGON AND
WASHINGTON.

   Hasong Pak, J. Ronald V. Zaneveld and J. Kitchen.
   Reprinted from Journal of Geophysical Research 85(C11):
   6697-6708.   1980.

Unclassified

REPORT DOCUMENTATION PAGE		READ INSTRUCTIONS BEFORE COMPLETING FORM
1. REPORT NUMBER 80-3	2. GOVT ACCESSION NO. AD-A106 412	3. RECIPIENT'S CATALOG NUMBER
4. TITLE (and Subtitle) TECHNOLOGY ILLUSTRATIONS FOR A TOWED DISTRIBUTED INSTRUMENTATION PROFILING SYSTEM.		5. TYPE OF REPORT & PERIOD COVERED Reprint
		6. PERFORMING ORG. REPORT NUMBER
7. AUTHOR(s) Roderick Mesecar Frank Evans James Wagner		8. CONTRACT OR GRANT NUMBER(s) N00014-76-C-0067
9. PERFORMING ORGANIZATION NAME AND ADDRESS School of Oceanography Oregon State University Corvallis, OR 97331		10. PROGRAM ELEMENT, PROJECT, TASK AREA & WORK UNIT NUMBERS NR 083-102
11. CONTROLLING OFFICE NAME AND ADDRESS Office of Naval Research Ocean Science and Technology Division Arlington, VA 22217		12. REPORT DATE 1980
		13. NUMBER OF PAGES 14
14. MONITORING AGENCY NAME & ADDRESS(if different from Controlling Office)		15. SECURITY CLASS. (of this report) unclassified
		15a. DECLASSIFICATION/DOWNGRADING SCHEDULE

16. DISTRIBUTION STATEMENT (of this Report)

Approved for public release; distribution unlimited

17. DISTRIBUTION STATEMENT (of the abstract entered in Block 20, if different from Report)

19. KEY WORDS (Continue on reverse side if necessary and identify by block number)

20. ABSTRACT (Continue on reverse side if necessary and identify by block number)

This paper describes some of the salient features of a towed thermistor cable system. The text includes information on the sensor designs for pressure, conductivity and temperature and how they are integrated into the tow cable. The cable is stored and transported on an aluminum winch which can be used on 30 m vessels.

DD FORM 1473 1 JAN 73   EDITION OF 1 NOV 68 IS OBSOLETE
S/N 0102-014-6601

Unclassified

Unclassified

REPORT DOCUMENTATION PAGE		READ INSTRUCTIONS BEFORE COMPLETING FORM
1. REPORT NUMBER 80-4	2. GOVT ACCESSION NO. AD-A106 462	3. RECIPIENT'S CATALOG NUMBER
4. TITLE (and Subtitle) APPLICATIONS OF A DATA-COMPRESSION ALGORITHM FOR XBT BATHY-MESSAGE PREPARATION		5. TYPE OF REPORT & PERIOD COVERED Reprint
		6. PERFORMING ORG. REPORT NUMBER
7. AUTHOR(s) Roderick Mesecar James Wagner		8. CONTRACT OR GRANT NUMBER(s) N00014-76-C-0067
9. PERFORMING ORGANIZATION NAME AND ADDRESS School of Oceanography Oregon State University Corvallis, OR 97331		10. PROGRAM ELEMENT, PROJECT, TASK AREA & WORK UNIT NUMBERS NR 083-102
11. CONTROLLING OFFICE NAME AND ADDRESS Office of Naval Research Ocean Science and Technology Division Arlington, VA 22217		12. REPORT DATE 1980
		13. NUMBER OF PAGES 9
14. MONITORING AGENCY NAME & ADDRESS(If different from Controlling Office)		15. SECURITY CLASS. (of this report) unclassified
		15a. DECLASSIFICATION/DOWNGRADING SCHEDULE

16. DISTRIBUTION STATEMENT (of this Report)

Approved for public release; distribution unlimited

17. DISTRIBUTION STATEMENT (of the abstract entered in Block 20, if different from Report)

18. SUPPLEMENTARY NOTES

Reprint from Near Surface Ocean Experimental Technology Workshop Proceedings.
February 1980, pg. 139-147. Naval Ocean Research and Development Activity.
NSTL Station, MS.

19. KEY WORDS (Continue on reverse side if necessary and identify by block number)

20. ABSTRACT (Continue on reverse side if necessary and identify by block number)

This paper describes an expendable Bathythermograph (XBT) system utilizing
a commercial microprocessor. An algorithm particularly suited for data
compression in such systems is presented in detail.

SECURITY CLASSIFICATION OF THIS PAGE *(When Data Entered)*

REPORT DOCUMENTATION PAGE		READ INSTRUCTIONS BEFORE COMPLETING FORM
1. REPORT NUMBER 80-6	2. GOVT ACCESSION NO. AD-A106 402	3. RECIPIENT'S CATALOG NUMBER
4. TITLE *(and Subtitle)* SMALL-SCALE SEA SURFACE TEMPERATURE STRUCTURE		5. TYPE OF REPORT & PERIOD COVERED Reprint
		6. PERFORMING ORG. REPORT NUMBER
7. AUTHOR(s) James J. Simpson Clayton A. Paulson		8. CONTRACT OR GRANT NUMBER(s) N0014-76-C-0067 N00014-79-C-004
9. PERFORMING ORGANIZATION NAME AND ADDRESS School of Oceanography Oregon State University Corvallis, OR 97331		10. PROGRAM ELEMENT, PROJECT, TASK AREA & WORK UNIT NUMBERS NR 083-102
11. CONTROLLING OFFICE NAME AND ADDRESS Office of Naval Research Ocean Science & Technology Division Arlington, VA 22217		12. REPORT DATE March 1980
		13. NUMBER OF PAGES 12
14. MONITORING AGENCY NAME & ADDRESS*(If different from Controlling Office)*		15. SECURITY CLASS. *(of this report)* Unclassified
		15a. DECLASSIFICATION/DOWNGRADING SCHEDULE

16. DISTRIBUTION STATEMENT *(of this Report)*

Approved for public release; distribution unlimited

17. DISTRIBUTION STATEMENT *(of the abstract entered in Block 20, if different from Report)*

18. SUPPLEMENTARY NOTES

19. KEY WORDS *(Continue on reverse side if necessary and identify by block number)*

20. ABSTRACT *(Continue on reverse side if necessary and identify by block number)*

Observations of sea surface temperature and wave height were made from a large, manned spar buoy (R/P FLIP) ~100km off the coast of Baja California. Surface temperature was measured with a radiation thermometer which viewed a disc on the surface 12 cm in diameter. The instrument responded to frequencies up to 3 Hz. Wave height was measured with a resistance gage located close to the field of view of the radiometer.

Log-log plots of spectra of sea surface temperature exhibit a plateau

DD FORM 1473 EDITION OF 1 NOV 65 IS OBSOLETE
1 JAN 73
S/N 0102-014-6601 |

SECURITY CLASSIFICATION OF THIS PAGE *(When Data Entered)*

between 0.05 and 0.5 Hz, followed by a rapid decrease in energy at fre-
quencies >1 Hz. A coherence of 0.5 between waves and surface temperature
occurs at the same frequency as the peak in the wave spectrum. Phase spectra
show that warm temperatures associated with the thinning of the surface
viscous layer occur systematically upwind of the crests of the dominant gravity
waves and downwind of the crests of steeply sloping, shorter period gravity
waves. The warm temperatures are hypothesized to be caused by enhanced wind
stress upwind from the crests and by surface instability and surface conver-
gence downwind from the crests.

  The magnitude of the mean temperature difference between the surface
and the warmer, well-mixed water below is estimated from the surface temper-
ature record. It is assumed that the warmest surface temperatures observed
are associated with thinning of the viscous layer and are representative
of the well-mixed water below. The dimensionless constant in a formula due
to Saunders (1967), which relates the temperature difference to wind stress
and heat flux, is found to be seven.

REPORT DOCUMENTATION PAGE		READ INSTRUCTIONS BEFORE COMPLETING FORM
1. REPORT NUMBER 80-9	2. GOVT ACCESSION NO. AD-A106 402	3. RECIPIENT'S CATALOG NUMBER
4. TITLE (and Subtitle) THE SCALING OF VERTICAL TEMPERATURE GRADIENT SPECTRA		5. TYPE OF REPORT & PERIOD COVERED Reprint
		6. PERFORMING ORG. REPORT NUMBER
7. AUTHOR(s) D. R. Caldwell, T. M. Dillon, J. M. Brubaker, P.A. Newberger, C.A. Paulson		8. CONTRACT OR GRANT NUMBER(s) N0014-76-C-0067
9. PERFORMING ORGANIZATION NAME AND ADDRESS School of Oceanography Oregon State University Corvallis, Oregon 97331		10. PROGRAM ELEMENT, PROJECT, TASK AREA & WORK UNIT NUMBERS NR 083-102
11. CONTROLLING OFFICE NAME AND ADDRESS Office of Naval Research Ocean Science & Technology Division Arlington, VA 22217		12. REPORT DATE April 1980
		13. NUMBER OF PAGES 8
14. MONITORING AGENCY NAME & ADDRESS(if different from Controlling Office)		15. SECURITY CLASS. (of this report) Unclassified
		15a. DECLASSIFICATION/DOWNGRADING SCHEDULE

16. DISTRIBUTION STATEMENT (of this Report)

Approved for public release; distribution unlimited

17. DISTRIBUTION STATEMENT (of the abstract entered in Block 20, if different from Report)

19. KEY WORDS (Continue on reverse side if necessary and identify by block number)

20. ABSTRACT (Continue on reverse side if necessary and identify by block number)

Tests of a formula derived for the cutoff wave number of vertical temperature gradient spectra, using data taken in the upper layers of the North Pacific, show encouraging results. To derive this formula, the cutoff wave number is assumed to be the Batchelor wave number, with kinetic energy dissipation calculated by combining a form used in the atmosphere for calculating the vertical eddy diffusivity in terms of the dissipation with the Osborn-Cox formula for calculating eddy diffusivity from the variance of the temperature

gradient spectrum.   Kinetic energy dissipation in the water column can be determined in this way; a vertical profile of dissipation shows value of the order of $10^{-3}cm^2s^{-3}$ at the base of a storm-tossed mixing layer.   In the thermocline below, dissipation occurs in patches.

REPORT DOCUMENTATION PAGE		READ INSTRUCTIONS BEFORE COMPLETING FORM
1. REPORT NUMBER 80-10	2. GOVT ACCESSION NO. AD-A106 402	3. RECIPIENT'S CATALOG NUMBER
4. TITLE (and Subtitle) THE BATCHELOR SPECTRUM AND DISSIPATION IN THE UPPER OCEAN		5. TYPE OF REPORT & PERIOD COVERED Reprint
		6. PERFORMING ORG. REPORT NUMBER
7. AUTHOR(s) Thomas M. Dillon Douglas R. Caldwell		8. CONTRACT OR GRANT NUMBER(s) N00014-76-C-0067
9. PERFORMING ORGANIZATION NAME AND ADDRESS School of Oceanography Oregon State University Corvallis, OR 97331		10. PROGRAM ELEMENT, PROJECT, TASK AREA & WORK UNIT NUMBERS NR 083-102
11. CONTROLLING OFFICE NAME AND ADDRESS Office of Naval Research Ocean Science & Technology Division Arlington, VA 22217		12. REPORT DATE April 1980
		13. NUMBER OF PAGES 7
14. MONITORING AGENCY NAME & ADDRESS(If different from Controlling Office)		15. SECURITY CLASS. (of this report) Unclassified
		15a. DECLASSIFICATION/DOWNGRADING SCHEDULE

16. DISTRIBUTION STATEMENT (of this Report)

Approved for public release; distribution unlimited

17. DISTRIBUTION STATEMENT (of the abstract entered in Block 20, if different from Report)

18. SUPPLEMENTARY NOTES

19. KEY WORDS (Continue on reverse side if necessary and identify by block number)

20. ABSTRACT (Continue on reverse side if necessary and identify by block number)

Observations of vertical temperature microstructure at ocean station P during the mixed layer experiment (Mile) indicate that the shape of the high-frequency temperature gradient spectrum depends on the relative strengths of turbulence and stratification. For low Cox number $((dT/dz)^2)/(dT/dz)^2$ the linear range of the Batchelor spectrum is not well approximated by observed spectra, while for high Cox number a remarkably close correspondence to the Batchelor spectrum is found. Dissipation rates calculated by the temperature gradient spectrum

cutoff wave number method show a dramatic contrast in turbulence between low and high wind speed periods separated by only 3 hours, showing that the response of the mixed layer and transition zone to wind forcing is rapid. Some indication is found that the thermocline may also respond rapidly to surface forcing.

SECURITY CLASSIFICATION OF THIS PAGE (When Data Entered)

REPORT DOCUMENTATION PAGE		READ INSTRUCTIONS BEFORE COMPLETING FORM
1. REPORT NUMBER Reference 80-13	2. GOVT ACCESSION NO. AD-A186 402	3. RECIPIENT'S CATALOG NUMBER
4. TITLE (and Subtitle) HIGH-FREQUENCY INTERNAL WAVES AT OCEAN STATION P		5. TYPE OF REPORT & PERIOD COVERED Reprint
		6. PERFORMING ORG. REPORT NUMBER
7. AUTHOR(s) Tom M. Dillon Douglas R. Caldwell		8. CONTRACT OR GRANT NUMBER(s) N00014-76-C-0067
9. PERFORMING ORGANIZATION NAME AND ADDRESS School of Oceanography Oregon State University Corvallis, Oregon 97331		10. PROGRAM ELEMENT, PROJECT, TASK AREA & WORK UNIT NUMBERS
11. CONTROLLING OFFICE NAME AND ADDRESS Office of Naval Research Ocean Science & Technology Division Arlington, Virginia 22217		12. REPORT DATE 1980
		13. NUMBER OF PAGES 8
14. MONITORING AGENCY NAME & ADDRESS(If different from Controlling Office)		15. SECURITY CLASS. (of this report) Unclassified
		15a. DECLASSIFICATION/DOWNGRADING SCHEDULE

16. DISTRIBUTION STATEMENT (of this Report)

Approved for public release; distribution unlimited

17. DISTRIBUTION STATEMENT (of the abstract entered in Block 20, if different from Report)

19. KEY WORDS (Continue on reverse side if necessary and identify by block number)

20. ABSTRACT (Continue on reverse side if necessary and identify by block number)

Slow perturbations of the drop speed of a nearly freely falling, winged, microstructure probe in the upper 200 m at station P are interpreted as vertical velocity fluctuations of an internal wave field. The frequencies of these fluctuations lie in the 2.5- to 4-cph band, near the buoyancy-frequency cutoff. A typical rms value is 1.3 cm/s. Indications of the vertical structure of the wave field and the partition of energy among modes are obtained by statistical comparison with discrete mode solutions of the

DD FORM 1473 1 JAN 73 EDITION OF 1 NOV 65 IS OBSOLETE
S/N 0102-014-6601 |

SECURITY CLASSIFICATION OF THIS PAGE (When Data Entered)

internal wave equation. It is found that the first and second modes carry most of the internal wave energy and that the partition of energy between them may change in 3 days.

REPORT DOCUMENTATION PAGE		READ INSTRUCTIONS BEFORE COMPLETING FORM
1. REPORT NUMBER 80-17	2. GOVT ACCESSION NO. AD-A1X6 402	3. RECIPIENT'S CATALOG NUMBER
4. TITLE (and Subtitle) AN ARC TANGENT MODEL OF IRRADIANCE IN THE SEA		5. TYPE OF REPORT & PERIOD COVERED Reprint
		6. PERFORMING ORG. REPORT NUMBER
7. AUTHOR(s) J. Ronald V. Zaneveld Richard W. Spinrad		8. CONTRACT OR GRANT NUMBER(s) N000k4-76-C-0067
9. PERFORMING ORGANIZATION NAME AND ADDRESS School of Oceanography Oregon State University Corvallis, Oregon 97331		10. PROGRAM ELEMENT, PROJECT, TASK AREA & WORK UNIT NUMBERS NR 083-102
11. CONTROLLING OFFICE NAME AND ADDRESS Office of Naval Research Ocean Science & Technology Division Arlington, Virginia 22217		12. REPORT DATE 1980
		13. NUMBER OF PAGES 4
14. MONITORING AGENCY NAME & ADDRESS(if different from Controlling Office)		15. SECURITY CLASS. (of this report) Unclassified
		15a. DECLASSIFICATION/DOWNGRADING SCHEDULE

16. DISTRIBUTION STATEMENT (of this Report)

Approved for public release; distribution unlimited

17. DISTRIBUTION STATEMENT (of the abstract entered in Block 20, if different from Report)

18. SUPPLEMENTARY NOTES

19. KEY WORDS (Continue on reverse side if necessary and identify by block number)

20. ABSTRACT (Continue on reverse side if necessary and identify by block number)

The solar energy flux as a function of depth (the irradiance profile) in the ocean is an important function. It influences the dynamics of the mixed layer via the heat budget as well as the biology of the euphotic zone. The following three-parameter model can take into account the very rapid decrease near the surface due to absorption of long-wavelength radiation by water as well as the eventual exponential decrease at great depths. $E(z) = E(0)e^{-k_1 z}(1 - K_2 \arctan K_3 z)$, where $E(z)$ is the irradiance at depth z and

DD _{1 JAN 73} FORM 1473   EDITION OF 1 NOV 65 IS OBSOLETE
S/N 0102-014-6601

K_1, K_2, and K_3 are constants that depend on the optical properties of the water. The constants are determined for Jerlov's water types. The constants can readily be calculated from any irradiance profile.

REPORT DOCUMENTATION PAGE	READ INSTRUCTIONS BEFORE COMPLETING FORM

1. REPORT NUMBER	2. GOVT ACCESSION NO.	3. RECIPIENT'S CATALOG NUMBER
80-19	AD-A106 402	

4. TITLE (and Subtitle)	5. TYPE OF REPORT & PERIOD COVERED
FIRST RECORDS OFF OREGON OF THE PELAGIC FISHES *PARALEPIS ATLANTICA, GONOSTOMA ATLANTICUM,* AND *APHANOPUS CARBO,* WITH NOTES ON THE ANATOMY OF *APHANOPUS CARBO*	Reprint
	6. PERFORMING ORG. REPORT NUMBER

7. AUTHOR(s)	8. CONTRACT OR GRANT NUMBER(s)
Kevin M. Howe David L. Stein Carl E. Bond	N00014-67-A-0369-007

9. PERFORMING ORGANIZATION NAME AND ADDRESS	10. PROGRAM ELEMENT, PROJECT, TASK AREA & WORK UNIT NUMBERS
School of Oceanography Oregon State University Corvallis, Oregon 97331	NR083-102

11. CONTROLLING OFFICE NAME AND ADDRESS	12. REPORT DATE
Office of Naval Research Ocean Science & Technology Division Arlington, Virginia 22217	1980
	13. NUMBER OF PAGES 4

14. MONITORING AGENCY NAME & ADDRESS(if different from Controlling Office)	15. SECURITY CLASS. (of this report)
	Unclassified
	15a. DECLASSIFICATION/DOWNGRADING SCHEDULE

16. DISTRIBUTION STATEMENT (of this Report)

Approved for public release; distribution unlimited

17. DISTRIBUTION STATEMENT (of the abstract entered in Block 20, if different from Report)

19. KEY WORDS (Continue on reverse side if necessary and identify by block number)

20. ABSTRACT (Continue on reverse side if necessary and identify by block number)

The species covered in this report are common in parts of the Atlantic Ocean and all are known to occur in the Pacific Ocean. We fill a gap in knowledge of the distribution of two species known formerly only north and south of Oregon, extend the northward range of *Gonostoma atlanticum* Norman, and report inshore occurrences of *Paralepis atlantica* Krøyer. The unusual gross anatomy surrounding the gas bladder of *Aphanopus carbo* Lowe is worthy of description.

DD FORM 1473 EDITION OF 1 NOV 65 IS OBSOLETE
1 JAN 73
S/N 0102-014-6601

SECURITY CLASSIFICATION OF THIS PAGE (When Data Entered)

REPORT DOCUMENTATION PAGE		READ INSTRUCTIONS BEFORE COMPLETING FORM
1. REPORT NUMBER 80-20	2. GOVT ACCESSION NO. AD-A106 402	3. RECIPIENT'S CATALOG NUMBER
4. TITLE (and Subtitle) SPATIAL AND TEMPORAL VARIATIONS IN THE POPULATION SIZE STRUCTURE OF THREE LANTERNFISHES (MYCTOPHIDAE) OFF OREGON, USA		5. TYPE OF REPORT & PERIOD COVERED Reprint
		6. PERFORMING ORG. REPORT NUMBER
7. AUTHOR(s) J. M. Willis W. G. Pearcy		8. CONTRACT OR GRANT NUMBER(s) N00017-76-C-0067
9. PERFORMING ORGANIZATION NAME AND ADDRESS School of Oceanography Oregon State University Corvallis, Oregon 97331		10. PROGRAM ELEMENT, PROJECT, TASK AREA & WORK UNIT NUMBERS NR083-102
11. CONTROLLING OFFICE NAME AND ADDRESS Office of Naval Research Ocean Science & Technology Division Arlington, Virginia 22217		12. REPORT DATE 1980
		13. NUMBER OF PAGES 11
14. MONITORING AGENCY NAME & ADDRESS(if different from Controlling Office)		15. SECURITY CLASS. (of this report) Unclassified
		15a. DECLASSIFICATION/DOWNGRADING SCHEDULE

16. DISTRIBUTION STATEMENT (of this Report)

Approved for public release; distribution unlimited

17. DISTRIBUTION STATEMENT (of the abstract entered in Block 20, if different from Report)

18. SUPPLEMENTARY NOTES

19. KEY WORDS (Continue on reverse side if necessary and identify by block number)

20. ABSTRACT (Continue on reverse side if necessary and identify by block number)

Size-frequency distributions were determined for 3 cmmon lantern-fishes (*Stenobrachius leucopsarus*, *Diaphus theta*, and *Tarletonbeania crenularis*) off Oregon in the summer. The fishes were caught mainly in sound-scattering layers by a large pelagic trawl with 5 opening-closing nets. Changes in depth distribution and diel vertical migration with growth were evident for all 3 species. The size of *S. leucopsarus* increased markedly with depth both at 0 to 90 m at night and 250 to 500 m during the day. Larger *D. theta* were also found deeper

DD FORM 1473 EDITION OF 1 NOV 65 IS OBSOLETE
S/N 0102-014-6601

during the day (between 250 and 450 m), but neither *D. theta* nor *T. crenularis*
demonstrated size segregation in the upper 90 m at night. Large *D. theta*
and small *T. crenularis* did not appear to migrate into surface waters at
night. Age-Group O (15 to 20 mm) *S. leucopsarus* were most abundant in deep
water (400 to 480 m) in the daytime and did not migrate into near-surface
waters at night. Age-Group I (30 to 40 mm) *S. leucopsarus* were common at
about 300 m by day and within the upper 30 m at night. Age-Group II-III
(50 to 60 mm) apparently followed the evening ascent of Age-Group I fish and
most resided at 75 to 90 m at night, beneath Age-Group I fish. Age-Group III+
fish (70 to 80 mm) were associated with Age-Group O at 400 to 480 m by day
and usually did not migrate above 200 m at night. The size structure of
S. leucopsarus differed among the nets of a single tow at one depth, or
between two tows that fished the same depths on successive hights, indicating
horizontal patchiness in age structure. *D. theta* demonstrated low within-tow
variability in size composition which indicated a spatially more uniform
age structure on a scale of kilometers. The size structures of these 3
lanternfishes were different in the same area and the same season during two
different years, suggesting variable survival of year classes or horizontal
patchiness of age composition in the area sampled.

REPORT DOCUMENTATION PAGE		READ INSTRUCTIONS BEFORE COMPLETING FORM
1. REPORT NUMBER 80-21	2. GOVT ACCESSION NO. AD-A106 402	3. RECIPIENT'S CATALOG NUMBER
4. TITLE (and Subtitle) A LARGE, OPENING-CLOSING MIDWATER TRAWL FOR SAMPLING OCEANIC NEKTON, AND COMPARISON OF CATCHES WITH AN ISAACS-KIDD MIDWATER TRAWL		5. TYPE OF REPORT & PERIOD COVERED Reprint
		6. PERFORMING ORG. REPORT NUMBER
7. AUTHOR(s) William G. Pearcy		8. CONTRACT OR GRANT NUMBER(s) N00017-76-C-0067
9. PERFORMING ORGANIZATION NAME AND ADDRESS School of Oceanography Oregon State University Corvallis, Oregon 97331		10. PROGRAM ELEMENT, PROJECT, TASK AREA & WORK UNIT NUMBERS NR083-102
11. CONTROLLING OFFICE NAME AND ADDRESS Office of Naval Research Ocean Science & Technology Division Arlington, Virginia 22217		12. REPORT DATE 1980
		13. NUMBER OF PAGES 6
14. MONITORING AGENCY NAME & ADDRESS(if different from Controlling Office)		15. SECURITY CLASS. (of this report) Unclassified
		15a. DECLASSIFICATION/DOWNGRADING SCHEDULE

16. DISTRIBUTION STATEMENT (of this Report)

Approved for public release; distribution unlimited

17. DISTRIBUTION STATEMENT (of the abstract entered in Block 20, if different from Report)

18. SUPPLEMENTARY NOTES

Reprint from Fishery Bulletin 78(2): 529-534.

19. KEY WORDS (Continue on reverse side if necessary and identify by block number)

20. ABSTRACT (Continue on reverse side if necessary and identify by block number)

No abstract

DD _{1 JAN 73} 1473   EDITION OF 1 NOV 65 IS OBSOLETE
S/N 0102-014-6601

REPORT DOCUMENTATION PAGE		READ INSTRUCTIONS BEFORE COMPLETING FORM
1. REPORT NUMBER 80-23	2. GOVT ACCESSION NO. AD-A106 402	3. RECIPIENT'S CATALOG NUMBER
4. TITLE *(and Subtitle)* OCEANIC RADIATION INSTRUMENTS		5. TYPE OF REPORT & PERIOD COVERED Reprint
		6. PERFORMING ORG. REPORT NUMBER
7. AUTHOR(s) C. A. Paulson		8. CONTRACT OR GRANT NUMBER(s) N00014-76-C-0067
9. PERFORMING ORGANIZATION NAME AND ADDRESS School of Oceanography Oregon State University Corvallis, Oregon 97331		10. PROGRAM ELEMENT, PROJECT, TASK AREA & WORK UNIT NUMBERS NR 083-102
11. CONTROLLING OFFICE NAME AND ADDRESS Office of Naval Research Ocean Science & Technology Division Arlington, Virginia 22217		12. REPORT DATE 1980
		13. NUMBER OF PAGES 13
14. MONITORING AGENCY NAME & ADDRESS*(if different from Controlling Office)*		15. SECURITY CLASS. *(of this report)* Unclassified
		15a. DECLASSIFICATION/DOWNGRADING SCHEDULE

16. DISTRIBUTION STATEMENT *(of this Report)*

Approved for public release; distribution unlimited

17. DISTRIBUTION STATEMENT *(of the abstract entered in Block 20, if different from Report)*

18. SUPPLEMENTARY NOTES

Reprinted from Air-Sea Interaction (1980). F. Dobson, L. Hasse, and R. Davis (eds.). pgs. 509-521.

19. KEY WORDS *(Continue on reverse side if necessary and identify by block number)*

20. ABSTRACT *(Continue on reverse side if necessary and identify by block number)*

No abstract

DD _{1 JAN 73} FORM 1473   EDITION OF 1 NOV 65 IS OBSOLETE
S/N 0102-014-6601

REPORT DOCUMENTATION PAGE		READ INSTRUCTIONS BEFORE COMPLETING FORM
1 REPORT NUMBER 80-24	2. GOVT ACCESSION NO. AD·A106 402	3. RECIPIENT'S CATALOG NUMBER
4 TITLE (and Subtitle) INTERMEDIATE NEPHELOID LAYERS OBSERVED OFF OREGON AND WASHINGTON		5. TYPE OF REPORT & PERIOD COVERED Reprint
		6. PERFORMING ORG. REPORT NUMBER
7. AUTHOR(s) Hasong Pak J. Ronald V. Zaneveld J. Kitchen		8. CONTRACT OR GRANT NUMBER(s) 0014-76-0067
9. PERFORMING ORGANIZATION NAME AND ADDRESS School of Oceanography Oregon State University Corvallis, Oregon 97331		10. PROGRAM ELEMENT, PROJECT, TASK AREA & WORK UNIT NUMBERS NR 083-102
11. CONTROLLING OFFICE NAME AND ADDRESS Office of Naval Research Ocean Science & Technology Division Arlington, Virginia 22217		12. REPORT DATE 1980
		13. NUMBER OF PAGES 12
14. MONITORING AGENCY NAME & ADDRESS(if different from Controlling Office)		15. SECURITY CLASS. (of this report) Unclassified
		15a. DECLASSIFICATION/DOWNGRADING SCHEDULE

16. DISTRIBUTION STATEMENT (of this Report)

Approved for public release; distribution unlimited

17. DISTRIBUTION STATEMENT (of the abstract entered in Block 20, if different from Report)

19. KEY WORDS (Continue on reverse side if necessary and identify by block number)

20. ABSTRACT (Continue on reverse side if necessary and identify by block number)

Two distinct kinds of particle maxima (nepheloid layers) were observed off Oregon in November 1977 and off Washington in October 1978 by an in situ light transmissometer: one in the thermocline in the euphotic zone and the other at intermediate depth well below the thermocline. The thermocline nepheloid layer is associated with well-defined maxima of dissolved oxygen, chlorophyll-a and phaeophytin, and these associations suggest that the nepheloid layer is primarily composed of phytoplankton undergoing active photosynthesis. The

DD _{1 JAN 73} FORM 1473   EDITION OF 1 NOV 65 IS OBSOLETE
S/N 0102-014-6601

intermediate nepheloid layer is found in connection with the bottom waters near the shelf break and shares some of the characteristic properties of the bottom water: high concentration of suspended particles, low concentrations of dissolved oxygen, chlorophyll-a, and phaeophytin. The particle size distributions in the intermediate nepheloid layer are different from those in the clear water above the nepheloid layer but similar to those in the bottom nepheloid layer. Two hypotheses for the generation of intermediate nepheloid layers, settling and horizontal advection, are examined, and the data support the latter hypothesis.

Technology Illustrations for a Towed Distributed
Instrumentation Profiling System

by

Staff*
Technical Planning and Development Group
School of Oceanography
Oregon State University
Corvallis, Oregon 97331

Abstract

Towed instrumentation has been developed for use in the marine research
community to obtain profile measurements of some physical oceanographic
parameters down to 100 m and over a lateral range. The Technical Planning
and Development Group at Oregon State University has been progressively
expanding and improving the capability and reliability of a faired instru-
mented cable system called DIPS (Distributed Instrumentation Profiling
System) that can be conveniently deployed and maintained by a four-man
research team on a 30 m research vessel.

DIPS, schematically illustrated in Figure 1, is instrumented to
measure 30 vertical temperature stations, 4 pressure (depth) stations, and
6 conductivity stations during a tow. The sensor stations can be reposi-
tioned along the cable at sea. During past month-long cruises** in 1977
and 1979, DIPS functioned reliably.

The purpose of this paper is to augment previous publications about
DIPS and to provide additional illustrations on newly integrated technology.

Introduction

Early in 1976, the Johns Hopkins Applied Physics Laboratory tested a
thermistor chain that had been developed in collaboration with Fathom
Oceanology, Ltd. and Sippican Corporation.[1,2] Their tests had confirmed
a smaller and more manageable cable system was practical. After we
reviewed their cable system, it was apparent that incorporated into the
cable assembly was a components modularity that made it feasible for a
small group to attain the same instrumented cable capability. The key
feature that makes it possible to duplicate this capability is a cable
fairing developed by Fathom Oceanology, Ltd. The fairing module functions
as a retainer and protective sheath for the individual sensor signal wires
to the surface. It also serves as a mounting for the sensors and a distri-
buted coupling to the load-bearing tow cable.

---

* Contributors: Dr. R. Mesecar, Head
                 Mr. F. Evans
                 Dr. J. Wagner
** Mixed Layer Experiment (MILE)
   Joint Air-Sea Interaction (JASIN)

WINCH

FAIRED CABLE

6 CONDUCTIVITY SENSORS

30 TEMPERATURE SENSORS

4 PRESSURE SENSORS

450 KG DEPRESSOR
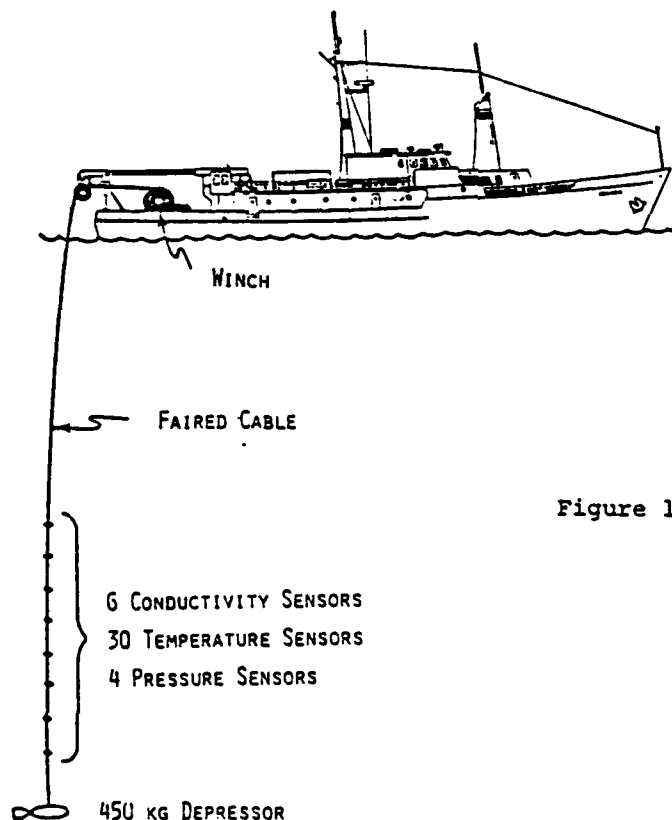
Figure 1. Schematic view
of the deployed
Distributed
Instrumentation
Profiling System

Because of the nature of operating personnel, budgets, and the goals of the research program, it was not possible to replicate the APL cable system. On the practical side, the OSU research group owned and wanted to use a PDP-11/10 computer for shipboard data acquisition and data management. Experience with underwater cable connections and sensor calibration and replacement also provided direction on how the sensor output signals would be conditioned before being sent to the surface. For instance, one system goal was to isolate the sensor electronic characteristics and calibrations from the electrical features of the tow cable.

The last major element in the cable system was the winch. Again our plan, for cost reasons, was to improvise a simple winch system to provide minimum cable handling and storage features.

The Cable System

The Fathom Oceanology, Ltd. fairing is the essential building block around which DIPS is assembled. The model 770T fairing is supplied in three parts: a flexible polyurethane nosepiece that is free to swivel about the support cable and two rigid ABS plastic tailsections that can be screw-mounted to each other and socketed to the nosepieces. This modularity made

it possible to use a "divide and conquer" approach to the problems inherent in merging electro-mechanical design features when developing an instrumented cable system. Some obvious system design advantages provided by the fairing modules are:

- All subsystems (fairings, cable wire bundles, tension members, etc.) can be specified independently of each other, purchased, and assembled at our facility under our quality control.

- The fairing modularity permits a mechanical separation of the tension cable and signal wires.

- There is ready access to the signal wire bundles by simply unscrewing the fairing parts.

- Sensors can be integrated into the fairings.

- Sensors can be readily moved to new locations.

- The fairings provide reduced cable drag.

Several sections of the fairing are shown assembled in Figure 2 on a steel load-bearing cable. Each fairing is approximately 10 cm high, 2 cm thick and 15 cm long. Also shown are three bundles of 19-pair signal wires. It is through these color coded signal wires that power to, and signals from, the sensors are transmitted. The bundles are clamped once in each fairing to incorporate a relief loop to allow the fairing tails to part when passing over the winch drum on the sheave. The bottom terminals of the three cable bundles are potted in one block of polyurethane. All subsequent breakouts along the cable are made with a special wire splice technique.

Figure 2. Shown are the components of the Fathom Oceanology fairing in states of assembly for DIPS. Included in this figure is a temperature sensor module that is being inserted in a previously assembled faired cable section.

The signal wires have a Tefzel® coating which offers a very abrasion-resistant surface, but one that is difficult to find a bonding agent for. In addition, the fairing compartment, where connections to the signal wires can be made, is space limited. These two conditions, plus the need for making expedient connections between sensors and the signal wires at sea, required the development of a unique splice technique.

Figure 3 shows the miniature splice developed for this project.[3] The splice incorporates a meltable tubing of two diameters and two very small O-rings within a single clear shrink tube. The O-ring is a standard part (Minnesota Rubber 8001) and the shrink tubing and clear melt tubing are AMP Special Industry Products. The splice relies on the O-ring for seal to the Tefzel® while utilizing the melt material for void fill and self-forming O-ring position seats. These splices have been very reliable in field trials. From a population of over 200 splices originally installed, two possible splice failures were suspected. Approximately 40 additional splices were made at sea over a 4-week period and one of these splices gave evidence of failure. These splices have also been exposed to 1000 psi of pressure in the laboratory for sustained periods and they have maintained isolation resistance above 100 megohms.
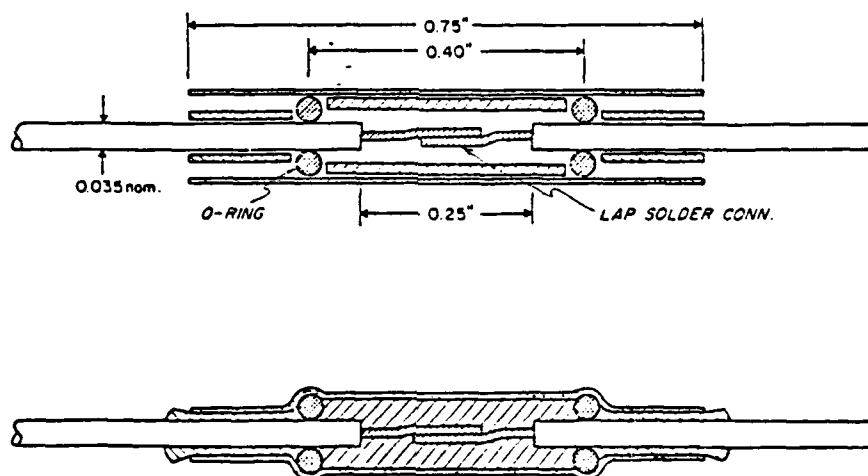
Figure 3. This illustration shows the before and after phase of a thermo shrink splice developed for the small diameter signal-wire connections in DIPS.

Winch System

A 1.3 m diameter winch drum was needed to handle and store the 100 m of faired cable used for DIPS. Because winches reflect the character of their application and budgets, they are generally custom designed. The one used with DIPS is no exception. The photographs in Figure 4 show a winch assembly scheme that can hoist 700 kg at fixed speeds of 15 or 30 cm/sec. Once the deadweight cable depressor and faired cable deployment
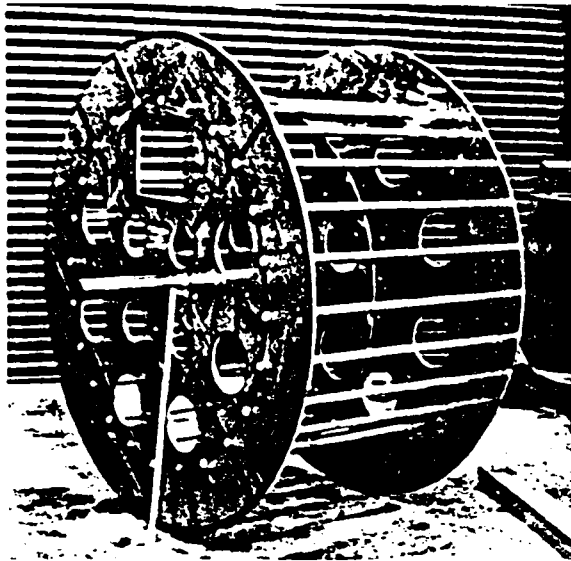
Figure 4a. The cable drum support discs were cut round with a metal band saw. Next, the discs were gang drilled for all the hole patterns. Twenty-four holes in the discs serve as sockets for the spacer rods that form the drum support structure. A metal inert gas (MIG) welder is used to weld the rods to the discs. A 70-mm thick skin is clamped over the support rods and welded as seen in Figure 4b.

Figure 4b. The winch base is made from 12.5 cm structural "I" beam stock that has been cut on the band saw and welded into a box frame. The drum rotates on a 7.6 cm OD by 1.27-cm-thick wall steel shaft which is supported by pillow blocks that bolt to the base frame. The shaft is keyed to the drum, but it is not the drive attachment for the power train. The power train drives a sprocket attached to one of the discs.
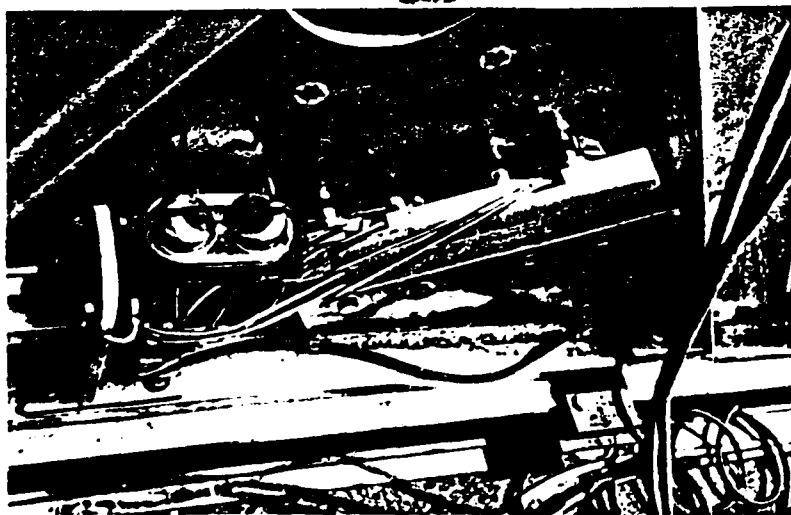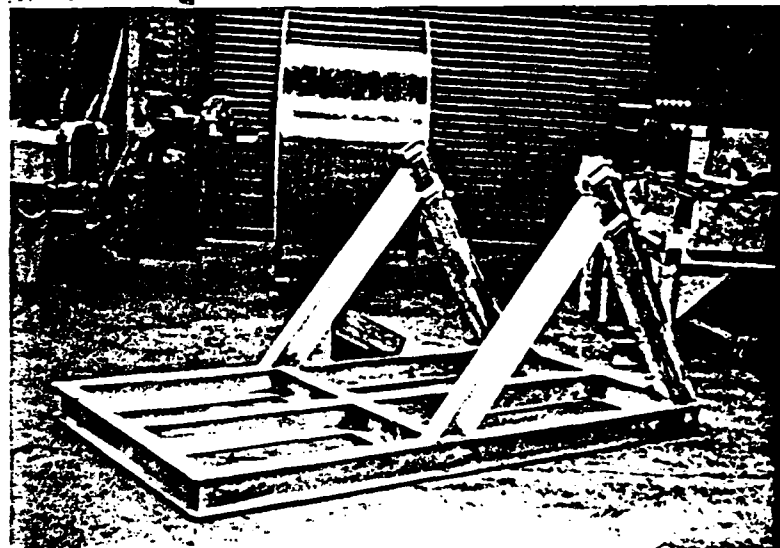
Figure 4c. Hydraulic automobile disc brakes, operating at the outer periphery on one of the drum discs, provide the drum breaking function. Two disc brake assemblies and a master cylinder are securely attached to the base frame. The brake control, which includes an electric cutout to the motor, can be manually operated from either side of the winch.

85

has been inititated, only one winch operator is necessary. A 10 m cord on the motor control wand allows the operator freedom to completely circle the winch. The payout rate of the cable is done under control of the motor drive train.
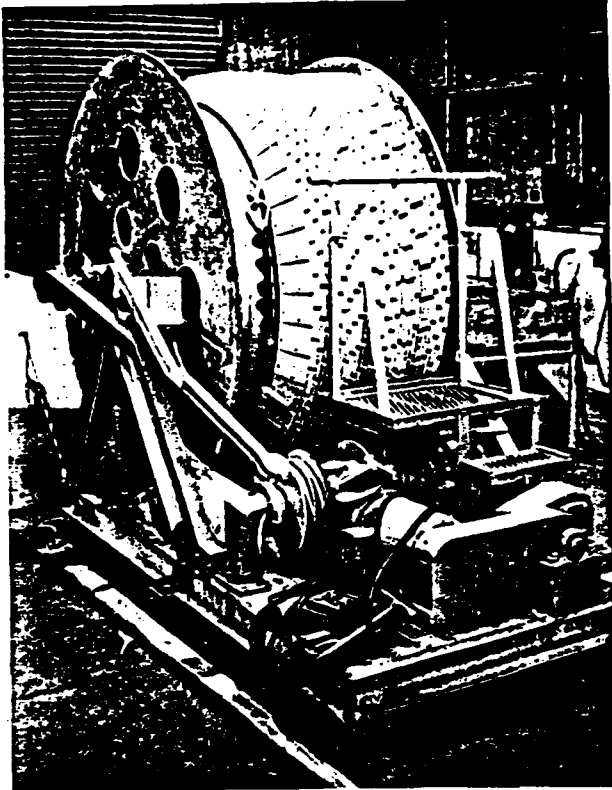
Figure 4d. The completed winch is shown with 100 m of faired cable on the drum. The operator's pedestal is mounted over the power train. From this position the operator can inspect the fairing as it is being spooled. This fairing does not require a fair lead system. The lay of the cable is determined by a preformed plastic groove cemented to the drum surface. With the exception of the power train the majority of the winch is made of aluminum.

A manually operated disc brake system, shown in Figure 4c, can be used to control cable payout when the motor control is off or the drum is to be locked up. This brake can be reached from either side of the winch. In the event that the drum drive chain parted, a mechanical deadfall would lock up the drum.

Bonded to the winch drum surface is a plastic extrusion contoured to mate with the radius of the fairing nosepieces. This extrusion circles around the drum, similar to a LEBUS groove, and functions to protect the shape of the nosepiece and guide the lay of the fairings. By proper separation of the extrusion wraps around the drum it is possible to pay cable in and out without a separate fair-lead mechanism.

The upper ends of the signal wire bundles are fed through a water blocked feed-through into a function box located within the winch drum. From barrier strips in the junction box, signal wires are branched. One branch is a connector mounted into the side of the drum. This connector port can be used to connect a cable to the surface electronic data systems; however, it has to be disconnected each time the winch is powered to move the faired cable.

A capability was added later that makes it possible to keep the signal wires electrically coupled to the surface data system while the winch is being powered. The mechanism that accomplishes this function is called a "sidewinder" and is similar to a design for an equivalent function manufactured by Fathom Oceanology. The second branch from the junction box is connected to the sidewinder (shown in Figure 5) with a jacketed 50-pair cable.

The sidewinder consists of two coaxial drums, a slipclutch/racket drive assembly, and a transfer sheave. One drum is attached to, and rotates with, the winch drum. The second drum does not rotate and is attached to the winch frame with a torque arm. In Figure 4d, the sidewinder is in a shipping cradle position with the torque arm resting on the winch shaft. In use, the sidewinder mounts on the drum shaft and appears as shown in Figure 5. As the winch rotates, the 50-pair cable is transferred from the rotating drum to the stationary one by the slipclutch assembly and transfer sheave. This mechanism permits the winch to rotate and still keep solid signal wire connections from the sensors to the surface electronics.

The first deployment with the sidewinder was successful. The only degradation of system performance which might be attributed to its use is a slight increase in susceptibility to ship radio operations, which is probably due to the increased length of cabling involved on deck.

Figure 5. The sidewinder mechanism couples to the winch shaft and functionally serves as a set of electrical sliprings for the 80 pair of signal wires in the faired cable that passes through the rotating drum to the surface electronics.
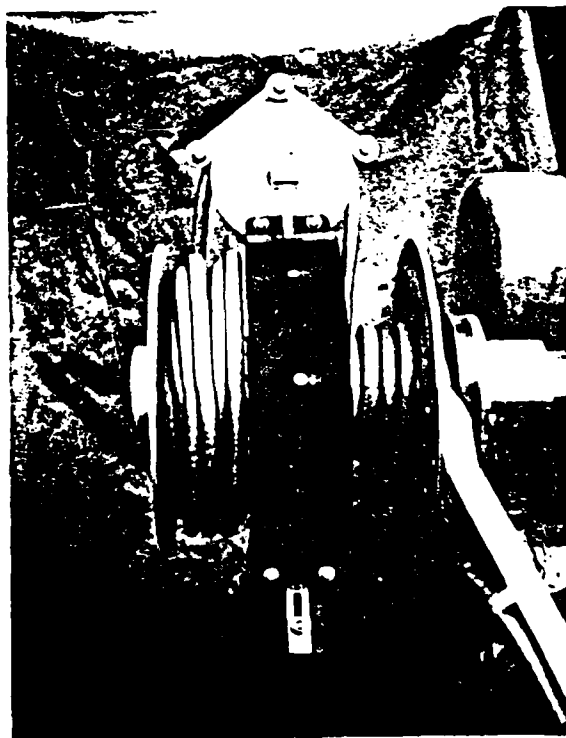
Pictured in Figure 6 is the sheave used with the cable system. The design and assembly concepts used for the winch drum are also used in the sheave. A sheave diameter of 120 cm has been found to function satisfactorily with the fairing modules. The polyurethane nosepieces which couple one fairing to another are flexible. If the distance between the drum and sheave is over 2.5 m, the fairings deployed from the top of the drum spiral in orientation, as partially illustrated in Figure 6. This can pose a problem for the sensors mounted in the nosepieces of the fairings. To keep the approaching fairings oriented inplane with the sheave, a fairing-flipper mechanism (shown in Figure 6) was added to the sheave. Depending upon the direction of rotation, a drag-clutch will move the fairing-orientation wheel against the incoming cable and gently transform the fairings inplane with the sheave.
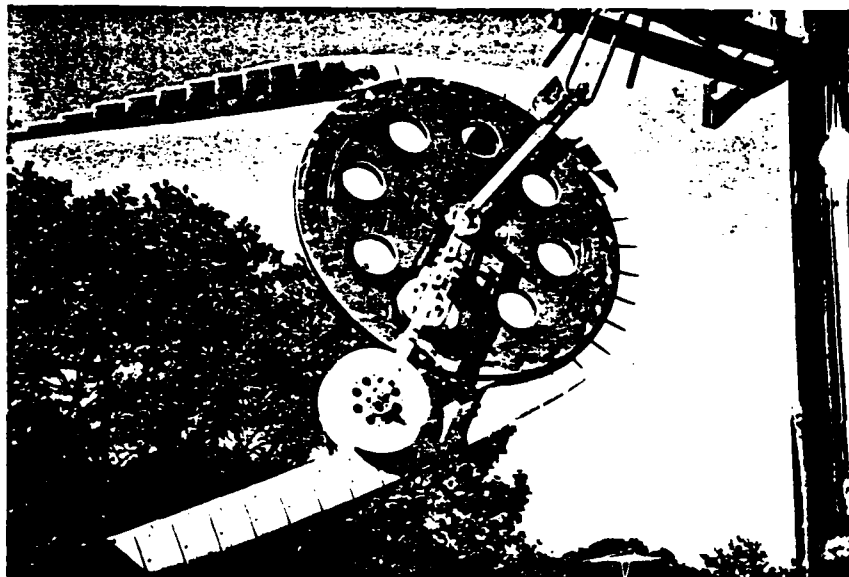
Figure 6. Shown is the sheave and fairing orientation wheel used. It is designed for use with the faired cable.

Instrumentation System

A simple block diagram of the electronic signal flow for DIPS is shown in Figure 7. Within the design criteria for DIPS is the need for sensor interchangeability and signal security which established the requirements for distributing some of the sensor signal conditioning electronics. Signal-conditioning amplifiers have been designed for temperature, pressure, and conductivity sensors. The circuit boards for the pressure and temperature sensors are essentially the same. The conductivity sensor signal conditioning is treated differently as will be noted later in the paper.

The amplifier/fairing/sensor assembly is integrated into the faired cable and connected to power and signal wires by the previously described method. The temperature and conductivity sensors with their associated signal-conditioning amplifiers are shown in Figures 8 and 9. The view ports cut in the fairing are for the reader's interest.

88

In all the conditioning amplifiers, low-offset amplifiers (Precision Monolothics OP-07) and precision resistors (Vishay networks) were used. This provided an amplifier with less than 0.1 percent tolerance in its zero and ± 1 percent tolerance in its gain parameters and reduced any limitations on dynamic range due to component tolerance bands. Amplifier output signals are ± 5 V dc.

With a low impedance drive to the signal wires, it is possible to sense the signal level with a high impedance surface instrumentation amplifier, with a common mode rejection ratio of greater than 100 dB, which rejects line pickup and eliminates the effects of signal wire resistance. A ground reference for the amplifers is obtained from the power source and a true differential signal sensing is possible without creating a source imbalance. With control of the worst-case error band, a high degree of signal data content (94%) is maintained.
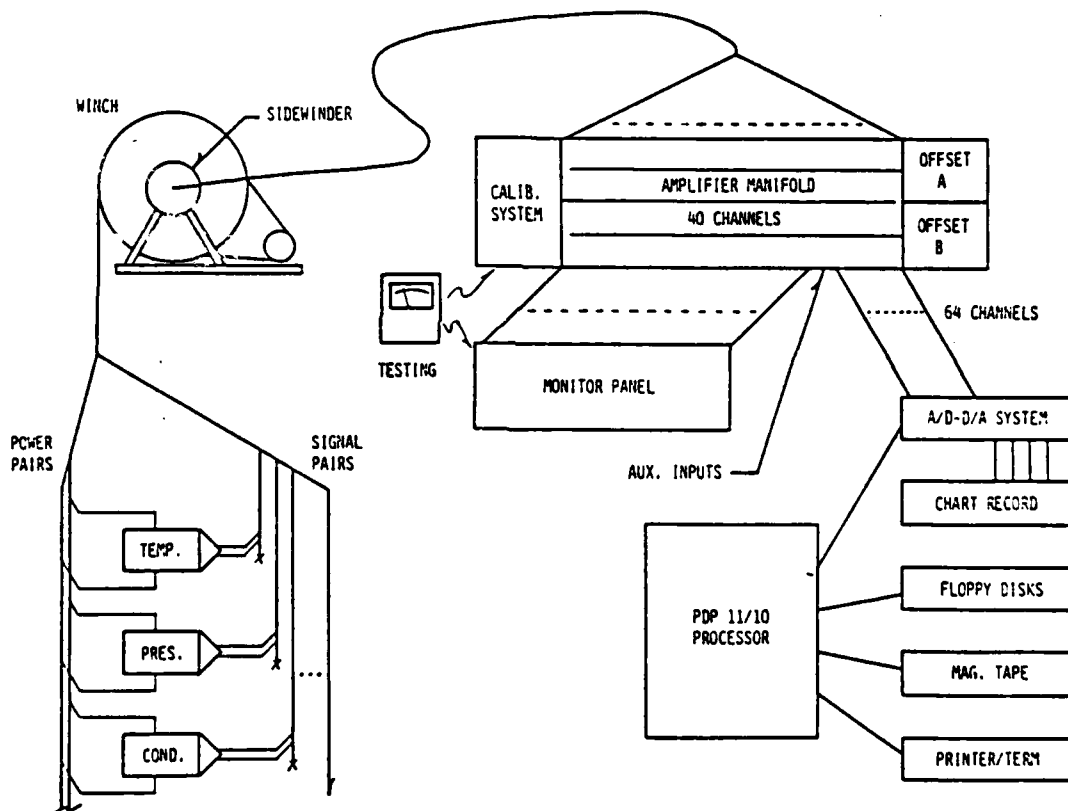
Figure 7. Electronics block diagram for DIPS.

From the temperature sensor through the output of the surface instrumentation amplifiers, resolutions better than .0005°C have been attained with a bandwidth of 5 Hz. To implement a .001°C resolution capability for a temperature span of 20°C, with a 12-bit analog-to-digital converter, it was necessary to provide quiescent offset voltage so that the digitizer
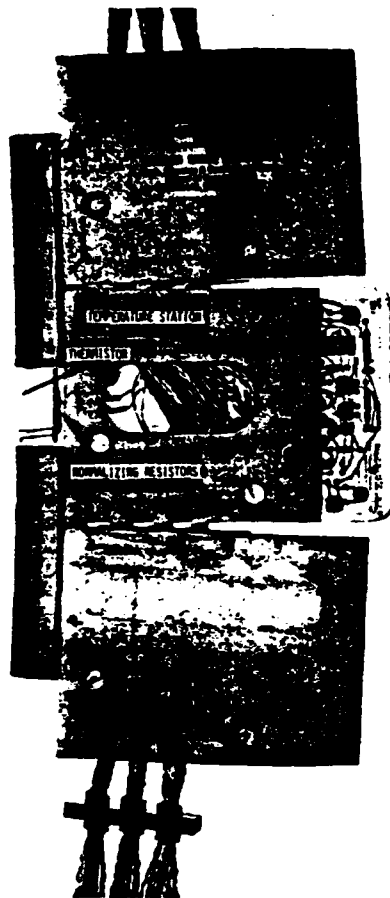
Figure 8. The thermistor for temperature sensing with its normalizing resistors is molded to fit within a segment of the fairing nosepiece. The thermistor/amplifier is calibrated as an assembly and then inserted into the faired cable as shown in Figure 2.

Figure 9. The conductivity cell and conditioning electronics are in separate fairings. They are also calibrated and function as a unit. Water enters the cell through scoops visible just above the top electrode and exits at the bottom.
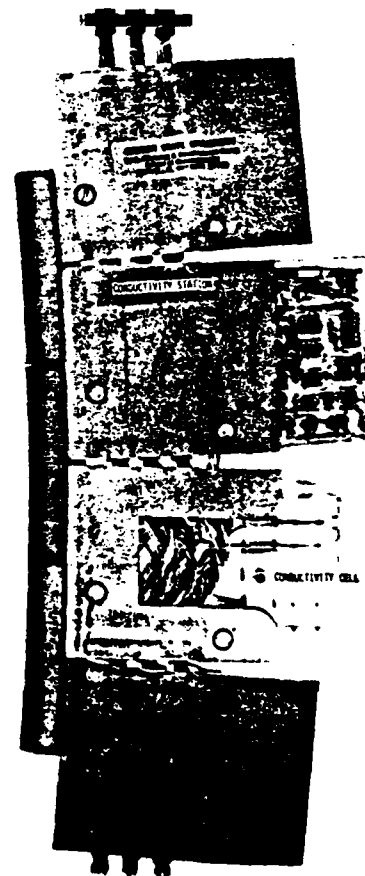
could be devoted to the dynamic signal range. Each of the surface ampli-
fiers are fitted with two offset voltage terminals that are under switch
control on the amplifier manifold panel. These voltages have a reference
accuracy of 5 p/m and a resetability of 100 p/m. This feature has been
accomplished with a combination of switched one volt and vernier voltage
offset references. The output from the offset reference voltages is inde-
pendently digitized to 12-bits which provides a resolution of one part in
40,000 of the offset voltage used at the time of data acquisition. One
offset voltage control is generally used with the conductivity sensors and
the other with the temperature sensors.

Thermistors are used for temperature sensors and miniature semiconductor
strain gauges for pressure sensors. For conductivity measurements, the
four-terminal-electrode geometry was adapted. The cell, as shown mounted
in the fairing in Figure 9, is made by a local glass blower of pyrexglass.
Cells made in this manner have proven to be consistent for sensor inter-
changeability purposes. The electrodes, composed of 90 percent platinum
and 10 percent irridium wire, are also replaceable. Laboratory tests on
the cell have shown it to be much less dependent on electrode configur-
ations than on the dimensional stability of the measurement chamber.
Flushing of the cell is provided by molded water scoops which take water
in at the top of the cell (Figure 9) and exit it from the bottom.

A block diagram of the conductivity cell electronics amplifier is shown
in Figure 10. The cell is a four-terminal resistive device which is ac-
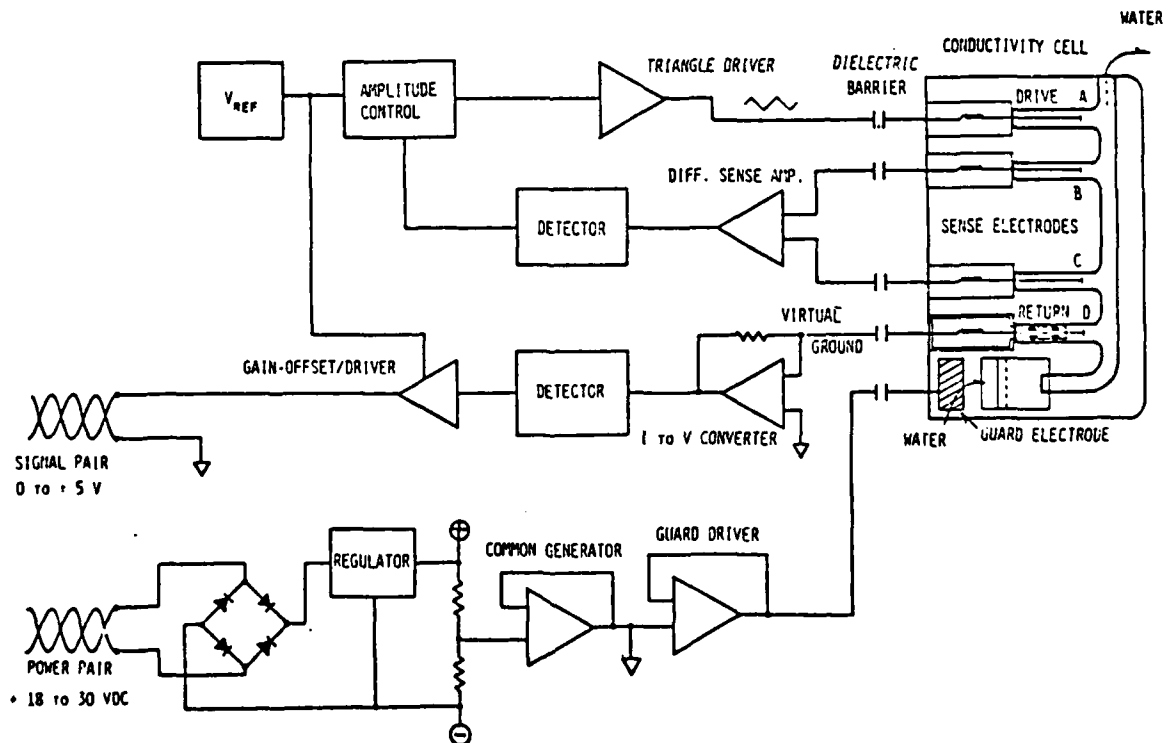
Figure 10. Block diagram for the conductivity cell and the
in situ signal conditioning amplifier.

91

coupled to the conditioning amplifier. One of the outer two electrodes (A)
is driven by a triangle waveform into the virtual ground created at the
other of the outer electrodes (D). The triangle waveform was chosen to
limit the slewing rate required of the amplifiers, thus allowing better
accuracy at higher frequencies than any simple waveform, including the
sine waveform. The two central electrodes (B and C), called the sense
electrodes, measure the drop across the measurement volume between them,
but at near zero current, thus eliminating electrode polarity problems
often encountered at saline/metal boundaries. This also eliminates elec-
trode geometry influences and the voltage drop due to nonzero impedance
between the electrodes and the measurement volume. The sensed signal is
used in a closed-loop control of the triangle waveform amplitude to sustain
a constant voltage drop across the measurement volume. The cell output is
derived by measuring the drive current into the return electrode (D). A
current-to-voltage converter drives a detector for ac to dc conversion.
The detected conductivity signal is then outputed to the surface through
a gain and offset stage.

The fifth electrode is driven at ac common. The return electrode is
connected to a virtual ground at the current-to-voltage converter. Any
currents entering this terminal from the exterior environment contribute
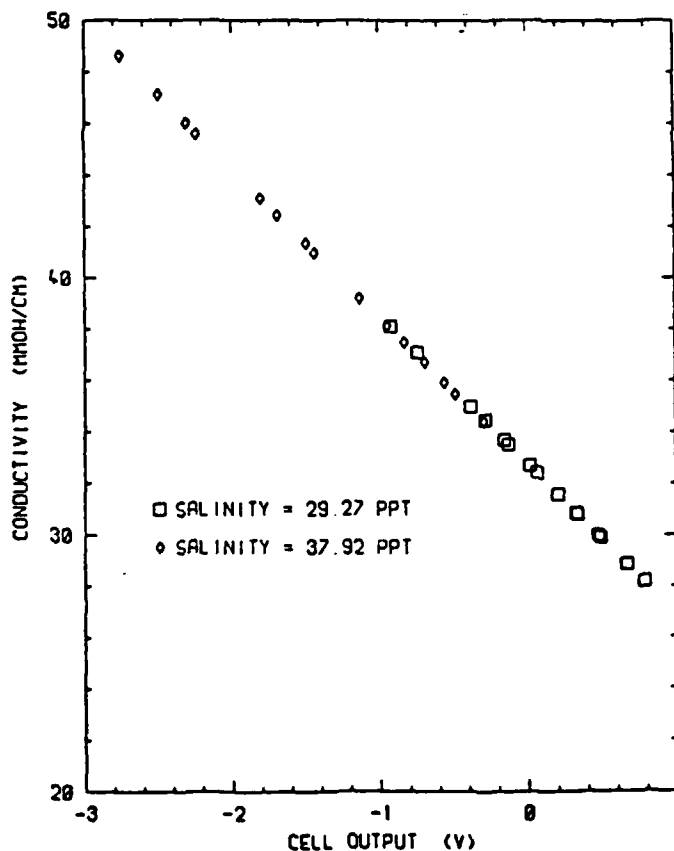
Figure 11.
Conductivity cell
calibration
response curve.

to the output level. The guard electrode, being driven to ac common, "guards" the return electrode, which is also at ac common, by providing or sinking any current from other sources. Since equivalent voltages exist at the guard and return electrodes, no current should flow from the inlet (where the guard is) to the return electrode (next adjacent electrode). Some questions still exist about the procedures of laboratory calibrations and their transfer to the field environment. The field environmental influences appear to be constant and thus will contribute to the cell constant in the actual measurement. The guard electrode by removing near and far environmental influences assures that the calibration environment is a good model of the measurement environment.

A typical temperature structure towed profile from data acquired with the DIPS cable system is shown in Figure 12.[3,4] During the MILE program (1977), DIPS had only the temperature and pressure sensors. The conductivity sensor prototype was added to DIPS for the JASIN cruise in 1979. Data reports for that cruise are in preparation. The DIPS sensor configurations, as previously illustrated in Figures 8 and 9, will be used during the FRONTS cruise in early 1980.

Figure 11 shows the relationship between conductivity, as determined by laboratory salinity samples, and cell/electronics output. The system has exhibited good linearity and repeatability.

RUN 01   20 AUG 77   TEMP VS TIME/DISTANCE

DEPTH = 22 7.23 8.24 8.25 9.26 9.28 0.29 0.32 2.35 3.41 6 M
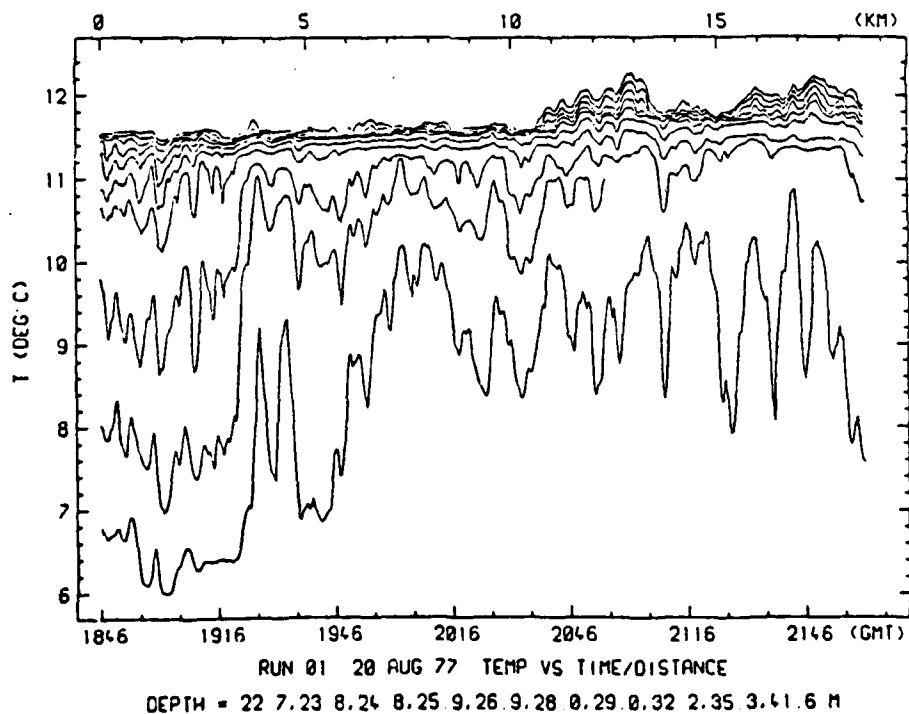
Figure 12. Some plotted upper ocean temperature structure
measured with DIPS during the MILE program.

Conclusion

The capability to make towed temperature, depth, and conductivity measurements in the upper 100 m of the ocean has been realized through the progressive development of the DIPS faired cable system. A number of technological problems were anticipated in developing this unit; however, after the fact it appears that solutions to simple problems, like wire splicing, may have been the most signficant contribution to our success. As the operating team has matured with the system development, DIPS has proven to be reliable at sea.

References

[1] F. F. Mobley, et al, "A New Thermistor Chain for Underwater Temperature Measurement," *Ocean 76 Conference*, September 13-15, 1976, Washington D.C.

[2] Sippican Corporation, Marion Massachusetts (Restricted Report), "Feasibility Study for a Towed Thermistor Chain."

[3] J. Wagner, "A Miniature Submersible Wire Splice," *Exposure*, VI (2), pp. 6-8, May 1978.

[4] T. J. Spoering, "Towed Observations of Internal Waves in the Upper Ocean," *M.S. Thesis, Oregon State University*, Reference Report 79-10, July 1979, 120 pp.

[5] T. J. Spoering, et al, "Towed Thermistor Chain Observations During MILE," Data Report 74, Reference 79-11, Oregon State University, July 1979.

Applications of a Data-Compression Algorithm
for XBT Bathy-Message Preparation

by

Staff*
Technical Planning and Development Group
School of Oceanography
Oregon State University

Abstract:

An expendable Bathythermograph (XBT) system utilizing a commercial
microcomputer is described. An algorithm particularly suited for data
compression in such systems is presented in some detail. Extension of the
digital XBT system to several other expendable probes is also described.

Introduction

Over the last 2 years, the Technical Planning and Development Group at
Oregon State University has been involved in the development of hardware and
software to function with a variety of expendable probes.[1] Our experience has
shown that "low-end" microprocessor-based computers offer significant
advantages, and previously unavailable capabilities, for this class of marine
instrumentation.

In the context of this paper, the term "microcomputer" (μC) is intended
to mean a unit of hardware which has a display (integral or attached by cable),
a keyboard, a microprocessor and memory, a recording device (e.g. magnetic
tape cassette), a means for attaching additional input/output hardware, and
a complete software operating system supporting a high level programming
language such as "BASIC", "FORTH", or "PASCAL". Commercial products of this
class include, but are not limited to, the Radio Shack "TRS-80", the
Commodore "PET", and the "APPLE II".

As part of a dedicated measurement system, a μC can perform a large
number of tasks. Most of these tasks can be done more easily with a μC than
with fixed logic hardware. For example, the display of a variety of messages
is quite simple; however, with fixed logic, any significant number of messages
would be fairly difficult. Similarly, a μC can control input/output hardware
such as digitizers, record/play back data (e.g. on cassette tape), compress
and format data, and can transfer data to other pieces of equipment. While
the μC can perform a number of tasks, what is just as important a consideration
is the users ability to redirect system data acquisition and processing tasks
with software skills and keyboard entry instead of new hardware implementation.

*Contributors: Dr. R. Mesecar, head
                Dr. J. Wagner

A

B

C

Figure 1.
The OSU
Digital XBT
System is
composed of
a Commodore
PET micro-
computer (A)
and an elec-
tronic inter-
face (B) to
the XBT probe.
The interface
mounted to
the micro-
computer is
shown in "C".
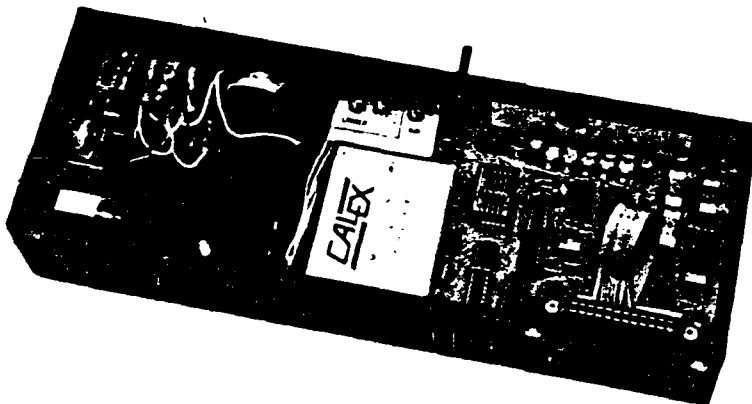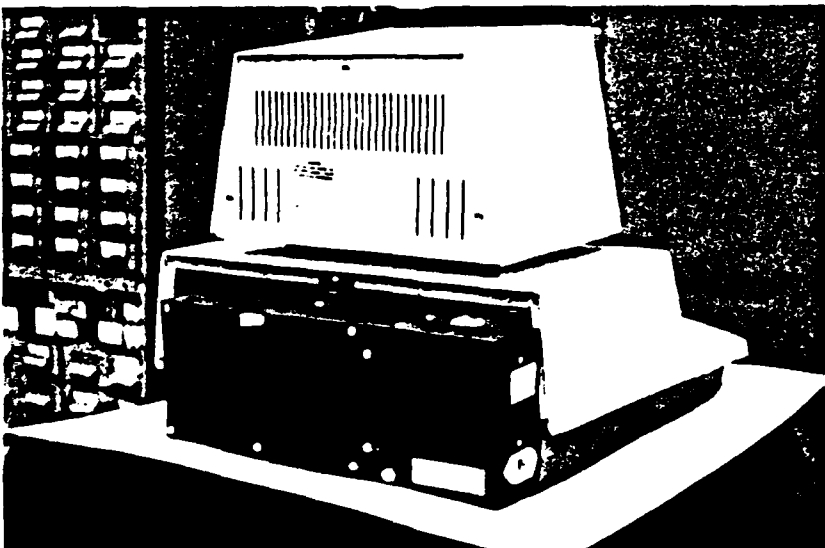
The flexibility offered by μCs makes them a prime candidate to improve the operation of existing sensor systems. This paper will focus on one unique application of μC technology to compress the number of data points needed to characterize the temperature profile from an XBT probe. However, while the following comments relate our experience with the digital XBT system, it should be remembered that the same principles are valid for a variety of measurement systems.

The Digital XBT System

The OSU digital XBT system includes a Commodore PET, an interface (Figure 1) which contains a digitizer, control circuitry and probe current supply, and an operating program written in "BASIC". The operations program is written to graph and prompt messages, test the interface, maintain current date and time, control the digitizers, and record data. An additional feature of this system is the capability to automatically generate bathy-messages in the format specified by the World Meteorological Organization.[2] The bathy-message represents a form of data compression in which 160 data points from an XBT probe temperature profile are reduced to approximately 20 significant points. Manual procedures have previously been used to generate the bathy-message which were time-consuming and subject to error. Automating this procedure has added a conforming interpretation of the data and a significant control on the manually induced errors.

The bathy-message algorithm (BMA) is an example of the versatility of microcomputer-based systems. The BMA was added to the system after it was designed, built, and operational. The original system did not include consideration of a bathy-message requirement; the only requirements were that the μC operating program be well-structured and that adequate memory space be available.

The Bathy-Message Algorithm

The BMA is relatively compact, requiring about 30 lines of "BASIC" code and about 700 bytes of memory. The mean-processing time is about 15 minutes although under special circumstances (near surface wire break) up to 45 minutes may be needed. The BMA is adapted from one developed at White Sands Missile Range[3] for real-time reduction of radiosonde data. The real-time capability of the algorithm is not used, but it is significantly faster and uses less memory than most other schemes we investigated.

The BMA functions by assuming an initial "tolerance limit". Next, the number of points required to approximate the data to that tolerance is determined. The tolerance is then adjusted according to whether there are too few or too many points. The entire procedure is then repeated until 19 to 21 points result (in this application). If more than 20 of these iterations have occurred, then 10 to 25 points will be accepted and a bathy-message determined. If more than 30 iterations have occurred, then a message is outputed on the display screen indicating that the bathy-message cannot be determined.

To begin an explanation of the BMA, assume two arrays of digitizer-quantity points, D_j and Q_j, and j=1 to Rs, representing depth and

temperature. Since these points are in digitizer units, they must be converted to depth and temperature before use. Assume a tolerance (TOL), which is arbitrarily specified initially and iteratively changed in successive trials. Assume that M1 is the index (value of j) of the last significant point (M1=1 at the start of each iteration with a new tolerance). Then compute T_{ml} (temperature) and D_{ml} (depth) from the digitized case values. For j=M1+1, find T_j and Dj. As shown in Figure 2, compute a pair of slope limits, M_u and M_l (upper and lower), with the following equations:

$$M_u = \frac{T_j + TOL - T_{ml}}{D_j - D_{ml}} \quad \text{and}$$

$$M_l = \frac{T_j - TOL - T_{ml}}{D_j - D_{ml}}$$

Label the points responsible for establishing the slope limits as $j_u=j$; $j_l=j$.

Next, increment j and find $M_j=(T_j-T_{ml})/(D_j-D_{ml})$. Note that this is the slope of the line between points M1 (last significant point) and j. Then, test this slope against M_u and M_l. If $M_u \geq M_j \geq M_l$, then the tolerance limit is

INITIAL SLOPE LIMITS
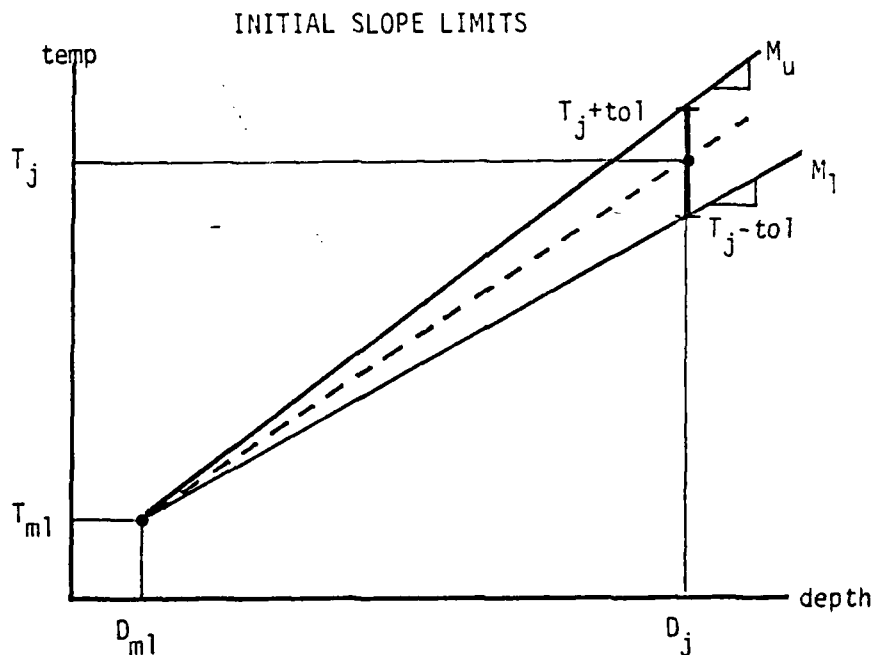
Figure 2.

142

not violated. If it is violated, the Ml is set to j_u (if the upper limit is violated) or j_l (lower limit violated), new test slopes are established and all is repeated (see Figure 3).

If the test slopes are not violated, then another set of tests is carried out. A new set of trial limit slopes are computed using points Ml and j. If either of these new trials results in a tighter limit, then the corresponding limit slope and labels are changed (see Figure 4). Note that both limit lines could be altered during this step.

Figure 3.   TOLERANCE LIMIT TESTS

TOLERANCE LIMIT NOT VIOLATED ($M_u = M_j = M_l$)

TOLERANCE LIMIT VIOLATED (M_j M_u)

Figure 4.   NEW LIMIT LINES

NEW UPPER LIMIT (JU=J)

NEW LOWER LIMIT (JL=J)
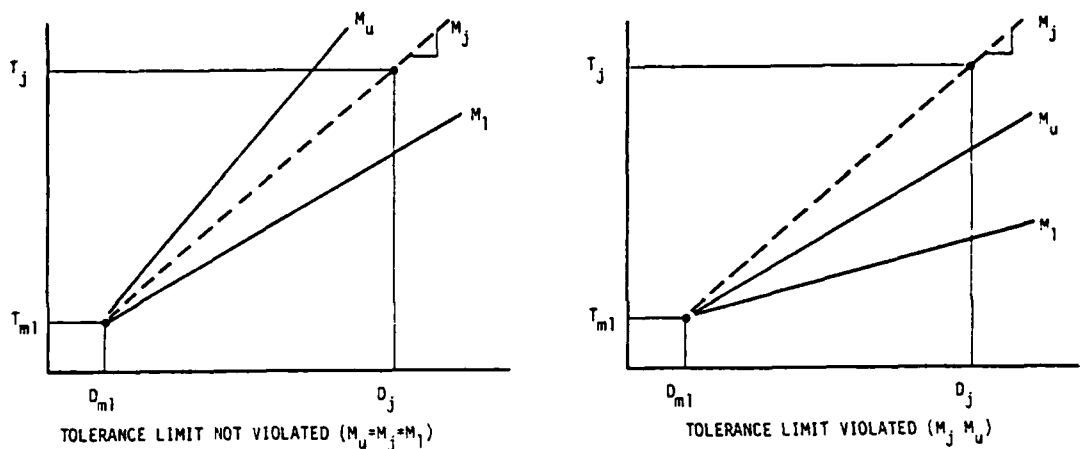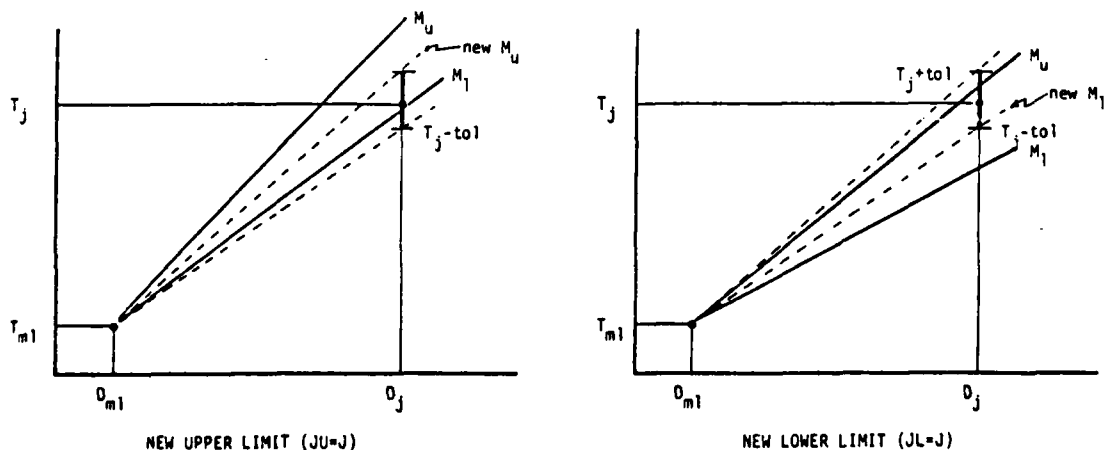
When the modification of the limit slopes is completed, if not all data points have been tested (i.e. j<Rs), the j is incremented and the tests are repeated for the new point.

When all points have been tested, the number of significant points is compared to the desired number of points. Twenty-three to 25 points is the desired number. But four of these points in the actual bathy-message label 100 meter crossings (100 m, 200 m, 300 m, and 400 m) so the actual number of data points is 19 to 21, with a target of 20. A new tolerance is now estimated with the goal of bringing the number of significant points closer to 20. The scheme used to estimate the new tolerance is based on the relationship between the number of significant points and the tolerance (see Figure 5).

NUMBER OF SIGNIFICANT POINTS VS TOLERANCE VALUE
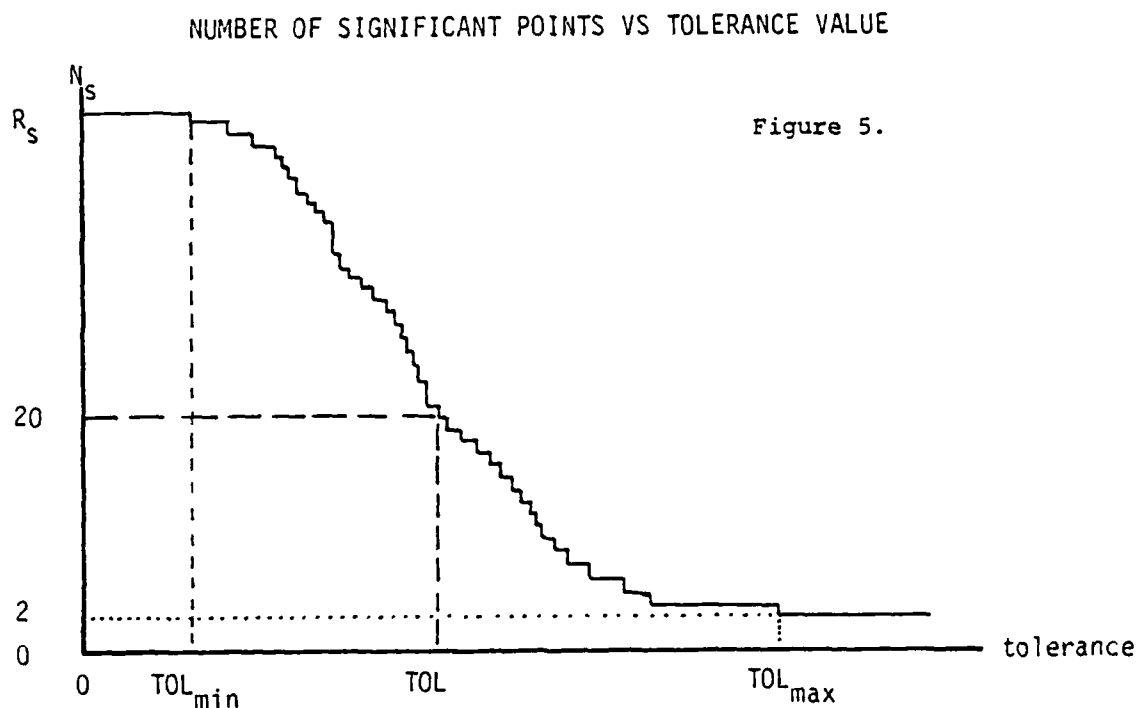
Figure 5.

The graph in Figure 5 is based on three observations concerning the number of significant points (N_s). First, if the tolerance is smaller than some values, TOL_{min}, all data points will be significant points; a tolerance smaller than TOL_{min} cannot result in an increase in the number of points. The second observation is that if the tolerance is increased from TOL_{min}, the number of significant points can decrease or stay the same; no tolerance increase can result in an increasing number of points. Thus, N_s is a monotonically decreasing function of TOL. Finally, as TOL is made larger, the number of significant points decreases until there are only two: the first and last points. Further increases in TOL cannot result in a decreased number of points when TOL exceeds TOL_{max}.

144

These three observations provide enough information for the programmer to estimate a new set of TOL values which will provide an appropriate number of significant points. There are two "known" points on this curve, TOL_{min}, Rs and TOL_{max}, 2. There are no local maxima or minima between these points since Ns is monotonic. If a value TOL results in Ns significant points, then using TOL, Ns, and the known end point, which is on the opposite side of Ns=20, define a line L_1 or L_2 on Figure 5 and determine where this line crosses Ns=20. If TOL is the current tolerance and Ns is the current number of significant points, TOL' is a new tolerance value, and Ns' is a new (estimated) number of significant points, then the equations for L_1 and L_2 are given by the following equations:

$$L_1: \quad (Ns>21) \quad Ns' = 2 + (Ns-2)\frac{TOL_{max} - TOL'}{TOL_{max} - TOL} \quad , \text{ and}$$

$$L_2: \quad (Ns<19) \quad Ns' = Rs + (Ns-Rs)\frac{TOL' - TOL_{min}}{TOL - TOL_{min}}$$

In each case, TOL' is found by setting Ns'=20, the desired number of significant points. The resulting value is then used at the tolerance in the next iteration. When Ns'=20, TOL' is given by the following equations:

$$(Ns>21) \quad TOL' = TOL_{max} - (TOL_{max} - TOL)\frac{2}{Ns - 2} \quad , \text{ and}$$

$$(Ns<19) \quad TOL' = TOL_{min} + (TOL - TOL_{min})\frac{20 - Rs}{Ns - Rs}$$

The data compression routine is convergent for linear, concave, and convex functions.

However one problem with this routine is that TOL_{max} and TOL_{min} are not constants. In fact, their values vary from data set to data set, and therefore values must be picked which represent reasonable values. The chosen values also limit, in each direction, the maximum and minimum attainable values to TOL. Thus, TOL_{max} must be large enough and TOL_{min} must be small enough to accommodate all expected data. The values $TOL_{max} = 2$ and $TOL_{min} = .05$ have been found to suffice for extremes of data well beyond the expected range for this application.

The complete bathy-message algorithm is shown in the flowchart in Figure 6. The flowchart is simplified by omitting the decision which alters the number of acceptable data points when the number of iterations becomes large.

Again, it should be remembered that this data compression scheme is not limited to expendable probe applications. It can be readily implemented on any µC with a floating point arithmetic capability. The algorithm shown

INITIALIZE TOLERANCE (TOL) Print Flag OFF

ENTER

INITIALIZE INDEX (J) #SIG POINTS (K)

INITIALIZE ML, Ju, JL

Print Flag ON — YES — PRINT First Sample

NO

COMPUTE Mu, ML

PRINT Last Sample — EXIT

$J = J+1$

Print Flag ON — NO

YES

$J \leq RS$ — NO — $K = K+1$

YES

$K = K+1$ $J = ML+1$

COMPUTE M_J

$K < 19$ — YES — COMPUTE TOL (ℓ_1)

NO

PRINT SIGNIFICANT POINT — YES — Print Flag ON

NO

$K > 21$ — YES — COMPUTE TOL (ℓ_2)

NO

$ML = Ju$ — YES — $M_J > Mu$

NO

SET Print Flag ON

$ML = JL$ — YES — $Mu < ML$

NO

$\dfrac{T_J - T_{ML} - TOL}{D_J - D_{ML}} > M_L$ — NO

YES

$\dfrac{T_J - T_{ML} + TOL}{D_J - D_{ML}} < M_U$ — NO

YES

$J_L = J$

$J_U = J$

Figure 6.

Bathy-Message Algorithm

here is particularly adapted to the situation where data is already stored. But in real-time operation, the only data (other than significant points) which needs storage is that between the smallest values of j_u or j_l and the current data point since these points may be needed when a new line is started. In real-time operation, of course, the iterative selection of the tolerance for a specific number of points is not appropriate.

Other Expendable Probes

The versatility of μC-based systems has also been demonstrated by the ease of adapting to several different expendable probes. In each case, the basic operating system was essentially unchanged. The only significant software alteration was to program the routine controlling the external hardware.

One interface has been built for the Sippican "XSV" (sound velocity) probe. The information is received over the probe wire via an FM signal. A simple counter controlled by the μC provides the digitizer function.

Several interfaces have also been built for the Grundy (Plessey) "XSTD" probe. In this probe, temperature and conductivity are received simultaneously as FM signals. Filters are used to separate the two channels. Otherwise, the interface design is very much like the design required for the XSV interface. Again, minimal software change is needed.

The relative ease with which these systems have been implemented is largely due to simplicity of changing a high level language computer program which is well structured. Another factor, of course, is that all of the systems have had similar operating requirements.

Future Directions

A recent study by the National Marine Fisheries Laboratory at Monterey, California,[4] has shown that approximately 50 percent of the received bathy-messages have major errors. The errors appear to be fairly evenly distributed among the bathy-message generation, message (CW) transmission, message reception, and message retransmission (to NMFL) functions.

The first of these error sources, bathy-message preparation, has been addressed by the BMA in the OSU digital XBT system. A major effort is underway to reduce the remaining error sources by using a satellite link directly coupled to the digital XBT system. Again, the versatility of a μC-based system makes such an undertaking quite feasible.

References

[1] Mesecar, R. S. & J. Wagner. "An XBT Digital Recording and Display System", *Oceans '79 Conference* (IEEE Cat. No. CH1478-7/79/000-0598).

[2] *Instructions for Preparing the Bathythermograph Log*, Feb. 1972, U.S. Dept. of Commerce, Nat. Oceanic and Atmospheric Admin., Nat. Weather Service, Office of Meteorological Operations, Silver Spring, MA.

[3] Merrill, M. Don & Don R. Veazey, "Linearization for Compact Storage of Digitized Analog Data", *IEEE 1977 Region 6 Conference Record*, (IEEE Cat. No. 77CH1206-2 Reg 6; Library of Congress No. 72-92043).

[4] Personal verbal communication.

Small-Scale Sea Surface Temperature Structure

JAMES J. SIMPSON[1] AND CLAYTON A. PAULSON

School of Oceanography, Oregon State University, Corvallis, 97331

(Manuscript received 4 September 1978, in final form 5 October 1979)

ABSTRACT

Observations of sea surface temperature and wave height were made from a large, manned spar buoy (R/P *FLIP*) ~100 km off the coast of Baja California. Surface temperature was measured with a radiation thermometer which viewed a disc on the surface 12 cm in diameter. The instrument responded to frequencies up to 3 Hz. Wave height was measured with a resistance gage located close to the field of view of the radiometer.

Log-log plots of spectra of sea surface temperature exhibit a plateau between 0.05 and 0.5 Hz, followed by a rapid decrease in energy at frequencies > 1 Hz. A coherence of 0.5 between waves and surface temperature occurs at the same frequency as the peak in the wave spectrum. Phase spectra show that warm temperatures associated with the thinning of the surface viscous layer occur systematically upwind of the crests of the dominant gravity waves and downwind of the crests of steeply sloping, shorter period gravity waves. The warm temperatures are hypothesized to be caused by enhanced wind stress upwind from the crests and by surface instability and surface convergence downwind from the crests.

The magnitude of the mean temperature difference between the surface and the warmer, well-mixed water below is estimated from the surface temperature record. It is assumed that the warmest surface temperatures observed are associated with thinning of the viscous layer and are representative of the well-mixed water below. The dimensionless constant in a formula due to Saunders (1967), which relates the temperature difference to wind stress and heat flux, is found to be seven.

1. Introduction

With the improvement of radiometric techniques, it became possible to investigate the surface or "skin" temperature of the sea. Ball (1954), Ewing and McAlister (1960), McAlister (1964) and McAlister and McLeish (1969) were among the first to make radiometric measurements of sea surface temperature which demonstrated that the surface is typically a few tenths of a degree Celsius cooler than the temperature some tens of centimeters below. Earlier measurements by other methods (e.g. Woodcock, 1941) also demonstrated that the upper few millimeters of natural water surfaces were typically cooler than the water below. The temperature difference occurs because the vertical flux of heat Q just below the surface is generally upward, the total being the sum of the fluxes to the atmosphere of net longwave radiation R, sensible heat H, and latent heat E, i.e., $Q = H + E + R$.

A schematic diagram of the upper centimeter of the sea is shown in Fig. 1. Just below the interface there is a viscous sublayer of thickness δ in which the transfer of heat and momentum is primarily by molecular processes, from which it follows that the vertical temperature gradient is approximately constant. Below the viscous sublayer, turbulent mixing dominates and the temperature gradient is small.

Saunders (1967), on the basis of dimensional arguments, suggested that the difference between the surface temperature T_s and the well-mixed bulk temperature T_b below the surface is given by

$$T_b - T_s = \frac{\lambda \nu Q}{k(\tau/\rho)^{1/2}},\qquad(1)$$

where λ is a dimensionless constant, ν the kinematic viscosity of water, k the thermal conductivity, τ the wind stress and ρ the density of water. Saunders suggested that the value of λ would lie between 5 and 10.

Hasse (1971) and Deacon (1977) have derived expressions similar to (1), but containing no arbitrary constants, derived from models of the viscous sublayer based on laboratory observations of flow near a solid boundary. Hasse (1971) found good agreement between his model and observations in which the surface temperature was determined by extrapolation of nearly adiabatic atmospheric temperature profiles to the surface. Hasse's observations are in good agreement with (1) when $\lambda = 8$ as shown by Paulson and Parker (1972). For a temperature of 20°C, Deacon's model is similar to (1) with $\lambda = 8.2$. For observations in the laboratory, λ ranges from 4

[1] Present affiliation: Scripps Institution of Oceanography, La Jolla, CA 92093.
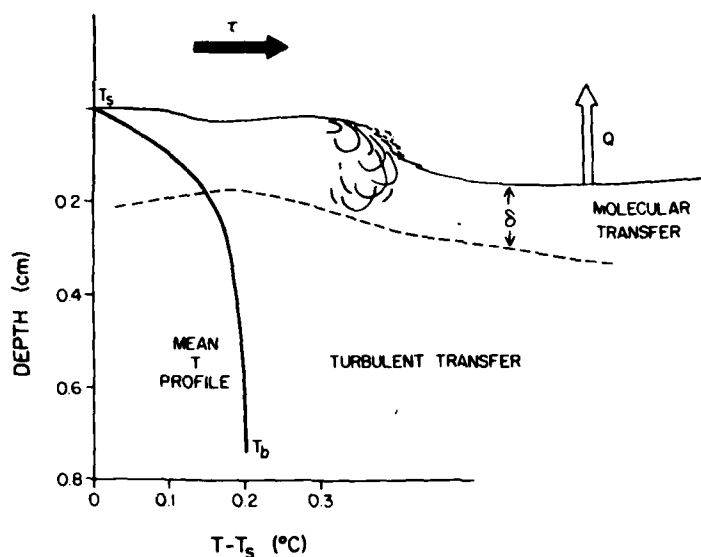
Fig. 1. Schematic diagram showing the processes affecting the temperature profile in the upper ocean. Here τ is the wind stress, Q the upward heat flux from just below the surface, δ the thickness of the viscous sublayer, T_s the mean surface temperature and T_b the mean temperature at a depth below 1 cm.

to 15, depending on whether or not waves are present (Hill, 1972; Paulson and Parker, 1972).

Radiometric observations of the sea surface temperature show temperature variations of a few tenths of a degree Celsius. The variability on small time scales (1–5 s) might be caused by the thinning or destruction of the viscous sublayer by the action of one of several possible mechanisms: 1) locally intense turbulence within the water, perhaps associated with a breaking wave; 2) a wind gust acting on the surface, causing a local increase in stress; or 3) the presence of waves. The occurrence of warm spikes in the temperature record particularly suggests the momentary destruction or thinning of the viscous sublayer.

Witting (1971) suggested on theoretical grounds that for an assumed constant heat flux, the presence of capillary waves could reduce $T_b - T_s$ by as much as a factor of 9 in comparison to the undisturbed case. Witting also suggested gravity waves would be an order of magnitude less effective and that the maximum in the temperature should lead the wave maximum by 45°.

Miller and Street (1978) recently reported a laboratory investigation of surface temperature fluctuations associated with waves. Waves were mechanically driven and various wind speeds and air-water temperature differences were imposed. The magnitude of the surface temperature variations was between 10 and 100% of $T_b - T_s$, in qualitative agreement with Witting (1971). For light winds, the peak of the temperature wave occurred on the lee-

ward side of the mechanically generated surface wave. For moderate to high winds, the trough of the temperature wave occurred on the leeward side. A satisfactory explanation for this behavior is lacking. The extent to which Miller and Street's results can be generalized for the open sea is uncertain.

The objective of this paper is to describe radiometric observations of the sea surface temperature made simultaneous to measurements of wave height and surface fluxes. Insight is sought into the physical processes associated with variability in surface temperature.

2. Observations

Observations of sea surface temperature and wave height were made from the R/P FLIP [Floating Instrument Platform, (Bronson and Glosten, 1968)] approximately 60 mi off the coast of Baja California during the period 23–28 March 1973. The FLIP is a large manned spar buoy with ~90 m of its 110 m length submerged, resulting in a high degree of stability. Typical heave amplitudes were ~10 cm, while pitch and roll amplitudes were usually less than 2°. The FLIP drifted freely during the experiment, generally toward the southeast, with positions ranging from 31°28'N, 118°17'W at the beginning of the experiment to 30°48'N, 117°35'W at the end.

Sea surface temperature was measured with a Barnes Engineering Co. PRT-5 radiation thermometer responding to radiation with wavelengths in the range 8–14 μm. The half-power field of view of the
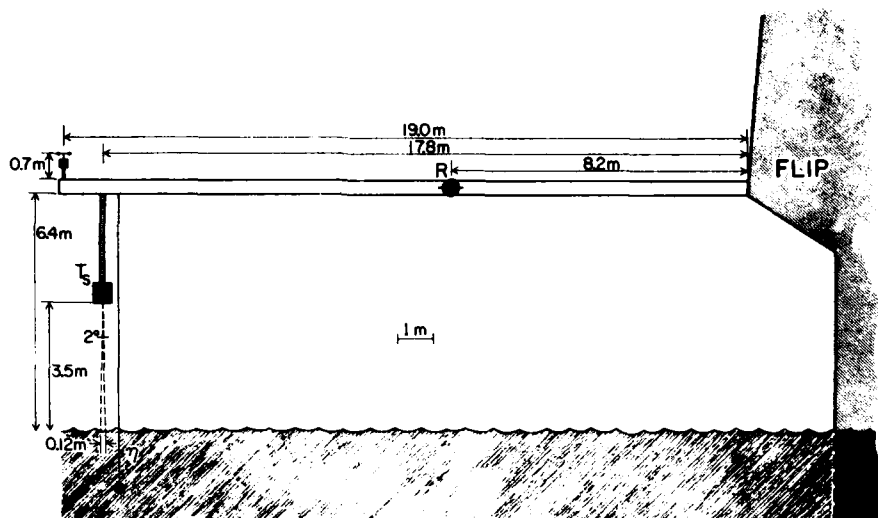
FIG. 2. Diagram showing the locations of instruments used to measure the sea surface temperature T_s, the wave height η, the wind speed U, and the net longwave radiative flux R. The diameter of *FLIP* at the surface is 4.2 m.

instrument is 2°. The instrument was mounted on the port boom of the *FLIP*, 18 m from the hull and 3.5 m above mean sea level, as shown schematically in Fig. 2. The *FLIP* naturally aligned itself with respect to the wind such that the boom extended perpendicular to the wind direction. The spot on the surface viewed by the instrument had a diameter of 12 cm (corresponding to the diameter at which the response has dropped to 50% of maximum). The instrument was operated with a low-pass filter on the output set at 3 Hz. The sensitivity of the instrument is ~0.03°C and the absolute accuracy is 0.5°C. Errors in the measurement of T_s caused by the reflection of longwave radiation from the *FLIP* are shown to be negligible in the Appendix.

Wave height η was measured with a resistance gage using nichrome wire having a diameter of 0.125 mm. The wire was suspended from the port boom of the *FLIP* as close to the radiation thermometer as practically possible. The wire was weighted with lead to keep its orientation near vertical. The resistance of the wire was measured before and after the experiment to insure that no change in resistance occurred because of stretching. The frequency response and sensitivity of the wave gage was limited by the effects of surface tension to about 3 Hz and 4 mm, respectively.

Wind speed was measured with a cup anemometer located near the end of the boom, as shown in Fig. 2. Dry-bulb and wet-bulb temperatures were measured approximately hourly by use of a ventilated psychrometer at a height of ~10 m above mean sea level. Bucket temperatures were recorded at the same time. Estimates of τ, H and E were ob-

tained by use of the standard bulk formula. The exchange coefficient employed was 1.4×10^{-3}. Net longwave radiation was measured with a C. A. Thornthwaite Associates net radiometer. All of the reported observations were at night, thereby eliminating any possible complications caused by absorption of solar radiation in the upper millimeters. A summary of the conditions during each run is given in Table 1.

Data were recorded in analog form on magnetic tape. The signals were monitored simultaneous to recording on a strip-chart recorder. Examples of the data are shown in Fig. 3. The records show the occurrence of warm spikes of temperature having a magnitude of 0.3°C, often associated with a steep part of the wave profile. Apart from the spikes, there are fluctuations in temperature over a broad range of frequencies with peak-to-peak amplitudes on the order of 0.1°C.

3. Analysis

Following the experiment, the surface temperature and wave height signals were low-pass filtered at 10 Hz and digitized at a rate of 20 samples per second. Blocks of 16 384 data points, corresponding to 13.6 min of observations, were then constructed. Each run consisted of from four to six contiguous blocks.

A spectral analysis was carried out on both the surface temperature and the wave record. Fourier coefficients were computed for each of the blocks. The coefficients were combined to obtain the spectral energy densities, ϕ_T and ϕ_η, the cospectrum

TABLE 1. Summary of measurements and statistics, including mean wind speed U, surface drift speed U_s, wind stress τ, flux of latent heat E, flux of sensible heat H, net longwave radiative flux R, upward heat flux just below the surface Q, fractional cloud cover C, rms wave height σ_η, mean surface temperature $\bar{T}_s$, rms sea surface temperature σ_{T_s}, mean difference between bulk oceanic temperature and surface temperature $\overline{\Delta T}$, the constant λ in Saunders' (1967) formula, and the symbol key used to identify individual runs in the composite spectra of Figs. 5, 8 and 9.

Run no.	Date (March 1973)	Time begin	$\dot{U}$ (m s⁻¹)	U_s (m s⁻¹)	τ (Pa)	E ←	H (W m⁻²)	R	Q →	C (tenths)	σ_η (m)	$\bar{T}_s$ ←	σ_{T_s} (°C)	$\overline{\Delta T}$ →	λ	Symbol key
2	23	1928	8.2	0.05	0.116	117	14	68	199	4	0.69	14.8	0.05	0.29	8	●
3	23	2115	7.7	0.05	0.102	108	10	51	168	5	0.67	15.3	0.06	0.29	9	☼
4	23	2303	8.5	0.18	0.125	124	17	60	201	4	0.70	15.2	0.07	0.29	8	▲
7	24	0418	5.5	0.12	0.052	124	17	37	178	6	0.42	15.3	0.10	0.26	5	△
10	24	1941	7.1		0.087	124	2	22	148		0.40	14.9	0.08	0.19	6	■
11	24	2127	6.7		0.077	99	2	18	119		0.61	15.4	0.08	0.16	6	□
12	24	2314	7.1	0.05	0.087	115	4	58	177	2	0.60	15.1	0.07	0.28	8	◆
14	25	0234	5.6	0.08	0.054	92	7	34	133	9	0.42	14.8	0.10	0.24	7	◇
29	26	2002	9.2	0.25	0.146	155	12	55	222	0	0.56	15.0	0.05	0.27	8	×
31	26	2325	7.0	0.22	0.085	113	9	32	154	9	0.60	15.1	0.09	0.26	8	⊙

$C_{n,T}$, and the quadrature spectrum $Q_{n,T}$. These spectra were averaged over non-overlapping frequency bands equally spaced on a logarithmic scale to obtain smoothed spectral estimates. Coherence and phase spectra ($\gamma_{n,T}$ and $\theta_{n,T}$, respectively) were calculated from the smoothed spectral estimates by use of

$$\gamma_{n,T} = [(C^2_{n,T} + Q^2_{n,T})/\phi_n\phi_T]^{1/2},$$

$$\theta_{n,T} = \tan^{-1}(Q_{n,T}/C_{n,T}).$$

FIG. 3. Simultaneous measurements of sea surface temperature (T_s) and wave height (η) illustrating the occurrence of warm spikes.

Then the smoothed spectral energy density, coherence and phase spectra were averaged over blocks.

Confidence intervals for the energy density were calculated using a chi-square random variable with n equivalent degrees of freedom. Within a given frequency band, the equivalent degrees of freedom $n(f)$ is defined as twice the square of the block and band-averaged spectral estimate divided by the estimated variance of the sample average associated with the estimate, i.e.,

$$n(f) = \overline{2\phi(f)}^2/\mathrm{var}[\phi(f)].$$

Confidence intervals so constructed reflect the measured spectral variability within a given block-averaged frequency band.

Confidence intervals for the coherence were calculated using the procedure of Bendat and Piersol (1971). Additionally, a 95% significance level for the coherence was calculated using the procedure of Panofsky and Brier (1958) in which the limiting coherence β at probability level p is given by $\beta = [1 - p^{(1/(df/2)-1)}]^{1/2}$. As pointed out by Julian (1974) the appropriate number of degrees of freedom (df), is not the Blackman and Tukey (1958) definition but rather the effective number of Fourier components in the spectral window, i.e., df/2. This relation compares the limiting coherence and the measured coherence for a given probability level on the null hypothesis of zero population coherence (Julian, 1974) and agrees to within three decimal places with values obtained by following the procedures of Amos and Koopmans (1963). For the limit of large N, β approaches zero as expected. Confidence intervals for the phase estimates were determined using procedures suggested by Jenkins and Watt (1968).

Since the wave spectrum falls off approximately as ω^{-5}, it was necessary to consider the possible effects of spectral leakage on estimates of the vector
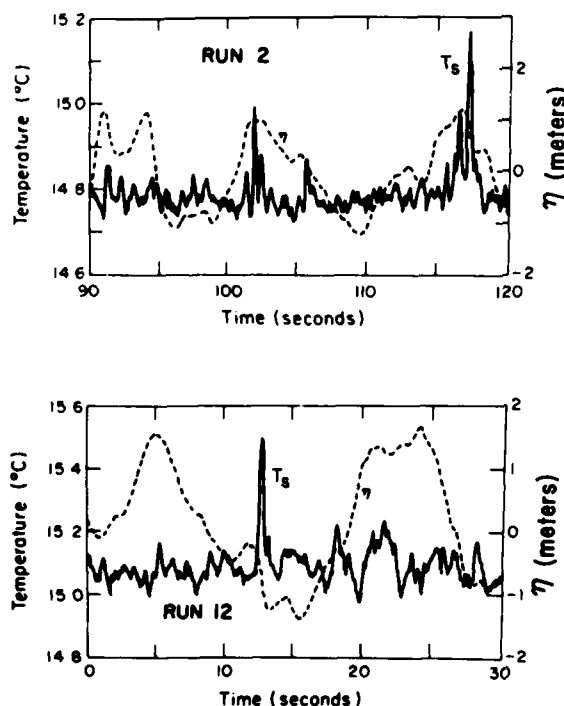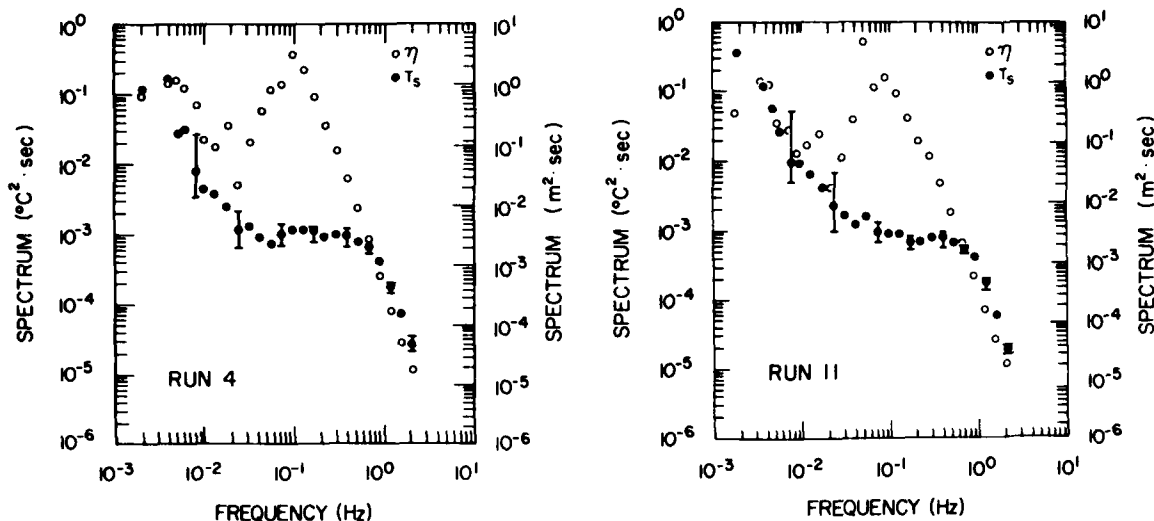
FIG. 4. Representative spectra of sea surface temperature (closed circles) and wave height (open circles). The vertical bars are the 95% chi-square confidence intervals.

coherence. For this purpose the data were partially prewhitened by calculating first differences. Differentiation is expected to reduce the slope of the spectrum of waves from ω^{-5} to ω^{-3} and hence is a good signal preconditioner with which to investigate the possible effects of spectral leakage. The resulting time series was Fourier-transformed as above. Coherence spectra for both (η, T_s) and $(\Delta\eta, T_s)$ for a typical run are shown in Fig. 6. The figure clearly shows that there is no significant difference between the two coherence spectra. A similar analysis was performed on most of the runs in Table 1 and the results were the same. These results indicate that spectral leakage did not affect the computation of the coherence spectra. Phase spectra for the same two cases are shown in Fig. 7. Where the coherence is high, the two phase spectra are similar. As higher frequencies are approached, the phase between surface temperature and differenced wave height becomes random at lower frequencies than the phase between surface temperature and wave height. This behavior may be caused by noise introduced by differencing the wave signal. In any case, the general behavior of the two spectra is consistent.

Estimates of spectral leakage can also be made on purely theoretical grounds by considering the effects of window shape and series length on the Fourier-transformed data. The data series was windowed with a boxcar window. The Fourier transform of the boxcar window has the form (Cooley et al., 1967)

$$h(\omega) = \frac{1}{2\pi N} \left[\frac{\sin(N\omega\Delta t/2)}{\sin(\omega\Delta t/2)} \right]^2,$$

where N is the number of data points in a block and Δt the sampling interval. Leakage can only affect the spectral estimates when the ratio of side-lobe to central-peak energy is large. However, from the analytical form of $h(\omega)$, it is easy to see that as $N \to \infty$, the width of the frequency range with considerable spectral energy in the side lobes of the $h(\omega)$ window approaches zero. For the analysis presented in this paper, the length of the blocks (16 384 data points) used in the computations minimized the effects of leakage.

4. Spectra

Representative spectra of sea surface temperature and wave height are shown in Fig. 4. The shape of the spectra of wave height is similar for all of the runs, with peaks in the wave spectra occurring at frequencies between 0.055 and 0.097 Hz. Swell was negligible during most of the runs and the waves were taken to be wind-driven, traveling slower than the wind. The magnitude of the spectra at the peak ranged from 1.0 to 5.1 m^2 s. The standard deviation of wave height and surface temperature is given in Table 1 for each of the runs.

As shown in Fig. 5, the individual spectra of surface temperature are all similar to the examples shown in Fig. 4, both in shape and in magnitude. A peak occurs at low frequencies and, as frequency increases, spectral energy declines to a plateau between 0.05 and 0.5 Hz, followed by a rapid decrease in energy for frequencies above 1 Hz. There is often a small peak at the same frequency as the peak in the wave spectrum.

The spectra at low frequencies may be spurious because, as has been suggested by Saunders (1970), the variation of sky temperature associated with variations in cloud cover and type can cause non-
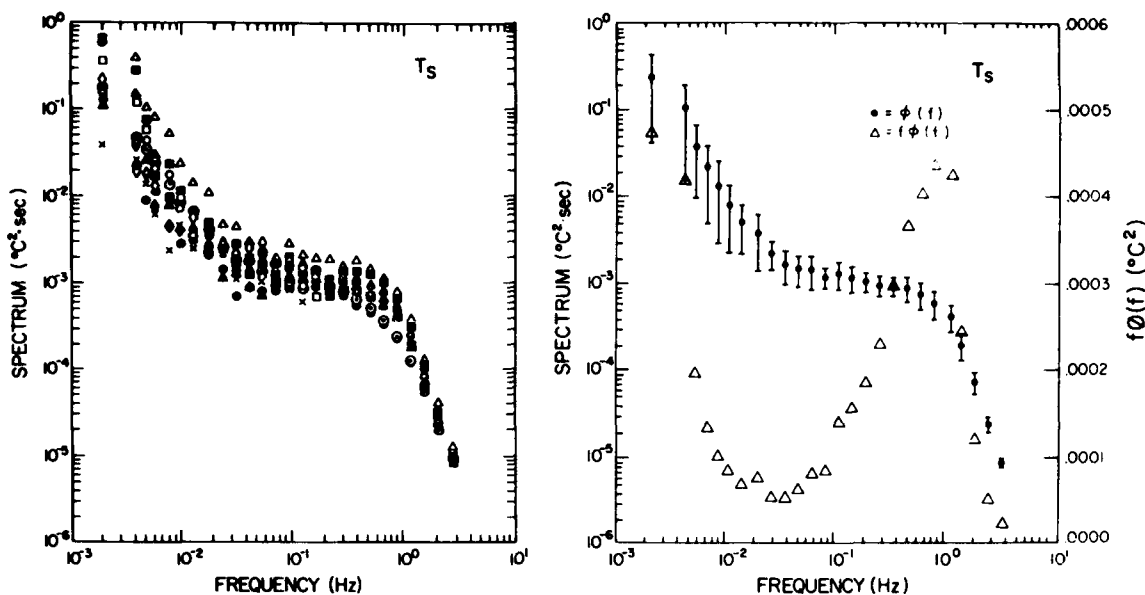
FIG. 5. Unaveraged and averaged spectra of sea surface temperature versus frequency. The symbols are defined in Table 1. The triangles in the figure represent the average spectrum of $f\phi(f)$ vs f, where f is frequency (Hz).

negligible, fictitious fluctuations in measured temperature. These fictitious fluctuations are caused by the reflection of longwave radiation from the surface. Even though the reflectivity is small (0.02), variation in sky temperature may cause erroneous fluctuations in observed temperature of several tenths of a degree Celsius (Saunders, 1970). Even under clear skies, variations in humidity and air temperature may cause variations in downward longwave radiation which would in turn cause spurious observed fluctuations in surface temperature. The likelihood of errors in the low-frequency fluctuations is supported by examination of time series of observations of surface temperature and net upward longwave radiation which reveal a negative correlation for periods longer than a few minutes. If the fluctuations were caused by fluctuations of surface temperature, the correlation would be positive. The magnitudes of the low-frequency fluctuations of observed T_x and R are on the order of 0.3°C and 2 mW cm^{-2} peak to peak, during periods of partial cloudiness. However, even during run 29 for which skies were reported to be clear, there were negatively correlated low-frequency fluctuations of T_x and R for about half the run. Conditions may not have been totally clear during this run because observations of cloudiness are difficult to make at night.

On the basis of the foregoing discussion, we conclude that observed fluctuations of T_x for periods greater than a few minutes may be in error. The magnitudes of the spectral estimates of T_x shown in

Fig. 5 may therefore be too large for frequencies below 0.01 Hz.

Interpretation of the spectra of sea surface temperature at higher frequencies is complicated because temporal changes cannot be ignored and advection by surface waves is not steady. Attempts were made to nondimensionalize the spectra of sea surface temperature (Fig. 5) in hopes of establishing a universal form. In one of the attempts, the right side of Eq. (1) was used as a temperature scale. The attempts at nondimensionalization all failed to significantly reduce the scatter in the observations.

Representative coherence spectra computed for wave height and surface temperature are shown in Fig. 6. In both runs 4 and 11 there is a peak at the frequency at which the peak in the wave spectrum occurs, 0.097 and 0.055 Hz, respectively. The peak is characteristic of all of the runs.

The large values of coherence at frequencies ~0.01 Hz shown in Fig. 6 are spurious. They are due to the low-frequency motions of FLIP. Vertical motions at the location of the wave gage cause an erroneous fluctuation in wave height, while pitch and roll cause fluctuations in measured surface temperature as the radiation thermometer scans along the surface in the presence of a horizontal temperature gradient. The vertical motion is inevitably correlated with rolling motions of FLIP, giving rise to the observed coherence.

The question arises whether the low-frequency motions of FLIP have caused significant error in
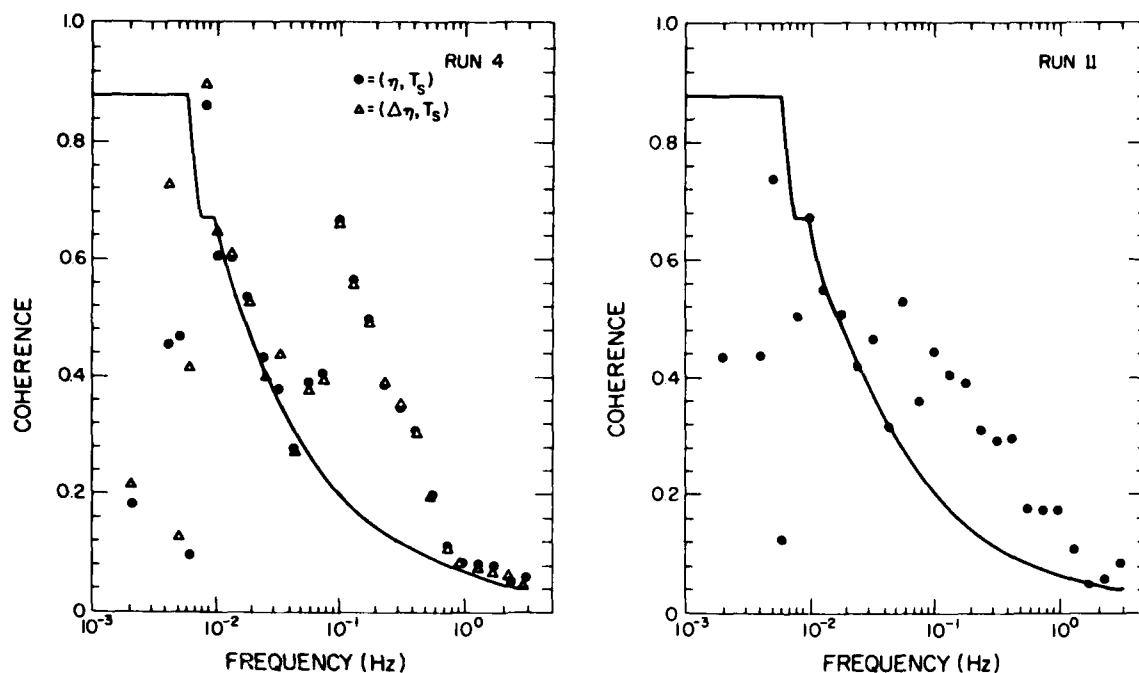
Fig. 6. Representative coherence spectra for sea surface temperature and wave height (circles). The line is the 95% significance level. The corresponding coherence spectrum (run 4) for sea surface temperature and first differenced wave height ($\Delta\eta$) is shown by the triangles.

the low-frequency spectra of sea surface temperature. Taking 1° as the typical pitch amplitude, this corresponds to a horizontal scanning by the radiometer over the surface of ~1 m. Taking a period of 100 s, the amplitude of the velocity of the scanning motion is 0.01 m s⁻¹, which is an order of magnitude less than typical surface drift velocities. We therefore conclude that the effects of the motion of *FLIP* on the low-frequency sea surface temperature spectra are negligible, even though the effects on coherence spectra are marginally significant at the 95% level.

Representative phase spectra computed for wave height and surface temperature are shown in Fig. 7. The phases at frequencies corresponding to the peak in the wave spectra are between zero and −30°, indicating that warm fluctuations in temperature are associated with the region just upwind of the crest of the dominant gravity waves. The cause of this behavior may be locally enhanced wind stress on the upwind side of the crest of the wave. This part of the wave profile is most favorably exposed to the wind. The increased wind stress could act directly to thin the viscous layer just beneath the surface (Saunders, 1967), thereby exposing the warmer water below, or the enhanced stress could generate a patch of capillary waves which could act to thin the viscous layer, as suggested by Witting (1971).

As shown in Fig. 7, when frequency increases

from 0.05 to 0.5 Hz, the phase between the surface temperature and wave height increases from between zero and −30° to about 100°, i.e., warm fluctuations occur on the downwind faces of the shorter period gravity waves. The downwind side of the wave profile has the greatest slope and is therefore the most unstable. It is also a region in which there is local convergence at the surface which tends to increase the amplitude of the capillary waves, giving rise to the possibility of thinning the viscous layer, as suggested by Witting (1971). There are warm spikes in the records of surface temperature shown in Fig. 3 which are associated with the steep downwind slopes of the waves.

All of the coherence and phase spectra are shown in Figs. 8 and 9, respectively, together with the averaged spectra. The characteristics are very similar to those in the representative spectra. There is a maximum in the coherence of 0.5 at 0.1 Hz. The mean phase is about −30° at a frequency corresponding to peaks in the wave spectra, and increases to about 100° at 0.4 Hz. As described above, the high values of coherence at low frequencies (0.01 Hz) are caused by the motion of *FLIP*.

5. Saunders' formula

An evaluation of the constant in Saunders' formula Eq. (1) was carried out. The mean differ-
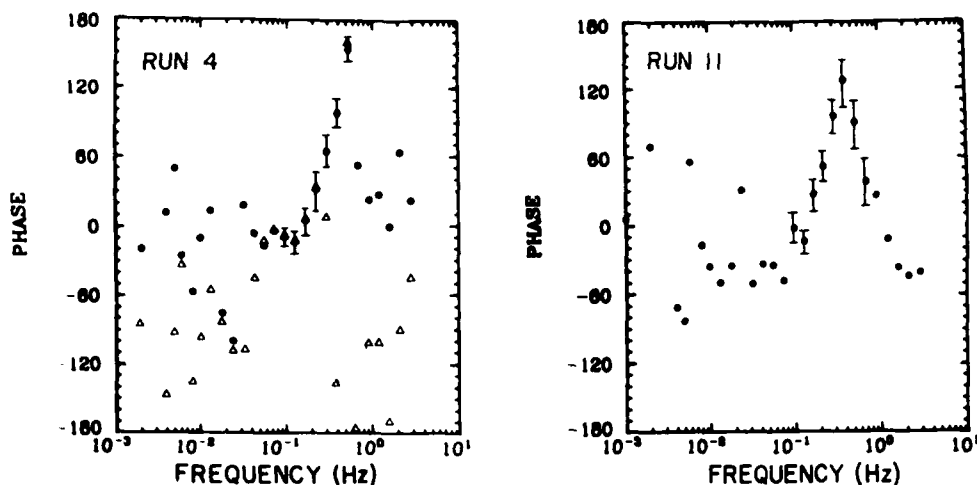
FIG. 7. Representative phase spectra for sea surface temperature and wave height (circles). A positive phase occurs when surface temperature leads wave height. The corresponding phase spectrum (run 4) for sea surface temperature and first differenced wave height ($\Delta\eta$) is shown by the triangles. The phase spectrum of ($T_s, \Delta\eta$) was recolored.

ence, $T_b - T_s$, between the surface temperature and the bulk temperature of the well-mixed water below was estimated by subdividing the surface temperature record for each run into intervals of 2 min. Within each interval, the maximum and mean surface temperatures were computed. The maximum difference between the mean and maximum values for the entire run was taken as an estimate of

$T_b - T_s$. Implicit in the method is the assumption that at least once during each run the viscous sublayer below the surface viewed by the radiation thermometer is thinned so that the observed temperature is representative of the bulk, well-mixed water below. The record was subdivided into 2 min intervals to minimize the effects of trends in surface temperature. The values of $T_b - T_s$ computed as
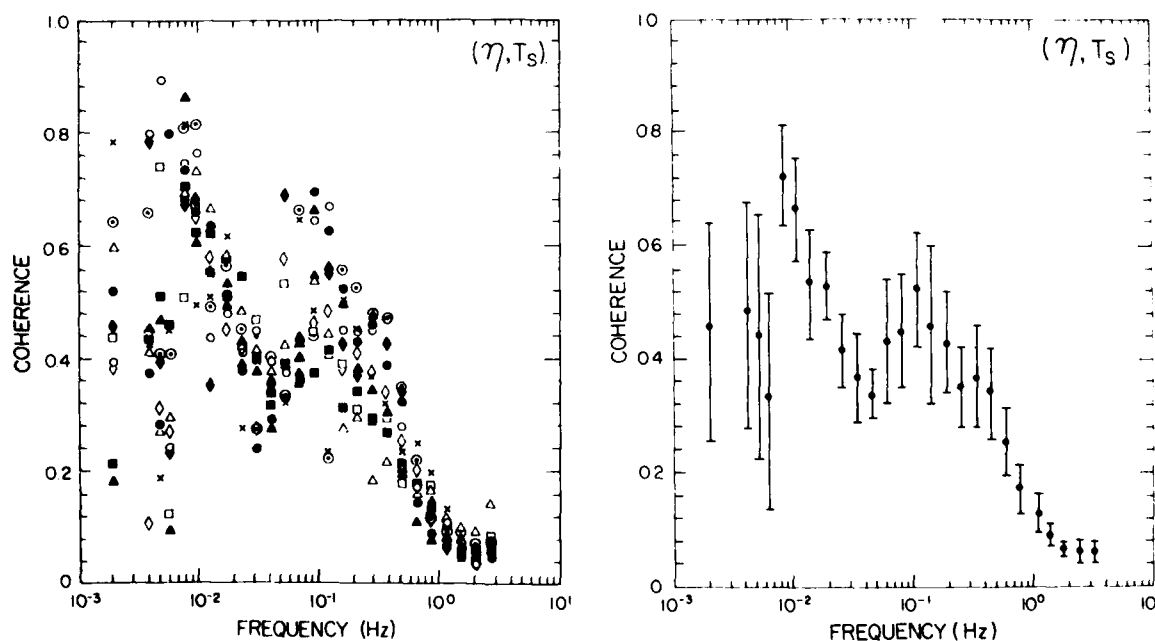
FIG. 8. Coherence spectra. Symbols are defined in Table 1. The average is over all runs.
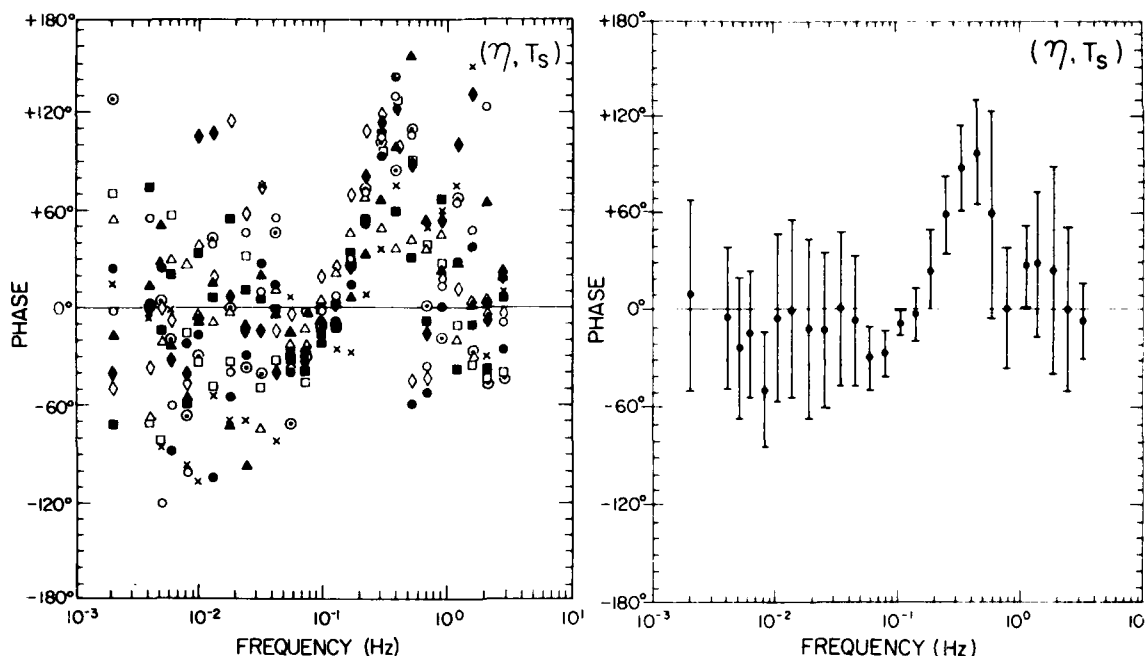
FIG. 9. Phase spectra. Symbols are defined in Table 1. The average is over all runs. Phase is defined as positive when surface temperature leads wave height.

described above are given in Table 1. Values of the dimensionless coefficient computed using Eq. (1) are also tabulated. The value of λ ranges from 5 to 9 with a mean of 7. This value is in good agreement with Saunders' (1967) suggested range of 5 to 10 and also agrees with Hasse's (1971) model and observations (Paulson and Parker, 1972) and with Deacon's (1977) model. Agreement is also good with observations over a cooling pond reported by Wesley (1979) who found λ = 6 at 15°C. He also found that λ was proportional to $Pr^{-1.3}$, where Pr is the Prandtl number. The agreement is less satisfactory with the value of λ = 5 determined by Grassl (1976) for a wind speed of 7 m s^{-1}. Grassl also suggests that λ varies with wind speed, increasing from λ = 2 at 1 m s^{-1} to λ = 6 at 10 m s^{-1}. Our observations are over too restricted a range of wind speed to draw any conclusions about a possible variation of λ. A plot of the left side of Eq. (1) vs $T_b - T_s$ is shown in Fig. 10.

The fact that the results reported here agree with the large body of observations reported by Hasse (1971), in which T_s was determined by extrapolating nearly adiabatic atmospheric temperature profiles to the surface, lends support to the method employed here. It was not possible to make an independent estimate of T_s and T_b in our case, because the absolute accuracy of the radiometrically determined temperatures was not adequate for reliable estimates of $T_b - T_s$. This is primarily because of

the reflection of sky radiation and the impracticability of frequent calibration of the radiation thermometer as was done by Grassl (1976).
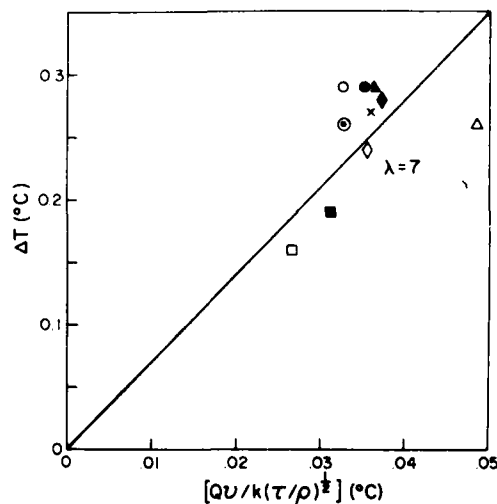
FIG. 10. The mean temperature difference ΔT between the surface and the well-mixed water below versus a quantity having dimensions of temperature where Q is the upward heat flux just below the interface, ν the kinematic viscosity of seawater, k the thermal conductivity, τ the surface stress and ρ the density of seawater. The line drawn represents Saunders' (1967) formula with λ = 7 (from Table 1).
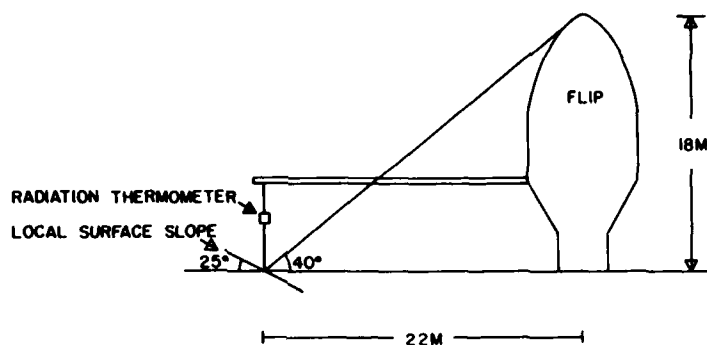
FIG. 11. Schematic diagram showing geometry associated with radiation coming
from the hull of *FLIP* which is reflected into the radiation thermometer.

6. Conclusions

The following conclusions can be drawn:

1) Spectra of surface temperature over the sea exhibit a plateau between 0.05 and 0.5 Hz, followed by a rapid decrease in energy for frequencies above 1 Hz. There is usually a small peak in the temperature spectrum at the same frequency as the peak in the wave spectrum.

2) There is a peak in the coherence spectra between surface temperature and wave height occurring at the same frequency as the peak in the wave spectra. The average magnitude of the peak in coherence is 0.5.

3) The phase angle between wave height and surface temperature at the frequency of the peak in the wave spectrum is $-30°$ on average, indicating warm surface temperature upwind of the crests of the dominant gravity waves. The cause of these warm fluctuations is thought to be locally enhanced wind stress which thins the viscous layer just beneath the surface, either directly or through generation of capillary waves (Witting, 1971).

4) The phase spectrum between surface temperature and waves increases from an average of $-30°$ at 0.06 Hz to $100°$ at a frequency of 0.4 Hz. The phase relation at 0.4 Hz implies that warm temperature fluctuations are associated with the steep portion of gravity waves downwind from the crest. The cause of the warm fluctuations may be due to the generation of turbulence in the water caused by instability of the surface or may be due to the enhancement of the amplitude of capillary waves caused by convergence of the surface. Both of these effects would tend to thin the viscous layer just below the surface, exposing warmer water from below.

5) On the basis of the observations of mean values of $T_b - T_s$ inferred from surface temperature fluctuations, the constant in Saunders' (1967) formula [Eq. (1)] is $\lambda = 7$. This value is in fair agreement with other determinations over the ocean which range from 5 to 8. It is perhaps surprising that the observations also agree with models of Hasse (1971) and Deacon (1977) which are based on laboratory observations of flow near solid boundaries. These models are similar to Saunders' formula, but they contain no arbitrary constants. This suggests that the effects of waves in determining ΔT may be small or compensating.

APPENDIX

Effect of Reflections on Measurement of Surface Temperature

The objective of this Appendix is to evaluate possible errors in the radiometric measurements of sea surface temperature caused by reflections of longwave radiation emanating from the hull of *FLIP*, the boom and supports, and from the radiation thermometer itself. These reflections are a possible source of error because the emitting surfaces are generally much warmer than the sky, the only remaining source of reflected longwave radiation at night. The errors are evaluated by use of simple models.

We first consider radiation reflected from the hull of *FLIP*. From Fig. 11 it is apparent that only waves sloping toward the hull can reflect radiation from the

hull into the radiometer. The height of the hull above the water is about 18 m and the horizontal distance from the centerline to the radiation thermometer is 22 m. The angles between the rays coming from the hull and the horizontal must therefore be less than $40° = \tan^{-1} (18/22)$. Snell's law states that the angle of incidence is equal to the angle of reflection. Consider a ray 40° from the horizontal arriving just below the radiation thermometer. The water surface below the instrument must be inclined toward the direction from which the ray is coming by an angle 25° from the horizontal for this ray to be reflected vertically into the instrument (Fig. 11). Radiation from the hull will be reflected into the instrument only when the water surface below the hull is inclined at an angle > 25° toward the hull.

According to Stokes (Kinsman, 1965, p. 19), the steepest gravity waves have a steepness (ratio of wave height to wavelength) of 1/7. A sinusoidal wave having a steepness of 1/7 has a maximum slope of $\pi/7$, corresponding to an angle with the horizontal of 24°. Thus, according to this criterion, we would expect negligible radiation from the hull to be reflected into the radiometer.

This conclusion is supported by other evidence. Cox and Munk (1954) observed that the probability distribution of surface slopes was approximately Gaussian with rms surface slope less than $\tan 16°$ for wind speeds less than 14 m s^{-1}. Slopes greater than 24° have a probability for winds at 10 m s^{-1} of ~0.01. Slopes greater than 24° oriented to reflect radiation from the hull into the instrument have a probability less than 0.001.

We next consider the reflection of radiation emanating from the boom. We consider the simplest case with the water surface horizontal as shown schematically in Fig. 12. The radius, r_{bm} of the disc on the boom emitting radiation which is reflected into the radiation thermometer is

$$r_{bm} = (h_1 + h_2) \tan(\alpha/2),$$

where α is the angular field of view of the instrument (2°). Assuming that the longwave radiation is emitted isotropically, the radiative flux density on an arc of radius h_1 whose origin coincides with the center of the disc on the boom is

$$\sigma T_{bm}^4 (r_{bm}^2/h_1^2) \cos\theta,$$

where r_{bm} is the radius of the disc on the boom and θ the angle between h_1 and the normal to the disc on the boom. Therefore, the radiative flux arriving from the boom which is reflected into the radiometer is

$$\Gamma \sigma T_{bm}^4 (r_{bm}^2/h_1^2) \pi r_s^2,$$

where Γ is the reflectivity of the surface for longwave radiation, taken equal to 0.02, σ the Stefan-Boltzman constant and r_s the radius of the disc on
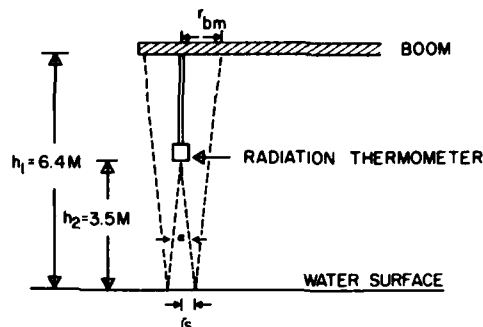
FIG. 12. Schematic diagram showing reflection of longwave radiation from the boom into the radiation thermometer.

the surface viewed by the radiation thermometer. We may then write

$$T_{sm}^4 = T_s^4 + \Gamma T_{bm}^4 (r_{bm}^2/h_1^2) \pi r_s^2,$$

where T_{sm} is the surface temperature measured by the radiometer, T_s is the true surface temperature, and we have assumed that reflected radiation from the boom is the only source of error. In estimating the error we take $T_{bm} = T_s$ because at night the boom is never colder than the dew point, which was never more than 2°C less than the surface temperature. Substituting numerical values we find that

$$T_{sm}/T_s = 1 + 4 \times 10^{-8}.$$

Taking $T_s = 287$ K, the mean for the experiment, the error is 5×10^{-5} °C which is certainly negligible in comparison to the magnitudes of the observed fluctuations in T_s and is also far below the resolution of the instrument.

We might also have considered the error due to reflected radiation from the radiation thermometer itself. It is clear that the error induced would be similarly negligible.

REFERENCES

Amos, D. E., and L. H. Koopmans, 1963: Tables of the distribution of the coefficient of coherence for stationary bivariate Gaussian processes. Sandia Corp., Monograph SCR-483, 328 pp.

Ball, F. K., 1954: Sea surface temperatures. Aust. J. Phys., 7, 649–652.

Bendat, J. S., and A. G. Piersol, 1971: Random Data: Analysis and Measurement Procedures. Wiley-Interscience, 407 pp.

Blackman, R. B., and J. W. Tukey, 1958: The Measurement of Power Spectra from the Point of View of Communications Engineering. Dover, 190 pp.

Bronson, E. D., and E. R. Glosten, 1968: Floating Instrument Platform. Scripps Institute of Oceanography, University of California, Mar. Phys. Lab. Tech. Rep., SIO Ref. No. 62-24, 23 pp.

Cooley, J. W., P. A. W. Lewis and P. D. Welch, 1967: The fast Fourier transform algorithm and its applications. Tech. Rep. RC 1743, IBM Watson Research Center, Yorktown Heights, NY, 157 pp.

Cox, C. S., and W. Munk, 1954: Statistics of the sea surface derived from sun glitter. *J. Mar. Res.*, **13**, 198–227.

Deacon, E. L., 1977: Gas transfer to and across an air-water interface. *Tellus*, **29**, 363–374.

Ewing, G., and E. D. McAlister, 1960: On the thermal boundary layer of the ocean. *Science*, **131**, 1374–1376.

Grassl, H., 1976: The dependence of the measured cool skin of the ocean on wind stress and total heat flux. *Bound.-Layer Meteor.*, **10**, 465–474.

Hasse, L., 1971: The sea surface temperature deviation and the heat flow at the sea-air interface. *Bound.-Layer Meteor.*, **1**, 368–379.

Hill, R. H., 1972: Laboratory measurement of heat transfer and thermal structure near an air-water interface. *J. Phys. Oceanogr.*, **2**, 190–198.

Jenkins, G. M., and D. G. Watt, 1968: *Spectral Analysis and Its Applications*. Holden-Day, 523 pp.

Julian, P. R., 1974: Comments on the determination of significance levels of the coherence statistics. *J. Atmos. Sci.*, **32**, 836–837.

Kinsman, B., 1965: *Wind Waves; Their Generation and Propagation on the Ocean Surface*. Prentice-Hall, 676 pp.

McAlister, E. D., 1964: Infrared optical techniques applied to oceanography, 1, Measurement of total heat flow from the sea surface. *Appl. Opt.*, **3**, 609–612.

——, and W. McLeish, 1969: Heat transfer in the top millimeter of the ocean. *J. Geophys. Res.*, **74**, 3408–3414.

Miller, A. W., Jr., and R. L. Street, 1978: On the existence of temperature waves at a wavy air-water interface. *J. Geophys. Res.*, **83**, 1353–1365.

Panofsky, H., and G. Brier, 1958: *Some Applications of Statistics to Meteorology*. The Pennsylvania State University Press, 224 pp.

Paulson, C. A., and T. W. Parker, 1972: Cooling of a water surface by evaporation, radiation and heat transfer. *J. Geophys. Res.*, **77**, 491–495.

Saunders, P. M., 1967: The temperature at the ocean-air interface. *J. Atmos. Sci.*, **24**, 269–273.

——, 1970: Corrections for airborne radiation thermometry. *J. Geophys. Res.*, **75**, 7596–7601.

Weseley, M. S., 1979: Heat transfer through the thermal skin of a cooling pond with waves. *J. Geophys. Res.*, **84**, 3696–3700.

Witting, J., 1971: Effects of plane progressive irrotational waves on thermal boundary layers. *J. Fluid Mech.*, **50**, 321–324.

Woodcock, A. H., 1941: Surface cooling and streaming in shallow, fresh and salt waters. *J. Mar. Res.*, **4**, 153–161.

The Batchelor Spectrum and Dissipation in the Upper Ocean

THOMAS M. DILLON AND DOUGLAS R. CALDWELL

School of Oceanography, Oregon State University, Corvallis, Oregon 97331

Observations of vertical temperature microstructure at ocean station P during the mixed layer experiment (Mile) indicate that the shape of the high-frequency temperature gradient spectrum depends on the relative strengths of turbulence and stratification. For low Cox number $((dT/dz)^2)/(dT/dz)^2$ the linear range of the Batchelor spectrum is not well approximated by observed spectra, while for high Cox number a remarkably close correspondence to the Batchelor spectrum is found. Dissipation rates calculated by the temperature gradient spectrum cutoff wave number method show a dramatic contrast in turbulence between low and high wind speed periods separated by only 3 hours, showing that the response of the mixed layer and transition zone to wind forcing is rapid. Some indication is found that the thermocline may also respond rapidly to surface forcing.

INTRODUCTION

Numerous comparisons of the theoretical universal temperature and temperature gradient forms predicted by *Batchelor* [1959] have been made with spectra measured in natural waters [e.g., *Grant et al.*, 1968; *Gregg*, 1976, 1977; *Nasmyth*, 1970; *Elliot and Oakey*, 1976; *Marmorino and Caldwell*, 1978]. While such measurements often compare favorably with the viscous-convective Batchelor spectrum by showing a linear range, it has seldom been possible to resolve the entire temperature gradient spectrum for a variety of reasons, including limited or unknown sensor frequency response characteristics and too much noise. When the spectrum has been resolved beyond the microstructure peak, a detailed comparison with the Batchelor spectrum has not proved favorable in certain cases [*Nasmyth*, 1970; *Elliot and Oakey*, 1976], prompting at least one investigator [*Elliot and Oakey*, 1976] to propose a different model for the high-frequency spectrum. Since the applicability of a Batchelor spectrum allows one to make an estimate of the kinetic energy dissipation rate from a temperature spectrum alone, it is important that the nature of the viscous-convective spectrum be well understood and that the universality of the Batchelor spectrum in stratified fluids be tested.

A companion paper describes a test of the hypothesis that the cutoff wave number in the spectrum is identifiable with the Batchelor wave number [*Caldwell et al.*, 1980]. The result is favorable when turbulent fluctuations are weak in comparison to the mean stratification, but because it assumes strong stratification, the test is not relevant to intense turbulence. The present paper shows that the Batchelor spectral form is followed more closely when the fluctuations are strong. It is thus plausible that the cutoff wave number is related to the Batchelor wave number in both cases and so can be used to estimate dissipation. The definitive test of the relation between the cutoff wave number and the dissipation will be direct simultaneous measures of the smallest scales of both velocity and temperature. This difficult task has not yet been accomplished, and so the present paper and its companion must be assessed as indirect evidence only, showing that the relations between the cutoff wave number, Batchelor scale, and dissipation rate are plausible and consistent.

During the Mile experiment at ocean station P (50°N, 145°W), August–September 1977, we performed a number of casts with a vertical microstructure profiling device in the surface layer and seasonal thermocline during a moderate storm

and found that the temperature gradient spectrum was almost always resolved to an easily identifiable cutoff. With this data set a test can be made of the universality of the Batchelor spectrum in natural stratified waters.

In addition, the particular meteorological conditions encountered during the microstructure casts on Julian date 244 at station P enable us to use the Batchelor scaling to address questions pertinent to mixed layer dynamics: (1) What is the time scale of response of the surface waters to surface forcing? (2) How is dissipation distributed vertically, and does the distribution vary as surface conditions change? (3) Can the vertical distribution of dissipation be associated with features of the stratification? (4) Does the upper seasonal thermocline respond significantly to surface forcing?

THEORETICAL BACKGROUND

The Batchelor spectrum of temperature gradient fluctuations in one dimension may be written [*Gibson and Schwarz*, 1963]

$$S(k) = (q/2)^{1/2} \chi_n k_n{}^{-1} D^{-1} f(\alpha) \qquad (1)$$

where k is the wave number (here in units of radians per unit length), q is a universal constant, χ_n is the temperature variance dissipation rate satisfying

$$\chi_n = 6D \int_0^\infty S(k)\, dk = 6D \left\langle \left(\frac{\partial T'}{\partial z} \right)^2 \right\rangle \qquad (2)$$

D is the molecular diffusivity, T' is a temperature fluctuation, z is depth, k_n is the Batchelor wave number $(\epsilon \nu^{-1} D^{-2})^{1/4}$, ϵ is the kinetic energy dissipation rate, ν is the kinematic viscosity, and α is a nondimensional wave number $k k_n{}^{-1}(2q)^{1/2}$. The nondimensional shape of the spectrum is given by

$$f(\alpha) = \alpha \left\{ e^{-\alpha^2/2} - \alpha \int_\alpha^\infty e^{-x^2/2}\, dx \right\} \qquad (3)$$

If an inertial subrange exists, the transition from inertial to viscous-convective behavior occurs at the wave number $k_* = C_* Pr^{-1/2} k_n$, and for wave numbers in the equilibrium range smaller than k_* the spectrum is given by

$$S(k) = \beta \chi_n \epsilon^{-1/3} k^{1/3} \qquad (4)$$

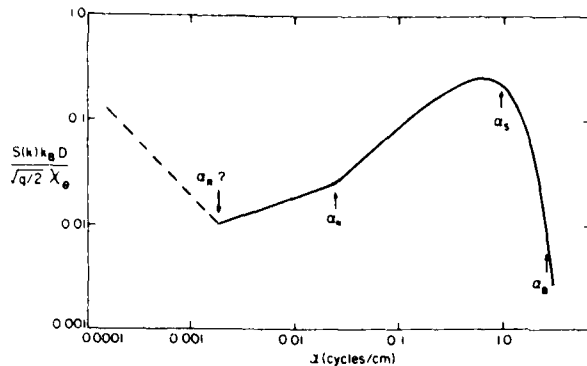Here both C_* and β are universal constants, and Pr is the Prandtl number ν/D.

Fig. 1. Nondimensional universal spectrum with a 'fine structure' range for $\alpha < \alpha_R$, the Richardson wave number; an inertial subrange for $\alpha_R < \alpha < \alpha_*$; and a viscous-convective Batchelor spectrum for $\alpha > \alpha_*$. The positions of the Kolmogorov wave number α, and Batchelor wave number α_B are determined by choice of the universal constant q ($2(3)^{1/2}$ assumed here), while the shape of the spectrum for $\alpha > \alpha_*$ is independent of universal constants. The inertial subrange is rarely observed in vertical microstructure.

Nondimensionalizing the spectrum by the Batchelor scale k_B and χ_θ yields the equilibrium range spectrum (Figure 1)

$$S(k)\left\{(q/2)^{1/2}\frac{\chi_\theta}{k_B D}\right\}^{-1} = f(\alpha) \qquad \alpha \geq \alpha_* \tag{5}$$

$$S(k)\left\{(q/2)^{1/2}\frac{\chi_\theta}{k_B D}\right\}^{-1} = 2^{1/3}Pr^{-1/3}\beta q^{-2/3}\alpha^{1/3} \qquad \alpha_R < \alpha < \alpha_* $$

where $\alpha_* = C_* Pr^{-1/2}(2q)^{1/2}$ and α_R marks the wave number at which the fine structure and internal wave effects become appreciable. Continuity at k_* establishes the relation between q, β, and C_* as [Williams and Paulson, 1977]

$$\beta = qC_*^{2/3} \tag{6}$$

Gibson [1968] advanced a theoretical argument that $3^{1/2} < q < 2(3)^{1/2}$; Grant et al. [1968] estimated $q = 3.9 \pm 1.5$ and $C_* = 0.024 \pm 0.008$ (standard error estimates). Williams and Paulson [1977] found from inertial subrange measurements in air that $\beta \simeq 0.5$ and noted a small but definite dependence of β upon Reynolds number. The atmospheric measurements of β are surely more accurate than one could reasonably expect from marine measurements, and there is no reason to expect inertial subrange parameters such as β to depend on Prandtl number. If q is $2(3)^{1/2}$ and β is 0.5, C_* becomes 0.055, twice as large as the value found by Grant et al. [1968] and substantially larger than the values 0.03 and 0.04 found by Gibson et al., [1970] but only half the value of 0.1 estimated by Gibson and Schwarz [1963] from laboratory measurements. There is thus a large uncertainty regarding the value of C_*.

If dissipation rates are to be estimated from the cutoff frequency of the Batchelor spectrum, q is the only relevant universal constant. A percentage error in q is reflected as a systematic error twice as large in ϵ. This error may not be as large as that resulting from direct high-frequency velocity determinations of ϵ in water and will not affect relative measures of ϵ, so that depth variability can be assessed without error from this source.

Although the Batchelor spectrum was proposed for homogeneous, locally isotropic turbulence in an unstratified fluid with large Prandtl number, it is clear, in contrast to inertial subrange turbulence, that the spectral form is not an asymptotic limit of high Reynolds number turbulence. Batchelor

[1959] suggests that even when the Reynolds number is so small that an inertial subrange does not exist, the Batchelor form may be found.

The effect of stratification on the Batchelor spectrum, however, has not been explored. In natural waters (Prandtl number of the order of 10), temperature fluctuations are usually caused by turbulent stirring in the presence of a mean gradient. The level of turbulence relative to the stratification is likely to be important in determining the scale at which local isotropy is approached and in determining whether or not a Batchelor spectrum is found.

A measure of the turbulence relative to the stratification may be constructed in the form of a 'stratification Reynolds number' $R_s = U l \nu^{-1}$, where U is estimated as $\epsilon^{1/3}l^{1/3}$ [Tennekes and Lumley, 1972] and the length scale is estimated as the Richardson length $l = \epsilon^{1/2}N^{-3/2}$, where N is the local buoyancy frequency. Thus R_s reduces to $(\epsilon\nu^{-1})N^{-2}$, a squared ratio of time scales of the turbulence and stratification. If ϵ is estimated by the Cox number $Cx = \langle(dT'/dz)^2\rangle/(dT/dz)^2$ and N [Caldwell et al., 1980], ϵ is proportional to DN^2Cx, so that R_s is proportional to $Pr^{-1}Cx$. We might therefore expect that the approach to the Batchelor spectrum in a stratified natural fluid would depend on the Cox number.

We imagine that for small Cox number (turbulence weak compared to the stratification), small-scale temperature features which are possibly remnants of the mean stratification may exist at wave numbers large enough to coincide with wave numbers in the viscous-convective subrange and alter the low wave number portion of the Batchelor spectrum. A similar situation was hypothesized by Gregg [1977], who, upon examining spectra from the main oceanic thermocline, which somewhat resembled the Batchelor spectrum but failed to reveal a distinct linear range, supposed that the low wave number viscous-convective spectrum was 'contaminated' by the fine structure–internal wave spectrum.

In the remainder of this work, following a brief experimental description, we report that for large Cox number in the oceanic surface layer the Batchelor spectrum closely approximates observed spectra. For smaller Cox number the observed spectra depart significantly from the Batchelor form, showing a broader, less peaked shape. We then present depth profiles of dissipation calculated by the cutoff wave number technique and compare profiles taken during low and high winds.

EXPERIMENTAL DESCRIPTION

The vertical microstructure profiles to be discussed here were collected at ocean station P during August–September 1977 as part of the Mile experiment. The microstructure profiler used was a small, winged, nearly freely falling device similar to that described by Caldwell et al. [1975]. The fall rate is adjustable; for these runs it was set at 10 cm s^{-1}. The probe carried two thermistors, a Neil Brown conductivity sensor, and a pressure sensor. The data were transmitted to the ship through a small-diameter (1.6 mm) cable containing four pairs of expendable bathythermograph (XBT) wire sheathed in a Kevlar strength member and coated with syntactic foam; the foam density is adjusted so that the entire cable has a slight tendency to sink.

One thermistor was redundantly amplified, and the two signals were sent to the surface through different wires, where it was again amplified, differentiated, filtered with a 12-pole Butterworth filter (3-dB frequency set at 30 Hz), and then digitized and recorded at a rate of 90 s^{-1}. Since most of the noise
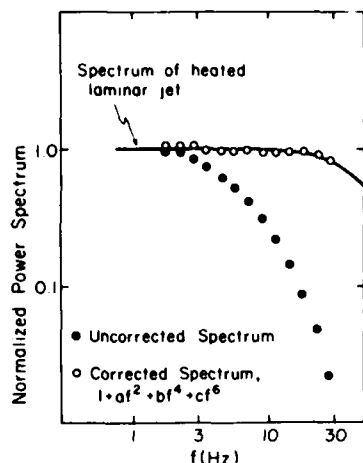
Fig. 2. Frequency response of the P-85 thermistor as determined by passing the thermistor through a heated laminar jet at 10 cm s^{-1}; $a = 2.6352 \times 10^{-2}$, $b = -2.1897 \times 10^{-5}$, and $c = 3.2556 \times 10^{-7}$.

content of the temperature signals originated in the first stage amplifier, these noise sources were incoherent on the two channels. A calculation of the in-phase power [Caldwell et al., 1969] allowed a significant reduction in noise level to be made. A second thermistor was differentiated inside the probe rather than at the surface but otherwise preprocessed in a manner similar to the first. The conductivity was sent to the surface on the remaining XBT pair, and the pressure signal was transmitted in frequency-modulated form in the range 500–1300 Hz.

The frequency response of the thermistors (Thermometrics P-85) was determined by a test similar to the Fabula test [Fabula, 1968], using for the plume a laminar jet emitted from 0.30 × 12.7 mm nozzle. The velocity of the jet was 2–3 cm s^{-1} at the height where the probe, moving at 10 cm s^{-1}, passed through. A detailed map of the jet revealed a nearly Gaussian temperature distribution with a spectral power 3 dB in wavelength of 1.9 mm. The frequency response, which substantially agrees with a similar test performed by M. C. Gregg (personal communication, 1979) on another P-85, could not be well described by either single or double pole response functions; for computational purposes, a power series in even powers of frequency up to the sixth power was used instead. It describes the response to 30 Hz with 3% standard error (Figure 2).

The data were collected on Julian date 244, 1977, between the hours 0500 and 1200 UT in the midst of a moderate storm (maximum sustained wind speeds of 16 m s^{-1}). This was the second storm encountered during the Mile experiment. The low-pressure center of the storm passed directly over station P, and a dramatic change in wind speed (Figure 3) was noted, along with a reversal of wind direction, at 0200 hours. Casts during the earlier part of the sampling period, when winds were low, show markedly less activity in the surface layer and thermocline than later casts in higher winds [Dillon and Caldwell, 1977], showing a rapid response of the upper waters to increasing wind stress. We sampled, in a short period of time, water with greatly different levels of turbulence relative to the mean stratification.

COMPUTATIONAL TECHNIQUES

A nondimensional form of the high-frequency gradient spectrum may be determined if both χ_θ and ϵ are known. If

the observed spectrum is well resolved, χ_θ may be found by integrating the spectrum. Without simultaneous high-frequency velocity measurements, ϵ cannot be measured directly. An estimate of the dissipation rate can be made from the spectrum if the transitional wave number $k_\ast$ can be determined. This technique is of limited applicability, however, because spectra exhibiting unambiguous transitions from the inertial to the viscous-convective subrange are found in only a few of the casts. We believe that this is so because the low wave numbers of the inertial subrange spectrum can be seen only in thick sections of the water column. The turbulence properties in such a thick section may change with depth, causing the observed spectrum to be nonstationary. These low wave numbers may also be contaminated by the fine structure–internal wave spectrum [Gregg, 1977].

If the entire spectrum has been resolved, a high wave number normalization can be used. Suppose that the fluid is turbulent and the signal is well above noise. Then the gradient spectrum will exhibit a peak of some sort followed by a very rapid roll-off. First, we calculate χ_θ by integration; then we define a cutoff wave number k_c as the wave number at which the spectrum falls to some fraction, say, one tenth, of its peak value. If the Batchelor spectrum does obtain, k_B will be some fraction (which depends on the value of q assumed) of k_c. Wave numbers are then nondimensionalized by $k_B^{-1}(2q)^{1/2}$, and the spectrum $S(k)$ is nondimensionalized by $(q/2)^{1/2} \chi_\theta k_B^{-1} D^{-1}$. Note that while the particular value of k_B (and also $\epsilon_B = k_B^4 \nu^{-1} D^{-1}$) depends on q, the shape of the nondimensionalized spectrum is independent of q. A number of such nondimensionalized spectra may then be ensemble-averaged and compared to the Batchelor spectrum. This comparison will be independent of the particular value used for q.

A slightly improved technique is to find the cutoff wave number k_c (and hence k_B and ϵ_B) by performing a nonlinear weighted least squares fit to the Batchelor spectrum. The weighting used corresponds to the degrees of freedom of the band-averaged spectral estimates [Otnes and Enochson, 1972]; hence the high-frequency roll-off portion of the spectrum is much more heavily weighted (by a factor of 25–50) than the lower-frequency, prepeak linear region of the spectrum. In
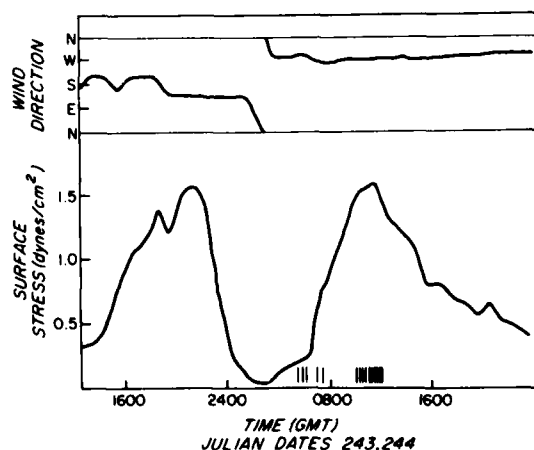

Fig. 3. Surface stress and wind direction during the second significant storm encountered during the Mile experiment. Wind speed dropped to near zero, and wind direction changed as the low-pressure storm center passed over station P. Times of the five microstructure drops during light winds and the 10 drops during storm winds are indicated as vertical bars on the lower portion of the figure.
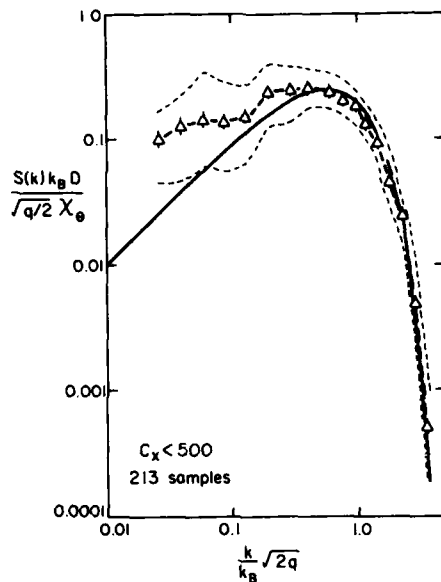
Fig. 4. Ensemble-averaged nondimensional spectrum for Cox numbers less than 500. The lower wave number portion of the spectrum departs significantly from the Batchelor spectrum (solid curve). Error bars are the standard error of the mean based on the standard deviation. The dashed envelope shows the average positive and negative deviation from the mean; that is, half of the spectral estimates lie within the envelope. Thus although the mean of the spectral values has a small uncertainty (the bars), the estimates in an individual spectrum may lie quite far from the mean.

addition, since the spectrum rolls off so rapidly, the fitting procedure will be very sensitive to the slope of the spectrum in the cutoff range of wave numbers and insensitive to the spectral estimates at low, prepeak wave numbers.

After performing the high-frequency normalization and en-
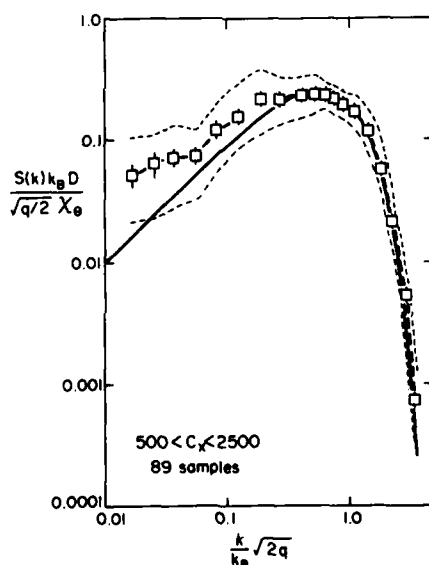
Fig. 5. Ensemble-averaged nondimensional spectrum for intermediate Cox numbers. The low wave number portion of the spectrum is closer to the Batchelor spectrum than the low Cox number spectrum but still is significantly different. Thus although the mean of the spectral values has a small uncertainty (the bars), the estimates in an individual spectrum may lie quite far from the mean.
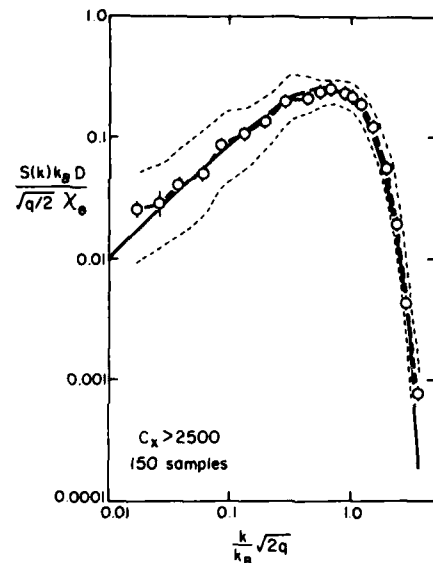
Fig. 6. Ensemble-averaged nondimensional spectrum for large Cox numbers. The low wave number portion of the spectrum is in remarkably close agreement with the Batchelor spectrum. Thus although the mean of the spectral values has a small uncertainty (the bars), the estimates in an individual spectrum may lie quite far from the mean.

semble averaging groups of spectra we will know that we have found a Batchelor form if the low wave number region of the ensemble average agrees with the linear region of the Batchelor spectrum. The high wave number roll-off region is constrained by the fit to follow the Batchelor spectrum as well as it may, but the low wavenumber region is not.

To minimize vertical intermittency, the data were broken into 512 point segments (~60 cm). (Even for these thin samples, however, there is no guarantee that the turbulence is homogeneous throughout the segment.) A Gaussian window was applied to each segment to reduce spectral leakage, and a fast Fourier transform was applied. After band averaging, the spectral estimates were corrected for thermistor attenuation. Only fully resolved spectra are included in this paper; a spectrum was operationally defined as 'resolved' if it fell to 10% of its peak value and was still above noise levels before the 3-dB frequency (30 Hz) of the analogue filter was reached. Approximately 90% of the spectra in the surface layer met this criterion.

SPECTRAL SHAPES

Nondimensional spectra from all surface layer runs on Julian day 244 were grouped together in ranges of Cox number for comparison to the Batchelor form (the surface layer was defined as the region of temperature within $0.25°$ C of the surface value). Spectra with low Cox numbers were markedly different from those with a high Cox number. The low Cx spectra ($Cx < 500$) characteristically exhibit a broad maximum before roll-off and do not agree well with the Batchelor form in the linear range (Figure 4). Spectra with higher values of Cx progressively approach the Batchelor spectrum at low wave number (Figure 5), and for $Cx > 2500$ the low-frequency fit to the Batchelor form is quite remarkable (Figure 6).

The same trend of the averaged spectra to approach the Batchelor spectrum is found if they are grouped by R, =

when compared with either systematic errors or the variability found in the upper waters. Another random error, associated with violation of Taylor's hypothesis due to possibly large turbulent intensity [*Lumley*, 1965], may cause a 40% overestimate of ϵ_B for intense turbulence. Surface wave orbital velocity may also introduce an uncertainty in the estimate of ϵ_B, for while the microstructure profiler responds well to vertical velocities at surface wave frequencies [*Dillon and Caldwell*, 1980], its response to a fluctuating horizontal velocity field is unknown. An imperfect response would cause fluctuations in the angle of attack of the sensor and deviations from the constant value assumed for application of the Taylor hypothesis (T. R. Osborn, personal communication, 1979). Systematic error in all estimates of ϵ_B results from uncertainty in the universal constant q. While this does not affect comparisons of the dissipation (Figure 9), it may be the major source of error in computing volume averages of the total mixed layer dissipation.

Another source of error pertinent to volume averages lies in the fact that an estimate of ϵ_B in intermittent turbulence is biased toward the larger values. This may be seen by considering the extreme hypothetical case of a 60-cm segment which contains a turbulent core with a vertical scale of a few centimeters surrounded by nonturbulent water. In this case the turbulent core would completely determine the cutoff wave number, but an ϵ_B computed from this should not be taken as being typical of the entire 60-cm segment. An attempt to delineate such regions of turbulent and nonturbulent fluid within a segment would be a painstaking and highly subjective task, possibly subject to interpretational errors as severe as imputing the single value of ϵ_B to the entire segment. Such circumstances may occur in the seasonal thermocline, so that caution should be used in volume averaging in highly stratified and intermittent regions.

Since most of these uncertainties are impossible to assess at this time, we choose to place no error estimate on ϵ_B and simply caution the reader that large uncertainties exist. It should be noted, however, that the conclusions of this study are based upon vertical variations in ϵ_B of an order of magnitude or more and so are independent of the above uncertainties.

CONCLUSIONS

1. The observed viscous-convective subrange spectrum of temperature gradients approaches the Batchelor spectrum as the Cox number increases. For low Cox number the spectrum is broader and flatter than the Batchelor spectrum.

2. Kinetic energy dissipation rate profiles as inferred from the spectral cutoff wave number are highly intermittent, and values grow larger with increasing wind. The response to surface forcing occurs on time scales comparable to the time scales of the forcing.

REFERENCES

Batchelor, G. K., Small-scale variation of convected quantities like temperature in turbulent fluid, *J. Fluid Mech.*, 5, 113–133, 1959.

Caldwell, D. R., F. E. Snodgrass, and M. H. Wimbush, Sensors in the deep sea, *Phys. Today*, 22(7), 34–42, 1969.

Caldwell, D. R., S. D. Wilcox, and M. Matsler, A relatively simple freely-falling probe for small-scale temperature gradients, *Limnol. Oceanogr.*, 20, 1035–1047, 1975.

Caldwell, D. R., T. M. Dillon, J. M. Brubaker, P. A. Newberger, and C. A. Paulson, The scaling of vertical temperature gradient spectra, *J. Geophys. Res.*, 85, this issue, 1980.

Dillon, T. M., and D. R. Caldwell, Temperature microstructure profiles at ocean station P: Preliminary results from the Mile experiment, *Ref. 77-22*, 215 pp., Sch. of Oceanogr., Oreg. State Univ., Corvallis, 1977.

Dillon, T. M., and D. R. Caldwell, Catastrophic events in a surface mixed layer, *Nature*, 276, 601–602, 1978.

Dillon, T. M., and D. R. Caldwell, High-frequency internal waves at ocean station P, *J. Geophys. Res.*, 85, in press, 1980.

Elliott, J. A., and N. S. Oakey, Spectrum of small-scale oceanic temperature gradients, *J. Fish. Res. Bd. Can.*, 33, 2296–2306, 1976.

Fabula, A. G., The dynamic response of towed thermistors, *J. Fluid Mech.*, 34, 449–464, 1968.

Gibson, C. H., Finestructure of scalar fields mixed by turbulence, 1, 2, *Phys. Fluids*, 11, 2305–2327, 1968.

Gibson, C. H., and W. H. Schwarz, The universal equilibrium spectra of turbulent velocity and scalar fields, *J. Fluid Mech.*, 16, 365–384, 1963.

Gibson, C. H., R. R. Lyon, and I. Hirschsohn, Reaction product fluctuations in a sphere wake, *AIAA J.*, 8, 1859–1863, 1970.

Grant, H. L., B. A. Hughes, N. M. Vogel, and A. Moilliet, The spectrum of temperature fluctuations in turbulent flow, *J. Fluid Mech.*, 34, 423–442, 1968.

Gregg, M. C., Finestructure and microstructure observations during the passage of a mild storm, *J. Phys. Oceanogr.*, 6, 528–555, 1976.

Gregg, M. C., Variations in the intensity of small-scale mixing in the main thermocline, *J. Phys. Oceanogr.*, 7, 436–454, 1977.

Lumley, J. L., Interpretation of time spectra measured in high-intensity shear flows, *Phys. Fluids*, 8(6), 1056, 1965.

Marmorino, G. O., and D. R. Caldwell, Temperature finestructure and microstructure observations in a coastal upwelling region during a period of variable winds (Oregon, summer 1974), *Deep Sea Res.*, 25, 1073–1106, 1978.

Nasmyth, P. W., Oceanic turbulence, Ph.D. thesis, 69 pp., Inst. of Oceanogr., Univ. of B. C., Vancouver, 1970.

Niiler, P. P., and E. B. Kraus, One dimensional models of the upper ocean, in *Modelling and Prediction of the Upper Layers of the Ocean*, edited by E. B. Kraus, Pergamon, New York, 1977.

Otnes, R. K., and L. Enochson, *Digital Time Series Analysis*, 467 pp., John Wiley, New York, 1972.

Schedvin, J. C., Microscale measurements of temperature in the upper ocean from a towed body, Ph.D. thesis, Univ. of Calif. at San Diego, La Jolla, 1979.

Tennekes, H., and J. L. Lumley, *A First Course in Turbulence*, 300 pp., MIT Press, Cambridge, Mass., 1972.

Turner, J. S., *Buoyancy Effects in Fluids*, 367 pp., Cambridge University Press, New York, 1973.

Williams, R. M., and C. A. Paulson, Microscale temperature and velocity spectra in the atmospheric boundary layer, *J. Fluid Mech.*, 82, 547–567, 1977.

The Scaling of Vertical Temperature Gradient Spectra

D. R. Caldwell, T. M. Dillon, J. M. Brubaker,
P. A. Newberger, and C. A. Paulson

School of Oceanography, Oregon State University, Corvallis, Oregon 97331

Tests of a formula derived for the cutoff wave number of vertical temperature gradient spectra, using data taken in the upper layers of the North Pacific, show encouraging results. To derive this formula, the cutoff wave number is assumed to be the Batchelor wave number, with kinetic energy dissipation calculated by combining a form used in the atmosphere for calculating the vertical eddy diffusivity in terms of the dissipation with the Osborn-Cox formula for calculating eddy diffusivity from the variance of the temperature gradient spectrum. Kinetic energy dissipation in the water column can be determined in this way; a vertical profile of dissipation shows values of the order of 10^{-3} cm^2 s^{-3} at the base of a storm-tossed mixing layer. In the thermocline below, dissipation occurs in patches.

1. Introduction

Measurements of small-scale temperature gradients from freely falling instruments, a technique pioneered by C. S. Cox [*Gregg and Cox*, 1971], have been performed in a number of locations in the ocean by various investigators [e.g., *Osborn and Cox*, 1972; *Gregg et al.*, 1973; *Gregg*, 1975, 1976, 1977a, 1977b; *Elliott and Oakey*, 1975, 1976; *Caldwell*, 1976, 1978; *Marmorino and Caldwell*, 1978a, 1978b; *Caldwell et al.*, 1978; *Dillon and Caldwell*, 1978]. Interpreting these data has been difficult because of doubt as to whether the full variance of the gradients has been correctly resolved and also because of the lack of an accepted paradigm for the interpretation. The universal turbulence scaling proposed by *Batchelor* [1959] for unstratified flows has been a tempting model, but it has never been shown that this scaling is appropriate in the ocean, which is usually stratified and which is subject to other complicating influences such as surface and internal wave fields.

Confirmation of the Batchelor prediction has been looked for with some success in the laboratory [*Gibson and Schwarz*, 1963] and in a tidal flow [*Grant et al.*, 1968]. In each of these experiments, problems with resolution or noise at the high-frequency end of the spectrum prevented full resolution of the diffusive subrange. In the atmosphere the diffusive limit has been resolved [*Gibson et al.*, 1970; *Williams and Paulson*, 1977], but there the spectral form is quite different from its form in the ocean because of the lower Prandtl number of air.

One attempt to match temperature spectra from a towed body with the Batchelor form failed [*Nasmyth*, 1970], probably because of the procedure followed, which was to force a fit at wave numbers well below the cutoff and then look for coincidence at high wave numbers. The difficulty may lie in the lower reliability of the low wave number points in the usual spectral band-averaging scheme or in the assumption that all of the signal at these frequencies represents turbulence. *Gibson et al.* [1974] suggested the use of a number of features of the universal form in interpreting records from a towed body and found resemblance to the Batchelor form in their spectra [*Gibson et al.*, 1974, Figure 5].

The most recent analyses of vertical temperature gradient spectra are those of *Gregg* [1977b] and *Elliott and Oakey* [1976]. *Elliott and Oakey* [1976] chose as a model for their data analysis a series of temperature steps, each spreading by diffusion. This assumption led them to a dependence of en-

ergy on the vertical wave number k as exp $(-k^2)$, the same dependence as that in the cutoff of the Batchelor form. They take the mean time since step formation, t, as an adjustable parameter found for each set of data. If the assumption is made that their spectra follow the Batchelor form, values of kinetic energy dissipation ϵ can be calculated from their values of t ($\epsilon = \nu t^{-2}$, where ν is the kinematic viscosity). Values of ϵ calculated in this manner range, quite reasonably, from 2×10^{-5} to 5×10^{-4} cm^2 s^{-3} for various casts. Thus there is nothing in their results inconsistent with an interpretation in terms of the Batchelor spectrum.

Gregg's conceptual picture is of a spectrum composed of (1) the signature of internal waves and 'fine structure' which dominates at low wave numbers (<0.02 cycles cm^{-1}) and (2) 'microstructure' at higher wave numbers, the source of which is uncertain. Figure 18 of *Gregg*'s [1977b] paper illustrates this idea, and an analysis based on it shows a high wave number peak similar to the Batchelor spectrum [*Gregg*, 1977b, Figure 16], although he does not choose to interpret it so. In the present work we use his concepts for interpreting the spectra, but we treat the data somewhat differently and attempt to test quantitatively the hypothesis that Batchelor scaling describes vertical temperature gradient spectra for the highest wave numbers.

We propose a scaling of the wave number k_c at which the energy in the spectrum has decreased to 12% of its value in the microstructure peak and use data obtained by dropping a freely falling instrument through surface layer, thermocline, and halocline in the North Pacific to test this scaling. We chose 12% because the Batchelor spectrum falls to this percentage of its peak value at the Batchelor wave number if $q = 2.2$ [*Williams and Paulson*, 1977].

In a companion paper [*Dillon and Caldwell*, 1980] the hypothesis that the shape of the vertical temperature gradient is similar to that of the Batchelor spectrum is examined. The reader should refer to it for more experimental detail and more discussion of the form and parameters of the spectrum.

2. The Proposed Scaling

Lilly et al. [1974] and *Weinstock* [1978] proposed for vertical eddy diffusivity in stably stratified flows a relation which, in Weinstock's form, is

$$K_z = 0.8\epsilon/N^2 \qquad (1)$$

where N is the buoyancy frequency and K_z is a vertical eddy diffusivity. If we combine this with the *Osborn and Cox* [1972]
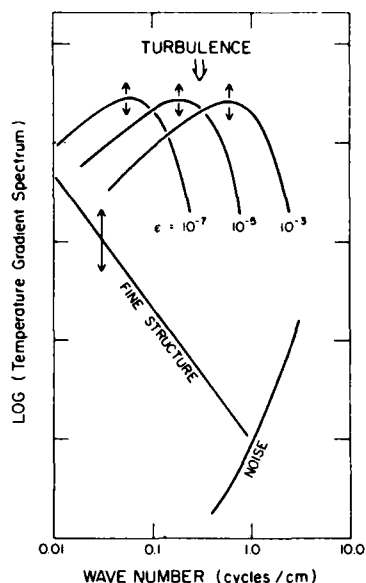
Fig. 1. Schematic of interpretation of spectra. The 'Fine structure' contribution has been plotted as $k^{-3/2}$. Both k dependence and level vary widely. The 'turbulence' contribution is placed in wave number by the value of ϵ, but its position vertically on this plot depends on mean gradient and Cox number as well. The 'noise' contribution is shown as modified by the thermistor response correction. Its position varies with drop speed only.

formula for obtaining eddy diffusivities from vertical temperature gradient data,

$$K_z = D \cdot Cx \tag{2}$$

where $Cx \equiv \langle (dT/dz)^2 \rangle / \langle dT/dz \rangle^2$ is the Cox number and D is the thermal diffusivity, we can solve for ϵ to obtain

$$\epsilon = (1/0.8)N^2 D Cx \tag{3}$$

All quantities on the right-hand side are available to us from vertical temperature and conductivity profiles if the variance of dT/dz is completely resolved. If next we insert this expression for ϵ in the formula for the Batchelor wave number (wave numbers are herein defined as the reciprocals of wavelengths), we obtain

$$k_B \equiv \frac{1}{2\pi} \left(\frac{\epsilon}{\nu D^2} \right)^{1/4} = \frac{1}{2\pi} \left(\frac{N^2 Cx}{0.8 \nu D} \right)^{1/4} \tag{4}$$

The hypothesis that we shall test is that the experimentally determined values of the cutoff wave number k_c are related to this formulation of k_B; conceivably, the two might be identical.

3. THE DATA

The freely falling instrument used was similar to one previously described [Caldwell et al., 1975]. Slowed by helicopter-type wings, it descends at a speed adjustable from 5 to 25 cm s^{-1}. Signals from thermistors in the nose (bottom) of the instrument and from a pressure sensor are transmitted through a data link to the ship and are processed and recorded on digital magnetic tape with a 45-Hz Nyquist frequency. The records used to compute temperature gradient spectra were processed by a 12-pole Butterworth low-pass filter with a 30-Hz 3-dB point and were time-differentiated before digitizing and recording. Frequency spectra were calculated, corrected for ther-

mistor and electronics transfer functions, and then translated to vertical wave number spectra by use of the drop speed determined from the pressure sensor record.

A conductivity sensor (Neil Brown), also mounted on the nose of the instrument, was used to derive salinities, densities, and buoyancy frequencies, especially in the halocline.

Let us consider what we expect to be able to see with such an instrument as it falls through the water column. Fall speeds must be slow enough to allow the temperature sensor to respond to the very thinnest temperature gradient to resolve fully the temperature gradient spectrum. For the data to be used in this paper the fall rate was 10 cm s^{-1}, and the 3-dB frequency response of the thermistors was about 7 Hz so that in terms of vertical wave numbers the 3-dB point is 0.7 cycles/cm^{-}. According to the Batchelor model, the value of ϵ corresponding to a cutoff wave number of 0.7 cycles cm^{-1} is approximately 2×10^{-5} cm^2 s^{-3}. Therefore to resolve spectra extending to the Batchelor wave number, the data must be corrected for transducer response if ϵ is larger than 2×10^{-5}
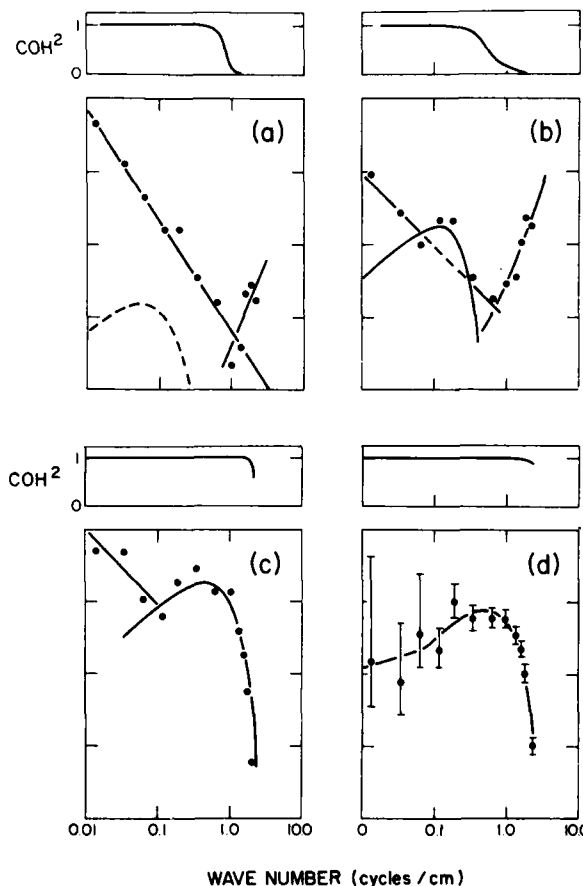
Fig. 2. Examples of observed spectra. Here 512 points at 90 points per second are used, Gaussian windowed. Two signals from the thermistor are amplified and recorded separately, so the coherence between them, shown above each spectrum, discriminates signal from noise (because the noise source lies mainly in the amplifiers). All data were recorded on August 23 in 18 m s^{-1} winds: (a) 51-m depth, turbulence level so low that fine structure dominates, noise shows up at right; (b) 54-m depth, all three components at comparable levels, turbulence just visible; (c) 40-m depth, turbulence signal dominates noise, fine structure just visible at left; (d) 32-m depth, only the turbulence signal is visible. The 95% confidence limits in Figure 2d apply to Figures 2a–2c also.
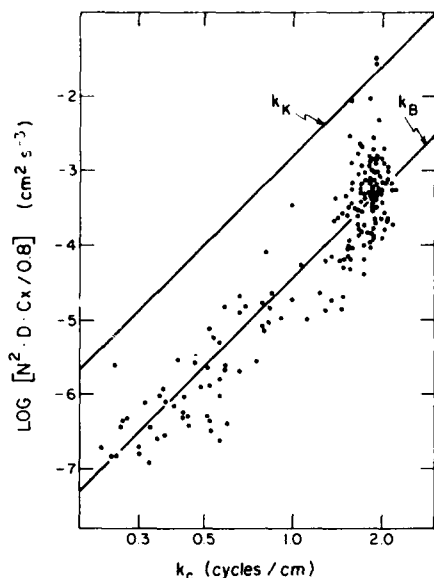
Fig. 3. Kinetic energy dissipation calculated as prescribed versus wave number k_c at which the spectrum has fallen to 12% of its peak value. The points come from the lower mixed layer and the thermocline on one cast on August 23, 1977. Lines are drawn to represent the Kolmogorov (k_k) and Batchelor (k_B) wave numbers.

cm^2 s^{-3}. Since the signals are low passed at 30 Hz before recording to suppress 60-Hz interference, the highest wave number accessible to us at the 10 cm s^{-1} descent rate is 3 cycles cm^{-1}, corresponding to an energy dissipation of 3.5×10^{-3} cm^2 s^{-3}. A lower bound on the wave numbers at which the turbulence signal can be seen is set by the background spectrum due to other causes, which dominates at low frequency. This varies, but the lowest resolvable value of ϵ is often approximately 10^{-7} cm^2 s^{-3} in the thermocline. The situation is therefore that the signal at the Batchelor wave number, if present can be seen in these records for $10^{-7} < \epsilon < 2 \times 10^{-5}$ cm^2 s^{-3} with no corrections for thermistor response and to 3.5 $\times 10^{-3}$ cm^2 s^{-3} with correction.

Because the fluctuations encountered by the instrument as it descends are often seen by the thermistor as being near the highest frequencies that it can resolve, it must be established that the cutoffs seen in the spectra represent the high wave number limit of fluctuations present in the water column
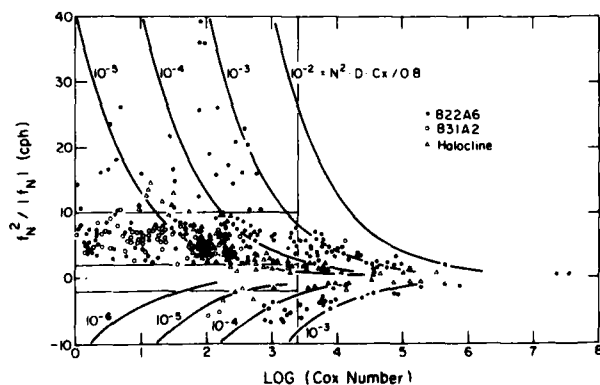
Fig. 4. Loci of all data used, in (f_N, Cx) space. The vertical scale is chosen to be linear in f_N, imaginary values of f_N appearing as negative numbers.
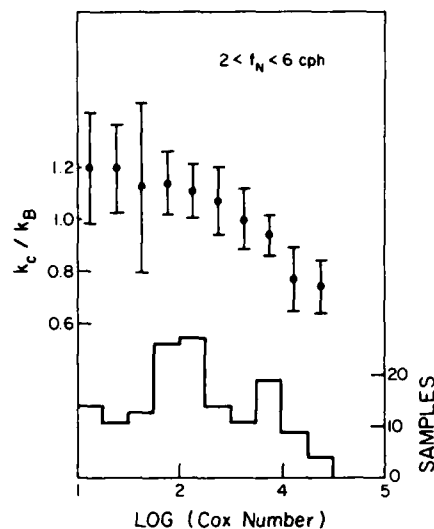
Fig. 5. Ratio of observed cutoff wave number to Batchelor wavenumber versus Cox number for $2 < f_N < 6$ cph. The number of samples averaged into each band is given. The error bars shown are 95% confidence limits.

rather than being caused by some instrumental effect. The reader is referred to the companion paper [*Dillon and Caldwell*, 1980] for a more detailed discussion of the shapes of these spectra and the method used to determine them, in particular for a description of the determination of the thermistor's frequency response correction. Without repeating the details given there we can list three reasons why this cutoff must be a property of the water column:

1. The correction used for frequency response, originally determined by comparison of data from a thermistor of the
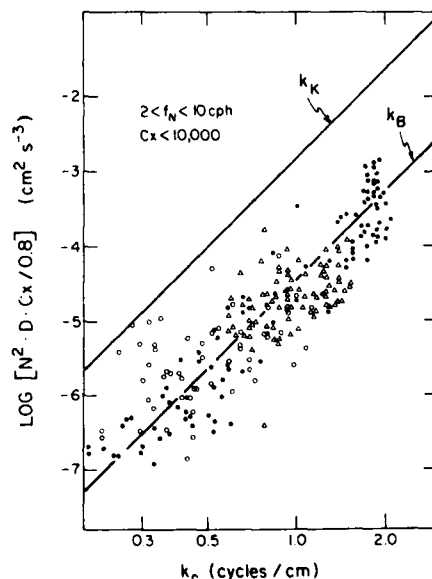
Fig. 6. Dissipation calculated as prescribed versus cutoff wave number. Cases with Cox number less than 10^4 and f_N between 2 and 10 cph are included. The data are those of Figure 4 (solid circles), together with data from the mixed layer on September 1 in 14 m s^{-1} winds (triangles) and data from various casts through the halocline (open circles). Lines are drawn to represent the Kolmogorov (k_k) and Batchelor (k_B) wave numbers.

TABLE 1. Results of Applying Regression Models of the Form $10^a f_N{}^b Cx^c$ to Cases for Which $f_N > 2$ cph, $Cx < 2500$

Model	a	b	c	E^2	F_i	F_1
1	−0.971	0.50	0.25	0.0188	38	
2	−0.92 ± 0.07	0.50	0.25	0.0164	3	−31
3	−0.97 ± 0.07	0.57 ± 0.07	0.25 ± 0.02	0.0162		
4	−0.47 ± 0.05	0.00	0.22 ± 0.03	0.0349	276	
5	−0.44 ± 0.11	0.43 ± 0.13	0.00	0.0609	659	
6	−0.98 ± 0.05	0.57 ± 0.07	0.25	0.0161	−1	
7	−0.91 ± 0.03	0.50	0.24 ± 0.02	0.0164	3	

*Values of a, b, and c with error limits are determined form the data. Other values of a, b, and c are assumed. The errors given are 95% confidence limits. E^2 is the mean square deviation relative to each model. F_i is the standard statistical parameter F calculated for each model relative to model 3, and F_1 is the value of F relative to Model 1. A value of F of 3 or greater corresponds to a chance of less than 1% that the mdoels are not significantly different; 242 samples are included, 68% of the total data set.

same model with data obtained simultaneously from a thermocouple with much faster response, is described in the appendix. A redetermination in the laboratory [*Dillon and Caldwell*, 1980] confirmed this correction with the required errors (see discussion below). A slightly different test performed by M. C. Gregg (personal communication, 1979) gave similar results. Therefore considerable confidence can now be placed in the correction.

2. In many of the determinations of the cutoff wave number the frequencies were well below those at which any correction is required according to these tests, and no systematic difference was seen between these and higher-frequency data.

3. The effect of the estimated error in this correction on the hypothesis test made in this paper is not significant, as is shown in the appendix. Even a much larger error would not change the conclusions.

These data were obtained on the mixed layer experiment (Mile) cruise in August 1977 at 50°N, 145°W (ocean station P) on board the R/V *Oceanographer*. For the present work only a few of the 381 microstructure profiles obtained are considered. One cast (822A6) through surface layer and thermocline during 18 m s^{-1} winds, one cast through the surface layer in lighter (14 m s^{-1}) winds in a latter storm (831A2), and a collection of data taken at various times in the halocline at 100–130 m are used. Thus the hydrographic regions sampled include active mixing layers at several wind speeds, the thermocline (35–62 m), and a temperature inversion well stabilized by its salt gradient.

4. PROCEDURE

Spectra were calculated for record segments spanning approximately 60 cm in the vertical, comprising 512 points recorded at the rate of 90 s^{-1}. A Gaussian window was applied to each segment before the Fourier transform was performed. Such thin sections were used to make certain that conditions would not change too much within the segment, particularly

the buoyancy frequency and the dissipation. In our interpretation the observed spectra result from the superposition of three separate components: fine structure, turbulence, and noise (Figure 1). We imagine the fine structure component to be due to the basic shape of the temperature profile, the straining of the temperature profile by internal waves, and the remnants of mixing events of medium scale. As judged from the spectra that it dominates, the spectral values usually fall as (wave number)^n, with n in the range −1 to −2. It dominates in parts of the thermocline where stratification is strong and turbulence is weak (Figure 2a). The noise spectrum has the form (frequency)^1 before differentiation of the signal and correction for thermistor response; after differentiation, correction, and translation to wave number it increases with wave number as $k \cdot [1 + (S_D k/f_1)^2]$, where s_D is the drop speed and f_1 the 3-dB frequency of the correction filter. Noise dominates only in the upper part of the mixed layer where temperature signals are very small because of the lack of stratification. Discrimination between signal and noise is made by examining the coherence between signals originating in the same thermistor but amplified separately. The source of the noise lies mainly in the amplifier, so coherence is lost when noise dominates (Figure 2b).

The Batchelor spectrum (Figure 2d) has a shape completely specified once the values of the 'universal' and molecular constants are set, but its vertical position on the plot depends on the Cox number and the mean gradient, and its position in wave number depends on the kinetic energy dissipation.

Depending on the relative power in these components of a particular observed spectrum, it may or may not be possible to detect the turbulence component. If one can be seen, the cutoff wave number k_c (operationally defined as the wave number at which the power density in the turbulence component falls to 12% of its peak value) and the Cox number can be calculated. In these calculations, care must be taken that only the turbulence signal is used.

TABLE 2. Results of Models for $2 < f_N < 10$ cph, $Cx < 2500$

Model	a	b	c	E^2	F_3
1	−0.971	0.50	0.25	0.0181	19
2	−0.93 ± 0.10	0.50	0.25	0.0165	−1
3	−0.97 ± 0.10	0.56 ± 0.12	0.25 ± 0.02	0.0165	
4	−0.53 ± 0.05	0.00	0.23 ± 0.02	0.0243	93
5	−0.32 ± 0.16	0.25 ± 0.22	0.00	0.0623	550
6	−0.97 ± 0.08	0.56 ± 0.11	0.25	0.0165	−1
7	−0.92 ± 0.04	0.50	0.25 ± 0.02	0.0165	0

Sample includes 202 cases, 57% of total. Values of a, b, and c with error limits are determined from the data. Other values of a, b and c are assumed.

TABLE 3. Results of Regression Models for All f_N, With $Cx > 2500$

Model	a	b	c	E^2	F_3	M
1	−0.971	0.50	0.25	0.0466	161	
2	−1.11 ± 0.24	0.50	0.25	0.0269	58	
3	−0.92 ± 0.22	0.72 ± 0.10	0.19 ± 0.04	0.0158		0.83
4	−0.07 ± 0.26	0.00	0.01 ± 0.06	0.0505	181	0.04
5	−0.03 ± 0.05	0.45 ± 0.12	0.00	0.0296	72	0.64
6	−1.21 ± 0.04	0.81 ± 0.09	0.25	0.0172	7	0.89
7	−0.62 ± 0.16	0.50	0.13 ± 0.04	0.0190	16	0.61

Sample includes 86 cases, 24% of the total. M is the multiple regression coefficient. Values of a, b, and c with error limits are determined from the data. Other values of a, b, and c are assumed.

The definition of Cox number given in section 2 on the proposed scaling is appropriate to a completely stratified situation in which horizontal gradients are negligible. For isotropic gradients these Cox numbers should be multiplied by 3. In the following discussion we shall not use the factor of 3, but bear in mind that these values may be lower than they should be.

The buoyancy frequency N and its equivalent in cycles per hour, f_N, are calculated for the same segment of data. The TS relation was found to hold so well in the surface layer over this period, and the saline component of the density gradient was so small, that N was calculated from the vertical temperature gradient with a linear correction for salinity. In the halocline, data from the conductivity cell had to be used, because the salinity completely dominates the density structure there.

5. RESULTS

If all the assumptions and approximations implicit in the derivation in section 2 have not led us astray, a plot of k_c versus $0.8^{-1} N^2 \cdot D \cdot Cx$ for many spectra should make sense, and indeed it does for all the data from one cast (Figure 3). The points cluster about the line representing (4) very nicely, even though both stable and unstable segments have been included, and the Cox number ranges from values as small as 1.05, where turbulence is so small that diffusion is almost precisely molecular, to values as large as 10^7, where stratification is nearly absent. Any possibility of circularity in this scaling is ruled out by the observation that molecular viscosity is included in the computation of the Batchelor scale and nowhere else.

To further investigate this scaling under varying conditions, all the cases available in the halocline (62) are added to the data set along with 113 cases from the mixed layer during milder (14 m s^{-1}) winds. The distribution in (N, Cx) space is not uniform (Figure 4). Large Cox numbers are never seen in regions with large N, and small N is never combined with small Cox number. Examination of the ratio k_c/k_B averaged

over regions in this plot reveal (1) a systematic trend to low values of k_c/k_B at large Cox numbers (Figure 5), (2) a trend to low values at small N, (3) some trend to larger values for very large N, and (4) no difference between stable and unstable cases at similar values of N. Values of k_c/k_B most consistently near 1 are found in the region $Cx < 2500$, $2 < f_N < 10$ cph, in which 57% of the points are located. By replotting ϵ versus k_c for these cases an even more consistent picture is seen (Figure 6).

To examine this scaling further, and in particular to find out if the inclusion of N is justified, a number of multiple regression analyses were performed on subsets of these 354 samples. A series of models was used, based on $k_c = 10^a |f_N|^b (Cx)^c$, expressed for analysis as

$$\log_{10} k_c = a + b \log_{10} |f_N| + c \log_{10} (Cx) \qquad (5)$$

to emphasize deviations properly as being fractional rather than absolute. Here f_N is the buoyancy frequency expressed in cycles per hour. To see which parameters were significant, various combinations of fixed and fitted parameters were used (Table 1). These models are (1) equation (4), (2) equation (4) with the constant given as $1/0.8$ allowed to be determined by the data, (3) equation (5) with a, b, and c determined by the data, (4) same as (3) but with no f_N dependence, (5) same as (3) but with no Cox number dependence, (6) c set to $\frac{1}{4}$ and a and b determined by the data, and (7) $b = \frac{1}{2}$ and a and c determined by the data. Results are as follows.

1. For stable stratification and moderate Cox numbers (when f_N is larger than 2 cph and the Cox number is less than 2500) the F test shows that models 2, 3, 6, and 7 cannot be differentiated on the basis of these data with 95% confidence (Table 1). We therefore conclude that the dependence on f_N and Cx is as $f_N^{0.5} Cx^{0.25}$, as hypothesized. Because model 4 fails badly in comparison with model 3, we conclude that the dependence on f_N is required to explain these data. By comparing model 2 with model 1 it might be concluded that the

TABLE 4. Results of Regression Models for $f_N < 2$ cph, $Cx < 2500$

Model	a	b	c	E^2	F_3	M
1	−0.971	0.50	0.25	0.010	0.0	
2	−0.96 ± 0.36	0.50	0.25	0.010	0.6	
3	−1.12 ± 0.34	0.46 ± 0.34	0.32 ± 0.09	0.010		0.91
4	−0.81 ± 0.30	0.00	0.33 ± 0.10	0.015	5.7	0.85
5	−0.27 ± 0.52	0.49 ± 0.74	0.00	0.049	48.5	0.33
6	−0.93 ± 0.25	0.46 ± 0.36	0.25	0.0106	1.5	0.57
7	−1.15 ± 0.24	0.50	0.32 ± 0.08	0.010	−0.9	0.90

Sample includes 16 cases, 4.5% of the total. Values of a, b, and c with error limits are determined from the data. Other values of a, b, and c are assumed.

TABLE 5.   Results of Regression Models for $f_N > 10$ cph, $Cx < 2500$

Model	a	b	c	E^2	F_1	M
1	−0.971	0.50	0.25	0.022	20.6	
2	−0.88 ± 0.30	0.50	0.25	0.014	−0.8	
3	−0.73 ± 0.28	0.39 ± 0.24	0.24 ± 0.05	0.014		0.88
4	−0.29 ± 0.10	0.00	0.26 ± 0.05	0.018		0.84
5	−0.66 ± 0.54	0.63 ± 0.44	0.00	0.049	90.7	0.42
6	−0.73 ± 0.28	0.38 ± 0.24	0.25	0.014	−0.9	0.46
7	−0.86 ± 0.08	0.50	0.24 ± 0.05	0.014	−0.1	0.85

Samples include 40 cases, 11% of the total. Values of a, b, and c with error limits are determined from the data. Other values of a, b and c are assumed.

constant term 10^a is 12% larger than was assumed. This could mean that the constant given as 0.8 by Weinstock is 12% smaller, 0.71; that the Cox numbers should have been multiplied, on the average, by a factor of 1.6; or that the universal constant q is not 2.2, as we have chosen it [Dillon and Caldwell, 1980]. Still more likely, all of these effects are involved, or perhaps the f_N dependence is a bit greater than is predicted (compare 1 versus 3).

2. For stable but not large stratification and moderate Cox numbers ($2 < f_N < 10$ cph, $Cx < 2500$) the result is the same as result 1 but with points in the steepest part of the thermocline rejected. Again, models 2, 3, 6, and 7 are indistinguishable, showing that with these data, model 2 cannot be rejected (Table 2). Again, the constant term is larger, by 10% this time. A comparison of models 3 and 4 shows that even for this restricted range in f_N the inclusion of f_N is justified.

3. For large Cox numbers ($Cx > 2500$), regardless of stability the results deviate from the models that work so well for smaller Cox numbers (Table 3). Perhaps the multiple regression coefficients are the most illuminating statistic, particularly in the comparison of model 4 and 5. Here it is seen that little of the variance can be explained by the Cox number dependence but much more by the f_N dependence. The nature of the sampling makes this even more impressive, the range in f_N being so much more restricted. In general, models 1 and 2 are very poor. We conclude that one or more of our assumptions are violated for large Cox numbers

4. For unstable stratification, moderate Cox number ($f_N^2/|f_N| < -2$ cph, $Cx < 2500$), few cases were found (Table 4). The results are consistent with those for stable stratification, but the resolution is very poor.

5. For small stratification and moderate Cox number ($|f|_N < 2$ cph, $Cx < 2500$): too few cases were found to draw any conclusions.

6. Cases with large, stable stratification and moderate Cox

number ($f_N > 10$ cph, $Cx < 2500$); also included with less stable points in the data of Table 1, are found only in the steepest part of the thermocline. The regression analyses (Table 5) show that these cases scale consistently with the less stable cases, but again resolution is poor.

7. For all stabilities and moderate Cox numbers ($Cx < 2500$) it must be noted that so many cases have moderate, stable f_N that these dominate. The results show that the f_N dependence may be significantly greater than 0.50 power; this calculation yields 0.60 ± 0.06 for the exponent of f_N (Table 6). Otherwise the scaling works very well. The model 3 results give the exponent of the Cox number as 0.25 ± 0.02 and the constant term as −0.97 ± 0.06, both precisely as in the proposed scaling.

Values of the Cox number and k_c cannot be calculated in every case. In the thermocline the mean stratification—and perhaps also the effects of internal wave straining—may dominate the spectrum, so that the turbulence signal cannot be seen. In the mixed layer, signal levels may be so low that noise interferes. In the 18 m s^{-1} storm in which many of these data were obtained, turbulence near the surface was so intense that the instrument was tipped and the drop speeds were erratic. Even with these difficulties a picture can be made of the dissipation versus depth (Figure 7) by using (3). Here dissipations in the mixed layer are of the order of 10^{-4}–10^{-3}. In the thermocline there are patches of dissipation of the order of 10^{-5}–10^{-4}, but apparently, dissipations in much of the thermocline are considerably lower. It must be kept in mind that some dissipative regions may be invisible to this method because turbulence is seen only as it manifests itself in temperature fluctuations; an isothermal layer gives no signal regardless of its dissipation.

6. DISCUSSION

Now that it has been shown that the Lilly-Weinstock formula for calculating vertical eddy diffusivity from ϵ and N,

TABLE 6.   Results of Regression Models for All f_N, $Cx < 2500$

Model	a	b	c	E^2	F_1	M
1	−0.971	0.50	0.25	0.0183	41	
2	−0.93 ± 0.06	0.50	0.25	0.0166	12	
3	−0.97 ± 0.06	0.60 ± 0.06	0.25 ± 0.02	0.0159		0.88
4	−0.45 ± 0.05	0.00	0.20 ± 0.03	0.0398	401	0.66
5						
6	−1.01 ± 0.05	0.60 ± 0.06	0.25	0.0158	−1	0.79
7	−0.91 ± 0.03	0.50	0.24 ± 0.02	0.0165	10	0.86

Sample includes 268 cases, 75% of total. Values of a, b, and c with error limits are determined from the data. Other values of a, b, and c are assumed.
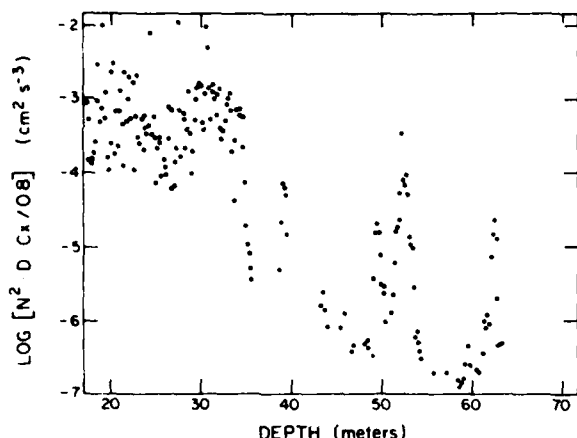
Fig. 7. Dissipation calculated as prescribed versus depth for the cast on August 23, 1977.

the Cox-Osborn formula for calculating eddy diffusivity from temperature gradient measurements, and the Batchelor universal spectral form can be combined to yield a relation between the cutoff wave number and the Cox number and buoyancy frequency (for limited Cox number), are we to conclude that all these relations are correct? Can we now assume that, as long as the Cox number is less than 2500, ϵ can be correctly calculated either from the Cox number and N or from k_c by inverting the formula for the Batchelor wave number? More confirmation is needed, the key information required being measurements of dissipation from microscale shear measurements [e.g., Osborn, 1974] made on a vehicle from which si-

multaneous measurements like those described in this paper are being made.

Why does this scaling for the cutoff wave number, which seems to work so well for conditions of moderate Cox number, fail when the Cox number is large? Additional evidence may be found in the companion paper [Dillon and Caldwell, 1980], in which it is shown that the spectrum of the turbulent fluctuations closely resembles the Batchelor form only when the Cox number is large. The failure then is not in the Batchelor spectrum or its assumptions. We suspect that the failure lies in the assumed formula for vertical eddy diffusivity in terms of ϵ and N. This formula cannot be expected to hold in weak stratification, where the turbulence is so strong that the remaining stratification cannot affect it. The observation (Table 3) that cutoff wave number becomes independent of Cox number in this case might mean that an asymptotic state has been reached. The scaling of k_B as we have expressed it still obtains, but the test can no longer validate it. Our hypothesis, which requires a further test, is now that the Batchelor scaling in terms of ϵ governs the high wave number cutoff of the temperature gradient spectrum whether or not the spectrum follows the Batchelor form at lower wave numbers. A method of determining ϵ for high Cox numbers, such as the small-scale shear measurement, is required for the test.

APPENDIX

As is seen above, to observe fluctuations at the Batchelor wave number with a 10 cm s^{-1} drop speed for dissipations greater than 2×10^{-5} cm^2 s^{-3}, the frequency response function for the thermistor must be established for correcting the spectra. Before discussing the response functions used, let us examine in detail the effect on determinations of Cox number
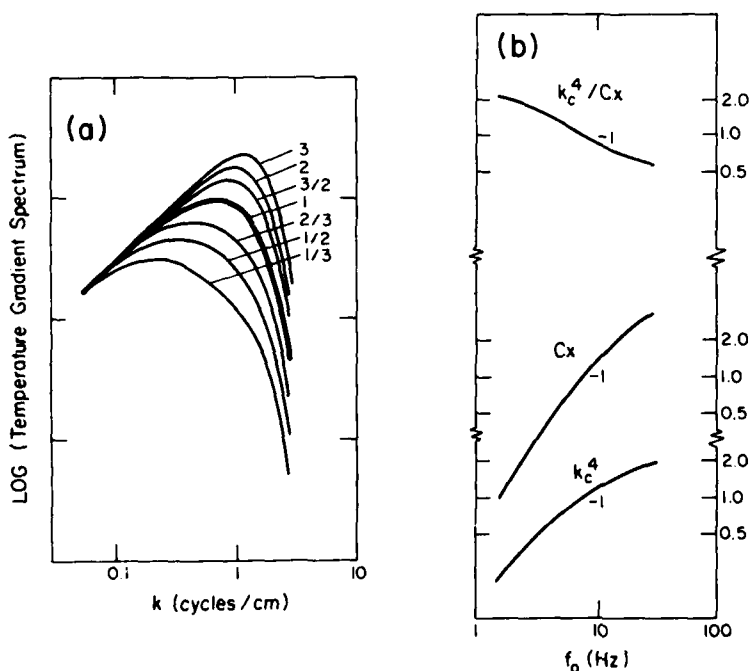
Fig. 8. Effect of erroneous correction for thermistor response. The assumed spectrum (labeled 1) is attenuated by the factor $[1 + (s_D k/f_0)^2]^{-1}$ and then corrected by the factor $[1 + (s_D k/f_1)^2]$, with f_0 assuming various values but f_1 always being 7.4 Hz (s_D is the drop speed in centimeters per second). (a) Resultant spectra labeled with the appropriate values of f_0/f_1. (b) Ratios of various quantities to their values when $f_0 = f_1$ is plotted versus f_0.

and k_c of errors in the response functions as follows: Assume that a spectrum with the Batchelor form and cutoff at 28 Hz (ϵ = 2.5 × 10^{-3} cm^2 s^{-3}) represents the temperature fluctuations in a segment of the water column. Assume also that a thermistor passes through this segment and observes these fluctuations, attenuating the signals at the various frequencies as $[1 + (f/f_0)^2]^{-1}$. Now examine the effect of correcting the spectrum with the factor $[1 + (f/f_1)^2]$ with various values of f_1. Then calculate the Cox number, and measure the cutoff frequency as a function of f_1/f_0, the ratio of assumed and real correction scales in frequency. Results of this numerical experiment (Figure 8) show the effect of various degrees of error in correction on spectra and determined values of k_c and the Cox number. The hypothesis test performed depends on k_c^4/Cx, a quantity which depends little on the correction (Figure 8).

The response function used in the present work was obtained by comparing simultaneous spectra obtained from a thermistor of the type used and from a 0.0025-cm-diameter thermocouple in freshwater. The correction is approximated by $1 + (f/f_1)^2$. At the descent rate of the instrument, 10 cm s^{-1}, f_1 is 7.4 Hz, so the correction is a multiplicative factor of 17.4 at the highest frequency used here, 30 Hz. A redetermination of the response function by passing the thermistor through a thin jet of warm water in a laboratory tank [*Dillon and Caldwell*, 1980] shows that the response is reasonably well described by a value of f_1 of 6.8 Hz, about 8% lower than that indicated by the field experiments. Referring to Figure 8, this discrepancy in f_1 corresponds to a difference in k_c of less than 1% and a change in the ratio $k_c/Cx^{1/4}$ of less than 1%. Similar results for the same type of thermistor are found by M. C. Gregg (private communication, 1979). Thus the corrections used in this paper are sufficiently accurate for the purpose. To examine the detailed form of the spectra, a more complicated response correction is required, such as that in the companion paper.

REFERENCES

Batchelor, G. K., Small scale variation of convected quantities like temperature in turbulent fluid, *J. Fluid Mech. 5*, 113-133, 1959.

Caldwell, D. R., Fine-scale temperature structure in the bottom mixed layer on the Oregon shelf, *Deep Sea Res., 23*, 1025-1036, 1976.

Caldwell, D. R., Variability of the bottom mixed layer on the Oregon shelf, *Deep Sea Res., 25*, 1235-1243, 1978.

Caldwell, D. R., S. Wilcox, and M. Matsler, A relatively simple and inexpensive probe for fine-scale temperature measurements, *Limnol. Oceanogr., 20*, 1035-1042, 1975.

Caldwell, D. R., J. M. Brubaker, and V. T. Neal, Thermal microstructure on a lake slope, *Limnol. Oceanogr., 23*, 372-374, 1978.

Dillon, T. M., and D. R. Caldwell, Catastrophic events in a surface mixed layer, *Nature, 276*, 601-602, 1978.

Dillon, T. M., and D. R. Caldwell, The Batchelor spectrum and dissipation in the upper ocean, *J. Geophys. Res., 85*, this issue, 1980.

Elliott, J. A., and N. S. Oakey, Horizontal coherence of temperature microstructure, *J. Phys. Oceanogr., 5*, 506-515, 1975.

Elliott, J. A., and N. S. Oakey, Spectrum of small-scale oceanic temperature gradients, *J. Fish. Res. Bd. Can., 33*, 2296-2306, 1976.

Gibson, C. H., and W. H. Schwarz, The universal equilibrium spectra of turbulent velocity and scalar fields, *J. Fluid Mech., 16*, 365-384, 1963.

Gibson, C. H., G. R. Stegen, and R. B. Williams, Statistics of the fine structure of turbulent velocity and temperature fields at high Reynolds number, *J. Fluid Mech., 41*, 153-167, 1970.

Gibson, C. H., L. A. Vega, and R. B. Williams, Turbulent diffusion of heat and momentum in the ocean, *Advan. Geophys., 18A*, 353-370, 1974.

Grant, H. L., B. S. Hughes, W. M. Vogel, and A. Moilliet, Some observations of the occurrence of turbulence in and above the thermocline, *J. Fluid Mech., 34*, 443-448, 1968.

Gregg, M. C., Microstructure and intrusions in the California current, *J. Phys. Oceanogr., 5*, 253-278, 1975.

Gregg, M. C., Finestructure and microstructure observations during the passage of a mild storm, *J. Phys. Oceanogr., 6*, 528-555, 1976.

Gregg, M. C., A comparison of finestructure spectra from the main thermocline, *J. Phys. Oceanogr., 7*, 33-40, 1977a.

Gregg, M. C., Variations in the intensity of small-scale mixing in the main thermocline, *J. Phys. Oceanogr., 7*, 436-454, 1977b.

Gregg, M. C., and C. S. Cox, Measurements of the oceanic microstructure of temperature and electrical conductivity, *Deep Sea Res., 18*, 925-934, 1971.

Gregg, M. C., C. S. Cox, and P. W. Hacker, Vertical microstructure measurements in the central North Pacific, *J. Phys. Oceanogr., 3*, 458-469, 1973.

Lilly, D. K., D. E. Waco, and S. I. Adelfang, Stratospheric mixing estimated from high-altitude turbulence measurements, *J. Appl. Meteorol., 13*, 488-493, 1974.

Marmorino, G. O., and D. R. Caldwell, Horizontal variation of vertical temperature gradients measured by thermocouple arrays, *Deep Sea Res. 25*, 195-181, 1978a.

Marmorino, G. O., and D. R. Caldwell, Temperature fine structure and microstructure observations in a coastal upwelling region during a period of variable winds, *Deep Sea Res, 25*, 1073-1106, 1978b.

Nasmyth, P. W., Oceanic turbulence, Ph.D. thesis, 69 pp., Inst. of Oceanogr., Univ. of B. C., Vancouver, 1970.

Osborn, T. R., Vertical profiling of velocity microstructure, *J. Phys. Oceanogr., 4*, 109-115, 1974.

Osborn, T. R., and C. S. Cox, Oceanic fine structure, *Geophys. Fluid Dyn., 3*, 321-345, 1972.

Weinstock, J., Vertical turbulent diffusion in a stably stratified fluid, *J. Atmos. Sci., 35*, 1022-1027, 1978.

Williams, R. M., and C. A. Paulson, Microscale temperature and velocity spectra in the atmospheric boundary layer, *J. Fluid Mech., 83*, 547-567, 1977.

High-Frequency Internal Waves at Ocean Station P

Tom M. Dillon and Douglas R. Caldwell

Oregon State University, Corvallis, Oregon 97331

Slow perturbations of the drop speed of a nearly freely falling, winged, microstructure probe in the upper 200 m at station P are interpreted as vertical velocity fluctuations of an internal wave field. The frequencies of these fluctuations lie in the 2.5- to 4-cph band, near the buoyancy-frequency cutoff. A typical rms value is 1.3 cm/s. Indications of the vertical structure of the wave field and the partition of energy among modes are obtained by statistical comparison with discrete mode solutions of the internal wave equation. It is found that the first and second modes carry most of the internal wave energy and that the partition of energy between them may change in 3 days.

INTRODUCTION

Temperature and isotherm displacement spectra measured in the ocean often show a peak located at a frequency just below the buoyancy frequency cutoff [*Voorhis*, 1968; *Cairns*, 1975; *Briscoe*, 1975; *Pinkel*, 1975]. Although in such a displacement spectrum the waves in this band contribute only a local maximum in a low-amplitude tail, they dominate a spectrum of vertical velocity (Figure 1); the vertical velocities associated with such waves may contain as much as one half the kinetic energy of vertical motion [*Pinkel*, 1975]. The vertical structure of these waves has been investigated to some extent, the result being that waves of small vertical wave number dominate [*Pinkel*, 1975; *Hayes et al.*, 1975], but the modal structure is still uncertain. The ideal data for a determination of modal structure would be a sequence of profiles of vertical velocity. Recently it has been demonstrated that perturbations of the rate of change of pressure seen by a freely falling instrument can be interpreted to yield the vertical velocity associated with an internal wave field [*Desaubies and Gregg*, 1978]. We have found that pressure records from our nearly freely falling microstructure instrument can also be so interpreted. Further, if the fall speed is increased so that the instrument falls through a vertical wavelength in less than a period, the record contains usable information about the vertical modal structure.

An experiment performed off the coast of Oregon (45°20′N) in 100 m of water provides convincing evidence that vertical velocities associated with internal waves influence the fall rate of our probe. Large fluctuations in drop speed are present above 60 m (Figure 2); these fluctuations decrease in amplitude below 60 m, and a constant drop speed is approached as the probe nears the bottom, where the vertical velocity of an internal wave must tend toward zero. Details of the wave field's vertical structure are obscured by temporal variation in this case because the drop speed was too slow (0.1 m s^{-1}). A similar decrease in amplitude is to be expected near the surface, but we did not observe it because the instrument was not brought to the surface after each cast but rather relaunched below the surface. Indeed, the near-surface behavior of the wave field is difficult to study by the methods described below because in the first few meters the turbulence of the ship's wake affects the instrument.

It might be thought that internal wave effects other than the vertical velocity might produce the fluctuations of Figure 2.

The mean shear of the wave field might tilt the instrument, or the oscillating horizontal velocity of the field might produce a variable drag on the line. These possibilities can be investigated by careful study of Figure 2. First, if line drag were a serious influence at internal wave frequencies, the effect would never be to decrease the oscillation amplitude as the bottom is approached. Second, if mean internal wave shear caused a tilting of the instrument, the result would be a decrease in the drag coefficient and a consequent increase in drop speed; tilting cannot account for slowing the drop speed. It seems clear that the major source of slow fluctuations is the vertical velocity of internal waves, since it is known from the instrument's behavior in a surface wave field (see the appendix) that it responds to vertical velocities at internal wave frequencies, that internal waves are present, and that the amplitude of fluctuation is that expected from high-frequency internal waves.

The instrument used by Desaubies and Gregg, the microstructure recorder (MSR), is a winged cylinder with temperature and pressure sensors and an internal recorder [*Gregg and Cox*, 1971]. Desaubies and Gregg have demonstrated that this probe responds well to fluctuations in the local vertical water velocity at internal wave frequencies because of the large drag coefficient of the wings. They conclude that fluctuations in the apparent drop speed determined from the pressure record are caused by fluctuations in the local vertical water velocity owing to the internal wave field. That is, the MSR falls at a constant rate relative to the water, its speed relative to the surface depending on the local vertical velocity of the water.

Desaubies and Gregg find that the vertical velocity variations they observe are due to the temporal variation of the waves. With their slower drop speed, temporal variations dominate because it takes many periods for the instrument to descend through a wavelength. Depth-dependent variations are revealed by using a drop speed sufficiently fast that a wavelength is traversed in less than a period. We are aided in this case by the fact that vertical wavelengths in the upper layers are much shorter than those in the permanent pycnocline where Desaubies and Gregg took their data.

Our probe, the microstructure profiler (MSP), is similar in concept to Gregg's MSR in that it is a freely falling vehicle measuring temperature and pressure, but it is much less massive, 5 kg versus 90 kg. The MSR records internally while the MSP sends signals to the surface through a cable composed of four XBT wire pairs encased in a Kevlar sheath coated with syntactic foam with the foam density adjusted so the cable is slightly heavy in water.

MOORED
TEMPERATURE
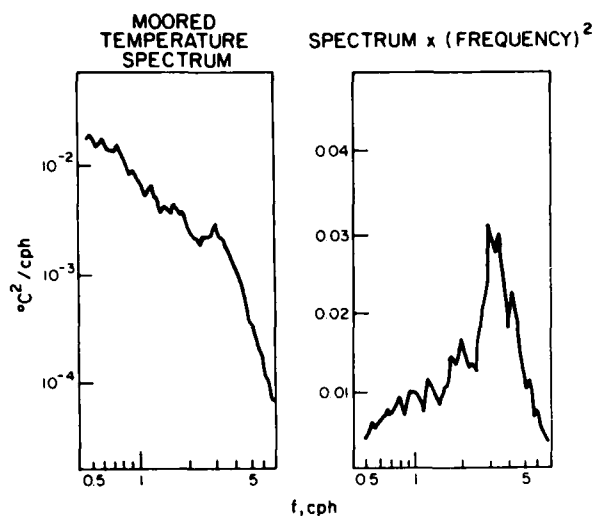SPECTRUM

SPECTRUM x (FREQUENCY)²

f, cph

Fig. 1. (Left) A moored temperature spectrum from the Mile experiment (courtesy of R. DeSzoeke, Oregon State University) which shows a slight peak and cutoff at 3 cph and (right) the spectrum is multiplied times frequency squared, giving an idea of the behavior of the vertical velocity spectrum. Depth of measurement was 50 m.

Initially, we were skeptical of determining vertical velocities from the MSP pressure record because of concern about the effect of cable drag. After examining a number of records, however, we can find no evidence of cable drag effects on the drop speed at internal wave frequencies; it manifests itself only at surface wave frequencies, as small-amplitude fluctuations constant with depth. After the energy at surface wave frequencies has been filtered out, the remaining fluctuations can be explained by internal waves in the 2.5- to 4-cph band. Thus there is a large spectral gap between cable drag at surface-wave frequencies and the variations seen in the speed record at internal wave frequencies.

Two series of casts through the upper 200 m at station P (50°N, 145°W) in August 1977 have a drop speed of the order of 0.2 m s⁻¹, fast enough for studying vertical structure. In this report we present methods of using this data to find indications of the vertical structure, and we show that the partition of energy among modes changed markedly in 3 days. One question not often mentioned in published discussions of the internal wave models [e.g., *Garrett and Munk*, 1972, 1975] involves the averaging time required to achieve the statistical conditions hypothesized. Over how much time must an average extend before the hypothesis of random direction of propagation holds? How long must the averaging extend before the hypothesized partition between vertical modes is attained? Surely these conditions are not obtained instantaneously, particularly in the seasonal thermocline. Perhaps the situation resembles that of the direction of propagation of surface waves. At a given time a certain direction will predominate; only over times longer than those characteristic of atmospheric disturbances could isotropy be imagined. For internal waves the generating mechanisms are not yet well specified, so the averaging time is not known.

For interpretation of these records, we require a model of the internal wave field at the dominant periods, the bands between 2.5 and 4 cph (Figure 1). The buoyancy frequency changes so rapidly with depth above 200 m at station P that a WKB approximation of the internal wave field is not appro-

priate. It turns out that the observations can be interpreted in terms of a few low-order modes confined to a narrow frequency band, and for this situation a discrete mode standing-wave solution of the internal wave equation provides a convenient framework within which to view the data. Following a brief description of the experimental apparatus and an examination of the observed variation with depth of the drop speed, we present the results of using discrete mode solutions to make simple statistical calculations of the effect on the observations of various distributions of energy with mode number. We find that the data is best described by a dominance of the first mode during one cast series and by second mode dominance during another series 3 days later. Waves of mode number higher than 4-5 are not energetic enough to be seen in these data.

EXPERIMENTAL DETAILS

The data were collected at ocean station P (50°N, 145°W) during August–September 1977 as part of the mixed layer experiment (Mile). In all, 381 casts were made with the MSP. Most casts, however, were shallow drops to 70 m or less at low fall rates and so are not very useful for studying the vertical structure of internal waves because greater depth is required to see enough of the modal structure and because for low mean fall rates the temporal variations of the waves obscure vertical variations. Seven casts with mean drop speeds of 0.2 m s⁻¹ were made to at least 130 m depth on August 26, 1977, (GMT) and eight similar casts were made on August 29.

The pressure was measured with a solid state sensor (Kulite Semiconductor Corp.). The sensor output was converted to a frequency in the 500- to 1300-Hz band for transmission to the ship. The signal was demodulated on board with an FM discriminator; its output was digitally recorded at a rate of 11.25 s⁻¹. The discriminator was calibrated to give a full-scale reading at a depth of 200 m, one least count corresponding to a depth change of 5 cm. The least count error was the largest source of high-frequency noise.

Six MSP units were used during the Mile experiment. The descent rate of each unit is adjusted by setting the angle of attack of the wings. Although the wing angles were constant until readjusted, they were difficult to reproduce exactly. Consequently, the mean descent rate of different instruments with similar wing angle settings varied by as much as 10%. We
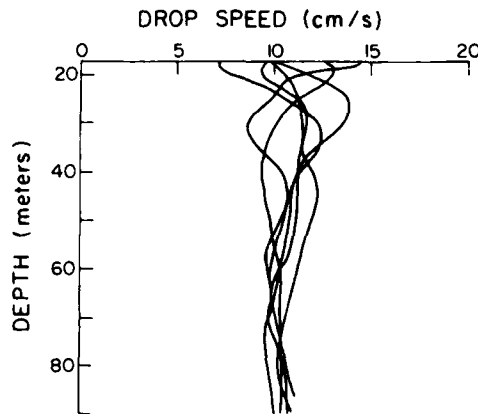
DROP SPEED (cm/s)

Fig. 2. Drop speed profiles off the Oregon coast in 100 m of water. Note the convergence to a well-defined constant drop speed near the bottom. High-frequency fluctuations have been filtered out.
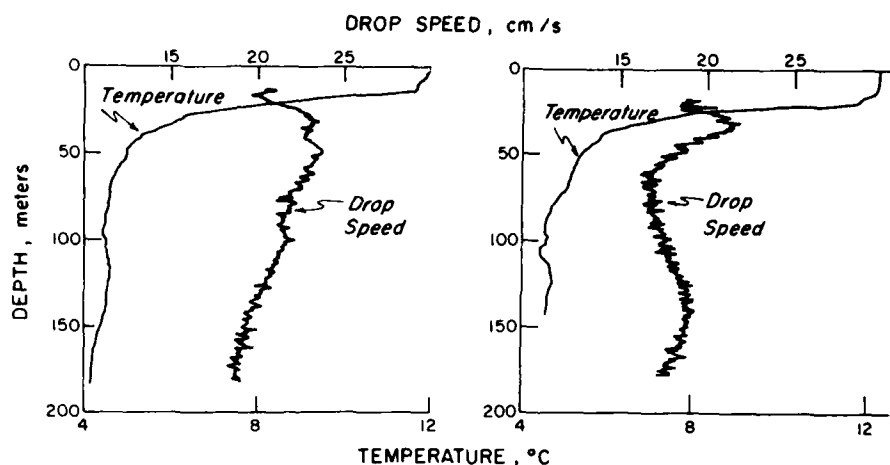
DROP SPEED, cm/s

Fig. 3.   Representative drop speed profiles from (left) August 26 and (right) August 29 at station P. Note the large fluctuations with length scale of several tens of meters. August 29 profiles characteristically show more structure than seen on August 26.

therefore find it impossible to define a precise mean drop speed for each wing angle. The best estimate of mean drop speed comes from an ensemble average of drop speeds with unchanged wing angle. Both series analyzed here were performed with the same unit with no wing angle adjustment between casts.

Our main contribution to the Mile experiment was the measurement of small-scale temperature features. The sampling scheme used was simply to make as many casts as was possible during our allotted time of 8 h/d. If all went well, the interval between 200 m casts was 20-30 min. Between measurements our horizontal position often changed by 500-600 m. Because some low-order modes have a horizontal wavelength in the range 500-1000 m, we sometimes see nearly the same phase between consecutive casts. Even so, because our data contains no information concerning the direction of the wave field, we must make the assumption that each cast views an independent realization of the field; that is, that the phase difference between casts is a random variable.

VERTICAL VELOCITY PROFILES

On August 27, seven drops of the MSP were made to depths of 130-195 m. Surface conditions were characterized by light winds (6 m s^{-1}) and a wave field with significant height of 0.5 m. No surface effects remained from the passage of a front on August 23-24 with winds of nearly 20 m s^{-1} and significant wave heights of 4 m. The profiles are characterized by slow variations in the vertical velocity (Figure 3, left panel). The drop speed averaged over all drops and all depths was 0.205 m s^{-1}. Variations in the vertical velocity as large as 0.05 m s^{-1} were seen. As is shown below, these variations are the result of temporal as well as spatial fluctuations in the internal wave vertical velocity field. Small, rapid fluctuations can also be seen. They are caused both by high wave number, by small amplitude spatial variations in the internal wave field, and by line drag.

On August 29, winds were 5-6 m s^{-1} and falling. Surface waves had a significant height of 1 m owing to winds to 12 m s^{-1} on August 27-28. In the eight drops made under these conditions to depths of 130-200 m, vertical velocities differ from those of August 26 in that more structure is present, especially

above 100 m. Again, low-frequency variations as large as 0.05 m s^{-1} are seen (Figure 3, right panel).

The ensemble averaged and vertically averaged rms internal wave velocity as was measured from the mean drop speed was 0.012 m s^{-1} for the August 26 casts and 0.014 m s^{-1} for the August 29 casts. Desaubies and Gregg found similar rms vertical velocities, 0.015 m s^{-1} at 30-150 m in the Gulf Stream.

While it is of course impossible to distinguish low-frequency high-mode waves from high-frequency low-mode waves from a single drop, an analysis of many drops makes feasible the separation of temporal and spatial effects. For example, the rms velocity variation W_{rms} was of the order of 0.013 m s^{-1}, and the maximum observed isotherm excursion ξ_{max} was less than 10 m. A 1-cph wave with 0.013 m s^{-1} rms vertical velocity would have an isotherm excursion of 20 m. We know therefore that waves of period greater than 1 hour are not a dominant contributor to the observed rms vertical velocity.

To clarify the differences between the August 26 and 29 series, a model is required which will statistically describe the internal wave structure in the upper 200 m. To this end, we seek discrete mode solutions to the internal wave equation.

THEORETICAL MODES

Since the region of interest is the upper 200 m of the water column where the buoyancy frequency changes rapidly with depth, the WKB approximation is not useful. Instead we resort to a discrete mode solution for the vertical velocity of a two-dimensional random standing internal wave field. These solutions may be expressed as

$$w(x, z, t; \omega) = \sum_{m=1}^{\infty} \psi_m(z; \omega) \{A_{1m}(\omega) \sin (k_m x - \omega t + \phi_{1m})$$

$$+ A_{2m}(\omega) \cos (k_m x - \omega t + \phi_{2m})\} \qquad (1)$$

where $A_{1m}(\omega)$ and $A_{2m}(\omega)$ are weights expressing the distribution of energy among phases and modes at frequency ω, k_m is the horizontal wavenumber, x is the horizontal coordinate, ϕ_{1m} and ϕ_{2m} are random phases, and the wave functions $\psi_m(z;$
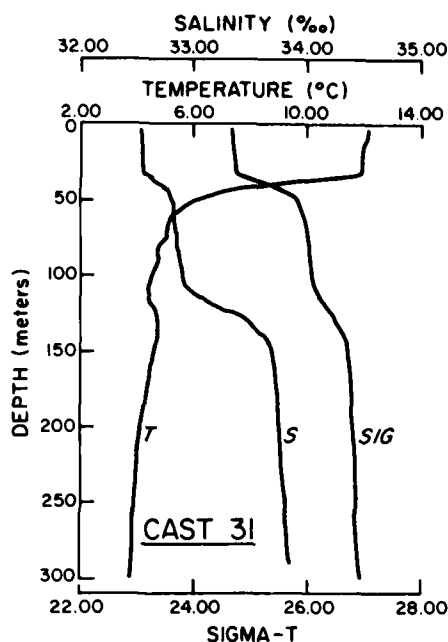
Fig. 4. CTD profile representative of the temperature and salinity structure found at station P during August–September, courtesy of S. Hayes (Pacific Marine Environmental Laboratories). Above 60 m, density is dominated by temperature, and below 100 m it is dominated by a strong halocline.

ω) must satisfy

$$\frac{d^2}{dz^2}\psi_m + k_m^2 \frac{(N(z)^2 - \omega^2)}{(\omega^2 - \Omega^2)} \psi_m = 0 \qquad (2)$$

[Turner, 1973], where Ω is the Coriolis parameter and $N(z)$ is the (horizontally uniform) buoyancy frequency. The wave function is defined with the normalization

$$\int_0^\infty \psi_m^2 \, dz = 1 \qquad (3)$$

The vertical velocity is then

$$W(x, z, t) = \int_0^\infty Q(\omega)w(x, z, t; \omega) \, d\omega \qquad (4)$$

where $|Q(\omega)|^2$ expresses the weighting of energy with frequency.

With $N(z)$ prescribed, the random field is fully defined if $A_{1m}(\omega)$, $A_{2m}(\omega)$, and $Q(\omega)$ are known. The *Garrett and Munk* [1972, 1975] models (GM72 and GM75) are attempts to find such functions consistent with observations in the permanent pycnocline. Both GM72 and GM75 assume A_m to be independent of frequency; GM72 uses the 'top hat' functional form A_m = constant for $1 \leq m \leq m_0$ (m_0 is called the mode number), $A_m = 0$ otherwise. The tapered form $A_m = A_0(\tau - 1)(1 + m/m_0)^{-\tau}$ with suggested values $m_0 = 6$, $\tau = 2.5$, and the normalization

$$\sum_{m=1}^\infty A_m = 1$$

was used by GM75. *Cairns* [1975] found high-frequency waves to be best described by the GM72 form with mode number $m_0 = 4$.

The density structure was dominated by a weakly stratified surface layer when winds were not blowing, a sharp seasonal thermocline starting at 30–40 m, and a strong halocline starting at 100–120 m (Figure 4). The mean buoyancy frequency profile, an ensemble average of profiles calculated from CTD casts (S. Hayes, personal communication, 1979) reflects these features (Figure 5). Individual profiles differ from the mean mainly in ±5 m variation of the depth of the seasonal thermocline and ±10 m variation of the depth of the halocline (caused by low-frequency internal waves). Above 25 m, the buoyancy frequency varies with local mixed-layer dynamics. The mean profile above 25 m in Figure 5 is typical of calm conditions, which obtained while the data analyzed here were gathered.

Quasianalytic eigenfunction solutions of (2) were obtained by approximating the vertical variation of the ensemble mean profile by a series of layers, each with constant N (Figure 5). Analytic solutions for ψ were obtained for each layer, and values of ψ and $d\psi/dz$ were matched at the boundaries between layers. A rigid lid was assumed at the surface. Far below the turning point, N was assumed constant to unlimited depths and the lower boundary condition was that $\psi \rightarrow 0$ at infinity. Eigenfunctions therefore consist of a set of constants, two per layer, multiplying a set of constant N basis functions, either trigonometric or hyperbolic, depending upon the sign of $N(z)^2 - \omega^2$ and an exponentially decreasing tail far below the turning point. These stepwise layered solutions are reasonable approximations as long as the vertical wavelength at a given layer is much larger than the layer thickness. As vertical wavelength approaches layer thickness, the layer thickness must be much smaller than $N/(dN/dz)$. Typically, these conditions are satisfied for $m < 10$ at frequencies of 4 cph and smaller. For frequencies above 4 cph, standing modes of higher order cannot be well approximated by linear theory because the N profile is significantly affected by lower-frequency waves.

The frequency distribution of energy $Q(\omega)$ is a continuous function. But if a narrow frequency band is under examina-
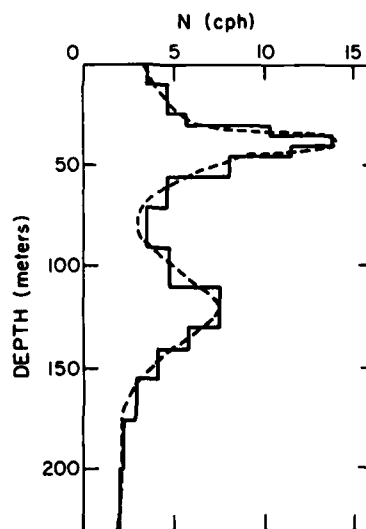

Fig. 5. Ensemble averaged profile of buoyancy frequency (dotted curve) and the layered approximation used in calculating modal structure.
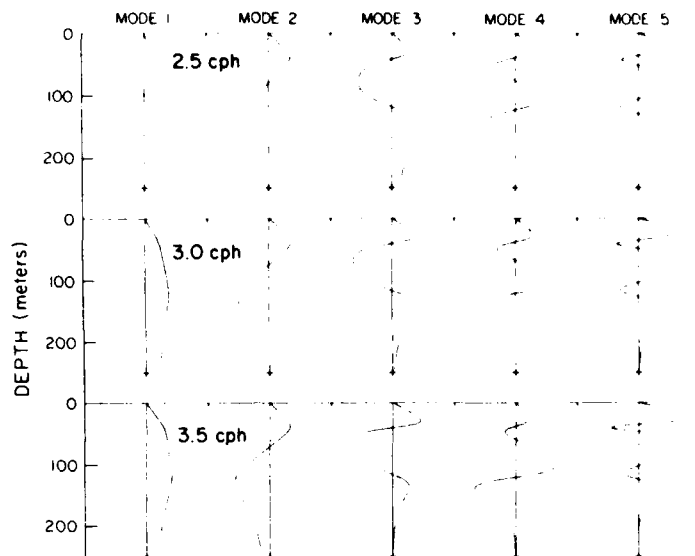
Fig. 6. Vertical velocity modes at 2.5, 3, and 3.5 cph calculated from the layered approximation of buoyancy frequency in Figure 5. Modal shapes for mode numbers less than six are only weakly dependent on frequency.

tion, and the wave function ψ is not strongly dependent on frequency within that band, a single frequency approximation may be used without introducing much error. The precutoff spectral peak occupies the frequency band from 2.5 to 4 cph (Figure 1), and the low-mode wave functions within that band are all very similar in that the relative maxima, the relative minima and zero crossings of a given mode all lie at about the same depth (Figure 6), that is, the vertical wave number, is relatively constant with frequency. This is because the depth of the turning point happens to be nearly constant in the 2.5-to 4-cph frequency range. We assume the 3-cph wave function is representative of all wave functions within the precutoff peak and limit all computations to this single frequency. Statistical evidence is given below, justifying the choice of 3 cph as the representative frequency.

COMPARISON WITH OBSERVATIONS

The eigenfunctions for each mode at a given frequency can be combined with an arbitrary initial phase and a specified energy distribution A_{1m}, A_{2m} to yield a representative instantaneous profile of vertical velocity, as was in (1). Fluctuations in vertical velocity seen by a winged vehicle falling freely with mean drop speed S_D can be obtained if the temporal variable in (1) is replaced by z/S_D, as long as S_D is much greater than the internal wave vertical velocity

$$w(z) = \sum_{m=1}^{\infty} \psi_m(z; \omega) \{A_{1m} \sin (\omega z/S_D + \phi_{1m})$$
$$+ A_{2m} \cos (\omega z/S_D + \phi_{2m})\} \quad (5)$$

where the horizontal variable x has been suppressed for clarity. Because the total time for a cast was always less than 20 min, a complete cycle of a 3-cph wave was never seen.

The shape of each individual profile is of course dependent on the (random) set of initial phases and the modal energy distribution. In general, if a given energy distribution weights higher-order modes heavily, more structure will be seen in regions where $N(z)$ is large than if the low-order modes are more heavily weighted. To quantify this effect, we need a

measure of the 'wiggliness' of the profile. One such measure is the number of times a given fluctuation profile crosses zero. At a given frequency, many more zero crossings will be seen if high-order modes are dominant than if low-order modes dominate.

One may compute a 'zero crossing density,' the probability of finding a zero-crossing in any given depth interval. To see what information this statistic yields, consider a taut string of length L vibrating with frequency ω and having only two modes excited, the first and second. The equation of motion of the string will be

$$f(x, t) = F_1 \sin\left(\frac{\pi x}{L}\right) \cos (\omega t + \phi_1) + F_2 \sin\left(\frac{2\pi x}{L}\right) \cos (\omega t + \phi_2)$$

$$(6)$$

where $f(x, t)$ represents the string velocity, x is distance along the string, and ϕ_1, ϕ_2 are random phases. A 'snapshot' of the string velocity may reveal zero crossings anywhere along the string, but the probability of finding a zero-crossing is greater near $x = L/2$ than at any point other than the string ends, because the second-mode velocity changes sign there. A zero-crossing density diagram for the string would thus yield a peak at $x = L/2$, if a substantial proportion of the energy lies in the second mode. It is easily seen that the peak height and width gives an indication of the relative importance of the second mode: if $F_2 \gg F_1$, the peak would be very high and narrow, while if $F_2 \ll F_1$, the peak would be small and broad. It is also easily seen that if a finite number of modes were present, each mode would show a unique set of peaks in the zero-crossing density, so that given sufficiently good statistics and resolution, the zero-crossing density would reveal the presence of each mode. In a like manner the zero-crossing density of the vertical velocity of internal waves provides information regarding the relative importance of discrete modes. Owing to limited statistical reliability, an exact modal energy distribution cannot be found by these methods; however, if one or two low-order modes are dominant, their presence is easily discerned even with limited data.

PROFILE CROSSING DENSITY
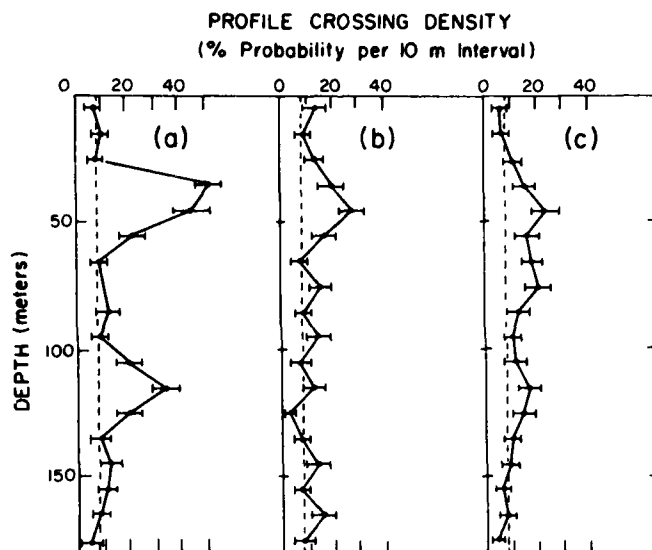(% Probability per 10 m Interval)

Fig. 7. Probability of finding a profile crossing in a 10-m interval versus depth. (a) With an equal distribution of energy among first five modes, probability is large at 35 m and 120 m. (b) With the energy distributed among the first five modes as (mode number)$^{-2}$, first mode is dominant. Probability peak is smaller at 35 m and not resolvable at 120 m. (c) With the second mode dominant (80% of energy in second mode, 20% in modes 3 and 4) peaks can be seen at 35m and at 80 m; a small peak is just resolvable at 120 m. Dotted curve is the background probability density owing to temporal variations.

The zero-crossing density must be found by comparing each individual drop speed profile with a mean drop speed. For our data the constant local drop speed is not exactly known; our best estimate, the average over all drops at all depths for unchanged wing angle, may be affected by phase-biasing, as was discussed later, or by depth-dependent effects. Another statistic related to the zero-crossing density which is

PROFILE CROSSING DENSITY
(% Probability per 10 m Interval)

Fig. 8. Probability of finding a profile crossing in a 10-m interval calculated from the August 26 drops. Small peak is resolved at 35-40 m. At greater depths, probability is not significantly different from the background temporal modulation, providing evidence that mode 1 is dominant. Uncertainties are assigned by assuming Poisson statistics.

less sensitive to such mean depth-dependent trends is the 'profile-crossing density' (PCD), which is computed by comparing each profile to all other profiles and determining the probability of finding a point of equality in a given depth interval.

The PCD statistic has in general much the same qualities as the zero-crossing density. Near nodes of a given dominant mode, the PCD will be large, and away from nodes it will be small. If high-order modes are energetic, the PCD is large where dN/dz is large (Figure 7a), while if the first mode is dominant, the PCD will be nearly constant with depth (Figure 7b). If the second mode is dominant, the PCD will be large at 80-m depth (Figure 7c), where the second mode has a node point. Below the turning point, no nodes can be present, and the vertical velocity can be approximated over small depth ranges by a function constant with depth and oscillatory in time. The PCD in such a region has the same value as the zero-crossing density and is determined only by the frequency; we term this value the 'background.' It can be easily shown that the frequency of the wave is given by $BS_D/(\pi\Delta z)$, where B is the PCD background level and Δz is the depth interval over which the PCD is calculated.

The profile crossing statistic for the August 26 drops (Figure 8) shows structure little different from that expected from purely temporal variations. The profile crossings are nearly uniform with depth below 40 m, indicating that the wave function ψ does not vary rapidly with depth, and the profile crossings that occur are explicable by the background zeros of the temporal modulation of the fundamental mode.

For August 29 the profile crossing statistics (Figure 9) have a different character. A peak occurs at ~80 m which is absent on August 26. The background temporal-modulation level is 7% per 130 m, corresponding to a 3-cph wave. Thus while the August 26 drops show a preponderance of first-mode energy (ψ nearly constant with depth), the August 29 drops show that more than the first mode is energetic. The August 29 peak occurs at ~80 m, and we surmise that the second mode is ener-
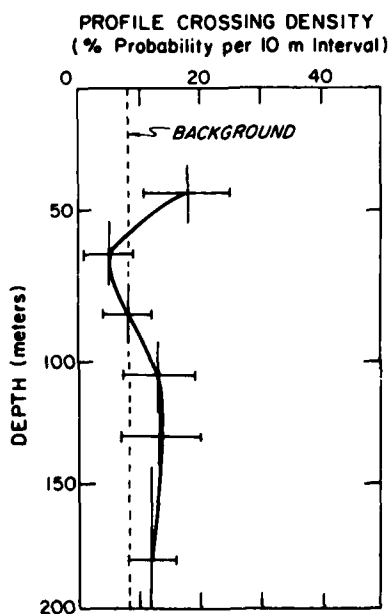
getic, since a 3-cph wave has a second-mode zero-crossing at ~80 m, leading to a high profile crossing density at that depth. The energy distribution necessary to produce a prominent 80-m peak is of course not unique, but if the relative weight of second-mode energy is less than 50%, the peak is greatly reduced in height. Clearly, on August 29 the second mode carried most of the internal wave energy; the remainder must have been mostly in the higher-order modes to have a prominent peak between 35 and 55 m. The fundamental mode could not have been very energetic.

The energy distribution for August 26 is quite different and considerably more complex. The first mode was dominant, but because of limited statistical reliability, the distribution among the higher modes cannot be discerned. Synthetic profile crossing densities consistent with the August 26 density can have energy distributed among the first five modes as m^{-n}, where $1 \le n \le 2$. If more than five modes are used, n must be greater than 2. Neither the equal partition of energy assumed by GM72 with a mode number ≥ 4 nor the tapered distribution assumed by GM75 with mode number ≥ 2 can explain the observed density. (We mention this contrast with the Garrett and Monk models even though they were constructed only for the permanent pycnocline because their application to surface waters is sometimes attempted.)

OTHER STATISTICAL MEASURES

A least squares fitting procedure can be used as an alternative to the above approach for estimation of the modal energy distribution. Letting $\mathscr{W}(z) \equiv \langle w(z)^2 \rangle \phi$, where $w(z)$ is the observed drop speed variation and the angle brackets indicate phase averaging, it can be shown that, if a single frequency ω is dominant, an estimator of $\mathscr{W}(z)$ is

$$\tilde{\mathscr{W}}(z) = \frac{1}{2} \sum_{m=0}^{\infty} \psi_m(z;\omega)^2 [A_{1m}^2(\omega) + A_{2m}^2(\omega)] \quad (7)$$

PROFILE CROSSING DENSITY
(% Probability per 10 m Interval)
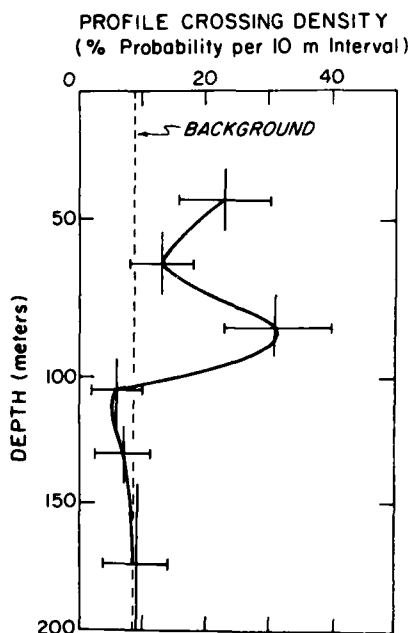
Fig. 9. Probability of finding a profile crossing in a 10-m interval calculated from the August 29 drops. Peaks at 35–40 and 80 m show strong dominance of second mode and weak contribution from higher modes. No peak is resolvable at 120 m.
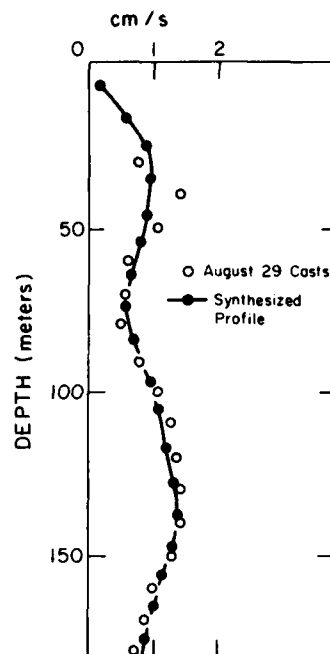
Fig. 10. Comparison of $\langle w(z)^2 \rangle_\phi^{1/2}$ calculated from the August 29 casts (open circle) and vertical velocity profiles calculated from the second-mode dominated energy distribution used in Figure 7c (crosses). Each profile is normalized to unity variance between 30 and 180 m. Note characteristic rectified second mode shape. Energy distribution among the individual modes is uncertain by ~50%, but second mode dominance is clear.

and the modal energy may be estimated by minimizing

$$\sum_z \{\langle w(z)^2 \rangle_\phi - \sum_m \psi_m(z;\omega)^2 [A_{1m}^2(\omega) + A_{2m}^2(\omega)]\}$$

with respect to $A_{1m}^2(\omega) + A_{2m}^2(\omega)$.

This fitting procedure yields a result quite consistent with the profile crossing analysis: For both days, most of the energy was in the first two modes, and the second mode was dominant on the later day. The characteristic rectified second mode shape can be clearly seen for August 29 (Figure 10). A detailed specification of the energy distribution would not be warranted on the basis of the number of drops available. By using synthetic profiles constructed from the wave functions with a specified energy distribution among modes and random phases one can show that 20 drops or more are necessary to determine the energy in modes other than the most energetic.

The effect of error in the assumed dominant frequency may be tested by constructing synthetic profiles of a given frequency and fitting to wave functions at a different frequency. It can thus be established that for the N profile at station P, waves of 2 cph cannot be distinguished from those of 3 cph when using only seven or eight drops, assuming either frequency as dominant yields the same result.

CONCLUSIONS

1. Vertical velocities associated with internal waves can be determined from the pressure record of a small, nearly freely falling probe.

2. Either spatial or temporal variability of the velocities may be emphasized in the records by adjusting the dropping

speed, in particular by making the time required to traverse a wavelength small or large, respectively, with respect to the period.

3. These velocities are associated with waves of frequency 2.5–4 cph, a band which contains a large fraction of the total kinetic energy of vertical motion.

4. During the Mile experiment, typical rms drop speed velocity variations in this band were 0.013 m s^{-1}.

5. Some indication of the partition of energy between modes can be obtained by zero-crossing analysis or by least squares fitting to assumed wave functions.

6. The energy partition between modes can change radically in three days; this implies that if a 'universal' modal energy distribution can be formulated for the seasonal thermocline, it can be valid only for an average over a period of at least several days.

7. On the occasions of the measurements, the motions were dominated by the first and second modes. Higher modes contributed little to the total energy.

With just two cases available for examination, firm reasons for the markedly different modal energy distributions seen on August 26 and August 29 cannot be given. *Käse and Clarke* [1978] find that the 2- to 5-cph frequency band is often dominated by the first mode and that waves in this band may not be stationary over periods of 1 day or less. Perhaps differences in meteorological and surface wave conditions, although not large, contributed to the difference we find in energy distribution. It seems more likely that some peculiarity in the low-frequency internal wave field, the density structure, or the forcing mechanism may preferentially select a given low-order mode. Any universal model of high-frequency waves must thus suppose an averaging interval of at least many days, perhaps even weeks or months, a particularly grim prospect for the experimentalist.

APPENDIX

To get some idea of the response of the instrument to variations of vertical velocity of the water, we consider its response to a surface gravity wave. If we assume that even at surface wave frequencies the instrument maintains a constant vertical velocity with respect to the water it passes through, then its instantaneous fall speed with respect to mean sea level is $S_D + w$, S_D being the terminal velocity of the instrument and w the vertical component of the orbital velocity of the wave. If we describe the wave in terms of a velocity potential ϕ, w and the pressure P are given by $w = \partial\phi/\partial z$ and $P = \rho g z + \rho(\partial\phi/\partial t)$ where z is downward, ρ is density, and g is the acceleration of gravity. We calculate the observed fall speed as

$$S_{OB} = \frac{1}{\rho g}\frac{dP}{dt} = \frac{1}{\rho g}\left[\frac{\partial P}{\partial t} + (w + S_D)\frac{\partial P}{\partial z}\right]$$

Inserting the expression for P in terms of ϕ and multiplying, we find

$$S_{OB} = -\frac{1}{g}\frac{\partial^2\phi}{\partial t^2} + w + S_D - \frac{1}{g}\frac{\partial^2\phi}{\partial z\partial t}w - \frac{1}{g}\frac{\partial^2\phi}{\partial z\partial t}S_D$$

At this point we find different conclusions for deep water and shallow water waves. For deep water waves $w = (1/g)(\partial^2\phi/\partial t^2)$ so the first two terms cancel, and

$$S_{OB} = S_D\left[1 - \frac{1}{g}\frac{\partial w}{\partial t}\left(1 + \frac{w}{S_D}\right)\right]$$

As long as $(\partial w/\partial t)/g \ll 1$ and w is not larger than S_D, $S_{OB} \approx S_D$. That is, surface waves will not be prominent in the pressure record as long as the instrument responds quickly enough that its speed is truly $S_D + w$. If its momentum were so great that its speed relative to mean sea level were constant, the pressure perturbation of the waves would be directly visible in the record. In shallow water waves, w is small and again pressure perturbations would appear directly in the record.

The observed pressure records are as was expected for the case where the instrument maintains speed constant with respect to the water near it. In deep water, little signal at surface wave frequencies is seen in the pressure record, while in shallow water the effect is quite prominent in the record. The swell-induced pressure oscillations actually increase as the instrument nears bottom, as was expected. Therefore we conclude that the instrument has such large drag relative to its inertia that it responds to local water velocity even at swell frequencies. It must then have no difficulty in responding at internal wave frequencies.

REFERENCES

Briscoe, M. G., Preliminary results from the trimoored internal wave experiment (Iwex), *J. Geophys. Res.*, 80, 3872–3884, 1975.

Cairns, J. L., Internal wave measurements from a midwater float, *J. Geophys. Res.*, 80, 299–306, 1975.

Desaubies, Y. J. F., and M. C. Gregg, Observations of internal wave vertical velocities by a free-fall vehicle, *Deep Sea Res.*, 25, 933–946, 1978.

Garrett, C., and W. Munk, Space-time scales of internal waves, *Geophys. Fluid Dyn.*, 2, 225–264, 1972.

Garrett, C., and W. Munk, Space-time scales of internal waves—A progress report, *J. Geophys. Res.*, 80, 291–297, 1975.

Gregg, M. C., and C. S. Cox, Measurement of the oceanic microstructure of temperature and electrical conductivity, *Deep Sea Res.*, 18, 925–934, 1971.

Hayes, S. P., T. M. Joyce, and R. C. Millard, Measurements of vertical fine structure in the Sargasso Sea, *J. Geophys. Res.*, 80, 314–319, 1975.

Käse, R. H., and R. A. Clarke, High frequency internal waves in the upper thermocline during GATE, *Deep Sea Res.*, 25, 815–825, 1978.

Pinkel, R., Upper ocean internal wave observations from Flip, *J. Geophys. Res.*, 80, 3892–3910, 1975.

Turner, J. S., *Buoyancy Effects in Fluids*, 367 pp., Cambridge University Press, New York, 1973.

Voorhis, A. D., Measurements of vertical motion and the partition of energy in the New England slope water, *Deep Sea Res.*, 15, 599–608, 1968.

An Arc Tangent Model of Irradiance in the Sea

J. RONALD V. ZANEVELD AND RICHARD W. SPINRAD

School of Oceanography, Oregon State University, Corvallis, Oregon 97331

The solar energy flux as a function of depth (the irradiance profile) in the ocean is an important function. It influences the dynamics of the mixed layer via the heat budget as well as the biology of the euphotic zone. The following three-parameter model can take into account the very rapid decrease near the surface due to absorption of long-wavelength radiation by water as well as the eventual exponential decrease at great depths. $E(z) = E(0)e^{-K_1 z}(1 - K_2 \arctan K_3 z)$, where $E(z)$ is the irradiance at depth z and K_1, K_2, and K_3 are constants that depend on the optical properties of the water. The constants are determined for Jerlov's water types. The constants can readily be calculated from any irradiance profile.

INTRODUCTION

Solar radiation in the region of 300–2500 nm is a source of energy for the upper ocean. This energy influences the dynamics of the ocean and is the ultimate power source of the entire oceanic ecosystem. Much of the light energy (with wavelengths of 800–2500 nm) is absorbed in the first meter. The profile of energy flux (irradiance) in the first meter is governed primarily by the absorption properties of pure water. At greater depths and for the shorter wavelengths, scattering and absorption by suspended particles becomes the dominant process. The spectrum of light continuously changes as a function of depth, since each wavelength has a different rate of attenuation. Heat budget and ecosystem modeling both require a simple mathematical model of irradiance as a function of depth. This paper describes a three-parameter model that can take account of the rapid decrease of solar energy near the sea surface as well as the eventual near-asymptotic exponential decrease at great depths.

In a homogeneous ocean, irradiance penetration for a given wavelength λ is given by

$$E_\lambda(\lambda, z) = E_\lambda(\lambda, 0) \int_0^z e^{-K(\lambda, z)} dz \qquad (1)$$

where $E_\lambda(\lambda, z)$ is the irradiance per unit wavelength for wavelength λ at depth z; $K(\lambda, z)$ is the irradiance attenuation coefficient for wavelength λ at depth z. The irradiance for all wavelengths, $E(z)$, is then governed by

$$E(z) = \int_{\lambda=0}^{\infty} E_\lambda(\lambda, z) \, d\lambda = \int_{z=0}^{z} \int_{\lambda=0}^{\infty} E_\lambda(\lambda, 0) e^{-K(\lambda, z)z} \, d\lambda \, dz \qquad (2)$$

or

$$E(z) = E(0) \int_{z=0}^{z} \int_{\lambda=0}^{\infty} \frac{E_\lambda(\lambda, 0)}{E(0)} e^{-K(\lambda, z)z} \, d\lambda \, dz$$

We can thus define

$$g(z) = \int_{z=0}^{z} \int_{\lambda=0}^{\infty} \frac{E_\lambda(\lambda, 0)}{E(0)} e^{-K(\lambda, z)z} \, d\lambda \, dz \qquad (3)$$

as the function which determines the penetration of solar energy into the ocean. $E_\lambda(\lambda, 0)/E(0)$ is the normalized spectral distribution of solar energy just beneath the ocean surface. The functional form of $g(z)$ has considerable bearing upon the absorption of energy as a function of depth, but it is not easy to model, since the attenuation coefficients $K(\lambda, z)$ decrease

sharply with decreasing wavelength down to a minimum for $\lambda \approx 475$ nm for the clearest ocean water. For more turbid waters the wavelength of maximum transmission may shift within the spectrum. All light with $\lambda \geq 800$ nm is attenuated mostly in the first meter of the sea surface [Jerlov, 1976]. A simple exponential model as is commonly used thus underestimates the attenuation near the surface. At much greater depths the irradiance becomes nearly monochromatic, and the exponential model is valid. In that case we can write [Jerlov, 1976; Tyler and Preisendorfer, 1962]

$$E(z) = E(z') \exp\left[(-K_1(z - z')\right] \qquad (4)$$

where $E(z)$ is the received irradiance at depth z (in W/m²); $E(z')$ is the irradiance at the reference depth z' (in W/m²); and K_1 is the irradiance attenuation coefficient (in m⁻¹).

The value of K_1 obtained from this expression is usually obtained from the straight-line portion of the curve of log I versus z [e.g., Smith et al., 1973].

Recently, the irradiance-depth curve has been modeled by means of a bimodal exponential expression [Kraus, 1972; Paulson and Simpson, 1977]. The expression used,

$$E(z) = E(0)[R \cdot \exp(-C_1 z) + (1 - R) \exp(-C_2 z)]$$

employs one exponential decay term for an upper layer where absorption of long-wave light is important and a second exponential decay term for greater depths where the light which is attenuated is in the blue-green region. The greatest errors in this expression occur in the surface layer, especially above 10 m, since the light there is attenuated faster than an exponential.

In the model developed herein, which is also a three-parameter model, the curve of the log of irradiance versus depth is assumed to be a product of the original irradiance decay expression (1) and a form of the arc tangent curve. This permits the near-surface irradiance to be attenuated very rapidly. By using the surface irradiance values and values of the irradiance at three other depths (two deep and one very shallow) the complete profile of irradiance with depth can be obtained. The four irradiance values permit one to calculate the three parameters which define the irradiance attenuation properties of a water mass. These parameters have been determined for all of the water types as classified by Jerlov [1976]. We are considering the total irradiance field (300–2500 nm), as does Jerlov [1976]. In addition, determinations of these parameters have been made for irradiance profiles from the eastern tropical Pacific [Spinrad et al., 1979], the Atlantic Ocean near the

TABLE 1. Calculated Values of K_1, K_2, K_3, and K_2 arctan K_3 for
Each of Jerlov's [1976] Water Types

Water Type	K_1, m^{-1}	K_2	K_3, m^{-1}	K_2 arctan K_3
I	0.0440	0.3963	4.4547	0.535
IA	0.0490	0.3981	4.4236	0.537
IB	0.0574	0.4103	4.0725	0.546
II	0.0670	0.4158	3.9865	0.551
III	0.1250	0.4234	3.7062	0.554
1	0.1360	0.4500	3.3772	0.577
3	0.2231	0.4495	3.7049	0.588
5	0.3541	0.4626	3.6806	0.604
7	0.5028	0.4789	3.7150	0.626
9	0.5913	0.5247	3.6026	0.682
Eastern tropical Pacific	0.0637	0.6280	0.4896	0.286
Eastern tropical Atlantic	0.0691	0.3650	0.6580	0.186
Lake Tahoe	0.0680	0.251	0.622	0.140

Congo River [Zaneveld et al., 1979], and Lake Tahoe [after Smith et al., 1973].

THE MODEL

In homogeneous water we may remove the depth dependence of K, and therefore

$$g(z) = \int_{z=0}^{z} \int_{\lambda=0}^{\infty} \frac{E_\lambda(\lambda, 0)}{E(0)} e^{-K(\lambda)z} \, d\lambda \, dz$$

$$= -\frac{1}{K} \int_{\lambda=0}^{\infty} \frac{E_\lambda(\lambda, 0)}{E(0)} [e^{-K(\lambda)z} - 1] \, d\lambda$$

If the wavelength of minimum attenuation is given by λ_m, then

$$g(z) = \frac{-e^{-K(\lambda m)z}}{K} \int_{\lambda=0}^{\infty} \frac{E_\lambda(\lambda, 0)}{E(0)} [e^{-[K(\lambda)-K(\lambda m)]z} - 1] \, d\lambda \quad (5)$$

or

$$g(z) = e^{-K(\lambda_m)z} f(z) \quad (6)$$

Now $f(z)$ must approach a constant value at a large depth at which the irradiance becomes nearly monochromatic. Also,

$f(z)$ must decrease much faster than a simple exponential. Such a function can be modeled by means of an arc tangent function, retaining a three-parameter model but permitting the energy to be attenuated rapidly in the surface layer. We thus set

$$f(z) = 1 - K_2 \arctan K_3 z \quad (7)$$

so that at $z = 0$, $f(z) = 1$, and at $z = \infty$, $f(z) = 1 - (K_2\pi/2)$. The rate at which $f(z)$ decreases from 1 to $[1 - (K_2\pi/2)]$ is determined by K_3. Our complete model then becomes

$$E(z)/E(0) = \exp(-K_1 z)(1 - K_2 \arctan K_3 z) \quad (8)$$

where we have set $k(\lambda_m) = K_1$.

The parameters K_1, K_2, and K_3 can be determined by using irradiance values at the surface (z_0), at a shallow depth (z_1), and at two large depths (z_2, z_3). The value of K_1 is obtained by using only the exponential factor of (8) with the irradiances at the two great depths. That is,

$$E(z_3)/E(z_2) = \exp[-K_1(z_3 - z_2)] \quad (^0)$$

or

$$K_1 = \frac{-[\ln E(z_3) - \ln E(z_2)]}{(z_3 - z_2)} \quad (10)$$

K_2 is then calculated by assuming that at the great depth (z_3), arctan $K_3 z_3$ can be approximated by $\pi/2$ so that

$$K_2 = \frac{2}{\pi} \left[1 - \frac{E(z_3)}{E(z_0)} \exp(K_1 z_3) \right] \quad (11)$$

Then to solve for K_3, K_1 and K_2 are substituted into (8), using the shallow irradiance value:

$$K_3 = \left\{ \tan \left[\frac{1}{K_2} \left(1 - \frac{E(z_1)}{E(z_0)} \right) \exp(K_1 z_1) \right] \right\} z_1^{-1} \quad (12)$$

In the solution of (11) the assumption that arctan $K_3 z_3 = \pi/2$ is true within 1% only when $K_3 z_3 \geq 64.5$. In the case of coastal water measurements it may be impossible to obtain
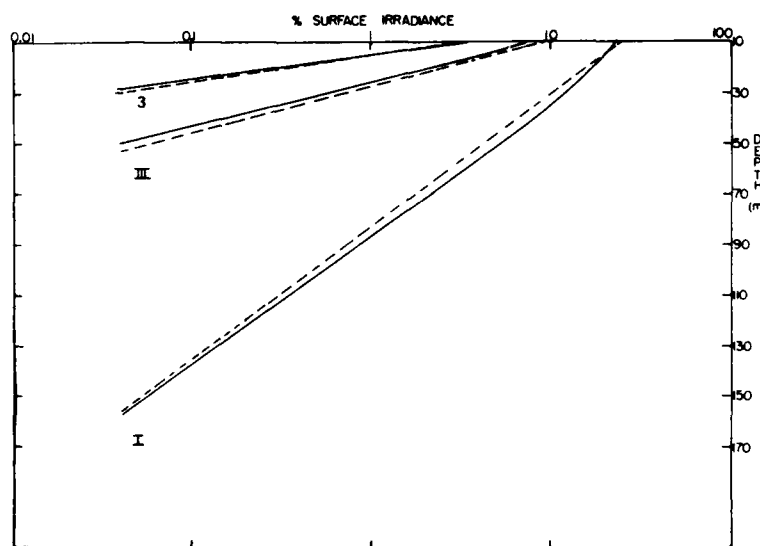

Fig. 1. Depth profiles of downward irradiance (below 10 m) in percent of surface irradiance for water types I, III, and 3.
Solid curves are from Jerlov [1976]. Dashed curves are as computed from the arc tangent model.
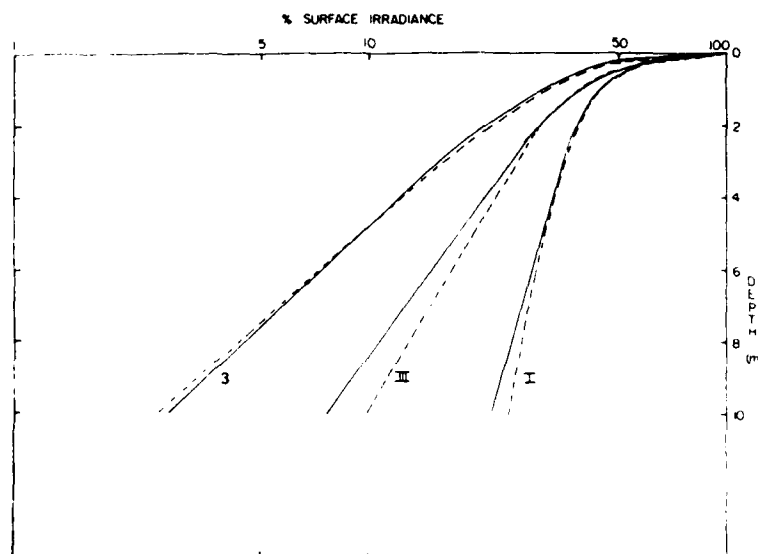
Fig. 2. Depth profiles of near-surface downward irradiance in percent of surface irradiance for water types I, III, and 3. Solid curves are from *Jerlov* [1976]. Dashed curves are as computed from the arc tangent model.

light levels adequate to measure at depths which satisfy this approximation. Consequently, an iterative calculation is carried out in which (11) is first solved for K_2, assuming $K_1 z_1 = \pi/2$. Equation (12) is then solved as before, and the solution for K_1 (along with the calculated value of K_1) is used in (8) to resolve the new value of K_2. This iterative process is used until the variation in K_2 with the previous iteration is less than 5%.

RESULTS AND OBSERVATIONS

The calculated values of K_1, K_2, K_3, and K_2 arctan K_1 are shown in Table 1 for each of *Jerlov*'s [1976] water types and for stations in the eastern tropical Pacific [*Spinrad et al.*, 1979], the eastern Atlantic [*Zaneveld et al.*, 1979], and Lake Tahoe [see *Smith et al.*, 1973].

Figure 1 shows the levels of total irradiance versus depth below 10 m for several of *Jerlov*'s [1976] water types and as computed from the arc tangent model. Similar results for the upper 10 m of ocean surface are shown in Figure 2. The arc tangent model fits the actual irradiance profile within 5% of the surface irradiance value for all depths. The model also approximates both coastal and oceanic irradiance profiles equally well.

The value of K_1 indicates the exponential slope of the irradiance profile with depth in the deep ocean, where the irradiance is nearly monochromatic. Generally, the wavelength of maximum irradiance transmission increases with increasing values of K_1. Clean ocean water (such as type I) with a value of K_1 from 0.03 to 0.05 has a peak transmission at a wavelength of approximately 475 nm; water type 9 has a peak transmission at 575 nm [*Jerlov*, 1976].

At great depths the value of arctan $K_1 z$ approaches $\pi/2$, which means that the deep irradiance is described as

$$\frac{E(z)}{E(0)} \cong \exp\left(-K_1 z\right)\left(1 - K_2 \frac{\pi}{2}\right) \quad (13)$$

As K_2 increases, the amount of irradiance at a given depth decreases. Since the irradiance at great depths is nearly monochromatic (as determined by K_1), it is seen that K_2 indicates

the relative amounts of monochromatic light available for each water type. Generally, after the surface attenuation of long-wave irradiance in the ocean there is more blue light available than green. Since clean ocean water has its maximum transmission in the blue light region, the value of K_2 should be lower for clean ocean water than for the more turbid coastal waters.

The magnitude of K_2 arctan $K_1 z$ describes the strong near-surface attenuation of long-wavelength irradiance. The values as indicated for *Jerlov*'s [1976] water types are higher than those measured in the Pacific, the Atlantic, and Lake Tahoe. This is due to the low response of the irradiance meters used in the latter examples for long-wave irradiance (infrared). The meter used in the Atlantic and Pacific does not detect any irradiance at wavelengths greater than 1000 nm. The maximum wavelength of detection for the meter used in Lake Tahoe is 750 nm. The determinations of K_1 for *Jerlov*'s [1976] water types are for measurements of irradiance up to 2500 nm. The irradiance between 1000 and 2500 nm is attenuated within the first meter of seawater, so consequently, the values of K_1 are much higher for *Jerlov*'s [1976] water types.

The importance of this arc tangent model lies in its accuracy at shallow depths. There is a strong attenuation of long-wave solar radiation in the upper 10 m of the sea surface. Accurate modeling of the irradiance profile in this layer is important for oceanic heat budget studies and photosynthesis determinations.

REFERENCES

Jerlov, N. G., *Marine Optics*, 231 pp., Elsevier, New York, 1976.
Kraus, E. B., *Atmosphere-Ocean Interaction*, 275 pp., Oxford University Press, New York, 1972.
Paulson, C. A., and J. J. Simpson, Irradiance measurements in the upper ocean, *J. Phys. Oceanogr.*, 7, 953-956, 1977.
Smith, R. C., J. E. Tyler, and C. R. Goldman, Optical properties and

color of Lake Tahoe and Crater Lake, *Limnol. Oceanogr.*, *18*, 189–199, 1973.

Spinrad, R. W., J. R. V. Zaneveld, and H. Pak, Irradiance and beam transmittance measurements off the west coast of the Americas, *J. Geophys. Res.*, *84*, 355–358, 1979.

Tyler, J. E., and R. W. Preisendorfer, Transmission of energy within the sea, in *The Sea*, vol. 1, edited by M. N. Hill, pp. 397–451, Interscience, New York, 1962.

Zaneveld, J. R. V., R. W. Spinrad, and D. W. Menzies, Hydrographic and optical measurements in the Congo River and Angola Basin during May 1978, *Data Rep.* *79-3*, Sch. of Oceanogr., Oreg. State Univ., Corvallis, 1979.

FIRST RECORDS OFF OREGON OF THE
PELAGIC FISHES *PARALEPIS ATLANTICA*,
GONOSTOMA ATLANTICUM, AND *APHANOPUS*
CARBO, WITH NOTES ON THE ANATOMY
OF *APHANOPUS CARBO*[1]

The species covered in this report are common in parts of the Atlantic Ocean and all are known to occur in the Pacific Ocean. We fill a gap in knowledge of the distribution of two species known formerly only north and south of Oregon, extend the northward range of *Gonostoma atlanticum* Norman, and report inshore occurrences of *Paralepis atlantica* Krøyer. The unusual gross anatomy surrounding the gas bladder of *Aphanopus carbo* Lowe is worthy of description.

Methods

Counts and measurements followed those of Hubbs and Lagler (1958) and all measurements were taken to the nearest 0.1 mm. Specimens are catalogued in the fish collections of the Department of Fisheries and Wildlife (OS) or the School of Oceanography (OSUO), Oregon State University. Anatomical terminology follows that of Lagger et al. (1962) and Romer (1970). Four specimens of *A. carbo* from Oregon were dissected and two were radiographed. Two specimens from the Atlantic Ocean off Madeira were dissected and radiographed. Complete vertebral counts could not be made from the radiographs due to poor resolution of the small posterior caudal vertebrae.

Notes on Distribution and Morphology

Paralepis atlantica has been recorded in the eastern Pacific from Baja California and California (Rofen 1966) and from the vicinity of Willapa Bay, Wash. (Kajimura 1969). Bakkala (1971) reported the species from surface waters of the central Pacific at lat. 48°00' N, long. 165°00' W.

Two specimens of *P. atlantica* were found on shore in northwestern Oregon. One (OS 956:456 mm SL) was taken alive on the beach at Netarts, Tillamook County, on 7 October 1963. Another (OS 5160:466 mm SL) was found dead on the beach 29 km north of Seaside, Clatsop County, on 16 May 1960. A specimen of *G. atlanticum* (OSUO 2402:59 mm SL) was captured on 30 July 1977, 65

km west of Newport (lat. 44°38' N), between 335 and 400 m deep with a small Cobb midwater trawl (10 m mouth opening) with an opening and closing cod end (Pearcy et al. 1977). This female fits the descriptions by Grey (1960, 1961, 1964) and Mukhacheva (1972). Maximum diameter of eggs in the ovary was 0.16 mm. Grey (1964) considered fish of this size to be mature.

Gonostoma atlanticum is usually distributed in warm water of the Atlantic, Pacific, and Indian Oceans. It is found in the eastern and central North Atlantic, and it has usually been recorded from equatorial waters in the Pacific and Indian Oceans. The northernmost previous record (lat. 34°18.6' N) for its occurrence in the Pacific Ocean was that of Berry and Perkins (1966), who captured several individuals off southern California. The temperature of the water in which the OSUO specimen was captured was 5.37°-5.70° C. Backus et al. (1965) reported the occurrence of *G. atlanticum* in the Atlantic Ocean in waters of 10°-11° C.

Aphanopus carbo was first reported from the Pacific Ocean off Bodega Bay and Fort Bragg, Calif., in 1969 (Fitch and Gotshall 1972). Peden (1974) reported a specimen from off the Strait of Juan de Fuca. Clarke and Wagner (1976) collected larvae and juveniles off Hawaii. Five specimens were taken off Oregon in 1976: OS 5381 (476 mm SL), about 29 km off Cape Meares, at about 183 m; OS 6115 (639 mm SL), about 37 km off Florence, at about 146 m; OSUO 2352 (570 mm SL), 2353 (558 mm SL), 2354 (547 mm SL), 120 km west of Newport, at about 400-480 m, in an opening and closing net.

Our specimens compared with those from Madeira, had slightly smaller horizontal orbit, slightly wider suborbital head width, and slightly shorter anal spines. Otherwise the Atlantic and Pacific Ocean specimens are very similar.

Gas Bladder Anatomy in *Aphanopus carbo*

Although Maul (1954) mentioned that on retrieval to the surface the gas bladder in *A. carbo* expands greatly, causing the skin of the abdomen to split, none of our specimens exhibited this characteristic. Shepel[2] stated that none of the specimens examined by him had their skin split, but that the stomach in most specimens (all from the Atlantic Ocean) were everted. Only one of our

---

[2]L. I. Shepel, Fishery Reconnaissance, Murmansk, U.S.S.R., pers. commun. 15 November 1977.

specimens had an everted stomach. These differences led us to examine the gas bladder and associated structures in *A. carbo*.

Bone (1971) described the anatomy and histology of the gas bladder of *A. carbo*. Tucker (1953) briefly mentioned the ribs and provided partial radiographs of the ribs and vertebral column in *A. carbo* and *A. schmidti*. However, we found no descriptions of the relationship of the bladder to the vertebral column, ribs, kidneys, and coelom. Our examination of *A. carbo* shows that the gas bladder of this species, and the structures associated with it, has several unusual characteristics. Little variation in anatomy was noted in our specimens.

The position of the gas bladder in *A. carbo* is typical of that in most fishes; it is ventral to the vertebral column and kidneys and dorsal to the peritoneal (abdominal) cavity (i.e., retroperitoneal) (Figure 1). The anterior end of the gas bladder is below the sixth vertebra. From it, two minute extensions proceed anterolaterally at 45°, but the size of the extensions did not allow us to trace them forward more than a few millimeters. Posteriorly, the gas bladder extends to a blunt end between vertebrae 42 and 45, directly dorsal or slightly anterior to the vent. Although the dorsoposteriad portion of the peritoneal cavity narrows and curves ventrally, the gas bladder continues to parallel the vertebral column except for a slight dip near the posterior end. The region between the gas bladder and the peritoneal cavity is filled with hypaxial muscle. The bladder is slightly narrowed at its anterior and posterior ends. It is oval in cross section and slightly smaller than the diameter of vertebral centra in our preserved specimens (Figure 1).

The kidneys extend anteriorly from the region dorsal to the vent to the posterior portion of the skull. They are enlarged in the area above the vent, and between the anterior of the gas bladder and posterior of the skull, and lie ventrolateral to the vertebral column and dorsolateral to the gas bladder. They terminate in a urinary duct that appears to empty into a urogenital sinus.

The ventral ribs are intimately associated with the gas bladder and kidneys. A pair of ventral ribs is present on all trunk vertebrae, but those anterior to the gas bladder are short and thin. These ribs are difficult to find but may be seen readily in radiographs. From immediately anterior to the gas bladder to about the ninth vertebra the ribs become progressively longer and
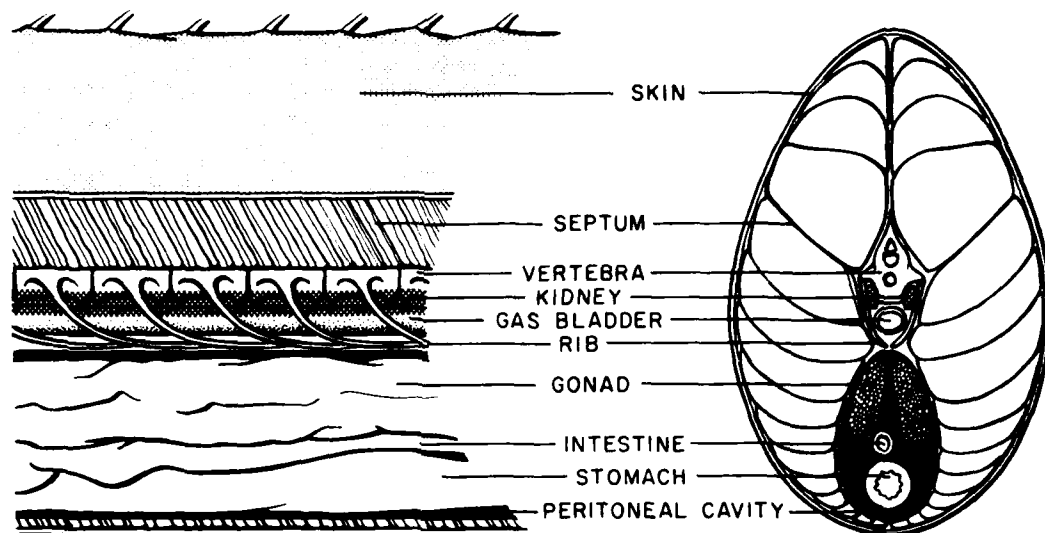
FIGURE 1.—Gross anatomy of the gas bladder and surrounding region in the black scabbardfish, *Aphanopus carbo*. Left: Partial sagittal section in region of the 14th-19th vertebrae. Muscle and other tissue have been removed from the region ventral to the indicated septum. Right: Cross section in the region of the 14th vertebra.

thicker. From that point posteriorly to the first caudal vertebra, all the ribs, except the last two to four, are of the same size, shape, and relative position. All the ribs extend laterally around the kidneys but the last few extend farther ventrally to encage the enlarged posterior portion of the kidneys. Where the ribs contact the gas bladder laterally, they turn abruptly posteriad and almost parallel the bladder while remaining in contact with it. In doing so, they curl beneath the bladder. Each rib extends posteriorly a distance almost equal to two vertebrae (Figure 1). Each rib appears to join a myocomma, then connect to the ventrolateral wall of the bladder. The gas bladder is thus surrounded by a "rib cage."

The hypaxial muscles, in conjunction with the ribs, surround the gas bladder almost completely. The only gap is a narrow medial band of connective tissue to which the ribs attach, present between the peritoneal membrane and the gas bladder (Figure 1).

The unusual anatomy of *A. carbo* invites speculation concerning its significance. The enclosure of the gas bladder in a rib cage apparently reinforces the gas bladder wall, which Bone (1971) has shown is composed of thick connective tissue. The combination of a thick, tough wall reinforced by muscle and bone seems likely to prevent the expansion of the gas bladder when ambient pressure decreases more rapidly than the gas contained in the bladder can be absorbed into the bloodstream. This species is known to feed on cephalopods (Zilanov and Shepel 1975). Possibly the anatomical modifications of its gas bladder and associated structures allow *A. carbo* individuals to pursue prey into significantly shallower water without having to adjust bouyancy and/or absorb gas.

Literature Cited

BACKUS, R. H., G. W. MEAD, R. L. HAEDRICH, AND A. W. EBELING.
   1965. The mesopelagic fishes collected during Cruise 17 of the R/V Chain, with a method for analyzing faunal transects. Bull. Mus. Comp. Zool. Harv. Univ. 134:139-158.
BAKKALA, R. G.
   1971. Occurrence of the barracudina, *Paralepis atlantica* Krøyer, in the central North Pacific Ocean. Fish. Bull., U.S. 69:881.
BERRY, F. H., AND H. C. PERKINS.
   1966. Survey of pelagic fishes of the California Current area. U.S. Fish Wildl. Serv., Fish. Bull. 65:625-682.
BONE, Q.
   1971. On the scabbard fish *Aphanopus carbo*. J. Mar. Biol. Assoc. U.K. 51:219-225.
CLARKE, T. A., AND P. J. WAGNER.
   1976. Vertical distribution and other aspects of the ecology ot certain mesopelagic fishes taken near Hawaii. Fish. Bull., U.S. 74:635-645.
FITCH, J. E., AND D. W. GOTSHALL.
   1972. First record of the black scabbardfish, *Aphanopus carbo*, from the Pacific Ocean with notes on other Californian trichiurid fishes. Bull. South. Calif. Acad. Sci. 71:12-18.
GREY, M.
   1960. A preliminary review of the family Gonostomatidae, with a key to the genera and the description of a new species from the tropical Pacific. Bull. Mus. Comp. Zool. Harv. Coll. 122:57-125.
   1961. Fishes killed by the 1950 eruption of Mauna Loa, Part V Gonostomatidae. Pac. Sci. 15:462-476.
   1964. *Family* Gonostomatidae. *In* Y. H. Olsen (editor), Fishes of the western North Atlantic. Part four, p. 78-240. Sears. Found. Mar. Res., Yale Univ., Mem. 1.
HUBBS, C. L., AND K. F. LAGLER.
   1958. Fishes of the Great Lakes region. Revised ed. Univ. Mich. Press, Ann Arbor, 213 p.
KAJIMURA, H.
   1969. Northern range extension for *Paralepis atlantica* Kroyer in the eastern North Pacific. Calif. Fish Game 55:246-247.
LAGLER, K. F., J. E. BARDACH, AND R. R. MILLER.
   1962. Ichthyology. John Wiley and Sons, Inc., N.Y., 545 p.
MAUL, G. E.
   1954. Notes and exhibitions. [A sketch of Madeiran ichthyology with observations on the ecology of the most important fishes.] Proc. Zool. Soc. Lond. 123:901-903.
MUKHACHEVA, V. A.
   1972. On the systematics, distribution and biology of the *Gonostoma* species (Pisces, Gonostomatidae). [In Russ., Engl. summ.] Tr. Inst. Okeanol. Akad. Nauk SSSR 93:205-249.
PEARCY, W. G., E. E. KRYGIER, R. MESECAR, AND F. RAMSEY.
   1977. Vertical distribution and migration of oceanic micronekton off Oregon. Deep-Sea Res. 24:223-245.
PEDEN, A.
   1974. Rare fishes, including first records of thirteen species, from British Columbia. Syesis 7:47-62.
ROFEN, R. R.
   1966. Family Paralepididae. *In* Fishes of the western North Atlantic. Part five, p. 205-461. Sears Found. Mar. Res., Yale Univ., Mem. 1.

ROMER, A. S.
   1970. The vertebrate body 4th ed. W B Saunders Co., Phila., 601 p.
TUCKER, D. W.
   1953. The fishes of the genus *Benthodesmus* (Family Trichiuridae). Proc. Zool. Soc. Lond. 123:171-197.
ZILANOV, V. K., AND L. I. SHEPEL.
   1975. A contribution to the ecology of black scabbardfish *Aphanopus carbo* Lowe in the North Atlantic. [In Russ.] Vopr. Ikhtiol. 93:737-740.

KEVIN M HOWE

Department of Fisheries and Wildlife
Oregon State University, Corvallis, OR 97331

DAVID L. STEIN

School of Oceanography
Oregon State University, Corvallis, OR 97331

CARL E. BOND

Department of Fisheries and Wildlife
Oregon State University, Corvallis, OR 97331

Spatial and Temporal Variations in the Population Size Structure of Three Lanternfishes (Myctophidae) off Oregon, USA

J. M. Willis and W. G. Pearcy

School of Oceanography, Oregon State University; Corvallis, Oregon 97331, USA

Abstract

Size-frequency distributions were determined for 3 common lantern-fishes (*Stenobrachius leucopsarus, Diaphus theta,* and *Tarletonbeania crenularis*) off Oregon in the summer. The fishes were caught mainly in sound-scattering layers by a large pelagic trawl with 5 opening-closing nets. Changes in depth distribution and diel vertical migration were evident for all 3 species. The size of *S. leucopsarus* increased markedly with depth both at 0 to 90 m at night and 250 to 500 m during the day. Larger *D. theta* were also found deeper during the day (between 250 and 450 m), but neither *D. theta* nor *T. crenularis* demonstrated size segregation in the upper 90 m at night. Large *D. theta* and small *T. crenularis* did not appear to migrate into surface waters at night. Age-Group O (15 to 20 mm) *S. leucopsarus* were most abundant in deep water (400 to 480 m) in the daytime and did not migrate into near-surface waters at night. Age-Group I (30 to 40 mm) *S. leucopsarus* were common at about 300 m by day and within the upper 30 m at night. Age-Group II-III (50 to 60 mm) apparently followed the evening ascent of Age-Group I fish and most resided at 75 to 90 m at night, beneath Age-Group I fish. Age-Group III+ fish (70 to 80 mm) were associated with Age-Group O at 400 to 480 m by day and usually did not migrate above 200 m at night. The size structure of *S. leucopsarus* differed among the nets of a single tow at one depth, or between two tows that fished the same depths on successive nights, indicating horizontal patchiness in age structure. *D. theta* demonstrated low within-tow variability in size composition which indicated a spatially more uniform age structure on a scale of kilometers. The size structures of these 3 lanternfishes were different in the same area and the same season during two different years, suggesting variable survival of year classes or horizontal patchiness of age composition in the area sampled.

Introduction

Ontogenetic changes in the patterns of depth distribution and diel vertical migration have been reported for many mesopelagic and deep-sea fishes, including members of the Macrouridae (Marshall, 1965; Merrett, 1978), Gonostomatidae (Grey, 1964; Badcock, 1970; Badcock and Merrett, 1976), Oneirodidae (Bruun, 1958; Pietsch, 1974), Scopelarchidae (Johnson, 1974), Paralepididae (Rofen, 1966) and Myctophidae (Fast, 1960; Badcock, 1970; Halliday, 1970; Clarke, 1973; Badcock and Merrett, 1976; Frost and McCrone, 1979). The general trend within these groups is for size to increase with depth. In his collections from near the Canary Islands, Badcock (1970) noted that ". . . a feature obvious with some of the abundantly caught species was the restriction of adolescent forms to the shallower regions of a given distribution." However, this is not a simple increase in size or age with depth. Bertelsen (1951) and Pietsch (1974) both noted that, while the larvae of ceratioid anglerfishes were epiplanktonic, post-metamorphic juveniles were found at the deepest reaches of a species' depth distribution, even deeper than the adults. Fast (1960) reported a similar phenomenon for the lanternfish *Stenobrachius leucopsarus.*

These ontogenetic depth changes may represent important adaptations in the life history strategy of a species for feeding, growth, reproduction and survival. Bruun (1958) and Pietsch (1974) speculated that interactions between ontogenetic vertical migrations and ocean currents may maintain a species within its optimal habitat.

The present paper examines size-frequency distributions of 3 common lanternfishes off Oregon: *Stenobrachius leucopsarus, Diaphus theta* and *Tarletonbeania crenularis,* and relates size structure to temporal, vertical and horizontal variations in sampling. Of these three species, *S. leucopsarus* is the best studied in terms of life history, age and growth (Fast, 1960; Smoker and Pearcy, 1970; Pearcy *et al.,* 1977, 1979). Tyler and Pearcy

Table 1. Summary of tows and nets used in this study. Those tows which provided sufficient data for all 3 species are marked with a cross. Blanks indicate that less than 40 individuals were captured for a tow. Depths that each net fished are given. All nets fished 40 min at depth, except Tows 2395 (30 min) and Tow 2396 (1 h). Cumulative percentage curves of size composition are included for some of these individual net catches in the text. *S.l.*: *Stenobrachius leucopsarus*; *D.t.*: *Diaphus theta*; *T.c.*: *Tarletonbeania crenularis*

Tow Nos.	Date	Time (hrs)	S.l.	D.t.	T.c.	Depths sampled by nets of a tow				
						1	2	3	4	5
2391	19.VII.1976	17.17-19.57	+	+			305-310	285	295-300	295
2392	19.VII.1976	22.30-01.20	+	+		0-55	55-80	80	80	80
2393	20.VII.1976	12.23-15.58	+	+	+		350	350	360	305-320
2394	20.VII.1976	18.35-21.15	+	+	+		300	240-250	230-240	360-430
2395	20.VII.1976	23.11-02.06	+	+	+	0-90	75-90	75	30	10-15
2396	21.VII.1976	12.55-16.55	+				480-400	440	440	440
2397	21.VII.1976	20.17-22.57	+	+	+		210	210	210	210
2398	22.VII.1976	09.44-12.24	+		+		320-210	210-200	200-195	200-240
2400	30.VII.1977	14.13-16.53	+	+	+		335-340	335-340	335-340	335-370
2401	30.VII.1977	20.00-22.40	+				310-330	310-300	300-320	295-320
2402	31.VII.1977	07.25-10.05	+	+	+		295-305	305-290	290-300	290-300
2404	31.VII.1977	18.22-21.02			+		200	200	200-250	200
2406	1.VIII.1977	15.53-18.33	+		+		345-350	missing	350-360	350-360

(1975) studied the feeding habits of all 3 species off Oregon, and Pearcy *et al.* (1977) presented data on vertical migration and distribution for all three.

None of these studies have addressed the vertical and horizontal size structure of these three species off Oregon. Previous studies have been made using smaller nets (1.8 m and 2.4 m Isaacs-Kidd midwater trawls, IKMT's), with small mouth areas. Consequently, relatively few fishes were captured, and larger individuals were undersampled. Larger nets, such as the one used in this study, are suited to capturing large numbers of micronekton of a broad size range.

Materials and Methods

Stenobrachius leucopsarus, Diaphus theta, and *Tarletonbeania crenularis* were collected from the R.V. "Pacific Raider" from 19 July through 22 July, 1976 and from the M.V. "Excalibur" from 30 July through 2 August 1977 at stations about 110 to 120 km off Newport, Oregon (44°40'N; 125°35'-125°40'W). Collections were made using a pelagic trawl with an effective frontal area (19 mm stretch-mesh) of about 50 m², equipped with a Multiple Plankton Sampler as an opening-closing device in the cod end with 5 separate nets, each with 9 mm stretch-mesh netting. An acoustical net monitor, mounted at the center of the headline, was used for depth determination (see Pearcy, in press).

The samples were not collected with this particular study in mind, but were part of a larger study on the correlation of net tow data with acoustic scattering data. Most tows were made in sound-scattering layers, and depths were not sampled systematically. The tows did not cover the entire range of the populations of these 3 species. In spite of these sampling limitations, some interesting features of large- and small-scale variations in size composition of all 3 species emerged which we feel

warrant presentation at this time. The conclusions presented herein should, however, be considered with these sampling limitations in mind.

Eight tows were made in 1976 and 9 in 1977. Fishes were preserved at sea in 10% formalin in seawater and later transferred to 50% isopropyl alcohol. Standard lengths (SL) were measured to the nearest 1 mm, and individuals of each species were grouped into 5 mm size intervals. A Kolmogorov-Smirnov (K-S) test of differences between cumulative size-frequency distributions was used (Tate and Clelland, 1957). A level of significance of 99% was used for all tests performed. Cumulative percentage curves were chosen for concise presentation of the data. Trends of increasing or decreasing size are shown by displacement of the curve to the left or right.

No actual measurements of surface irradiance were made during these two cruises; however, weather observations during the cruises show that conditions (cloud cover, fog, etc.) were relatively constant from day to day, and from night to night during both cruises. Therefore, the differences in size structure seen from day to day, or from night to night were probably due to size-specific depth or migration preferences, and not to variations in surface irradiance.

A study such as ours requires a large number of specimens to adequately represent the size structure of a species. This necessitates either towing a small net for a long time, which results in "blurring" of small-scale vertical and horizontal differences in size structure and poor condition of specimens, or shorter tows with a large net. We chose the latter method. A comparison of the large pelagic trawl used in this study with a 5.4 m² IKMT (Pearcy, in press) indicates that the pelagic trawl is effective in catching large numbers of mesopelagic fishes, as well as large-sized *Stenobrachius leucopsarus* and *Tarletonbeania crenularis* which were poorly represented in IKMT catches.
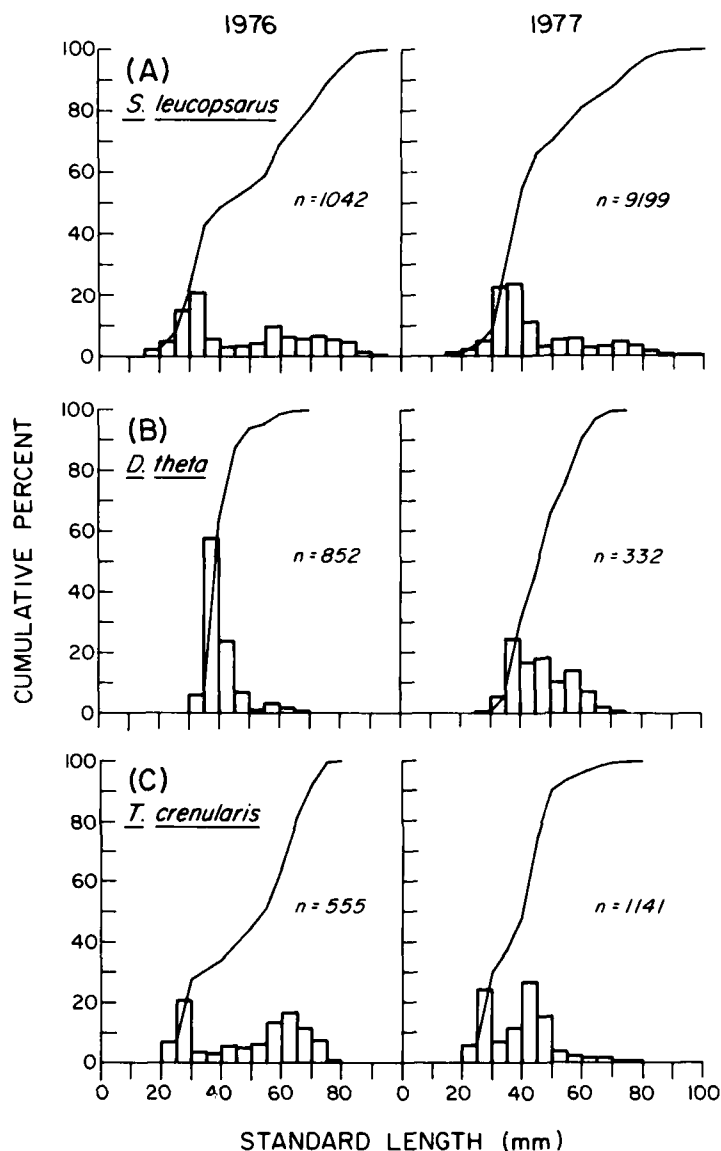
Fig. 1. *Stenobrachius leucopsarus* (A), *Diaphus theta* (B), and *Tarletonbeania crenularis* (C). Cumulative size-frequency curves and relative percentage histograms for 1976 and 1977 catches

For comparisons of "nets within a tow" and "tows within one cruise" only those nets or tows catching 40 or more individuals were considered, since this is the point where the values for the difference between curves are calculated rather than tabulated (Tate and Clelland, 1957). This allows comparison of nets or tows with unequal sample size. The first net of each sample, representing the oblique portion of the tow, generally was not included in this study if it fished more than about 150 m vertically, since it would not yield detailed information about depth distributions. Table 1 lists the inclusive times for all tows used in this study, the tows that contained 40 or more individuals of each of the 3 species, and the depths that each net fished.

Results

Year-to-Year Variations

Stenobrachius leucopsarus

Variations in size distributions of *Stenobrachius leucopsarus* collected in the summers of 1976 and 1977 are shown in Fig. 1A by cumulative percentage curves and relative-frequency histograms for each year. Only tows that sampled the common depth interval of 295 to 360 m (day and night) for both years are included in this figure. (The depth interval represented does not cover the entire vertical range of these 3 species, but lies at or
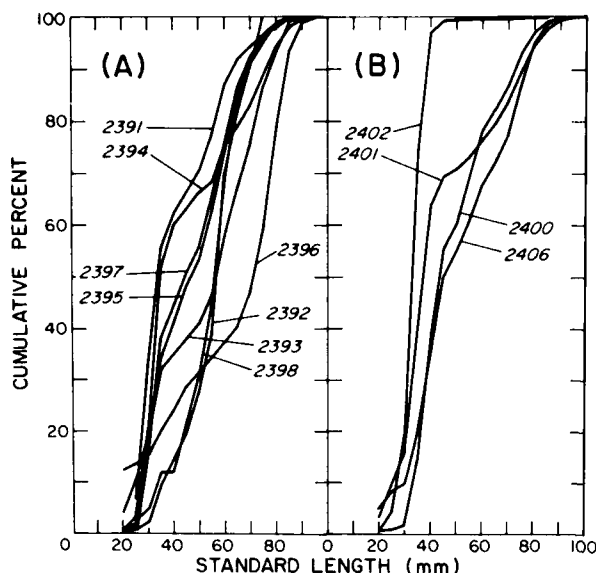
Fig. 2. *Stenobrachius leucopsarus.* Cumulative size-frequency curves for catches by tow, for 1976 (A) and 1977 (B). (A) Tow 2391, 285-310 m, 17.17-19.57 hrs, *n* = 146; Tow 2392, 0-80 m, 22.30-01.20 hrs, *n* = 950; Tow 2393, 305-360 m, 12.23-15.58 hrs, *n* = 489; Tow 2394, 230-430 m, 18.35-21.15 hrs, *n* = 407; Tow 2395, 0-90 m, 23.11-02.06 hrs, *n* = 515; Tow 2396, 400-480 m, 12.55-16.55 hrs, *n* = 791; Tow 2397, 210 m, 20.17-22.57 hrs, *n* = 849; Tow 2398, 195-320 m, 09.44-12.24 hrs, *n* = 42. Tows similar by Kolmogorov-Smirnov (K-S) tests (P>0.01) are: 2392 and 2398; 2393 and 2398; 2395 and 2397; (B) Tow 2400, 335-370 m, 14.13-16.53 hrs, *n* = 4755; Tow 2401, 295-370 m, 20.00-22.40 hrs, *n* = 1341; Tow 2402, 290-305 m, 07.25-10.05 hrs, *n* = 2139; Tow 2406, 345-360 m, 15.53-18.33 hrs, *n* = 964. All tows are different by K-S tests (P<0.01)

Table 2. *Stenobrachius leucopsarus.* Numbers of different size groups per hour of towing in Tows 2392, 0-80 m at 22.30-01.20 hrs; 2395, 0-90 m at 23.11-0206 hrs; and 2396, 400-480 m at 12.55-16.55 hrs, 19-21 July 1976

Size interval (mm)	0-90 m; Night (2392 + 2395)	400-480 m; Day (2396)
15-20	1.0	30.8
20-25	2.0	2.5
25-30	17.8	4.2
30-35	25.4	14.2
35-40	14.4	10.5
40-45	14.8	11.2
45-50	18.0	8.5
50-55	44.2	7.5
55-60	44.8	7.2
60-65	31.0	9.0
65-70	20.4	17.8
70-75	11.5	35.8
75-80	7.3	50.8
80-85	2.6	37.0
85-90	0.4	13.0
90-95	0.0	2.5
95-100	0.0	0.2

near the peaks in abundance for all three.) Although the cumulative percentage curves differ (K-S test, P<0.01), both years display a trimodal distribution, with the major modes occurring at 30 to 40, 50 to 60 and 70 to 80 mm SL. These modes apparently correspond to Age-Groups I, II-III and III+, respectively (Smoker and Pearcy, 1970). Both years had a main mode at 25 to 40 mm, as shown by the steep ascending arm of the cumulative percentage curve. The main difference between years is the higher percentage of individuals larger than 45 mm in the 1976 than the 1977 samples, or conversely, the higher percentage of 30 to 45 mm individuals in the 1977 than the 1976 samples.

Diaphus theta

Fig. 1B shows a similar comparison for *Diaphus theta.* Again, the cumulative percentage curves are different (P<0.01). The major difference was the presence of almost 60% of the individuals in the 35 to 40 mm size-class (presumably Age-Group I fish) in 1976, whereas only 25% of the 1977 catch was in this size-class.

Tarletonbeania crenularis

The year-to-year variations in size structure of *Tarletonbeania crenularis* were pronounced (Fig. 1C). The 1976 curve has two distinct modes, at 25 to 30 mm and 55 to 70 mm. The 1977 curve, while showing the 25 to 30 mm mode, lacks the 55 to 70 mm mode and instead has a 40 to 50 mm mode. Perhaps the 25 to 30 mm mode represents first-year fish, the 40 to 50 mm second-year fish, and the 55 to 70 mm mode third-year fish.

These 3 species of lanternfishes had different size structures in the same season during two different years. Although modes were usually present at approximately the same sizes and the smallest size-group predominated in all three species in both years, differences were obvious. These differences in relative abundance of different sizes are important because they indicate variable survival between years or significant horizontal patchiness in age structure in the area sampled.

Between-Tow Variations within Each Cruise

Stenobrachius leucopsarus

Differences in the size structure of *Stenobrachius leucopsarus* caught in different tows (usually 3 to 4 nets per tow) may be attributed to differences in depth, time of day, patchiness or random variability. Cumulative percentage curves for the 1976 samples, representing a broad depth range and various times of day show a trend of increasing size between 285 and 480 m depth during daylight hours (Fig. 2A). Curves 2391, 2393, 2394 and 2396 are each displaced further to the right than the preceding one, indicating increasing modal size.
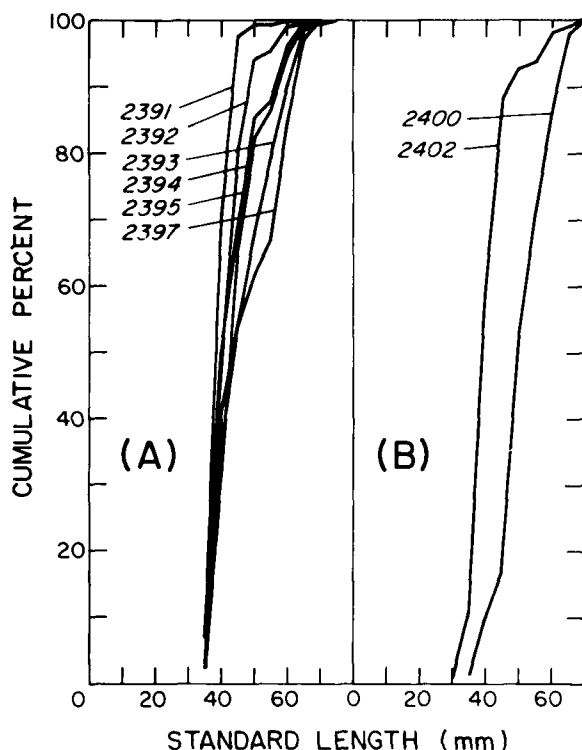
Fig. 3. *Diaphus theta*. Cumulative size-frequency curves for catches by tow, for 1976 (A) and 1977 (B). (A) Tow 2391, 285–310 m, 17.17–19.57 hrs, n = 540; Tow 2392, 0–80 m, 22.30–01.20 hrs, n = 207; Tow 2393, 305–360 m, 12.23–15.58 hrs; n = 72; Tow 2394, 230–430 m, 18.35–21.15 hrs, n = 312; Tow 2395, 0–90 m, 23.11–02.06 hrs, n = 299; Tow 2397, 210 m, 20.17–22.57 hrs, n = 166. Tows similar by K-S tests (P>0.01) are: 2392 and 2394; 2393 and 2394; 2393 and 2395; 2393 and 2397. (B) Tow 2400, 335–370 m, 14.13–16.53 hrs, n = 90; Tow 2402, 290–305 m, 07.25–10.05 hrs, n = 111; different by a K-S test (P<0.01)

Other curves of interest in Fig. 2A are (a) those which are similar under different conditions, (b) those which are different under similar conditions, and (c) those which differ significantly from the main trend in the tow series. Curves for Tows 2395 and 2397 fall into the first category. Tow 2397 was a twilight tow, beginning at 20.17 hrs, about 50 min after sunset (19.27 hrs local mean time, LMT) and continuing at 210 m until 22.57 hrs, well after sunset. Tow 2395, on the other hand, was a nighttime tow (23.11 to 02.06 hrs) at the surface (0 to 90 m). The size structure of these curves is very similar (P>0.01), and each may represent fish moving upwards at 210 m shortly after sunset, and proceeding to the surface where they were found well after dark. The curves for two other tows that fished at about the same depths as 2395 and 2397 are also similar under different conditions. Tow 2392 was at night (22.30 to 01.20 hrs) in surface waters (0 to 80 m), while Tow 2398 was during the day (09.44 to 12.24 hrs) in deeper waters (195 to 320 m). Size structures are very similar (P>0.01), again possibly as a result of vertical migration.

The two nighttime tows in the upper 80 to 90 m were significantly different in size distribution (P<0.01). However, this is probably due to relatively more sampling in deeper water by the first night's tow (2392) in comparison to the second night's tow (2395). A comparison of the deepest net of Tow 2395 (75 to 90 m) with the three horizontal nets of Tow 2392 (80 m) revealed no significant differences in size-frequency distributions (P>0.01). This indicates night-to-night consistency in size-structure of the vertically migrating population.

The deepest daytime tow in this series (Curve 2396 at 400 to 480 m) was unusual because the size structure of the catch was so different from that of the other tows taken on this cruise. It had a larger percentage (12%) of 15 to 20 mm individuals than any other tow in this study, including surface tows at night, and a higher percentage of 70 to 80 mm individuals than any other tow in this series. Hence, large proportions of Age-Group O (15 to 20 mm) individuals were caught with Age-Group III+ individuals in deep water. The absence of high percentages of these very small and large individuals in the surface layer at night further suggests that neither of these groups migrated in large numbers to the surface. The low catch of both the 15 to 20 mm group and the 70 to 90 mm group per hour of towing in the two surface tows (2392 and 2395) compared to this deep tow indicates real differences in abundances of size-groups at these depths (Table 2).

Fig. 2B shows cumulative percentage curves for four 1977 tows at 290 to 370 m separated by a horizontal distance of less than 10 km. Three curves (2400, 2401 and 2406), while statistically different, display a similar pattern. All three are trimodal, with modes at 30 to 40, 50 to 60 and 70 to 80 mm, similar to the curves in Fig. 1A. Curve 2402, the shallowest of the four tows (290 to 305 m), is very different from the rest, showing only one mode at 30 to 40 mm and almost no fish above a size of 45 mm. This indicates that the 300 m depth stratum was occupied only by Age-Group I fish during the day (07.25 to 10.05 hrs), whereas deeper catches had higher percentages of larger fish (Age-Groups II-III and III+). Also, since Tow 2401 has the second largest mode of small fish and is intermediate in depth between Tows 2402 and 2400+2406, it is probable that small *Stenobrachius leucopsarus* were proportionally more common at depths above about 335 m.

Diaphus theta

Size compositions of *Diaphus theta* caught at different depths were often similar (Fig. 3A). Cumulative percentage curves for a twilight tow (18.35 to 21.15 hrs) at 230 to 430 m (Tow 2394) and a nighttime tow at 0 to 80 m (Tow 2392) were similar (P>0.01). A daytime tow at 305 to 360 m (2393) was also similar to curves for tows at 0 to 90 m at night (2395) and 210 m and 230 to 430 m during twilight (2394 and 2397). Such similarity of size structure may again be the result of vertical migration.
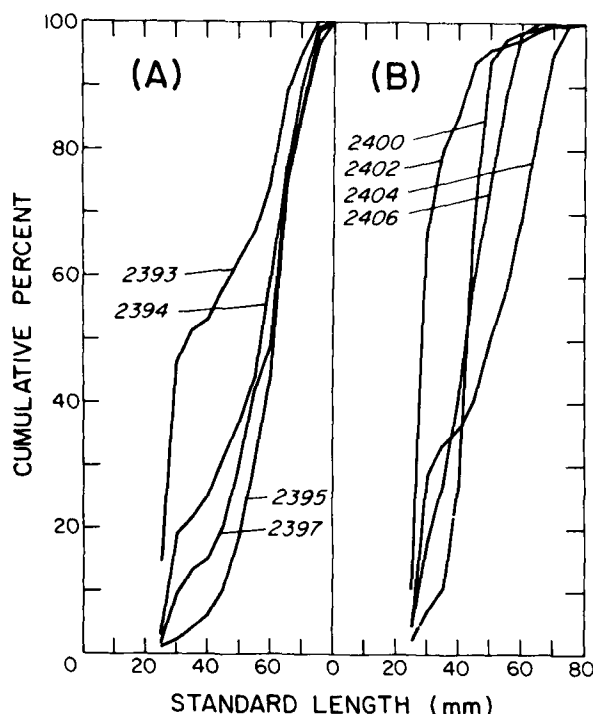
Fig. 4. *Tarletonbeania crenularis*. Cumulative size-frequency curves for catches by tow, for 1976 (A) and 1977(B). (A) Tow 2393, 305–360 m, 12.23–15.58 hrs, n = 169; Tow 2394, 230–430 m, 18.35–21.15 hrs, n = 386; Tow 2395, 0–90 m, 23.11–02.06 hrs, n = 194; Tow 2397, 210 m, 20.17–22.57 hrs, n = 127. Tows similar by K-S tests (P>0.01) are: 2394 and 2397; 2395 and 2397. (B) Tow 2400, 335–370 m, 14.13–16.53 hrs, n = 582; Tow 2402, 290–305 m, 07.25–10.05 hrs, n = 384; Tow 2404, 200–250 m, 18.22–21.02 hrs, n = 42; Tow 2406, 345–360 m, 15.53–18.33 hrs, n = 67. Tows similar by K-S tests (P>0.01) are: 2400 and 2406; 2404 and 2406

Table 3. *Diaphus theta*. Numbers of different size groups per hour of towing in Tows 2392, 0–80 m at 22.30–01.20 hrs; 2395, 0–90 m at 23.11–02.06 hrs; and 2397, 210 m at 20.17–22.57 hrs, 19–21 July 1976

Size interval (mm)	0–90 m; Night (2392 + 2395)	210 m; Twilight/ Night (2397)
30–35	3.0	1.5
35–40	31.0	24.0
40–45	29.3	8.2
45–50	13.5	4.9
50–55	2.4	3.0
55–60	5.7	10.9
60–65	2.4	7.9
65–70	0.4	1.9
70–75	0.2	0.0

Table 4. *Tarletonbeania crenularis*. Numbers of different size groups per hour of towing in Tows 2394, 230–430 m at 18.35–21.15 hrs; 2397, 210 m at 20.17–22.56 hrs; and 2395, 0–90 m at 23.11–02.06 hrs, 20–21 July 1976

Size group (mm)	230–430 m; Day (2394)	210 m; Twilight (2397)	0–90 m; Night (2395)
20–25	4.5	0.8	0.7
25–30	22.9	3.8	0.7
30–35	3.8	1.9	1.4
35–40	5.2	0.8	1.4
40–45	9.0	3.0	2.7
45–50	7.9	4.1	5.5
50–55	10.5	5.6	7.9
55–60	22.5	3.4	9.2
60–65	25.1	12.8	19.9
65–70	19.5	5.2	7.9
70–75	12.4	5.6	6.8
75–80	1.5	0.8	2.4

Although the two night tows in the upper 80 to 90 m were significantly different (P<0.01), this may be due to the greater amount of deeper water sampled by Tow 2392 than by 2395 (see *Stenobrachius leucopsarus*, earlier). However, no vertical size segregation was found for *Diaphus theta* in surface waters at night (see below), so these night-to-night differences in size structure may indicate differences in migratory behavior, or large-scale patchiness in the surface layer at night.

The size structure represented for Tow 2397, a tow at 210 m after sunset (19.27 hrs LMT) differs from that of other tows in that it had the largest mode of 55 to 65 mm individuals. Perhaps these large *Diaphus theta* migrate to near-surface waters later in the night. Conversely, such fish may reside at about 200 m on some nights and not ascend into the upper 50 m, the usual depth of maximum abundance of this species at night (Pearcy *et al.*, 1977). Our data on catch per hour show that the relative abundance of 30 to 45 mm individuals was largest in the surface tows and that of 55 to 65 mm individuals was largest at 210 m (Table 3). The larger sizes of *D. theta* at 335 to 370 m than at 305 to 360 m

(Tow 2393, Fig. 3A and Tow 2400, Fig. 3B) indicate that these large fish reside in relatively deep water during the day.

Tarletonbeania crenularis

Three of the 4 curves for the 1976 samples of *Tarletonbeania crenularis* are similar (P>0.01, Fig. 4A), having weak smaller modes and strong larger ones. The similarity of these 3 curves may be attributable to vertical migration from 230 to 430 m at twilight (Tow 2394) to around 210 m after sunset (Tow 2397) and then to the surface around midnight (Tow 2395). The major difference among the curves occurs below 30 mm. The deepest tow (2394) has the largest 20 to 30 mm mode, which diminishes in the intermediate tow (2397) and is almost absent in the surface tow (2395). The catch per hour of 20 to 30 mm individuals was also higher in the deep tow than the intermediate and shallow tows, while the catch per hour of the remaining size-groups remained relatively constant (Table 4). Apparently small *T. crenularis* did

not migrate in large numbers into the upper 90 m at night.

The curve for Tow 2393 (daytime at 305 to 360 m) varies significantly from the main trend shown in this series, having a distinctly bimodal distribution, with one mode at 20 to 30 mm and the other at 60 to 70 mm. The large proportion of small fish in this tow and in the daytime tow at 290 to 305 m (Tow 2402, Fig. 4B), and the lower proportion in nighttime or twilight tows in the upper 200 m (Tows 2395 and 2397), suggests that small *Tarletonbeania crenularis* may reside at the depth of about 290 to 360 m during both day and night.

In summary, *Stenobrachius leucopsarus* showed night-to-night consistency in size structure at depths of 75 to 90 m. Small and large individuals of *S. leucopsarus* appeared not to migrate in large numbers, whereas all but the largest individuals of *Diaphus theta* did migrate into the upper 90 m. The size structure of near-surface populations of *D. theta* was apparently different on successive nights, indicating either large-scale patchiness by size in the surface waters at night, or different size-groups coming to the surface on different nights. Small *Tarletonbeania crenularis* appeared not to migrate to surface waters in large numbers at night. *S. leucopsarus* and *D. theta* both exhibited trends of increasing size with depth during the daytime, but this trend was more pronounced in *S. leucopsarus*.

Within-Tow Variation

Stenobrachius leucopsarus

In the upper 90 m at night, there was an increase in size with depth for *Stenobrachius leucopsarus*. Cumulative percent curves and relative frequency histograms show that the two deeper nets of one tow (2395), which fished at 75 m and 75 to 90 m, caught mostly Age-Group II-III fish, with a predominant mode at 50 to 65 mm (Fig. 5). These curves are not different by a K-S test (P>0.01). The next shallower net (from 30 m) caught mostly Age-Group I fish of 25 to 35 mm, although some Age-Group II-III fish were present. The shallowest net (10 to 15 m) caught Age-Group I fish (25 to 35 mm) almost exclusively, with only a few Age-Group II-III fish. This conclusion that *S. leucopsarus* segregates vertically by size in surface waters at night is reinforced by another tow (Fig. 6A) which shows that Net 1 (0 to 55 m) also collected smaller individuals than the deeper nets (Nets 2-5).

The size-frequency distributions for 4 samples at the same depth (295 to 330 m) changed radically during the period of migration, from 20.00 to 22.40 hrs (Fig. 6B). The second net caught mainly 30 to 40 mm fish, probably the first group to ascend, the third caught a broad spectrum of sizes and the fourth and fifth captured a bimodal size distribution of largely 30 to 40 mm fish. Net 5 fished well after dark, so this bimodal population represents non-migratory individuals that remain at depth at night (see Pearcy et al., 1977, 1979). These

differences indicate that the migratory behavior of *Stenobrachius leucopsarus* is size-dependent and complex. Small fish (<40 mm) comprised over 50% of the catch in one net of a twilight tow (2397) at 210 m compared to less than 3% in the next later net, again indicating that small individuals temporally precede large ones in migrations toward the surface.

The large differences in the shapes of the cumulative percentage curves during a period of twilight migration in 1976 (Fig. 6B) contrast markedly with the similarity of the curves at the same depth during a non-migratory, daytime period in 1977 (Fig. 7A). These daytime curves are similar in shape to each other (although some are significantly different by K-S tests) and to the earliest net of the twilight series (Net 2, Fig. 6B) at the same depth. Small fish (<40 mm) apparently predominate at about 300 m depth. Statistical difference among curves for different nets within horizontal daytime tows (Tows 2393, 2400 and 2406; Fig. 7B) is good evidence for small-scale variations in size structure at depth.

Diaphus theta

In contrast to *Stenobrachius leucopsarus*, *Diaphus theta* showed no statistically significant (P>0.01) variability among nets within any of the 6 tows examined (2391, 2392, 2394, 2395, 2400, 2402; see Fig. 8, which illustrates nighttime catches in Tow 2392 as an example). Small-scale vertical or horizontal size segregation was, therefore, not evident in surface waters at night or deeper waters during the day. This unexpected lack of size segregation is due in part to the restricted size range of individuals, especially in near-surface tows at night.

Tarletonbeania crenularis

The small-scale or within-tow variability in the size structure of *Tarletonbeania crenularis* was intermediate between *Stenobrachius leucopsarus* and *Diaphus theta*. Eight of 13 comparisons of within-tow size compositions (for Tows 2393, 2394, 2395, 2400 and 2402) were not significantly different (P>0.01, see Fig. 9B, Tow 2400, as an example). Vertical stratification by size was not evident at night in the upper 90 m for *T. crenularis* (Fig. 9A). Most of the fish caught were large (>50 mm).

Discussion

According to Ahlstrom (1959) and Fast (1960), the larvae of *Stenobrachius leucopsarus* are confined to the upper 100 m, concentrated above 30 m, and do not appear to undertake diel vertical migrations off California. Richardson and Pearcy (1977) caught larvae of this species in the upper 50 m in depth-stratified tows off Oregon. Fast (1960) postulated an ontogenetic vertical migration of *S. leucopsarus* in Monterey Bay, California,
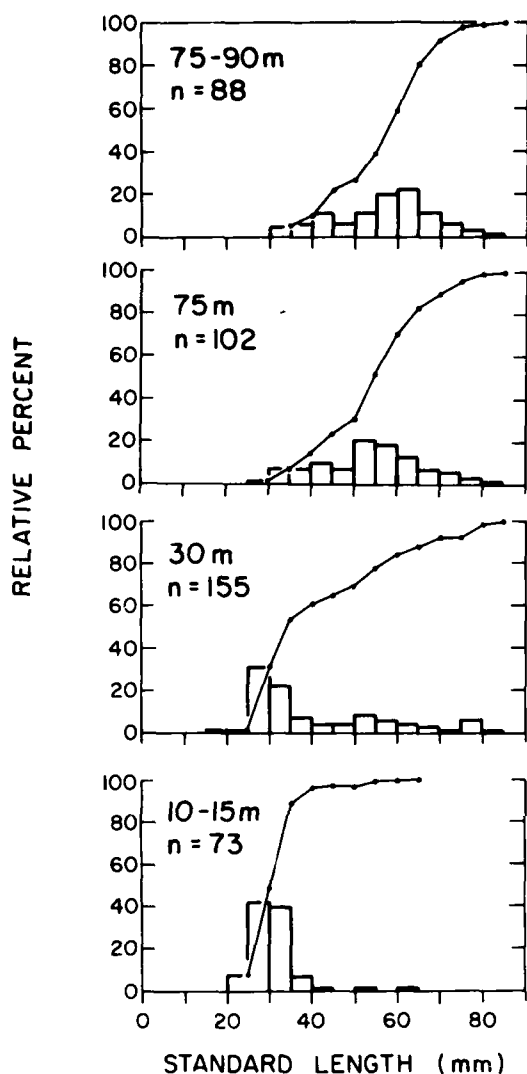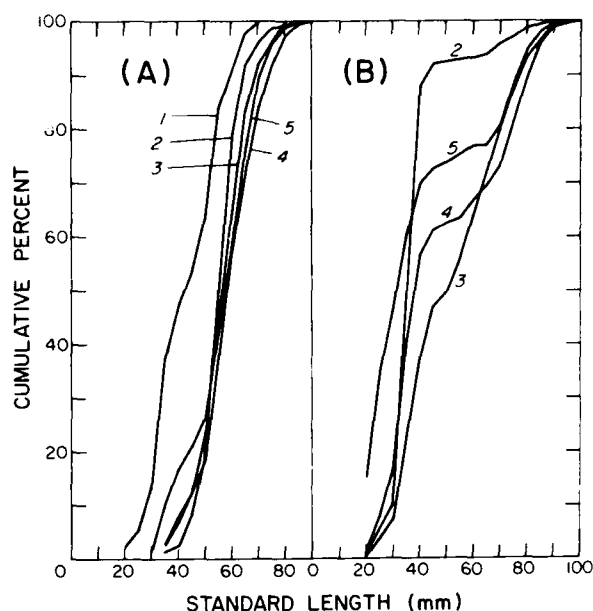
Fig. 6. *Stenobrachius leucopsarus.* (A) Cumulative size-frequency curves for catches by net, in the upper 80 m at night (Tow 2392). Net 1, 0–55 m, 22.30–22.40 hrs, n = 131; Net 2, 55–80 m, 22.40–23.20 hrs, n = 238; Net 3, 80 m, 23.20–24.00 hrs, n = 74; Net 4, 80 m, 24.00–00.40 hrs, n = 222; Net 5, 80 m, 00.40–01.20 hrs, n = 285. Nets similar by K-S tests (P>0.01) are: 2 and 3; 3 and 4; 3 and 5; 4 and 5. (B) Cumulative percent curves for catches by net, in a twilight tow at about 300 m (Tow 2401). Net 2, 310–330 m, 20.00–20.40 hrs, n = 463; Net 3, 300–310 m, 20.40–21.20 hrs, n = 378; Net 4, 300–320 m, 21.20–22.00 hrs, n = 309; Net 5, 295–320 m, 22.00–22.40 hrs, n = 190. All are different by K-S tests (P>0.01)

Fig. 5. *Stenobrachius leucopsarus.* Vertical distribution of different sizes of fish in the upper 90 m at night (Tow 2395), 1976

Fig. 7. *Stenobrachius leucopsarus.* (A) Cumulative size-frequency curves for catches by net, for a daytime tow at about 300 m (Tow 2402). Net 2, 295–305 m, 07.25–08.05 hrs, n = 335; Net 3, 290–305 m, 08.05–08.45 hrs, n = 295; Net 4, 290–300 m, 08.45–09.25 hrs, n = 625; Net 5, 290–300 m, 09.25–10.05 hrs, n = 857. Nets similar by K-S tests (P>0.01) are: 3 and 4; 2 and 5. (B) Cumulative percent curves for catches by net, for a daytime-twilight tow at about 350 m (Tow 2406). Net 2, 345–350 m, 15.53–16.33 hrs, n = 458; Net 4, 350–360 m, 17.13–17.53 hrs, n = 185; Net 5, 350–360 m, 17.53–18.33 hrs, n = 321. All nets are different by K-S tests (P<0.01).
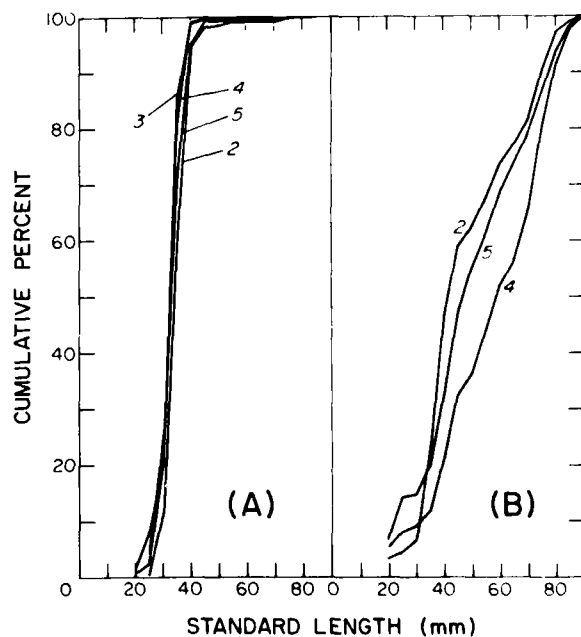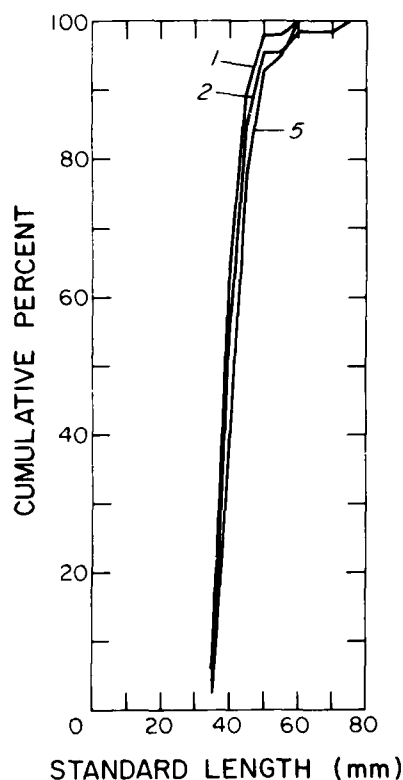
Fig. 8. *Diaphus theta.* Cumulative percentage curves for catches by net, for a nighttime tow in the upper 80 m (Tow 2392). Net 1, 0-55 m, 22.30-22.40 hrs, n = 47; Net 2, 55-80 m, 22.40-23.20 hrs, n = 67; Net 5, 80 m, 00.40-01.20 hrs, n = 41. All nets are similar by K-S tests (P>0.01)

Fig. 9. *Tarletonbeania crenularis.* (A) Cumulative percentage curves for catches by net, in a nighttime tow in the upper 90 m (Tow 2395). Net 1, 0-90 m, 23.11-00.06 hrs, n = 44; Net 4, 30 m, 01.06-01.36 hrs, n = 69; Net 5, 10 m, 01.36-02.06 hrs, n = 79. All nets are similar by K-S tests (P>0.01). (B) Cumulative percentage curves for catches in a daytime tow at about 335 m (Tow 2400). Net 3, 335-340 m, 14.53-15.33 hrs, n = 130; Net 4, 335-340 m, 15.33-16.13 hrs, n = 224; Net 5, 335-370 m, 16.13-16.53 hrs, n = 228. All nets are similar by K-S tests (P>0.01)

based on daytime stratified non-closing net samples. He thought that larvae of about 10 mm SL rapidly descend to depths of 400 to 500 m, the lower portion of the vertical range occupied by the species, and there undergo metamorphosis. Thereafter they ascend as newly transformed (15 to 20 mm) juveniles into the upper limits of the species' daytime bathymetric distribution (200 to 300 m). As fish grow they seek progressively deeper water, with the 50 to 70 mm fish being concentrated once more at 400 to 500 m. Fast mentioned that the largest specimens (>70 mm) appear to ascend to depths of 200 to 300 m during the day but, as he admits, this conclusion is uncertain because so few large fish were caught, and because open nets were used.

Our results for *Stenobrachius leucopsarus* during the summer confirm some of Fast's conclusions. We also found evidence for size segregation by depth, but the largest proportion of small juveniles (15 to 20 mm) were in deep water, 400 to 480 m, and not in the upper depths of the vertical range during daytime as observed by Fast. Larger fish were generally found in progressively deeper water during the day. Age-Group I (30 to
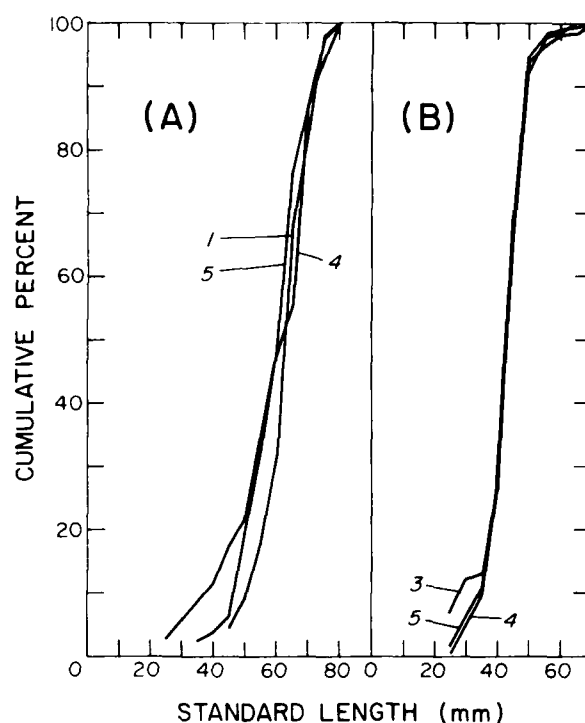
40 mm) fish were most common above 335 m; Age-Group II-III fish were common between 335 and 400 m; and Age-Group III+ were found in deep water of 400 to 500 m in association with Age-Group O (15 to 20 mm). We found no evidence for large fish (>70 mm) residing at depths of 200 to 300 m during the day.

We also found increasing size of *Stenobrachius leucopsarus* with increasing depth in near-surface waters at night in summer. Almost all the individuals caught at depths of 10 to 30 m were Age-Group I (25 to 35 mm). Age-Group II-III (50 to 65 mm) increased in frequency at 30 m, and predominated in the catches at 75 to 90 m. Neither 15 to 20 mm fish (Age-Group O) nor 70 to 80 mm fish (Age-Group III+) were common in near-surface waters at night, suggesting that these sizes migrated less frequently into surface waters and had different diel migratory behavior than the intermediate size groups.

These age-specific depth preferences of *Stenobrachius leucopsarus* are also related to differences in diel vertical migrations. The tow at 250 to 330 m during a sunset-darkness period caught mostly 30 to 40 mm fish during

twilight, then 70 to 80 mm fish moved into this stratum, and the 30 to 40 mm fish ascended, leaving a residual group of mainly 20 to 30 mm and 70 to 80 mm fish at this depth at night after migration was completed. Thus, different sizes of *S. leucopsarus* may respond to different factors, such as irradiance, in seeking depths and in initiating vertical migration. It should be remembered, however, that a broad spectrum of sizes was found at most depths and that segregation was not complete.

Pearcy *et al.* (1977) provided data on the catches of two size groups of *Stenobrachius leucopsarus* in the upper 1000 m off Oregon. They found that fish < 30 mm and ≥ 30 mm both demonstrated diel vertical migrations and both size groups included individuals that did not migrate into surface waters but remained in deep water at night. Both small and large fish had peak abundance in the upper 50 m at night, but small (< 30 mm) individuals were highly concentrated in the upper 50 m at night but not at 50 to 150 m; substantial numbers of fish ≥ 30 mm were caught at depths of 50 to 150 m. The mid-depth peaks of abundance of small fish were also shallower than those of large fish during both day and night. These trends agree with those presented in this paper: small *S. leucopsarus* in general seek shallower depths than large ones, but our results suggest that differences occur within these two broad size groups. Pearcy *et al.* (1977) failed to detect more detailed changes in size structure, probably because of the small sample size provided by the IKMT and the variability introduced by combining data from cruises during different years and seasons.

Pearcy *et al.* (1979) compared the size-frequency distributions of *Stenobrachius leucopsarus* caught in these same IKMT collections from 0 to 100 m and 300 to 700 m during the night, and found no significant difference. Although examination of their unpublished data suggests that 10 to 20 mm and 70 to 80 mm fish comprised a larger proportion of the catch in deep than shallow water, the difference was not significant, again probably because of small sample size. Only 696 fish were included in their analysis, and these were from several cruises at different times of the year.

Frost and McCrone (1979) studied the vertical distribution and migration of *Stenobrachius leucopsarus* in the eastern subarctic Pacific Ocean. They found vertical stratification by size both in surface waters at night and in deeper water during the day. The migration patterns for the three broad age-groups in their samples (roughly equivalent to our groups) are similar to ours. However, they indicated an extensive vertical migration of young fish (19 to 35 mm) from 275 to 330 m in the day to 0 to 55 m at night, whereas we found no evidence for migration of very small juveniles (15 to 20 mm) into surface water at night in summer. This conflict may reflect an overlap of the smallest age-grouping of Frost and McCrone with our Age-Groups O and I. Visual examination of the size-frequency distributions presented by Frost and McCrone for catches of *S. leucopsarus* during three successive summers indicates annual variations in the relative proportions of year-classes in the

subarctic Pacific in summer, confirming our results for Oregon waters.

A trend of increasing size of *Diaphus theta* with increasing depth within the upper 500 m at night was shown by Pearcy *et al.* (1977). The median size of fish in the upper 50 m was 35 to 40 mm compared to 45 to 50 mm at 50 to 100 m. In the present study, this trend was corroborated: the largest *D. theta* were below the upper 80 m at night, and below 300 m by day (Fig. 3). No change in size was found within the upper 90 m at night, however. Frost and McCrone (1979) also noted a trend of increasing size of *D. theta* with depth during the day as well as a trend of increasing size with depth in surface waters at night. We found no such trend in surface waters at night.

Tarletonbeania crenularis caught at various depths within the upper 90 m at night were also similar in size. These near-surface catches were composed almost exclusively of large (≥ 50 mm) fish. Small (20 to 30 mm) individuals were most common in deep water; they may not migrate into near-surface waters at night.

Major differences were found among the 3 species in the degree of variability in size structure among samples. The within-tow variation for *Stenobrachius leucopsarus* was largest, with significant differences among successive net collections at the same depth or among different depths. The size structure of *Diaphus theta*, on the other hand, was similar among nets of single collections. *Tarletonbeania crenularis* showed an intermediate degree of intra-tow variability. Thus, differences in kilometer-scale patchiness or variability of sizes are indicated among these 3 species. *S. leucopsarus* displays the most variability in vertical and horizontal dimensions. These differences in spatial structure may be important factors in the intra- and interspecific segregation of these 3 lanternfishes, which may form a competitive guild: they are all transitional-subarctic species (Pearcy, 1972) of similar size, that have maximum concentrations in the upper 50 m at night and between 300 and 400 m by day off Oregon (Pearcy *et al.*, 1977), and have a large dietary overlap (Tyler and Pearcy, 1975).

Literature Cited

Ahlstrom, E. H.: Vertical distribution of pelagic fish eggs and larvae off California and Baja California. Fishery Bull. Fish Wildl. Serv. U.S. 60, 107-146 (1959)

Badcock, J.: The vertical distribution of mesopelagic fishes collected on the SOND cruise. J. mar. biol. Ass. U.K. 50, 1001-1044 (1970)

Badcock, J. and N. R. Merrett: Midwater fishes in the eastern North Atlantic-I. Vertical distribution and associated biology in 30°N, 23°W, with developmental notes on certain myctophids. Prog. Oceanogr. 7, 3-58 (1976)

Bertelsen, E.: The ceratioid fishes. Ontogeny, taxonomy, distribution and biology. Dana Rep. *39*, 1–276 (1951)

Bruun, A. F.: On the restricted distribution of two deep-sea fishes, *Borophryne apogon* and *Stomias colubrinus*. J. mar. Res. *17*, 103–112 (1958)

Clarke, T. A.: Some aspects of the ecology of lanternfishes (Myctophidae) in the Pacific Ocean near Hawaii. Fish. Bull. U.S. *71*, 401–434 (1973)

Fast, T. R.: Some aspects of the natural history of *Stenobrachius leucopsarus* Eigenmann and Eigenmann, 197 pp. Ph.D. thesis, Stanford University, Stanford, California 1960

Frost, B. W. and L. E. McCrone: Vertical distribution, diel vertical migration, and abundance of some mesopelagic fishes in the eastern subarctic Pacific Ocean in summer. Fish. Bull. U.S. *76*, 751–770 (1979)

Grey, M.: Family Gonostomatidae. *In*: Fishes of the Western North Atlantic. Part 4, Mem. Sears Fdn mar. Res. *1*(4), 78–240 (1964)

Halliday, R. G.: Growth and vertical distribution of the glacier lantern-fish, *Benthosema glaciale*, in the northwestern Atlantic. J. Fish. Res. Bd Can. *27*, 105–116 (1970)

Johnson, R. K.: A revision of the alepisauroid family Scopelarchidae (Pisces: Myctophiformes). Fieldiana, Zool. *66*, 1–249 (1974)

Marshall, N. B.: Systematic and biological studies of the macrourid fishes (Anacanthini, Teleostii). Deep-Sea Res. *12*, 299–322 (1965)

Merrett, N. R.: On the identity and pelagic occurrence of larval and juvenile stages of rattail fishes (family Macrouridae) from 60°N, 20°W and 53°N, 20°W. Deep-Sea Res. *25*, 147–160 (1978)

Pearcy, W. G.: Distribution and ecology of oceanic animals off Oregon. *In*: The Columbia River estuary and adjacent ocean water, pp 351–377. Ed. by A. T. Pruter and D. L. Alverson. Seattle: University of Washington Press 1972

Pearcy, W. G.: A large opening-closing midwater trawl for sampling oceanic nekton, and comparison of catches with an Isaacs-Kidd midwater trawl. Fish. Bull. U.S. (in press)

Pearcy, W. G., E. E. Krygier, R. Mesecar and F. Ramsey: Vertical distribution and migration of oceanic micronekton off Oregon. Deep-Sea Res. *24*, 223–245 (1977)

Pearcy, W. G., H. V. Lorz and W. Peterson: A comparison of the feeding habits of migratory and non-migratory *Stenobrachius leucopsarus* (Myctophidae). Mar. Biol. *51*, 1–8 (1979)

Pietsch, T. W.: Osteology and relationships of the ceratioid and anglerfishes of the family Oneirodidae with a review of the genus *Oneirodes* Lütken. Sci. Bull. nat. Hist. Mus. Los Ang. Cty *18*, 1–113 (1974)

Richardson, S. L. and W. G. Pearcy: Coastal and oceanic fish larvae in an area of upwelling off Yaquina Bay, Oregon. Fish. Bull. U.S. *75*, 125–145 (1977)

Rofen, R. R.: Family Paralepididae. *In*: Fishes of the Western North Atlantic, Part 5. Mem. Sears Fdn mar. Res. *1*(5), 205–461 (1966)

Smoker, W. and W. G. Pearcy: Growth and reproduction of the lanternfish *Stenobrachius leucopsarus*. J. Fish. Res. Bd Can. *27*, 1265–1275 (1970)

Tate, M. W. and R. C. Clelland: Nonparametric and shortcut statistics in the social, biological and medical sciences. 171 pp. Danville, Illinois: Interstate Printers & Publishers 1957

Tyler, H. R., Jr. and W. G. Pearcy: The feeding habits of three species of lanternfishes (family Myctophidae) off Oregon, USA. Mar. Biol. *32*, 7–11 (1975)

NOTES

A LARGE, OPENING-CLOSING MIDWATER TRAWL FOR SAMPLING OCEANIC NEKTON, AND COMPARISON OF CATCHES WITH AN ISAACS-KIDD MIDWATER TRAWL

Avoidance of nets by agile micronekton and nekton is one of the major problems with small midwater trawls routinely used for oceanic sampling by oceanographers and marine biologists (e.g., Harrisson 1967; Pearcy 1975; Roper 1977). A major advantage of small trawls is that they can be equipped with opening-closing devices so that samples can be ascribed to discrete depths. This capability is especially important for sampling deep water where densities of animals are low. An opening-closing rectangular midwater trawl with a mouth area of about 25 m² is the largest opening-closing net described (Baker et al. 1973). Another important advantage of small nets is that they can be used from most oceanographic vessels.

Large, commercial-size midwater trawls used to sample oceanic micronekton (Berry and Perkins 1966; Harrisson 1967; Taylor 1968; Clarke 1973, 1974; Krefft 1974; Roper 1977) are usually not evaded as successfully by nektonic animals. Big nets which filter large volumes of water have the added advantage of catching enough animals to characterize species and size composition from sparsely populated waters. However, these large nets lack opening-closing capability, and most oceanographic research vessels are unable to handle large nets, otter doors, and bridles (Pearcy 1975).

This paper describes a 50 m² pelagic trawl especially designed for use with an opening-closing cod end, attempts to evaluate its performance, and compares its catches of mesopelagic fishes and cephalopods with those from a 5.4 m² Isaacs-Kidd midwater trawl.

Midwater Trawl Description and Operation

The midwater or pelagic trawl was designed by G. Loverich, Nor'Eastern Trawl Systems, Inc.,[1] Bainbridge Island, Wash., for sampling meso-

pelagic fishes and cephalopods in conjunction with a 1 m² five-net opening-closing device which is attached to the cod end of the trawl (Figure 1). The body of the trawl is lined throughout with 19 mm (¾ in) stretch mesh. The net is 42 m long and was constructed with a gradual taper from mouth to cod end in order to provide a large netting area for filtration in order to reduce the water velocity through the meshes, stagnation and hang-up of animals on the netting, and extrusion of animals through the netting. The wings of the trawl are made of large mesh (292 mm). It was assumed that micronekton (fishes, squids, and shrimps up to 200 mm in length) escape or pass through this large mesh rather than lead into the trawl body, giving an effective diameter of the net for micronekton equivalent to the small mesh body of the trawl. Unfortunately data do not exist to evaluate herding or leading of oceanic micronekton by the wings of trawls.

The trawl has six seams with four identical panels for the top and bottom (wing, body, and intermediate) two identical side (wing, body, and intermediate) panels, and four cod end panels (Figure 2). The meshes were hung at 29.3% in both directions to allow formation of square openings and laced to make six seamlines. Two riblines are located along the middle of the side panels and extend to the opening-closing device.

A 1 m² Multiple Plankton Sampler (MPS) with five separate nets, each 4.6 m long (see Pearcy et al. 1977 for details), was used as an opening-closing cod end device on the trawl. The levers for release of the five nets of the sampler are actuated by a modular timer which employed a crystal oscillator and a binary series of counters for selection of release times (Evans 1975). The timer is mounted on the MPS, started as the trawl is launched, and is set to give the trawl time to stabilize at a selected towing depth before net 1 is released (usually 30-60 min). Thus the first net fishes obliquely from the surface to the fishing depth of net 2. The four remaining nets (nets 2-5) all fish the same amount of time on a given tow (usually 40 min), either at the same depth (horizontal series) or at different depths (vertically stratified series).

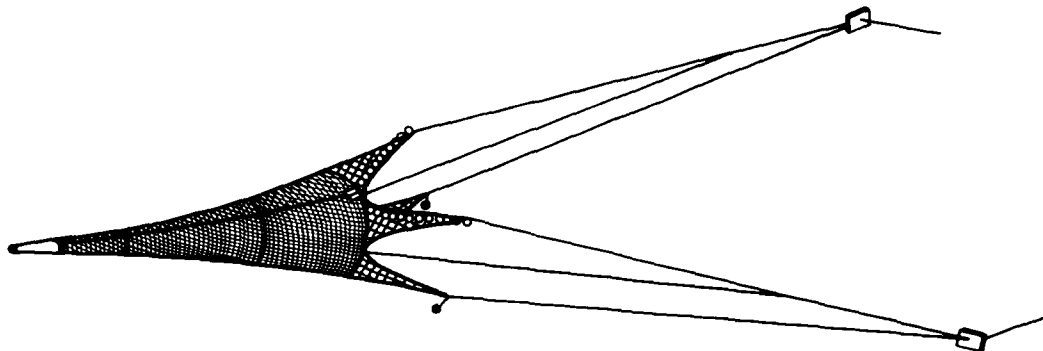The footrope and headrope are each 28.6 m of 16

FIGURE 1.—Sketch of the pelagic trawl in operation.

mm poly-Dacron rope. The wings are of #60 thread, the body of #3 thread, the intermediate of #4 thread, and the cod end of #6 thread. Nineteen 25.4 cm (diameter) aluminum floats (good to 1,000 m) are attached to the headrope. Galvanized chain is attached to the footrope and one 23 kg lead ball is attached to the tip of each of the bottom wings. The bridles to the bottom wings are 55 m long; bridles to the upper wing are 36 m long, and the middle bridle is 47 m long (Figure 1).

The trawl was designed to be towed with 1.5-1.8 × 2.4-2.7 m (5 × 8 ft or 6 × 9 ft) otter doors. A scale model of the trawl was first constructed and tested in a tank to test its design and performance.

Observations were made on the trawl by divers during trials in Puget Sound using 1.8 × 2.7 m doors and towing speeds of 1.0 to 1.6 m/s at depths of about 12 m. The towing characteristics of the net were observed and the number of floats needed to provide neutral buoyancy to the cod end opening-closing device was determined by trial. At a towing speed of 1.6 m/s the vertical opening of the mouth was measured to be about 8 m and the body of the trawl was observed to be nearly circular and about 8 m in diameter, providing an estimate of about 50 m² for the cross-sectional area of the fine mesh netting of the trawl body.

The depth that each net fished was determined from the depth-modulated signal from an acoustical pinger mounted on the headrope of the trawl, a hydrophone towed from the vessel, and a graphic recorder. An EG&G pinger was used initially but was replaced with an Institute of Oceanographic Sciences (IOS) 0-683 m (0-100 atmospheres pressure) acoustical net monitoring system (Baker et al. 1973) with an overall accuracy of 0.1% of the full depth range.

Methods

A timer-actuated ejection device was used as a method to provide some information on the flushing rate through the body of the trawl. This device, similar to the one described by Pearcy et al. (1977), has a modular timer (Evans 1975) to release the contents of two 1.3 l chambers. It was hung from the headrope inside the trawl mouth and its contents were ejected against the 19 mm mesh. Preserved juvenile salmon (10-20 cm total length) were released into the net at intervals of 5, 10, 15, or 25 min before closure of net 1 and opening of net 2.

The pelagic trawl-MPS combination was used on three chartered trawlers off Oregon. All vessels had net reels and used double-warp towing. A boom was used to launch and recover the MPS during 1975 and 1976 cruises. The vessel chartered in 1977 had a stern ramp, which greatly facilitated use of the pelagic trawl. Twelve tows were made in 1975 to test the monitoring equipment and to evaluate flushing of the net. Eight tows were made in 1976 and 10 in 1977. All tows were 110-130 km off the central Oregon coast; 18 of these tows provided the data for comparison of pelagic trawls and Isaacs-Kidd midwater trawls (IKMT's) (Table 1).

Tows were also made with a 5.4 m² IKMT with 10 mm stretch mesh and a 1 m² MPS opening-closing device (Pearcy et al. 1977) at 1.5-2.0 m/s at a similar location and within 10 days after each of three cruises that used the pelagic trawl (Table 1). Volume of water entering the IKMT was monitored with a modified TSK flowmeter on all tows. One of the purposes of these IKMT tows was to enable comparisons of the catches by the two different types of nets.
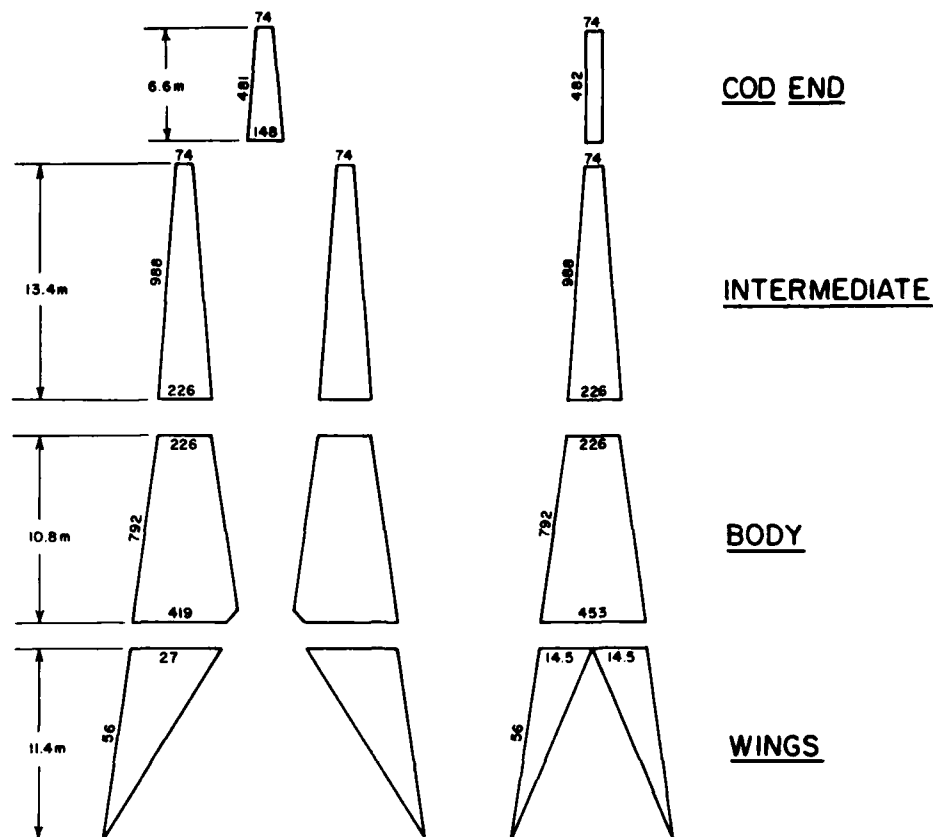
FIGURE 2.—Net plans for the pelagic trawl. Numbers on the net panels indicate number of meshes along the margins.

Collections were preserved in 10% Formalin at sea. In several instances large catches (>35 l) of the pelagic trawl were subsampled, but at least 14 l of the catch of each of the nets for discrete depths were preserved. Fishes and cephalopods were identified and measured [standard length (SL) of fishes and dorsal mantle length (DML) of squids].

TABLE 1.—Summary of pelagic trawl (PT) and Isaacs-Kidd midwater trawl (IKMT) tows made on the three "paired" cruises off Oregon.

Net	Dates	Vessel	No. Tows	Depth (m)	Time
	1975				
PT	23 Sept.	Betty-A	1	340-360	Day
IKMT	12-16 Sept.	Yaquina	5	334-362	Day
	1976				
PT	19-22 July	Pacific Raider	8	0-500	Day-night
IKMT	8-13 July	Wecoma	11	0-465	Day-night
	1977				
PT	30 July-2 Aug	Excalibur	9	185-365	Day-night
IKMT	8-10 Aug.	Wecoma	5	187-350	Day-night

Results

Flushing of the Pelagic Trawl

In Puget Sound, divers observed that dead salmon smolts released in the mouth of the trawl were never stuck against the netting in the forward part of the trawl where the meshes were taut from water pressure. Occasionally fish stalled against the mesh in the aft section of net where netting was less rigid, but these fish were easily dislodged and tumbled toward the cod end. Because live fishes usually swim away from the netting when inside a trawl, it seems unlikely that live, active fish would be pinned against the netting (G. Loverich[2]). Obviously, dead, preserved fish do not

---

[2]G. Loverich, Nor'Eastern Trawl Systems, Inc., Bainbridge Island, WA 98110, pers. commun. January 1979.

531

behave like live ones, but they do provide some information on flow characteristics through the net and how easily objects are pinned against the mesh.

The results of the release of preserved salmon smolts into the mouth of the pelagic trawl on two cruises in the open ocean are shown in Table 2. Ninety-seven percent of the fish released in the mouth were recovered in cod end nets 1 and 2 within 5-25 min after release; 82% were recovered in net 1. These data indicate an average residence time of preserved fish of 10 min in the body of the trawl.

If live animals were delayed by 10-120 min in passing through the net into the cod end, then the number of animals found in different cod end nets may vary, with largest numbers in latter nets and fewest in the first or second net as found by Foxton (1970) and Donaldson (1975) in other cod end opening-closing devices. Coefficients of concordance, W, (Tate and Clelland 1957) were not significant ($P > 0.2$) for rank order of abundance of fishes (12 tows), squids (10 tows), and *Stenobrachius leucopsarus*, the most common fish (10 tows) for nets 2-5 that sampled equal time intervals and also caught at least 10 of each of these three types of animals. Similar nonparametric tests of the rank order of abundance of 15 common species were not significant for nets 2-5 of nine tows with same net, where each net fished 2 h (Willis 1979). This lack of correlation of catch with net number provides no evidence for delay or stagnation of animals in the net over time periods of 10 min to 6 h. Characteristic species compositions or size-frequency distributions from specific depths (Willis and Pearcy[3]) also indicate that cod end catches are predominantly from the depths fished.

Entanglement or hang-up of fishes and cephalopods in the meshes of the trawl appeared to be restricted to a few types. Fishes such as the stomiatoid, *Tactostoma macropus*, were occasionally found hanging on the meshes of the trawl body by their teeth. Soft-bodied cephalopods, such as *Chiroteuthis calyx* and *Vampyroteuthis infernalis*, were sometimes entangled in the mesh. The number of animals hung on the net after a tow was always a small fraction of those in the cod ends. These entangled animals that are retained in the net from one tow are probably washed-down

---

[3]Willis, J. M., and W. G. Pearcy. Spatial and temporal variation in the population size structure of three lanternfishes (Myctophidae) off Oregon. Unpubl. manuscr.

532

TABLE 2.—Results of release of preserved salmon from the ejection device in front of the pelagic trawl. All tows were horizontal at 2.5-3.0 kn. ND means no data.

Vessel	Minutes that ejection device was set to go off before closure of net 1	Interval between closure of nets 2-5 (min)	No of fish in net					No recovered no. used
			1	2	3	4	5	
Betty-A	10	15	35	0	0	1†	1†	ND
	10	15	35	0	0	0	1†	ND
	10	15	30	3	0	0	0	ND
	25	20	36	0	0	0	0	ND
Pacific Raider	5	40	30	24	1	4	2	61/65
	10	40	†0	†34	†2	†0	†?	43/60
	10	40	33	25	0	0	0	58/60
	15	40	49	1	0	0	2	52/59
Percent recovered in each net			82	15	1	1	1	

† Net failed to close
? Cod end of trawl was twisted. This trawl was excluded from percentage calculations.

into the first net of the next trawl. Since this first net is the one that fishes obliquely from the surface to the selected depth of sampling, it is not usually used in studying vertical distribution of animals.

Pelagic Trawl-IKMT Comparisons

The 17 pelagic trawls caught almost twice as many species of fishes, and about the same number of cephalopod species as the 16 IKMT's during the two major cruises in 1976 and 1977. These differences are mainly due to the large volumes of water filtered by the pelagic trawl and consequently the large number of individuals captured.

One of the most significant differences between the catches was the presence of some fish species in the pelagic trawl and their complete absence in the IKMT catches (number caught-vessel, where PR = Pacific Raider and EX = Excalibur): *Aphanophus carbo* (3-PR), *Merluccius productus* (3-PR), *Idiacanthus antrostomus* (23-PR), *Aristostomias scintillans* (24-PR, 6-EX), Macrouridae (5-PR), *Lestidium ringens* (37-EX), *Nansenia candida* (22-EX), *Symbolophorus californiensis* (5-EX). In over 2,000 (2, 2.5, and 3 m mouth opening) IKMT tows made off Oregon since 1961, we have never before captured *Aphanophus carbo* or *M. productus* in oceanic waters. These fishes were large (436-570 mm) and presumably always avoid IKMT's.

Length-Frequency Comparisons

Significant differences [$P < 0.5$, Kolmogorov-Smirov (K-S) two sample comparisons (Tate and Clelland 1957)] were found in the size-frequency

distributions of four common species (where n -50 for fishes for each of the two nets, and n >20 for squid) for: *Stenobranchius leucopsarus* in two of the three comparisons, *Diaphus theta* in one of two comparisons, and *Tarletonbeania crenularis* in two of two comparisons. In all instances where length distributions differed, the pelagic trawl caught an appreciably higher percentage of large animals. Even though the one K-S test for the squid *Gonatus pyros* was not significant (because of small numbers caught in the IKMT), 15% of numbers of this squid from the pelagic trawl were >35 mm DML and no animals >35 mm were caught in the IKMT.

Length-frequency distributions for *S. leucopsarus* and *T. crenularis* from both trawls (Figure 3) show that large lanternfishes are clearly undersampled by the IKMT. The modes composed of fishes >45 mm, which are prominent in pelagic trawl catches, are absent in IKMT catches.

Another notable example of differences between catches of large fish in these collections were captures of *Tactostoma macropus*. Few large individuals (>250 mm) have been collected in IKMT tows off Oregon. Three tows with the pelagic trawl at depths of 470-1,070 m in 1978, however, captured many large fish. Twenty-nine percent of the *T. macropus* caught in these pelagic trawl collections were >250 mm, compared with only 8.2% in 252 IKMT tows to 500 m depth or deeper during previous years.

Effective Cross-Sectional Area of the Pelagic Trawl

The cross-sectional area of the pelagic trawl was indirectly estimated from the catches of four species of lanternfishes caught in both the pelagic trawl and IKMT on the three "paired" cruises (Table 1) to see how it compared with the divers' estimates of 50 m². The following equation was used:

$$A = \frac{C_1 V}{C_2 D}$$

where A = area in square meters,
$\quad C_1$ = number of fish caught by pelagic trawl,
$\quad V$ = volume filtered by the IKMT, in cubic meters,
$\quad C_2$ = number of fish caught by the IKMT,
$\quad D$ = distance trawled by the pelagic trawl in meters.
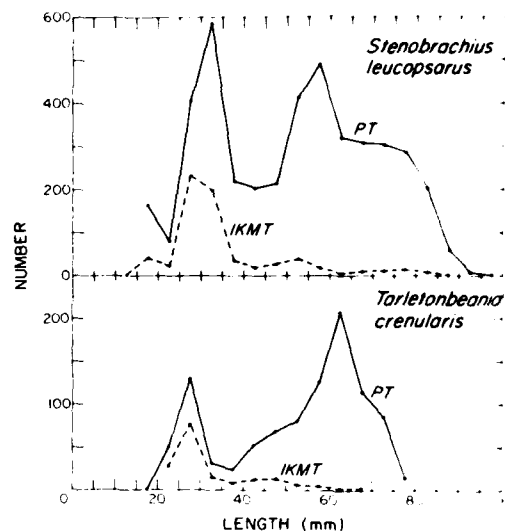
The volume of water filtered by the IKMT was

FIGURE 3.—Length-frequency distribution for *Stenobrachius leucopsarus* and *Tarletonbeania crenularis* in pelagic trawl and IKMT collections, July 1976, 0-500 m.

calculated from a flowmeter mounted in the MPS and monitored aboard ship via electrical cable (see Pearcy et al. 1977). Distances trawled by the pelagic trawl were calculated from ship speed (based on Loran readings) and the duration of the tow. In each comparison, tows and nets selected fished similar depths at the same time of day. The mouth area estimated in this way varied from 19 to 3,161 m² with a median value between 48 and 62 m² (Table 3). The smallest area (19 m²), for *D. theta*, can be largely explained by the retention of small fish (10-15 mm) in the IKMT but not by the slightly larger mesh of the pelagic trawl. This is the only obvious example of differences in size-frequency distributions that can be explained by escapement of small fish. The large values of mouth area may result from different population densities of two species at the times of sampling during the 1977 cruises.

The present study indicates that large nets usually catch more individuals, and usually, but not always, more species and larger animals than small IKMT-type nets. Detailed quantitative comparisons are needed with nets of known cross-sectional areas, with similar mesh size, at the same depths and locations (Roper 1977). Large nets will never replace the smaller IKMT's and rectangular midwater trawls because of the specialized equipment needed to launch and re-

TABLE 3.—Estimates of the effective mouth size of the pelagic trawl (PT) based on estimated distance trawled (speed × time), the catches of four lanternfishes, and the catches of four lanternfishes and volumes for IKMT's on "paired" cruises.

Item	Stenobrachius leucopsarus	Diaphus theta	Tarletonbeania crenularis	Protomyctophum thompsoni
1975—1 PT. 5 IKMT, 340-350 m. day				
Distance trawled by PT 23.718 m				
Vol. filtered by IKMT 435.210 m³				
No. caught in PT	2.121	216	146	218
No. caught in IKMT	816	212	61	123
Effective mouth area, m²	48	19	44	32
1976—8 PT. 11 IKMT, 0-350 m, day/night				
Distance trawled by PT 148.425 m				
Vol. filtered by IKMT 1.525.860 m³				
No. caught in PT	4.306	1.663	1.007	183
No. caught in IKMT	718	644	167	60
Effective mouth area. m²	62	27	62	31
1977—2 PT, 3 IKMT, 290-325 m, day/night:				
Distance trawled by PT = 18.931 m				
Vol. filtered by IKMT 630.385 m³				
No. caught in PT	2.658	149	388	192
No. caught in IKMT	28	4	2	100
Effective mouth area. m²	3.161	1.240	646	64

cover large nets from oceanographic vessels. We need to compare catches of different-sized trawls, however, in order to evaluate biases and to learn what portions of the plankton-micronekton-nekton spectrum are effectively sampled by different nets.

Acknowledgments

References

BAKER, A. DE C., M. R. CLARKE, AND M. J. HARRIS.
1973. The N.I.O. combination net (RMT 1 + 8) and further developments of rectangular midwater trawls. J. Mar. Biol. Assoc. U.K. 53:167-184.
BERRY, F. H., AND H. C. PERKINS.
1966. Survey of pelagic fishes of the California Current area. U.S. Fish Wildl. Serv., Fish. Bull. 65:625-682.
CLARKE, T. A.
1973. Some aspects of the ecology of lanternfishes (Myctophidae) in the Pacific Ocean near Hawaii. Fish. Bull., U.S. 71:401-434.
1974. Some aspects of the ecology of stomiatoid fishes in the Pacific Ocean near Hawaii. Fish. Bull., U.S. 72:337-351.
DONALDSON, H. A.
1975. Vertical distribution and feeding of sergestid shrimps (Decapoda: Natantia) collected near Bermuda. Mar. Biol. (Berl.) 31:37-50.

EVANS, F.
1975. Universal modular timer. Exposure 3:8-11.
FOXTON, P.
1970. The vertical distribution of pelagic decapods (Crustacea: Natantia) collected on the SOND cruise 1965. J. Mar. Biol. Assoc. U.K. 50:939-960.
HARRISSON, C. M. H.
1967. On methods for sampling mesopelagic fishes. Symp. Zool. Soc. Lond. 19:71-126.
KREFFT, G.
1974. Investigations on midwater fish in the Atlantic Ocean. Ber. dtsch. wiss. Komm. Meeresforsch., Neue Folge, 23:226-254.
PEARCY, W. G. (editor).
1975. Workshop on problems of assessing populations of nekton. Off. Nav. Res. Rep. ACR 211, 30 p.
PEARCY, W. G., E. E. KRYGIER, R. MESECAR, AND F. RAMSEY.
1977. Vertical distribution and migration of oceanic micronekton off Oregon. Deep-Sea Res. 24:223-245.
PEARCY, W. G., AND R. M. LAURS.
1966. Vertical migration and distribution of mesopelagic fishes off Oregon. Deep-Sea Res. 13:153-165.
ROPER, C. F. E.
1977. Comparative captures of pelagic cephalopods by midwater trawls. Symp. Zool. Soc. Lond. 38:61-87.
TATE, M. W., AND R. C. CLELLAND.
1957. Nonparametic and shortcut statistics in the social, biological, and medical sciences. Interstate Printers and Publishers, Inc., Danville, Ill., 171 p.
TAYLOR, F. H. C.
1968. The relationship of midwater trawl catches to sound scattering layers off the coast of northern British Columbia. J. Fish. Res. Board Can. 25:457-472.
WILLIS, J. M.
1979. Vertical distribution and migration of fishes from the lower mesopelagic zone off Oregon. M.S. Thesis, Oregon State Univ., Corvallis, 52 p.

WILLIAM G. PEARCY

School of Oceanography
Oregon State University
Corvallis, OR 97331

27

Oceanic Radiation Instruments

C.A. Paulson

1. INTRODUCTION

The ability to measure the distribution of light and optical prop-
erties in the upper ocean is useful for a number of applications.
Among these are: (1) the estimate of solar heating as a function
of depth; (2) the study of biological processes; and (3) the in-
vestigation of the motion of surface waters using optical proper-
ties as tracers. The purpose of this chapter is to describe rela-
tively simple instruments for measuring light and optical proper-
ties which would yield results useful for air-sea interaction in-
vestigations. The description of the instruments is prefaced by an
elementary description of the distribution of light and optical
properties in the upper ocean.

It is important to emphasize that the scope of this chapter is lim-
ited to instruments most appropriate for air-sea interaction stud-
ies. Optical oceanography has a long history and there has grown a
large body of theoretical and observational literature which has
been excellently summarized by Jerlov (1976). The theoretical as-
pects of radiative transfer in water have also been comprehensively
treated by Preisendorfer (1976), and Ivanoff (1977) has recently
reviewed radiative processes in the lower atmosphere and upper
ocean with a view toward modelling the upper ocean. Tyler and
Preisendorfer (1962) and Jerlov (1976) have described instruments
used in optical oceanography.

Instrument developments have contributed greatly to advances made
in optical oceanography. The design, construction, calibration,
and use of oceanic instruments have been undertaken primarily by
laboratories with extensive and specialized capabilities in optical

oceanography. However, the simplest of existing optical instru-
ments are the most suitable for air-sea interaction investigations
and require only a modest amount of resources and experimental ex-
pertise for their successful use. The discussion below is limited
to these instruments.

2. LIGHT IN THE UPPER OCEAN

A comprehensive description of the distribution of light and opti-
cal properties in the upper ocean is given by Jerlov (1976). Of
the solar radiation striking the sea surface, about 7% on average
is reflected and backscattered upward into the atmosphere (see,
e.g., Payne, 1972) and the remainder is absorbed in the sea. The
upward solar radiative flux just above the surface is mainly caused
by reflection at the surface and secondarily by backscattering from
below the surface. The contribution from backscattering is only
about 0.5% of the radiative flux striking the surface (Payne, 1972;
Ivanoff, 1977). Solar radiation is attenuated in sea water by both
absorption and scattering with absorption dominating. The downward
irradiance, defined as the flux of radiant energy per unit area ar-
riving at a horizontal surface that is facing upward, falls to one-
half the surface value within the uppermost metre of the sea. As
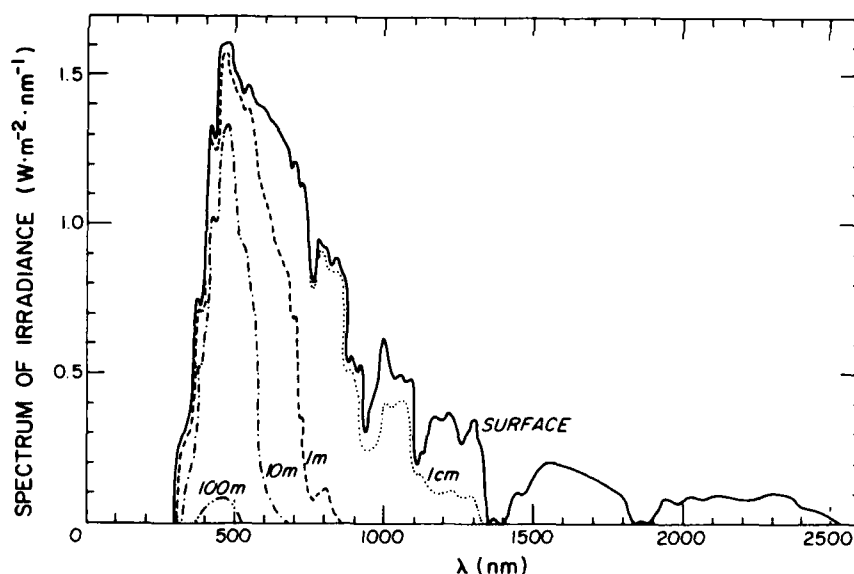

Fig. 1   The spectrum of downward irradiance at various
           depths in the ocean (after Jerlov, 1976)

shown in Figure 1, the attenuation is strongly dependent on wave-
length; water acting as a monochrometer leaves only blue-green
light below a depth of 10 m. The distribution of radiant energy as
a function of direction depends on the location of the sun, but,
with increasing depth, tends toward a maximum at the zenith, be-
comes symmetric about the zenith, and falls off rapidly with in-
creasing zenith angle. The symmetric distribution about the zenith
results because light rays following vertical paths are least at-
tenuated.

Because of backscattering, there is also an upward irradiance: the
flux density of radiant energy striking a horizontal surface that
is facing downward. The ratio of upward to downward irradiance is
less than 0.1 and is typically about 0.05 below a depth of 2 m
(Jerlov, 1976, Table XXXIII, p. 148).

As shown in Figure 2, the downward irradiance falls nearly exponen-
tially with depth below 10 m. Above 10 m, the rate of decrease
with depth is much faster than exponential because of the depend-
ence of attenuation on wavelength as shown in Figure 1. The curves
drawn to the observations are the sum of two exponentials, as sug-
gested by Kraus (1972):
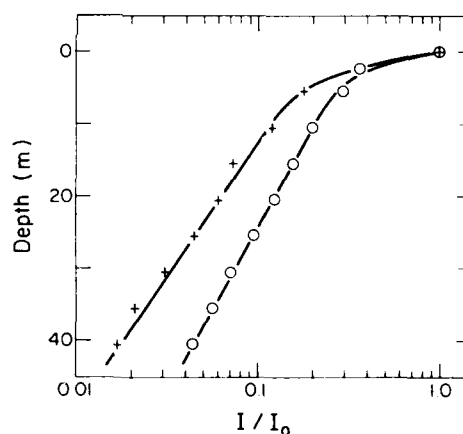
Fig. 2   Observations in the North Pacific (35°N, 155°W) re-
           ported by Paulson and Simpson (1977) of normalized
           downward irradiance as a function of depth. The
           circles are an average of five sets of observations
           under overcast skies with solar altitudes ranging
           from 30 to 38 degrees. The crosses are a single set
           of observations under clear skies with a solar alti-
           tude of 16 degrees.

$$I_d(z)/I_d(0) = R \exp(\gamma_1 z) + (1 - R) \exp(\gamma_2 z) \qquad (1)$$

where I_d is the downward irradiance, z is the vertical space coordinate which is positive upwards with z = 0 at mean sea level, $I_d(0)$ is the downward irradiance just below the surface, R is a constant depending on water clarity and solar altitude, and γ_1 and γ_2 are attenuation coefficients for downward irradiance. The first term dominates near the surface and represents the attenuation of the long-wave components of the solar radiation; the second term represents the attenuation of approximately monochromatic blue-green light below a depth of about 10 m.

Heating of the upper ocean occurs because of the absorption of radiative energy. The heating rate, dQ/dt, is equal to the divergence of the net downward radiative flux:

$$\frac{dQ}{dt} = \frac{\partial}{\partial z}(I_d - I_u) ,$$

which may be rewritten:

$$\frac{dQ}{dt} = \frac{\partial}{\partial z}[I_d(1 - \frac{I_u}{I_d})]$$

As was stated above, I_u/I_d is nearly independent of z below a depth of 2 m; thus the terms in the above equation containing I_u/I_d can be neglected. Above a depth of 2 m, I_u/I_d decreases with decreasing depth from about 0.05 to about 0.005 just below the interface. It can easily be shown that terms containing I_u/I_d contribute less than 5% to the heating rate in the upper 2 m; thus for many purposes the divergence of the upward irradiance can be safely neglected. Radiative heating of the upper ocean is discussed more extensively by Ivanoff (1977).

Oceanic water has variable optical properties depending on the amount and kind of suspended and dissolved material. Jerlov (1976) has devised a system of classifications of surface water based on spectral transmittance of downward radiation at high solar altitude. Surface water tends to be clearest in the open ocean at mid-latitudes, while coastal areas and high latitudes often have reduced clarity because of high biological productivity. Paulson and Simpson (1977) have computed values of R, γ_1, and γ_2 (Eq. 1) for each water type.

An optical property which is useful for characterizing sea water and which is relatively easy to measure is the beam transmittance, τ, defined as the radiant flux, F_t, transmitted over a distance r

by a beam of infinitesimal width, divided by the incident flux:

$$\tau = \frac{F_t}{F_0}$$

The beam attenuation coefficient, c, is the proportional change in flux, $\Delta F/F$, across an infinitesimally thin layer of the medium normal to the beam divided by the thickness, Δr, of the layer:

$$c = \frac{\Delta F}{F \Delta r}$$

The beam attenuation coefficient and transmittance depend on wavelength. For a homogeneous medium
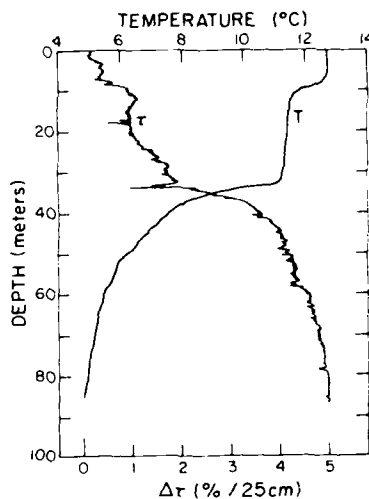
$$\tau = \exp (- c \ r). \tag{2}$$

TEMPERATURE (°C)

Fig. 3   Observations of the change of beam transmittance with respect to the value near the surface (pathlength of 25 cm) and temperature versus depth in the North Pacific (50°N, 145°W), August 1977 (observations supplied courtesy of D.R. Caldwell and T.M. Dillon, School of Oceanography, Oregon State University, Corvallis, OR).

Vertical profiles of transmittance show whether the water column
has uniform optical properties. An assumption underlying Equation
1 is that the attenuation coefficients Y_1 and Y_2 are independent of
depth. This assumption can be tested by measurements of transmit-
tance.

An example of measurements of transmittance and temperature as a
function of depth is shown in Figure 3. The general increase of
transmittance with depth is consistent with the expectation of a
higher concentration of biological material near the surface. The
small-scale variability in transmittance is caused by variability
in the concentration of particles and may be useful for drawing in-
ferences about mixing processes. The small-scale variability may
also be of biological interest.

3. BEAM TRANSMITTANCE METER

As the name implies, the beam transmittance meter or transmissome-
ter, as it is often called, measures beam transmittance, τ, from
which one may obtain the attenuation coefficient, c, by use of
Equation 2. A schematic diagram of a representative instrument is
shown in Figure 4. The essential elements are a light source of
constant intensity, optics to produce a parallel beam with a large
length-to-width ratio, windows which protect sensitive elements and
determine the fixed path length, a filter which transmits light in
a particular wavelength band, and a cell which measures light in-
tensity. Mirrors or internally reflecting prisms are sometimes
used to minimize the size of the instrument for a given path length
(e.g., Tyler et al., 1974).

An instrument for measuring beam transmittance has been described
by Tyler et al. (1974), and is shown schematically in Figure 5.
The light beam is 0.2 cm in diameter and traverses 1 m through the
water. The source is a 20 W tungsten-iodide lamp. The intensity
of the lamp is monitored on command by the detector through a light
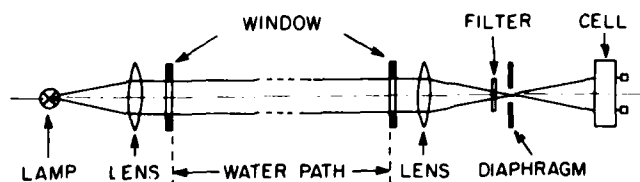pipe and shutter as shown in Figure 5. The detector is a silicon

Fig. 4   Schematic diagram of a beam transmittance meter
          (after Joseph. 1949)
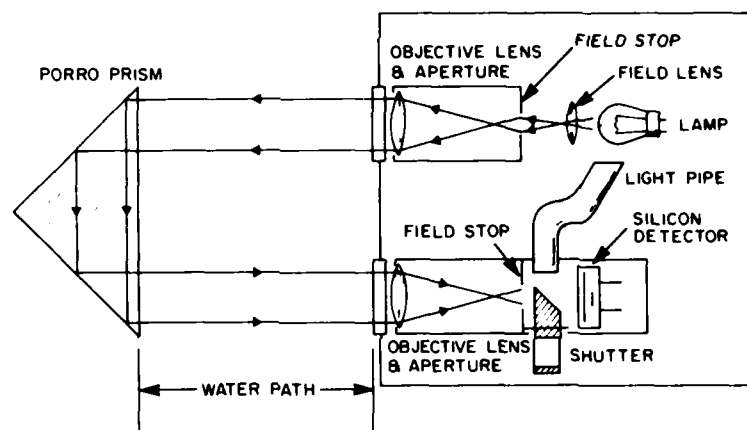
Fig. 5   Schematic diagram of a beam transmittance meter
          (after Tyler et al., 1974)

photovoltaic cell. Although not shown in Figure 5, there is placed
in front of the detector a filter to restrict the sensitivity of
the instrument to a band centered at a wavelength of about 530 nm.
The spectral characteristics of the source and detector have to be
considered together with the filter in obtaining the desired spec-
tral sensitivity.

Jerlov (1976, p. 104) has reviewed the merits of different types of
collectors. In addition to the silicon photovoltaic cells, pos-
sible choices include selenium photovoltaic cells and photomulti-
plier tubes. Photomultiplier tubes are more sensitive than photo-
diodes but are much larger in size, require a well stabilized high
voltage, and are subject to changes in calibration; they are sensi-
tive to light intensity over a range of approximately ten orders of
magnitude compared to about seven for a photodiode.

The following is a list of precautionary measures to be taken in
the design and use of a beam transmittance meter:

    Care must be taken to minimize errors due to fluctuations in
    intensity of the light source. The intensity of the source may
    be monitored as in Figure 5.

Daylight must be excluded from the detector or its effects may
be excluded electronically by blinking the source and measuring
the amplitude of the signal. Care must be taken so that shiel-
ding does not reflect scattered light from the beam into the
detector (as discussed by Tyler et al., 1974).

The sensitivity of the calibration of the instrument to varia-
tions in temperature needs to be minimized. Electronics to
compensate for temperature effects may be required.

Because of the finite width of the beam, some extraneous scat-
tered light can enter the detector. The ratio of the path
length to beam width must be sufficiently large to minimize
this error (Jerlov, 1976). The instrument shown in Figure 5
has an error due to this effect of less than 1%.

To obtain reliable absolute measurements, readings should be
taken in air prior to a profile. Because the beam diverges
less in water than in air, care must be taken to ensure that
the beam is not blocked in air. The index of refraction of the
windows must be known to obtain absolute values of τ by use of
measurements in air.

There may be a false minimum in τ if the beam is tilted from
the horizontal while passing through an interface separating
fluid of two densities. The error occurs because of refraction
at the interface.

Transmissometers are usually lowered from a ship, but may be towed
(Joseph, 1957) or moored (Zaneveld et al., 1978). The measurements
shown in Figure 3 were taken by a transmissometer, thermistor, and
pressure sensor mounted on a microstructure profiler (see Chapter
37 by Lange) which has wings to cause rotation and slow the descent
rate to several centimetres per second. The profiler is mechanic-
ally decoupled from the ship during descent and data is transmitted
through a very light multiconductor cable.

4. IRRADIANCE METER

Irradiance meters measure the total amount of radiant flux striking
a plane collector of known area. They are used most often with the
collector horizontal and facing upward to measure downward irradi-
ance but they may be inverted to obtain upward irradiance. A draw-
ing of an irradiance meter is shown in Figure 6. The collector is
diffusive, typically opal glass or opal plastic, and the dimensions
of the materials surrounding the collector are adjusted so that the
response nearly obeys a cosine law (Smith, 1969). There may be a
filter between the collector and the quartz window depending on
whether a particular wavelength band is of interest as in some bio-
logical investigations. A filter may also be required to compensate

PHOTOCELL
EDGE
STOP
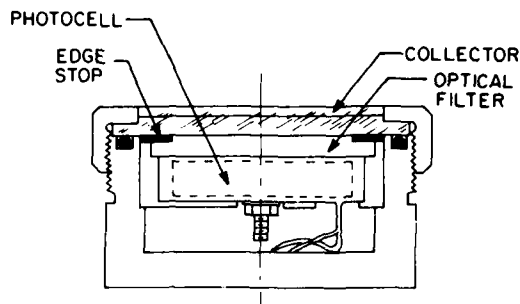COLLECTOR
OPTICAL
FILTER

Fig. 6   Schematic diagram of an irradiance meter (after
            Tyler and Preisendorfer, 1962)

for spectral characteristics of the collector and detector. The
detector is usually a photomultiplier tube or a photodiode. The
signal from the detector is ordinarily amplified nonlinearly to ob-
tain better signal-to-noise ratios for low light levels.

Tyler and Preisendorfer (1962) quote an uncertainty in irradiance
measurements of 2% for the meter shown schematically in Figure 6.

Some precautionary measures to be taken in the design and use of an
irradiance meter follow:

    Small departures from a cosine response are not serious when
    measuring downward irradiance because the downward radiance
    field approaches a maximum near the vertical. However, errors
    may be introduced when measuring upward irradiance because the
    upward radiance is more nearly isotropic.

    The spectral response of the collector is an important concern
    when the total irradiance is desired. Many collectors attenu-
    ate strongly in the short-wave end of the solar spectrum. Cal-
    ibrations to determine the spectral response are required. The
    spectral response of the instrument used to obtain the measure-
    ments shown in Figure 2 was uniform within $\pm 5\%$ for wavelengths
    from 400 to 1000 nm.

    When absolute values of irradiance are desired, one needs to
    make routine comparisons of the irradiance meter in air with a
    well calibrated pyranometer. Comparisons are necessary because

of possible sensitivity of the electronics to variations in
temperature and because of changes in calibration of the detec-
tor.

When comparing underwater measurements to measurements in air,
correction must be made for the 'immersion effect' which is a
combination of effects caused by reflection at the sea surface
and at the collector surface. The effect is discussed by West-
lake (1965) and is illustrated in Figure 7.

When measuring vertical irradiance profiles, it may be neces-
sary to make corrections for variations in surface irradiance,
particularly when conditions are cloudy. Continuous surface
measurements are therefore desirable.

The irradiance meter is usually lowered over the side of the ship.
Care must be taken to minimize effects of shadowing or reflection
caused by the supporting cable and the ship. Ship motion and waves
may make it difficult to keep the collector horizontal, particular-
ly near the surface. Accurate measurements can only be made in
calm or moderate sea states. Weighting the base of the irradiance
meter and gimballing it may help ensure that the collector is hori-
zontal. It is probably possible to make accurate measurements in
the upper few metres, only from stable platforms; such observations
have been made from FLIP by Paulson and Simpson (1977) and from the
Bouée Laboratoire by J.P. Bertoux (Ivanoff, 1977). Even from sta-
ble platforms, waves are a problem because of the variable depth of
the water over the instrument. Linear averaging of the irradiance
signal may not be appropriate unless the depth of the instrument
below mean sea level is much greater than the amplitude of the
waves. This problem arises because of the highly nonlinear depen-
dence of I_d on z when the magnitude of z is small.

5. THE SECCHI DISC

One of the oldest oceanographic instruments is the 'Secchi' disc,
named after Professor P.A. Secchi who, in the 1860s, investigated
the effect of many variables on the visibility of a white disc sus-
pended from a ship. The Secchi disc has a diameter of 30 cm and is
painted white. The 'Secchi depth' is the depth at which the disc
ceases to be visible by an observer above the surface. A descrip-
tion of the Secchi disc and instructions in its use are given in
the Instruction Manual for Obtaining Oceanographic Data (U.S. Naval
Oceanographic Office, 1968).

The Secchi disc is widely used because of its simplicity, but the
interpretation of the observation, except as a rough measure of
transparency, is difficult. The Secchi depth may depend on solar
elevation, cloud type, cloud amount, and sea state. In spite of
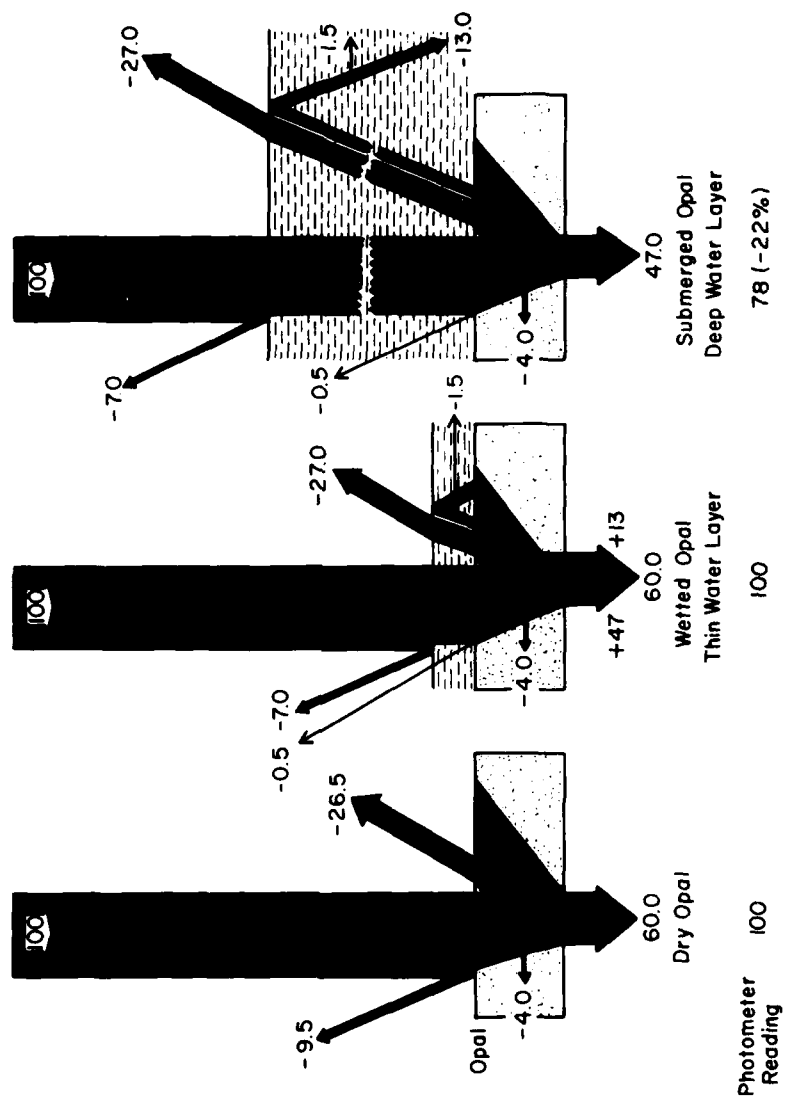these difficulties, the numerous observations of Secchi depth may

Fig. 7   A diagram illustrating the immersion effect (after Westlake, 1965).

be useful in estimating the heating rate in the upper ocean as a function of depth.

Tyler (1968) has described the theory of the Secchi disc observation and has suggested that

$$\frac{3.78 \, K_d}{(c + K_d)} = \frac{D}{I_{d.1}} \tag{3}$$

where c and K_d are the attenuation coefficients for collimated and diffuse light respectively, D is the Secchi depth and $I_{d.1}$ is the depth at which the downward irradiance is 10% of the surface value. If a fixed ratio between c and K_d is assumed, $I_{d.1}$ can be related to D. Tyler (1968) plots observations which are in rough agreement with

$$I_{d.1} = D \tag{4}$$

for D less than 30 m. Paulson and Simpson (1977) also report observations in fair agreement with Equation 4 if cases of high wind speed (rough surface) and low solar elevation are neglected. Caution, however, should be exercised. As stated by Tyler (1968), c is not necessarily a fixed multiple of K_d, and other assumptions are made in the derivation of Equation 3.

Given an estimate for $I_{d.1}$ from Equation 4, one may determine the water type (Jerlov, 1976, Fig. 71, p. 136). One may then use Equation 1 to compute downward irradiance using the values of R, Y_1, and Y_2 given by Paulson and Simpson (1977) for different water types. The heating rate can then be calculated as shown above.

ACKNOWLEDGEMENTS

REFERENCES

IVANOFF, A. 1977. Oceanic absorption of solar energy. In *Modeling and Prediction of the Upper Layers of the Ocean*, edited by E.B. Kraus, Pergamon, Oxford: 47-71.
JERLOV, N.G. 1976. *Marine Optics*. Elsevier, Amsterdam, 231 pp.
JERLOV, N.G. and E.S. NIELSEN, editors. 1974. *Optical Aspects of Oceanography*. Academic Press, London, 494 pp.

JOSEPH, J.   1949.   Durchsichtigkeitsmessungen im Meere im ultrabio-
          letten Spektralbereich.   *Deutschen Hydrographischen Zeit-
          schrift.*, 2:   212-218.

JOSEPH, J.   1957.   Extinction measurements to indicate distribution
          and transport of water masses.   In *Proceedings of the
          UNESCO Symposium on Physical Oceanography,* 1955, Tokyo:
          59-75.

KRAUS, E.B.   1972.   *Atmosphere-Ocean Interaction.*   Clarendon, Ox-
          ford, 275 pp.

PAULSON, C.A. and J.J. SIMPSON.   1977.   Irradiance measurements in
          the upper ocean.   *Journal of Physical Oceanography,* 7:
          952-956.

PAYNE, R.E.   1972.   Albedo of the sea surface.   *Journal of Atmo-
          spheric Sciences,* 29:   959-970.

PREISENDORFER, R.W.   1976.   *Hydrologic Optics.*   Volumes I-IV, U.S.
          Department of Commerce, National Oceanic and Atmospheric
          Administration, Environmental Research Laboratories,
          Honolulu, Hawaii.

SMITH, R.C.   1969.   An underwater spectral radiance collector.
          Journal of Marine Research, 27:   341-351.

TYLER, J.E. and R.W. PREISENDORFER.   1962.   Transmission of energy
          within the sea: Light.   In *The Sea,* edited by M.N. Hill,
          Interscience, New York: 397-451.

TYLER, J.E.   1968.   The Secchi disc.   *Limnology and Oceanography,*
          13:   1-16.

TYLER, J.E., R.W. AUSTIN and T.J. PETZOLD.   1974.   Beam transmis-
          someters for oceanographic measurements.   In *Suspended
          Solids in Water,* edited by R.J. Gibbs, Plenum, New York:
          51-59.

U.S. NAVAL OCEANOGRAPHIC OFFICE.   1968.   *Instruction Manual for
          Obtaining Oceanographic Data, 1968.*   Publication No. 607,
          third edition, Washington, D.C.:   1314-1315.

WESTLAKE, D.F.   1965.   Some problems in the measurement of radia-
          tion under water: A review.   *Photochemistry and Photo-
          biology,* 4:   849-868.

ZANEVELD, J.R.V., R. BARTZ and H. PAK.   1978.   A transmissometer
          for profiling and moored observations.   In: *Ocean Optics
          V.*   American Society of Photogrammetry, *Proceedings of the
          Society of Photo-Optical Instrumentation Engineers,* Volume
          160, Rochester, New York.

Intermediate Nepheloid Layers Observed off Oregon and Washington

HASONG PAK, J. RONALD V. ZANEVELD, AND J. KITCHEN

School of Oceanography, Oregon State University, Corvallis, Oregon 97331

Two distinct kinds of particle maxima (nepheloid layers) were observed off Oregon in November 1977 and off Washington in October 1978 by an in situ light transmissometer: one in the thermocline in the euphotic zone and the other at intermediate depth well below the thermocline. The thermocline nepheloid layer is associated with well-defined maxima of dissolved oxygen, chlorophyll-*a*, and phaeophytin, and these associations suggest that the nepheloid layer is primarily composed of phytoplankton undergoing acti e photosynthesis. The intermediate nepheloid layer is found in connection with the bottom waters near the shelf break and shares some of the characteristic properties of the bottom water: high concentration of suspended particles, low concentrations of dissolved oxygen, chlorophyll-*a*, and phaeophytin. The particle size distributions in the intermediate nepheloid layer are different from those in the clear water above the nepheloid layer but similar to those in the bottom nepheloid layer. Two hypotheses for the generation of intermediate nepheloid layers, settling and horizontal advection, are examined, and the data support the latter hypothesis.

INTRODUCTION

Natural waters contain large numbers of suspended particles. The distribution and characteristic properties of the suspended particulate matter (spm) are subject to the structure and changes in the oceanic environment. Particles are introduced into the ocean by streams and by the wind. They are also generated by in situ production through biochemical processes. What happens to the particles after they are introduced into the ocean is of considerable interest: they are transported by currents and gravitational settling; they may change their characteristic properties by dissolution, consumption by organisms and aggregation [*Zaneveld*, 1971; *Lerman et al.*, 1974].

Tracing individual particles in the ocean is impractical, if not impossible, so particles contained in natural water samples are studied collectively. One of the common approaches to studying particle transfer processes is to identify specific particle characteristics so that the particles can be related to known source(s). There are a number of particle properties which have been used for such purposes: organic/inorganic fraction, chemical composition, optical properties, particle size distributions (PSD), species identification of the biological fraction, etc.

Concentration of spm was traditionally determined by weighing particles collected on a 0.45-μm pore diameter membrane filter. Recently, optical instruments measuring either light scattering or beam attenuation have been applied successfully to the determination of concentration of spm in the ocean [*Drake*, 1974; *Peterson*, 1977]. Optical instruments are particularly useful in obtaining vertical profiles of spm in situ rather than at discrete points, and long-term measurements at a point are possible if the instruments are moored. From light transmission profiles, for example, we have learned the major sources of spm in the ocean; from temporal variations of light transmission profiles, we began to recognize some of the important processes of particle transfer [*Pak and Zaneveld*, 1977, 1978].

Vertical distribution of suspended particulate matter in the

ocean generally reveals one or more layers of maximum particle concentration. Regional differences are large near land and river plumes, and where biological productivity is high [*Jerlov*, 1953; *Beardsley et al.*, 1970; *Carder et al.*, 1971; *Matlack*, 1974]. A vertical particle maximum has been widely observed in seasonal thermoclines, usually in the upper part of the thermocline. The long-standing interpretation of such a spm maximum is based on a decreased particle settling rate in combination with a minimum in turbulent diffusion. Maximum phytoplankton production is assumed to occur in the surface layer and to decrease with depth. The biologically produced particles are then thought to accumulate at some depth in the thermocline due to (1) downward increase in density of water (mainly from decrease in temperature), (2) reduction in particle size as a result of decomposition and dissolution during settling, and (3) minimum turbulent mixing at the depth of the spm maximum. A downward increase of turbulent diffusion below the particle maximum is also required in order to form a maximum [*Riley et al.*, 1949; *Jerlov*, 1959; *Lerman et al.*, 1974].

Over the continental shelves and slopes off Oregon, Washington, and Peru, intermediate nepheloid layers (INL) have been observed below the euphotic zone [*Pak and Zaneveld*, 1977, 1978; *Pak et al.*, 1980a]. Although its long-term variation has not been confirmed, the INL off Oregon (in approximately 420 m of water) was observed to be stable for the period of a week [*Pak and Zaneveld*, 1978]. Observations off Peru suggest that a well-defined INL persists over a period of months [*Pak et al.*, 1980a]. Since there is no major source of particles beneath the euphotic zone and above the bottom, presence of an INL at several hundred meters depth indicates spm in transit. There are two hypotheses for the origin of such layers: the settling hypothesis and the horizontal advection hypothesis. These hypotheses conflict with one another to a large degree. In this paper, we will examine the two hypotheses by means of vertical distributions of spm, particle size distributions (PSD), dissolved oxygen, cholorophyll-*a*, phaeophytin, and hydrographic data. Particle transfer processes are of major significance to biological, chemical, and geological processes. In addition, since an INL is often a well-defined and easily detectable phenomenon it may be a simple
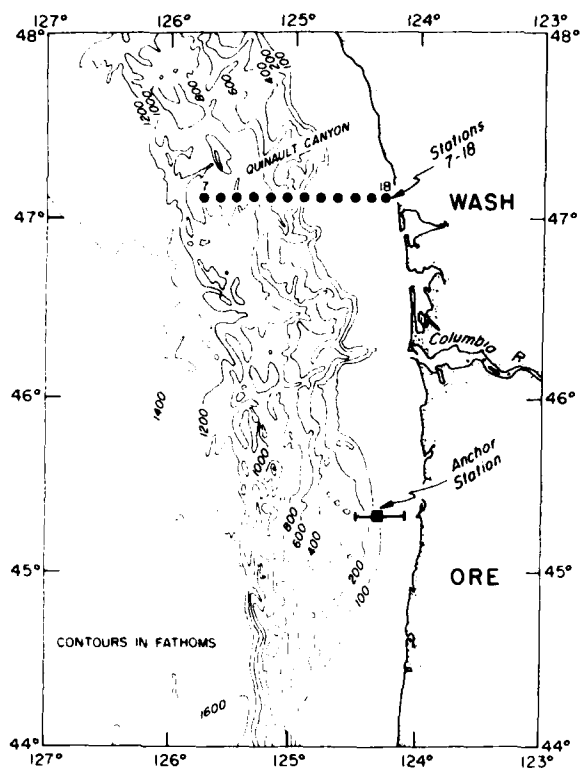
Fig. 1. Bathymetry and approximate locations of stations occupied during the TT135 cruise (near Quinault Canyon) and the W7711A cruise (off Oregon).

and useful indicator of particle transfer and of the dynamics of the water containing the INL.

METHODS AND OBSERVATIONS

Hydrographic and light transmission measurements were made in situ over the continental shelves and slopes off Oregon during November 6-13, 1977, and off Washington during

October 18-21, 1978 (Figure 1). During the November 1977 cruise on R/V *Wecoma* a CTD and a light transmissometer were used (both instruments were designed and built by the OSU optical oceanography group). Particle size distribution was determined by an in vitro electronic particle counter using water samples obtained by a Niskin rosette water sampler. Descriptions of these instruments and their operation and data reduction procedures are given by *Zaneveld et al.* [1978] and *Bartz et al.* [1978].

During the October 1978 cruise on the R/V *Thompson*, a light transmissometer [*Bartz et al.*, 1978] and an oxygen sensor (Beckman high-pressure oxygen sensor) were rigged in a stainless steel cage which also housed a Neil Brown CTD and a Niskin rosette water sampler. Profiles of light transmission, oxygen, and CTD were determined simultaneously, primarily in a zonal section at 47°-07.0'N latitude (Figure 1).

A number of chemical and biological analyses also were performed on the water samples. The sampling depths were determined by means of on-line temperature and light transmission profiles. Some of the chlorophyll-*a* and phaeophytin concentration data are presented in this paper to corroborate arguments made based on the in situ light transmission and hydrographic data. Light is attenuated by spm and 'yellow matter' in the water in addition to water itself. Light transmission has been shown to be useful for the determination of the temporal and spatial distribution of spm concentration in the ocean because it can be measured in situ [*Peterson*, 1977; *Bartz et al.*, 1978]. Thus we are able to infer spm distributions from light transmission data; the conversion of light transmission to spm concentration is particularly justified when the spatial distribution of spm is the main interest rather than absolute values of spm concentration. Chlorophyll-*a* is an indicator of live phytoplankton biomass, and phaeophytin is indicative of dead or moribund phytoplankton biomass [*Lorenzen*, 1965]. These plant pigments were determined according to the procedures described by *Strickland and Parsons* [1972].

Particle size distributions (PSD) were measured with a Nuclear Data pulse height analyser coupled to Coulter glassware
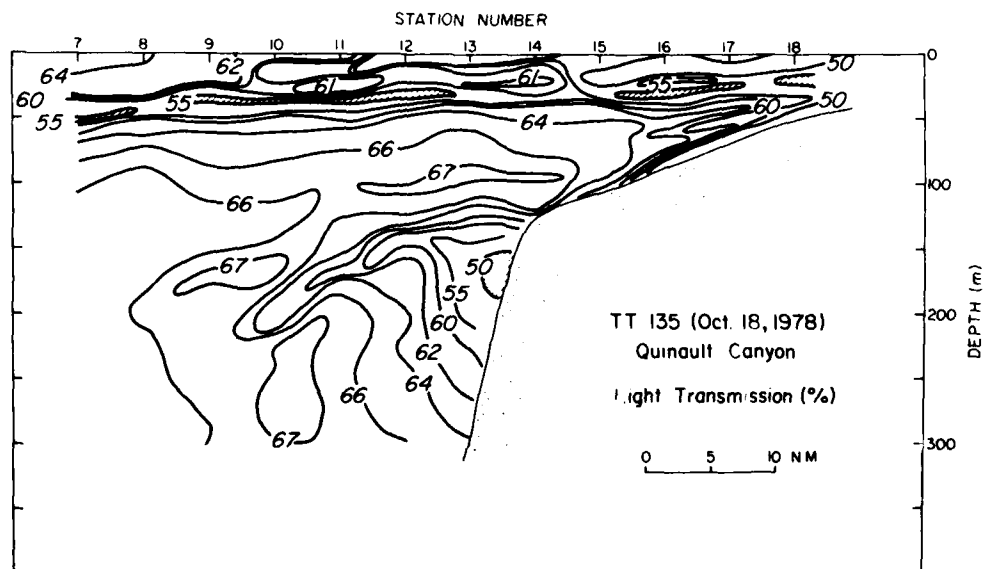

Fig. 2. Distribution of light transmission (in percent) in the zonal section near Quinault Canyon observed during the TT135 cruise (October 18, 1978).
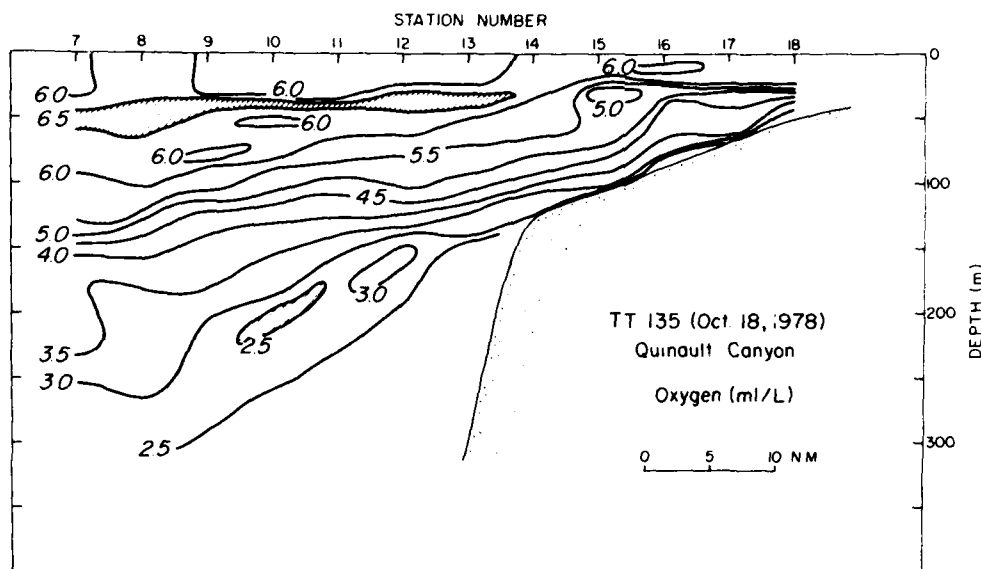
STATION NUMBER

Fig. 3.   Distribution of dissolved oxygen (ml/l) in the zonal section near Quinault Canyon observed during the TT135
cruise (October 18, 1978).

using 100 and 400 μm apertures. The effective size range measured was from 3.5 to 126.0 μm diameter. Each successive data window of the pulse height analyzer covers a particle volume of a half-power of 2 μm³. For example, the first window covers particles with volumes between $16(2)^{1/2}$ and $32 \ \mu m^3$, and the second window covers from 32 to $32(2)^{1/2} \ \mu m^3$.

Volume concentrations (in ppm) were computed by multiplying the particle concentration in each window by the average of the delimiting volumes for that window. Assuming a hyperbolic distribution, this method of computing volume concentrations gives a value that is 0.5 to 2% too high over a reasonable range of PSD slopes.

Slopes of PSD are computed by means of linear regression of the logarithms of the particle number concentration in windows versus the logarithm of the central diameter for each window. Assuming the hyperbolic distribution holds this is mathematically equivalent to determining the cumulative slope. This method was compared with the standard method of determining cumulative slope [Kitchen, 1978], and the mean difference was found to be negligible. The correlation coefficient was 0.96. The method used in this paper is much simpler from a computational standpoint.

RESULTS

SPM Maximum in Seasonal Thermoclines

The thermocline spm maximum (transmission minimum) is a relatively thin layer (about 20 m thick) over the shelf and extending offshore to the westernmost station (Figure 2). This layer is presumed to extend farther to the west. There is a slight but definite tendency of the spm maximum layer to become deeper away from the coast, which is probably due to the increased sunlight penetration as the surface water gets more transparent. An offshore increase in transparency in the surface water is evident in Figure 2. Another example can be found in Figure 7, where the light transmission in the surface layer is around 55%, clearly less than those further offshore shown in Figure 2. Distribution of dissolved oxygen (Figures 3 and 4) show a well-defined maximum corresponding to the

thermocline spm maximum over the slope. Over the shelf the oxygen maximum is absent, and thus no oxygen maximum is corresponded to the spm maximum. Distributions of both spm and oxygen show patchiness, suggesting that more than a simple one-dimensional (vertical) process is involved. In addition, the spm maximum is characterized by maxima in offshore chlorophyll-a and phaeophytin (Figures 5 and 6). Depth resolution of the dissolved oxygen profiles is excellent because it is based on in situ oxygen measurements. The oxygen concentrations in the maximum are in excess of the values in the surface layer, and the concentrations in the surface layer exceed saturation levels. The supersaturated oxygen concentration extends to about 80-m depth in the region where the oxygen maximum was observed in the thermocline (stations 7–13 in Figures 2 and 3).

The most significant implication of the maxima in oxygen, chlorophyll-a, and phaeophytin observed concurrently with the spm maximum is that the spm maximum layer contains large amounts of phytoplankton which are producing oxygen photosynthetically.

Intermediate Nepheloid Layers

A layer of turbid water is equivalent to a nepheloid (cloudy) layer, and the nepheloid layer is called either intermediate nepheloid layer (INL) or bottom nepheloid layer (BNL) depending on its location. Descriptively, an INL may be called intermediate spm maximum or intermediate particle maximum. In this paper, however, we use thermocline spm maximum to identify the particular INL located at the thermocline.

Over the continental shelves and slopes off Oregon/Washington, light transmission profiles typically show an intermediate nepheloid layer well below the thermocline [Pak and Zaneveld, 1978]. This layer is in addition to the spm maximum at the seasonal thermocline, described in the previous section.

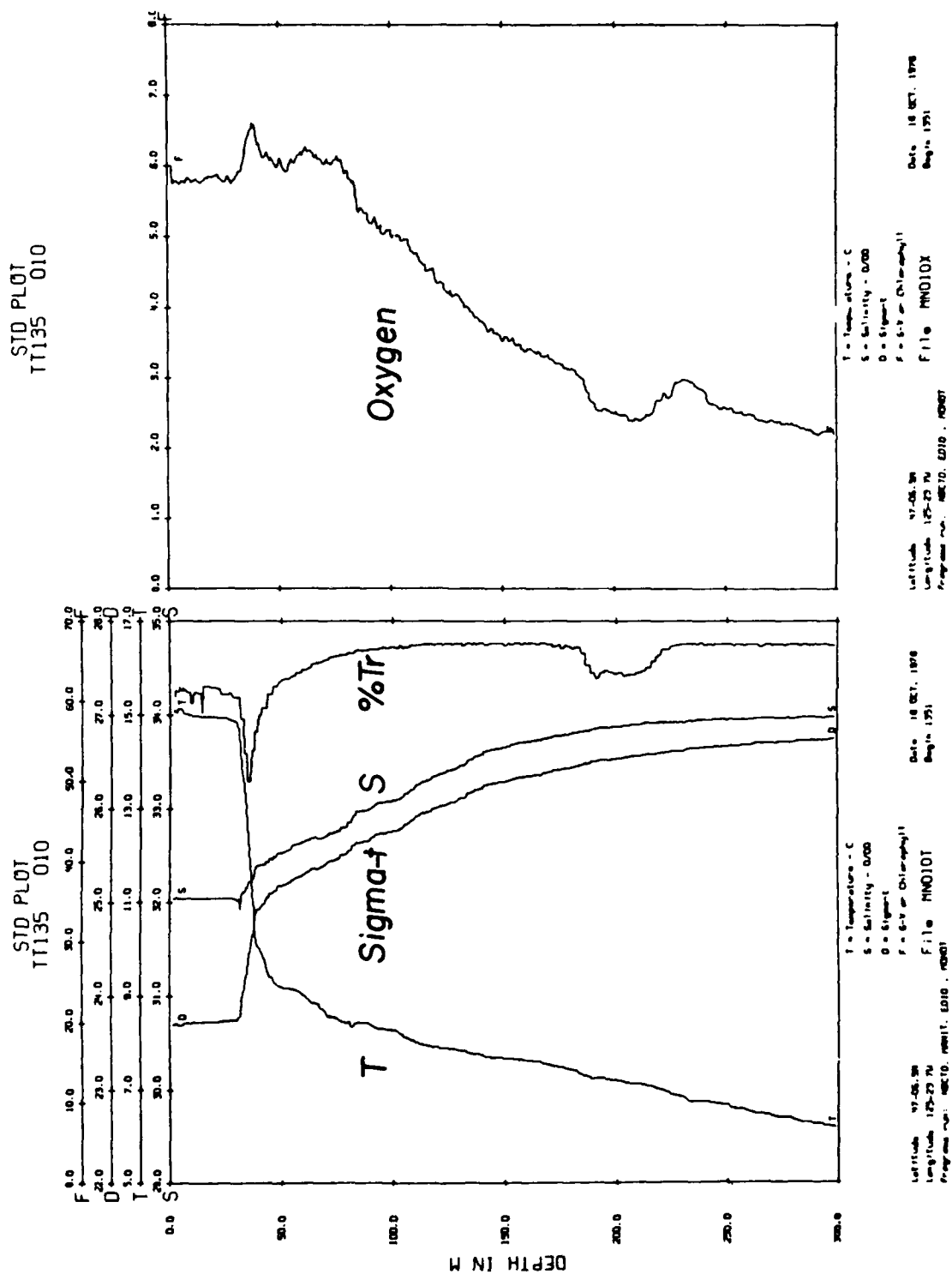Intermediate nepheloid layers observed during November 1977.   During the R/V Wecoma cruise in November 1977,

Fig. 4. Profiles of T, S, σ_t, light transmission (% Tr), and dissolved oxygen over the continental slope (station 10 in Figures 1 and 2) observed during the TT135 cruise (October 18, 1979).

W7711A, the INL was observed over the continental shelf off Oregon in a zonal section (Figure 7) and at an anchor station located at mid-shelf in approximately 170 m of water (Figure 8). The INL over the shelf extended offshore a distance of about 15 km at an intermediate depth with its eastern end connected to the bottom nepheloid layer near station 9-8. At the anchor station, two separate INL's were observed most of the time.

When the slope of the PSD is plotted against light attenuation (total particle concentration) for the entire cruise (W7711A), as in Figure 10, it is found that data from BNL's, INL's, surface water and clear water at intermediate depths lie in well-defined areas on the graph. The slopes of the PSD for the INL and the BNL are nearly linearly correlated with spm concentration (Figure 10). From the graph, the mid-depth clear waters and the surface mixed layers were clearly separated from the INL and BNL, but are located very close to each other (Figure 10). The slopes of PSD from the mid-depth clear water and surface mixed layer were widely scattered over narrow ranges of total particle concentration. The scatter may have been due partly to reduced precision caused by the low number of particle counts when the concentration is small.

In Figure 11 are illustrated the shapes of the PSD of two water samples with different total spm concentrations. It is clear that the concentrations of the large particles differed little in the two water samples, but the concentrations of the small particles differed a great deal. The water with large spm concentration can be characterized by a steep slope (Figure 11) which implies a large concentration of small particles without appreciable difference in large particles (relative to water with smaller total spm concentration).

We took water samples at five depths at a station 8 n. mi. offshore (Figure 12) in order to study vertical changes in PSD, particularly within the BNL. The PSD's of these five samples indicate that the slope of the PSD increases with increasing
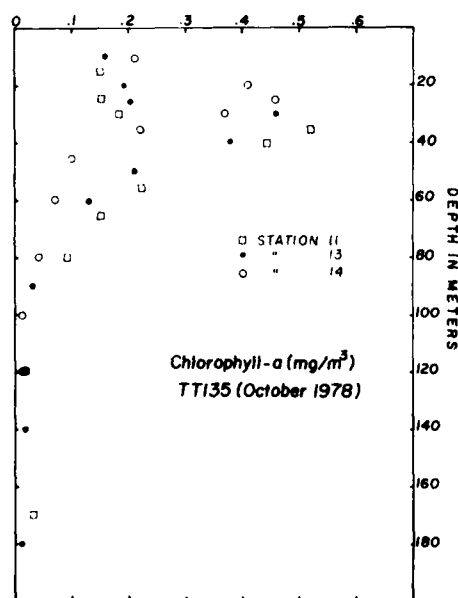

Fig. 6. Profiles of phaeophytin (mg/m³) over the continental slope (stations 11, 13 and 14 in Figures 1 and 2) observed during the TT135 cruise (October 18, 1978).

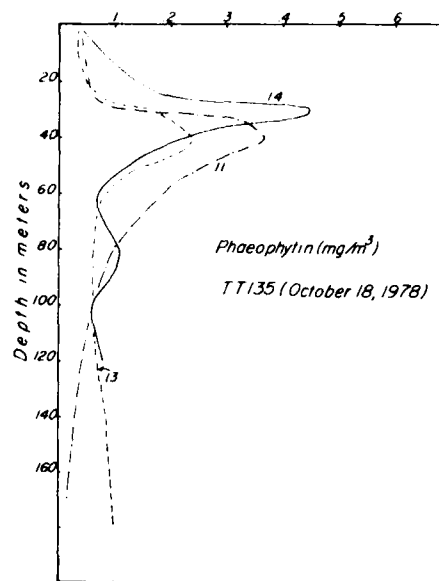spm concentration. Figure 13 is a plot of particle volume concentration against particle volumes. The volume concentrations of small particles clearly increase with depth.

Intermediate nepheloid layers observed during October 1978. A well-defined INL was observed at about 200-m depth during the R/V *Thompson* cruise in October 1978 over the continental slope off Washington near the Quinault Submarine Canyon (Figure 2). The INL extended from the shelf break at 150-m depth to 220-m depth, 20 nm further offshore. The layer was also characterized by a minimum in oxygen (Figure 4) and by low values of chlorophyll-*a* which prevailed at all depths below about 100 m (Figure 5). The phaeophytin concentration, on the other hand, showed a slight increase at the shoreside of the INL (stations 13 and 14 in Figure 6).

PSD measurement was made only for one sample in the INL, and its slope-concentration relation is consistent with the result from the W7711A cruise data (Figure 10).

Intermediate nepheloid layers and distributions of hydrographic data. The depths of spm maxima are usually observed to be parallel to isotherms. This trend has been verified by several observations over the past 5 years [*Pak and Zaneveld*, 1978; *Pak et al.*, 1980a]. The trend holds true when the isotherms are not horizontal. An example of a downward extending INL offshore is shown in Figure 2, and an upward extending INL is given by *Pak and Zaneveld* [1978]. In the two examples cited above, the layers were parallel to the local isotherms. Because salinity changes with depth are often small below the halocline, isotherms are usually also parallel to isopycnals.

A comparison of light transmission and temperature distributions (Figures 8 and 9) shows that the clear water at about 60-m depth is associated with relatively low temperatures, and the INL around 100-m depth is associated with relatively high temperatures. The clear water appears to be directly correlated with the minimum temperatures, while the INL lies just under, rather than at, the maximum temperature. *Huyer* [1974] described the existence of a subsurface layer of rela-

Fig. 5. Profiles of chlorophyll-*a* (mg/m³) over the continental slope (stations 11, 13 and 14 in Figures 1 and 2) observed during the TT135 cruise (October 18, 1978).
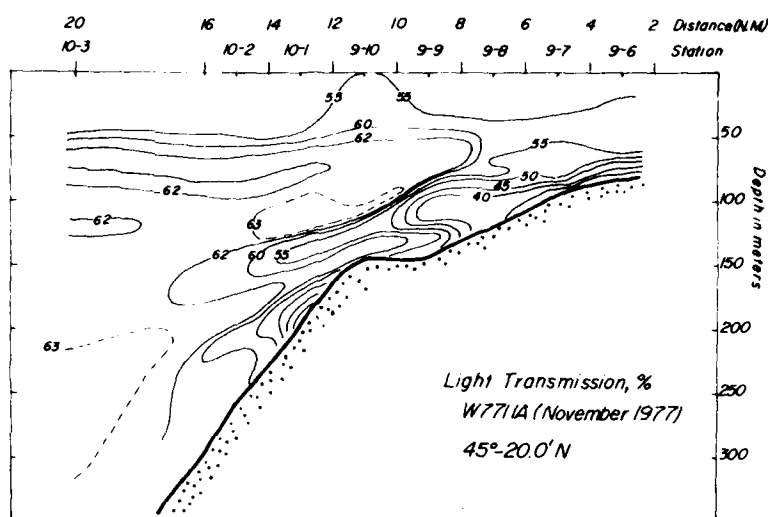
Fig. 7. Distribution of light transmission over the shelf off Oregon (Figure 1) observed during the W7711A cruise (November 9 10, 1977).

tively cold water in this region, and the layer was accounted for by advection of subarctic water by the coastal jet associated with the coastal upwelling regime. The low spm concentration in the cold water implies an offshore origin, while the low temperatures imply a northern source.

DISCUSSION

We have presented data which demonstrate the presence of spm maxima at several depths, and have also presented characteristic properties of the spm. Based on these observations, we now proceed to examine two hypotheses for the origin of such spm maxima.

The Settling Hypothesis

The settling hypothesis is based on downward transport of spm from the surface layer to the depth of the INL by gravitational settling. Stokes settling was examined extensively by Lerman et al. [1974], including effects of particle shapes, eddy diffusion, and the dissolution of particles. According to Lerman et al. [1974], an INL is formed as a result of changes in settling velocity, through the following processes: (1) due to increase in viscosity with depth and decrease in particle size by particle dissolution, settling velocity decreases resulting in increase in particle concentration with depth: and (2) at greater depths, particle concentration is reduced both in number and mass by dissolution of particles and rapid settling as a result of aggregation. A particle maximum requires an increase in particle concentration with depth, but it also requires fewer particles below the particle maximum. Thus an INL formed by particle settling alone requires accumulation of particles above and elimination of particles below the maximum.

Direct verification of the settling hypothesis seems difficult partly because (1) settling velocities are generally small, (2) vertical changes in settling velocity are small, (3) dissolution and aggregation are difficult to observe, and (4) the water column is usually moving at least 3 orders of magnitude faster horizontally than the prevailing settling velocity. Furthermore, trajectories of settling particles may be complicated by

vertical currents and vertical shear from variations in horizontal currents.

Settling. Stokes settling velocity w is expressed by

$$w = \frac{2}{9} r^2 \frac{g(\rho_s - \rho)}{\eta}$$

where ρ_s and ρ are the densities of the particle and water, respectively, η is molecular viscosity, r is the radius of the settling particle, and g is acceleration due to gravity. Within the normal range of water densities of the ocean, the maximum effect of water density on Stokes settling velocities is found to
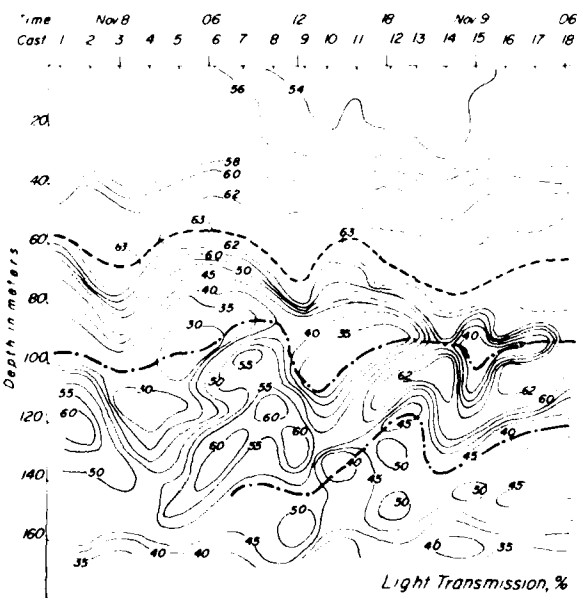

Fig. 8. Vertical distribution of light transmission (in percent) observed during the W7711A cruise at the anchor station approximately 10 n. mi. offshore (Figure 1). The clear water of over 63% transmission is denoted by a broken curve, and the intermediate nepheloid layers are denoted by dash-dot curves.

be approximately 0.5%, which is negligibly small. The viscosity of water increases, however, by 36% from 15° to 0°C, and Stokes settling decreases with increasing viscosity.

As shown above, changes in water properties could reduce Stokes settling by as much as, but no more than, 36%; hence particle concentration could increase by no more than 36% because of reduced settling. A large vertical gradient in water density has, nevertheless, often been considered to trap settling particles, particularly at a sharply developed thermocline [Jerlov, 1959; Carder et al., 1971; Lerman et al., 1974]. Changes in settling velocities at the thermocline are usually insufficient to fully account for the large spm maxima often observed there. Our data indicate that intermediate particle maxima often entail an increase of 300 to 1000% in particle volume compared to the water above the peak.

Particle settling has long been thought to be the dominant downward particle transfer process in the ocean. Based on Stokes settling velocities calculated from observed particle sizes and reasonable estimates of the other parameters in Stokes settling, McCave [1975] concluded that particles in aggregation, though rare, constitute most of the vertical flux. The other, much smaller, particles settle so slowly that their distribution is controlled by horizontal currents. Observed vertical distributions of spm, especially distributions that appear stable, are considered to consist of the slowly settling particles which are labelled 'background material' by McCave [1975]. The rapidly sinking particles, whether in aggregation or not, cannot be an important source to the INL because their residence at any one level will be short unless their settling velocity somehow changes abruptly to near zero. Thus when we consider settling as an important process of INL formation, the settling particles have to be the slowly settling background material.

Temperature of water decreases with depth; therefore the Stokes settling decreases with depth accordingly. In spite of smaller settling velocities in deep water, an INL is rarely ob-
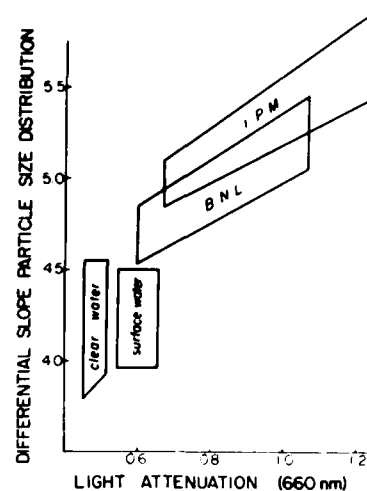
Fig. 10. Differential slope of particle size distribution plotted against light attenuation (660 n. mi.).

served in deep waters of the open ocean. Unless particles are eliminated from the water column by dissolution filter-feeders or aggregation and subsequent fast settling, more INLs would be expected in deep waters. Contrary results are found in observations.

Off the northern Peru coast (approximately 4°S latitude), a well-defined spm maximum was observed at approximately 400-m depth, and this maximum extended over 600 km offshore to the west from the coastal region [Pak et al., 1980a]. At the same depth, sharp vertical temperature and density gradients were also observed. The layer is well below the euphotic zone. This INL is one rare example of an INL found at maximum temperature and density gradients well below the seasonal thermocline.

Types of spm inferred from oxygen, chlorophyll-a and phaeophytin distributions. The spm distributions determined by a transmissometer do not indicate anything about the nature of the particles. This information has to be obtained by other means. Particles in the oceans are generally classified as belonging to one of two types: terrigenous and biogenous. Terrigenous particles are brought into the ocean by winds and river plumes. Most biogenous particles are produced in the upper part of the ocean where solar radiation penetrates. Detrital materials derived from phytoplankton and zooplankton are also present in the ocean. Thus the spm maximum, for example, may contain particles of terrigenous and detrital origins in addition to living phytoplankton cells. Living phytoplankton, however, are the only kind of particle that can produce oxygen. An oxygen maximum in excess of saturation can result only from the photosynthetic process.

The presence of the spm maximum concurrent with the oxygen maximum (Figure 4) points out that the spm maximum contains a large population of oxygen-producing particles, and these phytoplankton cells are most likely produced at the depth of the oxygen maximum. The oxygen maximum therefore indicates that the spm peak mainly consists of locally produced phytoplankton and is not produced by an accumulation of settling phytoplankton generated in the surface water above the spm maximum.

The maximum phytoplankton production at the upper part of the thermocline is probabl· due to an optimum photosynthesis condition. Solar irradiance decreases nearly ex-
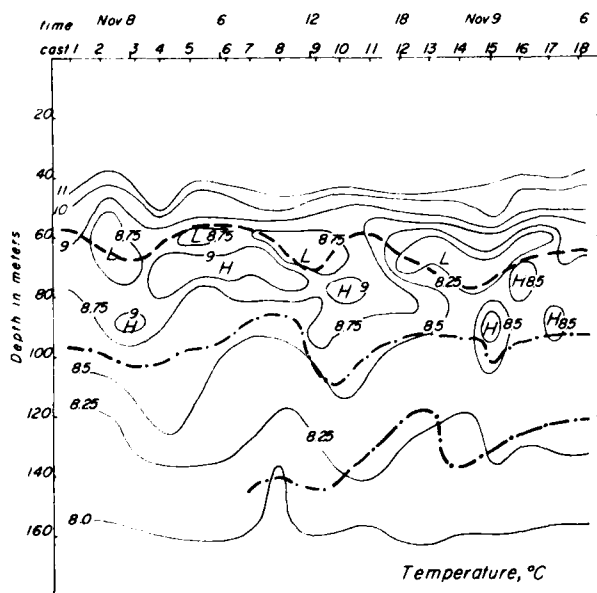

Fig. 9. Vertical distribution of temperature (°C) observed during the W7711A cruise at the anchor station approximately 10 n. mi. offshore (Figure 1). The axes of the clear water (broken curve) and intermediate nepheloid layers (dash-dot curves) in Figure 8 are added.
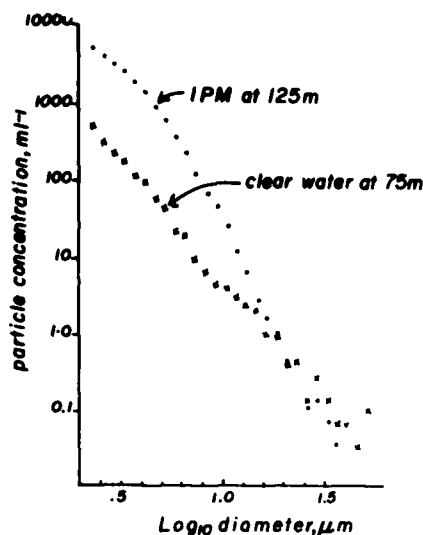
Fig. 11. Particle size distribution determined by a Coulter counter during the W7711A cruise at a station 10 n. mi. offshore on the 45°–20.0'N latitude.

ponentially with depth, but the nutrient concentration generally increases with depth from very low values in the surface water. Consequently, an optimum condition for photosynthesis usually exists at some distance below the sea surface, but still within the photic zone. The depths of the chlorophyll-*a* maximum (Figure 5) and phaeophytin maximum (Figure 6) also correspond to the spm and oxygen maxima, corroborating that the maximum photosynthetic production occurs in the spm maximum layer.

The vertically homogenous surface layer, indicated in all the parameters (Figure 4) including spm and dissolved oxygen, is obviously a result of mixing. Since the concentrations of spm and oxygen at their thermocline maxima are larger than those in the mixed layer above them, the maxima could not have been formed by the mixing process in the surface layer. Furthermore, the spm maximum is located in the thermocline where vertical mixing is limited.

Biochemical changes might change settling velocities of phytoplankton in the surface layer and contribute to the accumulation of phytoplankton at the thermocline. Those biochemical changes that might lead to retardation of settling phytoplankton are likely to be in the nature of degradation, and degradation of phytoplankton will consume rather than produce oxygen. Thus based on the oxygen maximum at the spm maximum, phytoplankton in the spm maximum layer are more likely to be living cells rather than dead cells; accordingly, they are more likely to be produced locally rather than be accumulated by settling from the surface layer.

Evidence is thus convincing that the thermocline spm maximum is a result of in situ phytoplankton production due to the optimum photosynthetic conditions present at the upper part of the thermocline. The settling hypothesis is therefore not corroborated by our observations of the thermocline spm layer.

The INL observed during October 1978 is not new in its shape, size, and location relative to the bottom topography [Pak and Zanveld, 1978] but its association with low oxygen concentration is newly observed. The distribution of oxygen in the section (Figure 3) shows that low oxygen concentration

is found in the deep water and in the bottom waters over the shelf and slope. Thus we can consider these low oxygen waters as possible sources of the oxygen minimum layer; that is, advection of the low oxygen water from the sources might have resulted in the observed oxygen minimum layer. We must not, however, neglect oxygen loss due to biochemical processes in the organic particulate matter in suspension. We do not have data to verify how much organic matter was present in the INL. Earlier data taken over the shelf off Oregon using an ozone method [Pak et al., 1980b] indicated that both the BNL and INL contained relatively small amounts of organic matter. Under this circumstance, advection of low oxygen water may be the primary contribution to the formation of the oxygen minimum layer, and the local reduction of oxygen by suspended organic particles only a minor contribution.

Observed PSD. PSD slope is expected to be a relatively stable property of spm since it can be changed only by addition and subtraction of particles or by changes in particle sizes over a limited range of the size spectrum. The increase or decrease in particle size may come from particle disintegration or aggregation within a given water sample. The slopes of PSD in the surface water are approximately the same as those of the clear water below the surface water (Figure 10), indicating that the PSD did not change appreciably even if the particles had to settle through the surface layer and the clean water. Furthermore, the concentration of large-sized particles varies little from the INL to the clear water above it (Figure 11). The large population of small-sized particles in the INL therefore suggests addition of small-sized particles rather than internal shifts of particles sizes. If settling particles are to generate an INL with the observed characteristic PSD, the settling particles must reduce their size as soon as they reach the INL, not before, in order to maintain a constant concentration of large-sized particles. The decrease in settling velocity as a function of depth must correspond to the increase in spm concentration as a function of depth.

Lal and Lerman [1975] studied the changes in the particle size spectrum when particles undergo dissolution while settling. They considered dissolution at a constant rate and independent of particle size and water depth. Relative to a reference depth below the sea surface, dissolving particles are shown to generate domes or peaks at the small end of the size spectrum (size range of 1–10 μm), and location of the peak moves toward the large size with an increase in depth. Such a feature is a consequence of dissolution in proportion to the surface-to-volume ratio of particles. Dissolution is more effective in small-sized particles since a small particle has a higher surface-to-volume ratio than a large particle. Our observation of PSD's below the surface layer, however, show no indications of domes, both in and out of the INL.

Boundaries of INL's are often sharply defined (Figure 14). Such sharp boundaries are not likely to be the result of large differences in settling velocities. Similarly, bottom boundaries of INL's are sometimes defined as sharply as the upper boundary (Figure 14), and it is equally difficult to imagine that elimination of particles by dissolution and rapid settling by particle aggregation can result in such a sharp boundary.

Viscosity is strongly controlled by temperature, yet nepheloid layers are not often found at greater water depths beneath the euphotic zone, even in regions with a sharp temperature gradient or in the region of minimum temperature in the water column. As mentioned earlier, an exceptional case was observed off northern Peru where a neph-
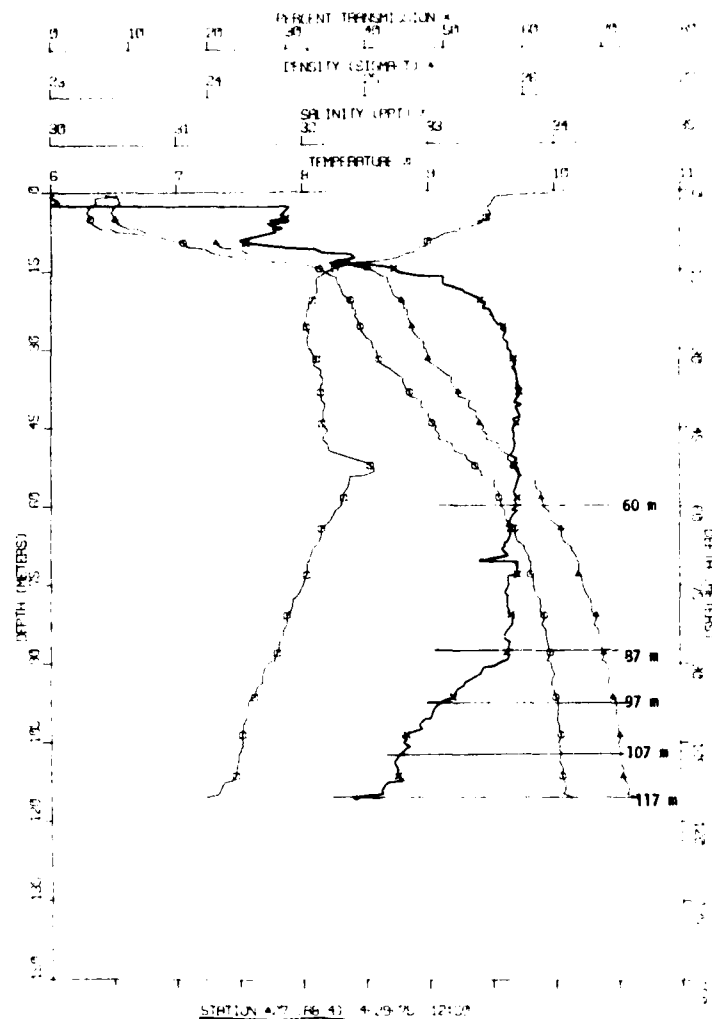
Fig. 12. Profiles of T, S, σ_t and light transmission (in percent) observed during the W7504 cruise at a station 8 n. mi. offshore on the 45°-10.0'N latitude. Depths of water samples for particle size analyses are denoted by horizontal lines.

eloid layer was found at a maximum temperature gradient at 400-m depth. Turbulence associated with internal waves at the temperature gradient may disturb the continental slopes [Cachione and Wunch, 1974], and particles may spread offshore in the layer. In this case, the particle transfer is a horizontal process, not a settling process.

Temporal variations of spm distribution. Time series of light transmission and temperature profiles were taken simultaneously during the W7711A cruise at an anchor station 10 n. mi. off the coast at 45°-20'N latitude. Observations were made for 36 hours at intervals of 2 hours. The data from the anchor station show the typical light transmission distribution of shelf water (Figure 8). The INL shows vertical displacements of up to 25 m in a few hours, and changes of the thickness of the INL centered around 100-m depth from 10 to 70 m. The temporal variations shown in Figure 8 (i.e., changes in thickness, depth, and spm concentration in the INL), are considerably larger than what Stokes settling by small particles can account for. The temporal variations clearly suggest that processes other than Stokes settling prevail.

Horizontal Advection Hypothesis

Observations at the thermocline spm maximum clearly suggest that the thermocline spm maximum is the result of a local maximum in photosynthetic production of phytoplankton. Deep INL's are obviously produced by other processes since they are not in the euphotic zone.

The distributions of spm concentration, PSD, oxygen, and hydrographic data at about 125-m depth off the Oregon coast (Figure 7) cannot be accounted for by the settling hypothesis. We now use the same evidence to examine an alternative hypothesis, the horizontal advection hypothesis.

Generation of an INL by horizontal advection of BNL's. There are two prominent sources of spm in the ocean, one in the surface layer and the other in the BNL. The possibility of generating an INL by drawing spm from the surface layer via the settling process has already been discussed. Alternatively, an INL may be generated by drawing particles from a BNL, the other prominent spm source in the ocean. In this case, the primary mode of particle transport will be hori-
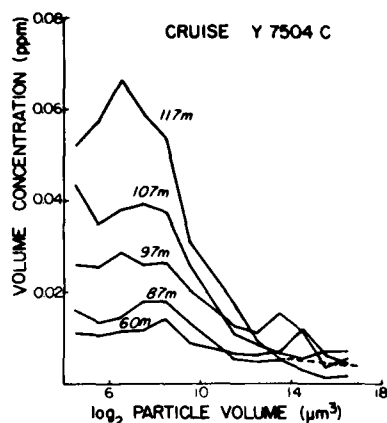
Fig. 13. Particle concentration by volume at five depths shown in Figure 12.

The horizontal advection hypothesis has been suggested by the present authors [*Pak and Zaneveld*, 1978; *Pak et al.*, 1980a] on the basis of (1) a distinct tongue-shaped pattern of an INL extending horizontally from a BNL over the outer continental shelves off Oregon and Peru; (2) the presence of an INL along a narrow range of water densities; and (3) the association of the INL with maxima in nitrite and particulate protein and minima in oxygen and nitrate.

In addition to the above, the PSD data presented in this paper indicate that the PSD's in the INL are similar to those in the BNL, but dissimilar to those in the clear water above and below the INL. The similarity in PSD between the INL and the BNL suggests that the two are related. The relationship requires horizontal advection from the BNL into the INL. A BNL over a sloped bottom can be considered as a source from which particles can be spread horizontally to generate an INL. Since the spm in the BNL has the same PSD characteristics as the INL, the spm need not undergo any radical change in moving laterally from the BNL to the INL.

zontal advection rather than vertical settling. This process will be more effective in areas where the bottom is sloped. BNL's are nearly ubiquitous, although their intensity and thickness may vary substantially in time and space (Figures 7 and 8).

Both the upper and lower boundaries of the spreading turbid water (INL) can be sharp or diffuse, depending only on the mixing conditions of the INL, rather than on the dissolution behavior of the particles. It is only required that the
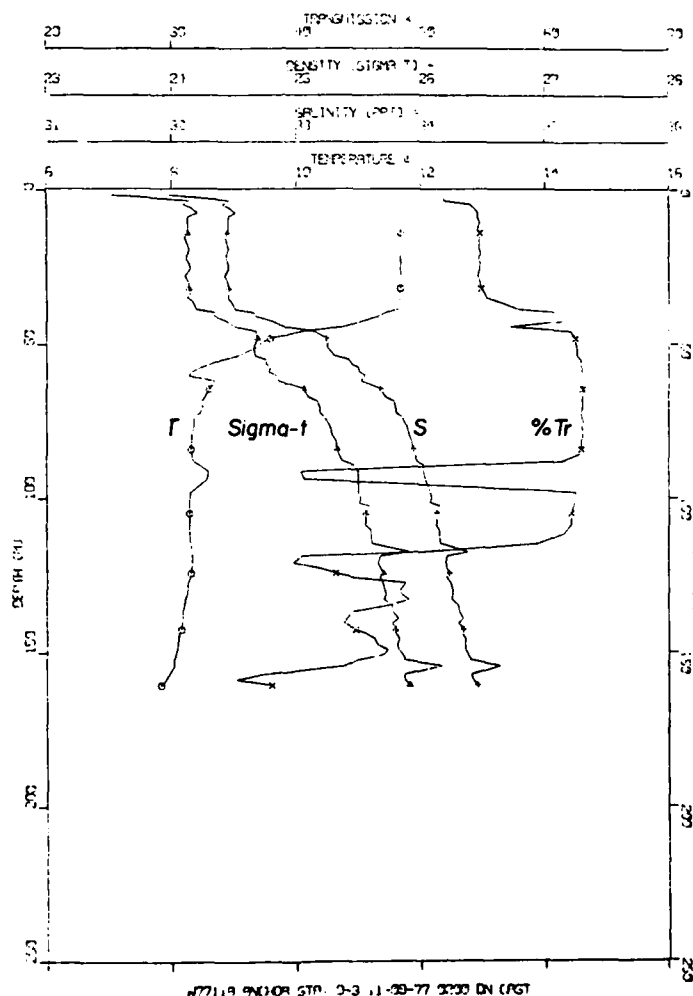

Fig. 14. Profiles of T, S, σ_t, and light transmission observed during the W7711A cruise at a station 10 n. mi. offshore on the 45°–20.0'N latitude.

particles be nearly neutrally buoyant, settling very slowly. The predominance of small particles, indicated by large slopes in PSD, assures that those particles meet this requirement.

An spm maximum, as shown in this paper, can be associated with either an oxygen maximum or minimum. The distribution of oxygen in the zonal section shown in Figure 3 suggests that the source of the low oxygen water (or oxygen sink) for the oxygen minimum layer near 200 m is in the bottom water over the shelf. Thus the process of the INL formation suggested above and in earlier papers [Pak and Zaneveld, 1978; Pak et al., 1980a] is also consistent with the formation of the oxygen minimum layer. The oxygen minimum layer presented in Figure 3 is a smaller-scale feature than that off Peru. It is not possible to ascertain from the data whether the spm maximum produces the oxygen minimum or whether they are advected jointly from the shelf. It is certain, however, that INL's such as those observed off Oregon, Washington, and Peru cannot be generated locally and must be the result of horizontal advection.

Other Remarks

It is noteworthy that similar INL's have been observed over widely separate areas (off the coasts of Peru, Oregon, and Washington) and over a span of several years. Observations off Peru have not been repeated, but repeated measurements were made off Oregon and Washington. The common features of these INL's suggest that these layers might be generated by common processes. All the observations made so far happened to be in the vicinity of the eastern boundaries of the Pacific, in connection with continental shelves and slopes, and approximately at depths of shelf edges. We would speculate that one or more physical processes together with the common topographic features may be important in generation of the observed INL's. We can think of several examples of such processes: coastal upwelling, eastern boundary currents, and interaction between internal waves and bottom topography. These topics are suggested for future studies.

The linear relationship between spm concentration and PSD slope (Figure 10) is remarkable. The BNL's and INL's have similar properties, but they are different from the surface layer and clear water at mid-depth. During the W7711A cruise (when the data for Figure 10 were taken), the seas were very rough, so that the bottom water might have been associated with unusually high turbulence. The unusually well-developed INL's observed during this cruise seem to substantiate the higher-energy conditions.

CONCLUSIONS

Significant vertical transport of particulate matter occurs only for larger particle sizes. Small suspended particles have settling velocities that are many orders of magnitude smaller than horizontal advection and their distribution is thus determined by processes other than vertical settling.

Vertical profiles of beam transmission, oxygen, and hydrographic parameters presented here demonstrate that the thermocline spm maximum is due to in situ phytoplankton generation. The upper part of the thermocline has sufficient light from above, a sufficient supply of nutrients from below to provide optimum photosynthetic conditions. Vertical mixing is also a minimum in the upper part of the thermocline, permitting large residence times for phytoplankton.

The intermediate nepheloid layers below the thermocline

are shown to be a result of offshore quasi-horizontal transport of bottom nepheloid material away from the shelf edge. A diagram mapping the slope of the particle size distribution and the beam attenuation coefficient clearly showed the relationship of INL and BNL materials. The increase in suspended volume in the INL and BNL relative to adjacent waters is due to small particles. An oxygen minimum coincident with the INL as well as hydrographic data corroborate the horizontal advection hypothesis for the generation of intermediate particle maxima.

REFERENCES

Bartz, R., J. R. V. Zaneveld, and H. Pak, A transmissometer for profiling and moored observations in water, Proc. Soc. Photo Opt. Instrum. Eng., 160, 102-108, 1978.

Beardsley, G. F., Jr., H. Pak, K. Carder, and B. Lundgren, Light scattering and suspended particles in the eastern equatorial Pacific Ocean, J. Geophys. Res., 75(15), 2837-2845, 1970.

Cachione, D., and C. Wunch, Experimental study of internal waves over a slope, J. Fluid Mech, 66(2), 223-239, 1974.

Carder, K. L., G. F. Beardsley, Jr., and H. Pak, Particle size distributions in the eastern equatorial Pacific, J. Geophys. Res., 76(21), 5070-5077, 1971.

Drake, D. E., Distribution and transport of suspended particulate matter in submarine canyons off southern California, in Suspended Solids in Water, edited by R. J. Gibbs, pp. 133-153, Plenum, New York, 1974.

Huyer, A. Observations of the coastal upwelling region off Oregon during 1972, Ph.D. thesis, 149 pp., Oregon State Univ., Corvallis, 1974.

Jerlov, N. G., Particle distribution in the ocean, Rep. Swed. Deep Sea Exped., 3, 73-97, 1953.

Jerlov, N. G., Maxima in the vertical distribution of particles in the sea, Deep Sea Res., 5, 178-184, 1959.

Kitchen, J. C., Particle size distributions and the vertical distribution of suspended matter in the upwelling region off Oregon, M.S. thesis, 118 pp., Oreg. State Univ., Corvallis, 1978.

Lal, D., and A. Lerman, Size spectra of biogenic particles in ocean water and sediments, J. Geophys. Res., 80(3), 423-430, 1975.

Lerman, A., D. Lal, and M. F. Dacey, Stokes settling and chemical reactivity of suspended particles in natural waters, in Suspended Solids in Water, edited by R. J. Gibbs, pp. 17-47, Plenum, New York, 1974.

Lorenzen, C. J., A note on the chlorophyll and phaeophytin content of the chlorophyll maximum, Limnol. Oceanogr., 10(3), 482-483, 1965.

Matlack, D. E., Deep ocean optical measurement (DOOM) report on the North Atlantic, Caribbean, and Mediterranean cruises, Tech. Rep. 74-42, Nav. Ordnance Lab., White Oak, Silver Spring, Md., 1974.

McCave, I. N., Vertical flux of particles in the ocean, Deep Sea Res., 22, 491-502, 1975.

Pak, H., and J. R. V. Zaneveld, Bottom nepheloid layers and bottom mixed layers observed on the continental shelf off Oregon, J. Geophys. Res., 82(27), 3921-3931, 1977.

Pak, H., and J. R. V. Zaneveld, Intermediate nepheloid layers observed over the continental margins off Oregon, Proc. Soc. Photo Opt. Instrum. Eng., 160, 9-17, 1978.

Pak, H., L. A. Codispoti, and J. R. V. Zaneveld, An intermediate particle maximum associated with the low oxygen water off Peru, Deep Sea Res., in press, 1980a.

Pak, H., J. Kitchen, P. Donaghay, and J. R. V. Zaneveld, Some observations on the effect of ozone treatment on suspended particulate matter in seawater, submitted to Estuarine Coastal Mar. Sci., 1980b.

Peterson, R. L., A study of suspended particulate matter: Arctic Ocean and Northern Oregon Continental Shelf, Ph.D. thesis, Oreg. State Univ., Corvallis, 1977.

Riley, G. A., H. Stommel, and D. F. Bumpus, Quantitative ecology of the plankton of the western North Atlantic, *Bull. Bingham Oceangr. Coll., 12*, 1-169, 1949.

Strickland, J. D. H., and T. R. Parsons, A practical handbook of seawater analysis, *Fish. Res. Board Can., 167*, 1-310, 1972.

Zaneveld, J. R. V., Optical and hydrographical observations of the Cromwell Current between 92°-00'W and Galapagos Islands, Ph.D. thesis, Oreg. State Univ., Corvallis, 1971.

Zaneveld, J. R. V., J. C. Kitchen, R. Bartz, D. Menzies, S. Moore, R. Spinrad, and H. Pak, Optical, hydrographical, and chemical observations in the Monterey Bay area during May and September 1977, *Ref. 78-13*, Oreg. State Univ., Corvallis, Aug. 1978.